



Modeling of Sonar Transducers and Arrays

Dr. George W Benthien

Dr. Stephen Hobbs

September 27, 2005

george@gbenthien.net

Steve.hobbs@spawar.navy.mil

Contents

1	Introduction	1-1
2	Acoustic Modeling	2-1
2.1	The Acoustic Wave Equation	2-1
2.2	Analytic Solutions of the Wave Equation	2-7
2.3	Plane Wave Solutions	2-11
2.4	Point Sources and Dipoles	2-11
2.5	Integral Relations	2-12
2.6	Nonuniqueness of solution to Helmholtz Integral Equation	2-14
2.7	Integral Equation Methods	2-19
2.8	Far-Field Approximations	2-20
2.9	The Kirchhoff Time-Domain Integral Equation	2-22
2.10	Infinite Element Methods	2-28
2.11	Wave Envelope Method	2-29
2.12	Radiation Boundary Conditions	2-30
2.13	An Integral Equation Variational Method	2-32
2.14	Doubly Asymptotic Approximations	2-33

2.15	Array Acoustic Interactions	2-36
2.16	Pritchard Approximation	2-41
2.17	Nearest Neighbor Approximation	2-42
2.18	T-matrix Approach to Array Interactions	2-46
2.19	Velocity Control of Arrays	2-51
2.20	Use of Virtual Resistors in Arrays	2-53
2.21	Acoustic Radiation Modes	2-55
2.21.1	Axisymmetric sphere problem	2-56
2.21.2	General problem	2-59
3	Structural Modeling	3-1
3.1	Variational Methods	3-1
3.1.1	Example Problem	3-2
3.1.2	Variational Based Numerical Methods	3-7
3.1.3	Example Dynamic Problem	3-10
3.1.4	Nodes vs. elements	3-12
3.2	Interpolation Schemes	3-13
3.3	Structural Finite Elements	3-16
3.4	Fluid Finite Elements	3-19
3.5	Piezoelectric Finite Elements	3-23
3.5.1	Mechanical Equations	3-23
3.5.2	Electrical Equations	3-24
3.5.3	Constitutive Equations	3-24
3.5.4	Interpolation Functions	3-24

3.5.5	Finite Element Equations	3-25
3.6	Magnetostrictive Finite Elements	3-29
3.6.1	Magnetic Potential	3-29
3.6.2	Basic Equations	3-30
3.6.3	Interpolation Functions	3-31
3.6.4	Elastic Finite Element Equations	3-32
3.6.5	Magnetic Finite Element Equations	3-33
3.6.6	Current Finite Element Equations	3-34
3.6.7	Summary of Finite Element Equations	3-36
3.7	Variational Approximations	3-37
3.7.1	Longitudinal Vibration of a Cylindrical Bar	3-37
3.7.2	Vibration of a Ceramic Stack with Nonuniform Material Properties	3-40
3.8	One-dimensional (plane wave) Model of a Piezoelectric Rod	3-46
3.9	One-dimensional Model of a Magnetostrictive Rod	3-53
3.10	Cascading of Plane Wave Segments	3-62
4	Structure-Acoustic Coupling	4-1
5	Electrical Interconnections	5-1
6	Material Parameters	6-1
7	Specific Projector types	7-1
7.1	Class VII Terfenol Driven Flexensional Projector	7-1
7.2	Slotted Cylinder Projector	7-3

7.3 Hydroacoustic Projector	7-4
8 Transducer Modelling Contributions of Ralph Woollett	8-1
9 Lead Magnesium Niobate Materials (Dr. S. Pilgrim)	9-1
10 Terfenol Magnetostrictive Materials (Dr. A. Clark)	10-1

LIST OF DOCUMENTS ON CD

Chapter 1

Introduction

This report contains a number of topics that the authors have found to be important in the modeling of sonar transducers and transducer arrays. The work was sponsored by ONR code 321SS under the direction of Jan Lindberg. Much of the material in this report is taken from the Handbook of Acoustic Projector Technology [G. Benthien and D. Barach, *Handbook of Acoustic Projector Technology*. SPAWAR Technical Document 2980, Rev. 1 (1998)]. This handbook had limited distribution since some of the material was classified as military critical. The primary purpose of this report is to present the non military critical parts of the handbook in a form that is available to a larger audience. In addition, some of the sections have been expanded and some new material added. The portions of this report that deal with transducer and array modeling were compiled primarily by the authors with assistance from Don Barach, David Gillette, and Jerry Dejaco. The chapter on PZN ceramic materials was compiled by Dr. Steven Pilgrim of Alfred University. The chapter on Terfenol magnetostrictive materials was supplied by Dr. Arthur Clark formerly of NSWC, Carderock and now with Art Clark Associates. This report was placed on a CD-ROM so that a number of non copyright protected reference documents could be included. The included documents are listed in the LIST OF DOCUMENTS ON CD section. Throughout this report, references to documents that are contained on the CD-ROM are highlighted in blue. The highlighted documents can be accessed by clicking on the highlighted links. Internal links such as equation or figure references are highlighted in red. It will be noticed that not all subjects are covered to the same depth. In those cases where the material is widely available in the literature, only a summary is usually given. In those cases where the material is either not available or is difficult to obtain, a more detailed discussion is given.

The second chapter contains material on acoustic modeling. It is well known that acoustic loading has a big impact on transducer and array performance. This chapter contains a review of acoustic fundamentals as well as a description of various methods for computing the acoustic loading and radiation. The third chapter contains material on modeling the struc-

tural components of a transducer. It covers finite element modeling of elastic, piezoelectric and magnetostrictive components as well as one-dimensional plane-wave and “lumped parameter” models. The fourth chapter contains material on structure-acoustic coupling. Here it is shown how the acoustic and structural models can be combined to predict the output of a transducer or an array of transducers. The fifth chapter discusses electrical interconnections. In an array it is possible for the elements to interact electrically as well as through the acoustic medium depending on how the elements are connected electrically. This chapter presents a unified approach to handling of these electrical interactions. The sixth chapter contains some typical material parameters that can be used in transducer modeling when more accurate parameters are not available from measurements. The seventh chapter discusses briefly some specific transducer types that are currently of interest to the Navy as well as private industry. Some of the relevant material in this chapter can not be presented in this report since it is regarded as military critical. In those cases references are given to reports that discuss the modeling details. Chapter eight contains links to several transducer documents published by Ralph Woollett who was a pioneer in this area. The referenced documents are contained on this CD-ROM. The last two chapters contain information on some newer transducer materials. Chapter nine contains information on Lead Magnesium Niobate as an active source material. Chapter ten contains information on rare earth magnetostrictive materials.

It is hoped that the material in this report will be of use to future transducer designers and analysts.

Chapter 2

Acoustic Modeling

2.1 The Acoustic Wave Equation

The principal quantity of interest in classical (linear) acoustics is the acoustic pressure $p(x, t)$ which is a function of both position and time. The acoustic pressure is the excess pressure over the hydrostatic pressure due to compressional waves in the medium. The acoustic pressure $p(x, t)$ satisfies the wave equation

$$\Delta p = \frac{1}{c^2} \ddot{p} = \frac{1}{c^2} \frac{\partial^2 p}{\partial t^2}. \quad (2.1.1)$$

Here Δ is the spatial Laplacian operator and c is the speed of sound in the fluid medium. For water c is approximately 1500 m/s and for air c is approximately 330 m/s. The pressure p is related to the particle acceleration \ddot{u} by the equation of motion

$$-\nabla p = \rho \ddot{u} = \rho \frac{\partial^2 u}{\partial t^2}. \quad (2.1.2)$$

Here ∇ is the spatial gradient operator and ρ is the static density of the fluid medium. For water ρ is approximately 1000 kg/m³ and for air ρ is approximately 1.2 kg/m³. Two good references on the fundamentals of acoustics are [Allan D. Pierce, Acoustics, Acoustical Society of America Publication (1989)] and [P.M. Morse and K.U. Ingard, Theoretical Acoustics, McGraw-Hill (1968)]. Although the acoustic equations for air and water have the same form, the differences in their sound velocity and density leads to quite different behavior. Since air is easily compressed, the acoustic pressure in air is relatively small and the particle motions are relatively large. In water the behavior is just the opposite — the acoustic pressure is relatively high and the particle motions are extremely small. For this reason, most acoustic receivers in water are pressure sensing devices.

Let us now consider some general ideas relating to the production of sound in water. Recall that acoustic waves are compressional in nature. Thus, to produce sound a vibrating source must compress the water. Two properties of water work against its compression. First, as a material water is relatively incompressible. In fact, it is often considered incompressible in the analysis of fluid flow. Second, water has the ability to flow. This means that water will tend to flow away from a vibrating source rather than stay put and be compressed. How then do we produce sound in water? The main thing we have going for us is the inertia of the water. If the vibrating source can accelerate fast enough, the inertia of the fluid will restrain its flow and it can be compressed. Thus, the acceleration of the source is key to sound production. This is the reason it is much easier to produce sound with a high frequency vibrator than with a low frequency one. For a given maximum displacement, a high frequency vibrator has greater acceleration than its low frequency counterpart. Thus, at low frequencies a source generally must produce larger displacements and have a larger radiating area.

Often in acoustics it is more convenient to work in the frequency domain than in the time domain. By frequency domain we mean the Fourier transform domain. The Fourier transform P of p is defined by the pair of relations

$$p(x, t) = \int_{-\infty}^{\infty} P(x, \omega) e^{i\omega t} d\omega \quad (\text{inverse Fourier transform}), \quad (2.1.3a)$$

where

$$P(x, \omega) = \int_{-\infty}^{\infty} p(x, t) e^{-i\omega t} dt. \quad (\text{Fourier transform}) \quad (2.1.3b)$$

The transform variable ω is called the angular frequency, and the related quantity $f = \omega/(2\pi)$ is called the frequency. It should be noted that whereas the pressure p is a real quantity, the transformed pressure P is in general complex. The Fourier transform is useful in linear problems where the transform operator commutes with the differential or integral operators involved in the problem. Time derivatives become algebraic operations in the frequency domain. For example, the Fourier transform of \dot{p} is $i\omega P$. Time delays are also easy to handle in the frequency domain. For example, the Fourier transform of $p(t - \tau)$ is $e^{-i\omega\tau} P(\omega)$. The time delay most often encountered in acoustic problems is the time d/c for a sound wave to travel a distance d . The Fourier transform of $p(t - d/c)$ is $e^{-ikd} P(\omega)$, where $k = \omega/c$ is called the acoustic wavenumber. Parseval's theorem for Fourier transforms relates the time integral of p^2 to the frequency integral of $|P|^2$, i.e.,

$$\int_{-\infty}^{\infty} p^2(x, t) dt = \int_{-\infty}^{\infty} |P(x, \omega)|^2 d\omega. \quad (2.1.4)$$

Since p is a real quantity, it can be shown that the Fourier transform P satisfies

$$P(-\omega) = P^*(\omega), \quad (2.1.5)$$

where $*$ denotes complex conjugate. Thus, the pressure p is completely determined by $P(\omega)$ for positive frequencies. In fact

$$p(t) = \int_0^\infty [P(\omega)e^{i\omega t} + P^*(\omega)e^{-i\omega t}] d\omega. \quad (2.1.6)$$

Let us denote the integrand of equation (2.1.6) by $p_\omega(t)$, i.e.,

$$p_\omega(t) = P(\omega)e^{i\omega t} + P^*(\omega)e^{-i\omega t}. \quad (2.1.7)$$

Clearly, p_ω is a real sinusoidal function of time with frequency f . The function p_ω can also be written in terms of trigonometric functions as follows

$$p_\omega(t) = 2 \operatorname{Real}(Pe^{i\omega t}) \quad (2.1.8a)$$

$$= 2 \operatorname{Real}(P) \cos(\omega t) - 2 \operatorname{Imag}(P) \sin(\omega t) \quad (2.1.8b)$$

$$= 2|P| \cos(\omega t + \phi), \quad (2.1.8c)$$

where ϕ is defined by

$$\cos(\phi) = \frac{\operatorname{Real}(P)}{|P|} \quad \text{and} \quad \sin(\phi) = \frac{\operatorname{Imag}(P)}{|P|}. \quad (2.1.9)$$

Clearly, the peak value \hat{p}_ω of p_ω is given by

$$\hat{p}_\omega = 2|P(\omega)|. \quad (2.1.10)$$

The root-mean-square value $p_{\text{rms}}(\omega)$ is the square root of the average over a period of p_ω^2 . It is given by

$$p_{\text{rms}}(\omega) = \sqrt{2}|P(\omega)| = \frac{1}{\sqrt{2}}\hat{p}_\omega. \quad (2.1.11)$$

The Fourier transformed pressure can be normalized so that its absolute value is the rms pressure. If we define \bar{P} by

$$\bar{P} = \sqrt{2}P, \quad (2.1.12)$$

then $|\bar{P}| = p_{\text{rms}}$.

The Fourier transformed pressure $P(x, \omega)$ [and also \bar{P}] satisfies the reduced wave equation

$$\Delta P + k^2 P = 0, \quad (2.1.13)$$

where $k = \omega/c$ is the acoustic wavenumber. The equation of motion given in (2.1.2) can be expressed in terms of transformed variables as

$$-\nabla P = -\omega^2 \rho U = i\omega \rho V, \quad (2.1.14)$$

where U is the Fourier transform of the displacement u and V is the Fourier transform of the velocity $v = \dot{u}$.

The pressure p and particle velocity v also satisfy the following analog of Poynting's theorem in electromagnetics

$$\dot{W} + \mathbf{div} I = 0, \quad (2.1.15)$$

where

$$W = \frac{1}{2}\rho(v \cdot v) + \frac{1}{2}\frac{p^2}{\rho c^2} \quad \text{and} \quad I = pv. \quad (2.1.16)$$

The quantity $\frac{1}{2}\rho(v \cdot v)$ is called the acoustic kinetic energy density, the quantity $\frac{1}{2}p^2/(\rho c^2)$ is called the acoustic potential energy density, and the quantity I is called the acoustic intensity vector. Integrating equation (2.1.15) over a fluid volume \mathcal{V} bounded by the surface S , we have

$$\dot{K} + \dot{U} + \int_S pv \cdot n = 0, \quad (2.1.17)$$

where $K = \frac{1}{2} \int_{\mathcal{V}} \rho v \cdot v$ is the kinetic energy and $U = \frac{1}{2} \int_{\mathcal{V}} p^2/(\rho c^2)$ is the potential energy. Equation (2.1.17) is a power balance relation for the fluid volume \mathcal{V} . It basically says that the power entering the volume through the boundary equals the time rate of change of the sum of the kinetic and potential energy in the volume.

If p_ω and v_ω are the sinusoidal functions of time associated with the pressure p and velocity v as in equation (2.1.6), then it can be shown that the relation (2.1.15) also holds for p_ω and v_ω . For these sinusoidal functions the average I_{avg} of I over a period is given by

$$I_{\text{avg}} = 2 \text{Real}(PV^*) = \text{Real}(\bar{P}\bar{V}^*). \quad (2.1.18)$$

Since p_ω and v_ω are periodic functions of time, the average over a period of \dot{W} is zero and hence equation (2.1.15) implies

$$\mathbf{div} I_{\text{avg}} = 0. \quad (2.1.19)$$

If S_{rad} is a radiating surface and S is a surface completely enclosing S_{rad} and no other sources, then the divergence theorem applied to equation (2.1.19) gives

$$\int_{S_{\text{rad}}} I_{\text{avg}} \cdot n = \int_S I_{\text{avg}} \cdot n, \quad (2.1.20)$$

where n is the outward unit normal vector. The integrals in equation (2.1.20) represent the average power \mathcal{P}_{avg} radiated by the source. Moreover,

$$\mathcal{P}_{\text{avg}} = 2 \text{Real} \int_{S_{\text{rad}}} P(V^* \cdot n) = \text{Real} \int_{S_{\text{rad}}} \bar{P}(\bar{V}^* \cdot n) \quad (2.1.21)$$

$$= 2 \text{Real} \int_S P(V^* \cdot n) = \text{Real} \int_S \bar{P}(\bar{V}^* \cdot n). \quad (2.1.22)$$

If we let S be a very large spherical surface of radius R surrounding the source, then the pressure and normal particle velocity on this surface approximately obey the plane wave relation

$$\bar{P} = \rho c (\bar{V} \cdot n). \quad (2.1.23)$$

Combining equations (2.1.22) and (2.1.23), we have

$$\mathcal{P}_{\text{avg}} = \frac{1}{\rho c} \int_S |\bar{P}|^2 \quad (2.1.24)$$

$$= \frac{|\bar{P}_{\text{ax}}|^2}{\rho c} \int_S \frac{|\bar{P}|^2}{|\bar{P}_{\text{ax}}|^2} \quad (2.1.25)$$

$$= \frac{4\pi R^2 |\bar{P}_{\text{ax}}|^2}{\rho c} \frac{1}{4\pi} \int_0^\pi \sin \theta d\theta \int_0^{2\pi} B(\theta, \phi) d\phi, \quad (2.1.26)$$

where $B(\theta, \phi) = |\bar{P}|^2 / |\bar{P}_{\text{ax}}|^2$ is called the beam pattern of the source and \bar{P}_{ax} is the pressure on S in some preassigned direction (usually the direction of maximum response). Taking the logarithm of equation (2.1.26), we obtain

$$10 \log_{10} \mathcal{P}_{\text{avg}} = 10 \log_{10} \left(\frac{4\pi}{\rho c} \right) + 10 \log_{10} (R^2 |\bar{P}_{\text{ax}}|^2) + 10 \log_{10} \left(\frac{1}{4\pi} \int_0^\pi \sin \theta d\theta \int_0^{2\pi} B(\theta, \phi) d\phi \right). \quad (2.1.27)$$

Let P_0 be a reference pressure (usually one micro Pascal), let R_0 be a reference distance (usually one meter), and let \mathcal{P}_0 be a reference power (usually one watt). Equation (2.1.27) can be rearranged to give

$$\text{SL} = -10 \log_{10} \left(\frac{4\pi P_0^2 R_0^2}{\rho c \mathcal{P}_0} \right) + 10 \log_{10} \mathcal{P}_{\text{avg}} + \text{DI}, \quad (2.1.28)$$

where SL is called the source level and is defined by

$$\text{SL} = 10 \log_{10} \left(\frac{R^2 |\bar{P}_{\text{ax}}|^2}{R_0^2 P_0^2} \right); \quad (2.1.29)$$

DI is called the directivity index and is defined by

$$\text{DI} = 10 \log_{10} \left(\frac{4\pi}{\int_0^\pi \sin \theta d\theta \int_0^{2\pi} B(\theta, \phi) d\phi} \right). \quad (2.1.30)$$

For $\rho = 1000 \text{ Kg/m}^3$, $c = 1500 \text{ m/sec}$, $P_0 = 1 \text{ } \mu\text{Pa}$, $R_0 = 1 \text{ m}$, and $\mathcal{P}_0 = 1 \text{ Watt}$, the first term on the right-hand side of equation (2.1.28) is approximately equal to 170.8. For an omnidirectional source $\text{DI} = 0$. Quantities such as source level and directivity index that are logarithms of ratios of power like quantities are given the label dB (decibel). For example, if SL has the value 10, we say that the source level is 10 dB re $1 \mu\text{Pascal}$ at 1 meter. It should be noted that although the reference distance in the definition of SL is 1 meter, the axial

pressure occurring in the definition must be in the far-field of the source (where pressure magnitude decays like $1/R$).

In scattering problems the incident pressure p^{inc} is the pressure that would be present if the scattering object were removed. If the source of the incident pressure is far from the scattering object, p^{inc} is usually taken to be a plane wave since the wave is approximately planar in the vicinity of the scatterer. If p is the total acoustic pressure present in a scattering problem, then the scattered pressure p^s is defined by

$$p^s = p - p^{\text{inc}}. \quad (2.1.31)$$

Clearly, the incident and scattered pressures also satisfy the acoustic wave equation.

To uniquely determine the pressure it is necessary to specify some initial and boundary conditions in addition to the requirement that the wave equation be satisfied. In the time domain we usually specify initial conditions throughout the region of interest for both p and \dot{p} as well as boundary conditions on either p or its normal derivative. It follows from equation (2.1.2) that the normal derivative of pressure is proportional to the normal acceleration. In the time domain these boundary and initial conditions are sufficient to uniquely determine p for both interior (bounded region) and exterior (unbounded region) problems. In the frequency domain we usually specify either P or its normal derivative on the boundary. It follows from equation (2.1.14) that the normal derivative of P is proportional to the normal acceleration and also to the normal velocity. These boundary conditions are sufficient to determine p uniquely for interior problems as long as the frequency is not one of the resonance frequencies of the interior region. For exterior problems in the frequency domain it is necessary to supplement the boundary conditions with a radiation condition at infinity in order to eliminate the possibility of waves coming in from infinity. This condition usually takes the form

$$\lim_{r \rightarrow \infty} r \left(\frac{\partial p}{\partial r} + ikp \right) = 0 \quad (2.1.32)$$

due to Sommerfeld. In effect this condition says that the pressure field looks locally like an outgoing spherical wave at large distances from the sound source. This condition can be eliminated if the fluid is considered to be slightly lossy (complex sound velocity). If the incident field in a scattering problem is taken to be a plane wave, then neither the incident pressure nor the total pressure satisfies the outgoing radiation condition. Therefore, in scattering problems, the outgoing radiation condition is applied to the scattered pressure.

For reference purposes we have included expressions for the gradient, divergence and Laplacian operators in Cartesian, cylindrical, and spherical coordinate systems.

Cartesian Coordinates:

$$\nabla p = \left(\frac{\partial p}{\partial x}, \frac{\partial p}{\partial y}, \frac{\partial p}{\partial z} \right) \quad (2.1.33a)$$

$$\mathbf{div} v = \frac{\partial v_x}{\partial x} + \frac{\partial v_y}{\partial y} + \frac{\partial v_z}{\partial z} \quad (2.1.33b)$$

$$\Delta p = \frac{\partial^2 p}{\partial x^2} + \frac{\partial^2 p}{\partial y^2} + \frac{\partial^2 p}{\partial z^2}. \quad (2.1.33c)$$

Cylindrical Coordinates ($x = r \cos \phi$, $y = r \sin \phi$, $z = z$):

$$\nabla p = \left(\frac{\partial p}{\partial r}, \frac{1}{r} \frac{\partial p}{\partial \phi}, \frac{\partial p}{\partial z} \right) \quad (2.1.34a)$$

$$\mathbf{div} v = \frac{\partial v_r}{\partial r} + \frac{1}{r} \frac{\partial v_\phi}{\partial \phi} + \frac{\partial v_z}{\partial z} \quad (2.1.34b)$$

$$\Delta p = \frac{1}{r} \frac{\partial}{\partial r} \left(r \frac{\partial p}{\partial r} \right) + \frac{1}{r^2} \frac{\partial^2 p}{\partial \phi^2} + \frac{\partial^2 p}{\partial z^2}. \quad (2.1.34c)$$

Spherical Coordinates ($x = r \sin \theta \cos \phi$, $y = r \sin \theta \sin \phi$, $z = r \cos \theta$):

$$\nabla p = \left(\frac{\partial p}{\partial r}, \frac{1}{r} \frac{\partial p}{\partial \theta}, \frac{1}{r \sin \theta} \frac{\partial p}{\partial \phi} \right) \quad (2.1.35a)$$

$$\mathbf{div} v = \frac{\partial v_r}{\partial r} + \frac{1}{r} \frac{\partial v_\theta}{\partial \theta} + \frac{1}{r \sin \theta} \frac{\partial v_\phi}{\partial \phi} \quad (2.1.35b)$$

$$\Delta p = \frac{1}{r^2} \frac{\partial}{\partial r} \left(r^2 \frac{\partial p}{\partial r} \right) + \frac{1}{r^2 \sin \theta} \frac{\partial}{\partial \theta} \left(\sin \theta \frac{\partial p}{\partial \theta} \right) + \frac{1}{r^2 \sin^2 \theta} \frac{\partial^2 p}{\partial \phi^2}. \quad (2.1.35c)$$

2.2 Analytic Solutions of the Wave Equation

Most analytic solutions of the reduced wave equation are obtained by a technique called separation of variables. In this technique we look for solutions that are products of functions

each of which depends on only one coordinate. For example, in spherical coordinates we would look for solutions of the form $F(r)G(\theta)H(\phi)$. Of course, if we find solutions of this form, we can construct other solutions from sums and/or integrals of these solutions. In fact, it is sums and integrals of separable solutions that we are most interested in. It is not always possible to find solutions which are separable. In fact, there are only eleven independent coordinate systems which allow separable solutions to the reduced wave equation. These coordinate systems are 1) rectangular coordinates, 2) circular cylinder coordinates, 3) elliptic cylinder coordinates, 4) parabolic cylinder coordinates, 5) spherical coordinates, 6) conical coordinates, 7) parabolic coordinates, 8) prolate spheroidal coordinates, 9) oblate spheroidal coordinates, 10) ellipsoidal coordinates, and 11) paraboloidal coordinates. Thus, to find a separable solution we must work in one of these eleven coordinate systems. In addition, the boundary surface must coincide with one of the coordinate surfaces. For example, a finite cylinder could not be solved using this technique. It is clear that most problems that occur in practice can not be solved by separation of variables. In fact, in most cases one must resort to a purely numerical technique in order to obtain a solution. Nevertheless, analytic solutions like those obtained by separation of variables do serve at least two purposes. One, they help us develop our intuition as to how solutions should behave. Secondly, they provide useful test cases for validating numerical procedures. In developing a numerical method it is always helpful to try it out on a problem for which we know the answer.

In this section we will illustrate the method of separation of variables by means of the problem of a circular piston radiator on a rigid spherical baffle. The geometry of the problem is shown in Figure 2.1.

Clearly, with the coordinate system shown, the pressure is not a function of the circumferential angle ϕ . Thus, the reduced wave equation in spherical coordinates reduces to

$$\frac{1}{r^2} \frac{\partial}{\partial r} \left(r^2 \frac{\partial P}{\partial r} \right) + \frac{1}{r^2 \sin \theta} \frac{\partial}{\partial \theta} \left(\sin \theta \frac{\partial P}{\partial \theta} \right) + k^2 P = 0. \quad (2.2.1)$$

The boundary condition on the normal velocity $V(\theta)$ takes the form

$$V(\theta) = \begin{cases} \bar{V} & 0 \leq \theta \leq \theta_0 \\ 0 & \theta_0 < \theta \leq \pi. \end{cases} \quad (2.2.2)$$

In addition, the solution must satisfy the outgoing radiation condition at infinity. It can be shown that in a separable solution $F(r)G(\theta)$, both F and G must be eigenfunctions of the differential operator in equation (2.2.1). Thus, in this case we can take $G(\theta)$ to be a Legendre polynomial $P_n(\cos \theta)$ in $\cos \theta$. These Legendre polynomials satisfy the differential equation

$$\frac{1}{\sin \theta} \frac{d}{d\theta} \left[\sin \theta \frac{dP_n(\cos \theta)}{d\theta} \right] + n(n+1)P_n(\cos \theta) = 0 \quad (2.2.3)$$

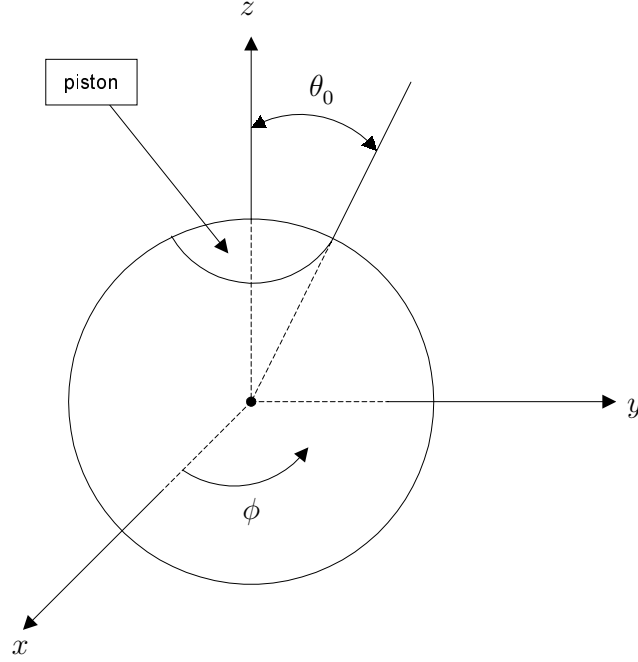


Figure 2.1. Coordinate system for circular piston on a sphere

and the orthogonality condition

$$\int_0^\pi P_m(\cos \theta) P_n(\cos \theta) \sin \theta d\theta = \begin{cases} 0 & m \neq n \\ \frac{2}{2n+1} & m = n \end{cases}. \quad (2.2.4)$$

Since the Legendre polynomials form a complete set of orthogonal functions, we can expand the pressure P in terms of these functions as follows

$$P(r, \theta) = \sum_{n=0}^{\infty} F_n(r) P_n(\cos \theta). \quad (2.2.5)$$

Substituting equation (2.2.5) into the reduced wave equation (2.2.1) and making use of equation (2.2.3), we get

$$\sum_{n=0}^{\infty} \left\{ \frac{1}{r^2} \frac{d}{dr} \left(r^2 \frac{dF_n}{dr} \right) + \left[k^2 - \frac{n(n+1)}{r^2} \right] F_n \right\} P_n(\cos \theta) = 0. \quad (2.2.6)$$

Since the Legendre polynomials are orthogonal functions, the coefficients in equation (2.2.6) must all be zero, i.e.,

$$\frac{1}{r^2} \frac{d}{dr} \left(r^2 \frac{dF_n}{dr} \right) + \left[k^2 - \frac{n(n+1)}{r^2} \right] F_n = 0 \quad \text{for all } n \quad (2.2.7)$$

or equivalently

$$\frac{d}{dr} \left(r^2 \frac{dF_n}{dr} \right) + [k^2 r^2 - n(n+1)] F_n = 0 \quad \text{for all } n. \quad (2.2.8)$$

Equation (2.2.8) is a spherical Bessel equation having the general solution

$$F_n(r) = \alpha_n h_n^{(1)}(kr) + \beta_n h_n^{(2)}(kr), \quad (2.2.9)$$

where $h_n^{(1)}$ and $h_n^{(2)}$ are spherical Hankel functions of the first and second kind. Recall that

$$h_n^{(1)}(kr) = j_n(kr) + iy_n(kr) \quad \text{and} \quad h_n^{(2)}(kr) = j_n(kr) - iy_n(kr). \quad (2.2.10)$$

Since $h_n^{(1)}$ behaves like an incoming wave at large distances from the source, we must have $\alpha_n = 0$ for all n . Thus,

$$F_n(r) = \beta_n h_n^{(2)}(kr). \quad (2.2.11)$$

Substituting equation (2.2.11) into equation (2.2.5), we obtain

$$P(r, \theta) = \sum_{n=0}^{\infty} \beta_n h_n^{(2)}(kr) P_n(\cos \theta). \quad (2.2.12)$$

The normal velocity $V(\theta)$ can be expanded in terms of Legendre polynomials as follows

$$V(\theta) = \sum_{n=0}^{\infty} V_n P_n(\cos \theta), \quad (2.2.13)$$

where

$$V_n = \frac{(2n+1)\bar{V}}{2} \int_0^{\theta_0} P_n(\cos \theta) \sin \theta d\theta. \quad (2.2.14)$$

It follows from the equation of motion and equation (2.2.12) that

$$V(\theta) = -\frac{1}{i\omega\rho} \frac{\partial P}{\partial r}(a, \theta) = -\frac{1}{i\rho c} \sum_{n=0}^{\infty} \beta_n h_n^{(2)'}(ka) P_n(\cos \theta). \quad (2.2.15)$$

Comparing equations (2.2.13) and (2.2.15), we see that

$$\beta_n = -\frac{i\rho c V_n}{h_n^{(2)'}(ka)}. \quad (2.2.16)$$

Thus,

$$P(r, \theta) = -i\rho c \sum_{n=0}^{\infty} V_n \frac{h_n^{(2)}(kr)}{h_n^{(2)'}(ka)} P_n(\cos \theta). \quad (2.2.17)$$

Equation 2.2.17 is the solution we were seeking.

2.3 Plane Wave Solutions

In this section we consider a problem in which the boundary condition has the form of a travelling plane wave with wavenumber κ . The solution will illustrate an important relation between the wavenumber of the boundary excitation and radiated acoustic energy. Let us consider a Cartesian coordinate system with coordinates x, y, z and suppose that the normal velocity distribution on the plane $z = 0$ has the form of a plane wave of unit amplitude travelling in the negative x -direction, i.e.,

$$v(x, y, z) = e^{i\kappa x}. \quad (2.3.1)$$

In Cartesian coordinates the reduced wave equation has the form

$$\frac{\partial^2 P}{\partial x^2} + \frac{\partial^2 P}{\partial y^2} + \frac{\partial^2 P}{\partial z^2} + k^2 P = 0. \quad (2.3.2)$$

We will assume a solution of the form

$$P(x) = A(z)e^{i\kappa x}. \quad (2.3.3)$$

Substituting equation (2.3.3) into equation (2.3.2), we see that A must satisfy

$$A''(z) + (k^2 - \kappa^2)A(z) = 0. \quad (2.3.4)$$

The general solution of equation (2.3.4) satisfying the outgoing radiation condition is

$$A(z) = \begin{cases} \alpha e^{-i\sqrt{k^2 - \kappa^2}z} & k > \kappa \\ \alpha e^{-\sqrt{\kappa^2 - k^2}z} & \kappa > k, \end{cases} \quad (2.3.5)$$

where α is a constant which can be determined from the boundary condition. For the case we are considering

$$\alpha = \begin{cases} \frac{\omega\rho}{\sqrt{k^2 - \kappa^2}} & k > \kappa \\ \frac{i\omega\rho}{\sqrt{\kappa^2 - k^2}} & \kappa > k. \end{cases} \quad (2.3.6)$$

Notice that for $\kappa > k$ the solution decays exponentially away from the boundary surface. Thus, such waves are not effective radiators of acoustic energy. A wave for which $\kappa > k$ is called an evanescent wave. Similar results hold for high wavenumber waves on other types of surfaces.

2.4 Point Sources and Dipoles

In this section we will discuss two solutions of the wave equation that play a special role in acoustics. The function $G(x, y)$ defined by

$$G(x, y) = \frac{e^{-ikr(x, y)}}{4\pi r(x, y)} \quad r(x, y) = \text{distance between } x \text{ and } y \quad (2.4.1)$$

is called the free-space Green's function. As a function of x it satisfies the reduced wave equation

$$\Delta_x G + k^2 G = 0 \quad (2.4.2)$$

in any region not including the point y . Clearly, G is singular when $x = y$. Physically, G represents a point source located at y . The function G is symmetric in the variables x and y , i.e., $G(x, y) = G(y, x)$.

The function $G'(x, y)$ defined by

$$G'(x, y) = \nabla_y G(x, y) \cdot \vec{q} \quad (2.4.3)$$

also satisfies the reduced wave equation in x in any region not including the point y . Physically, G' represents a dipole source oriented in the direction of \vec{q} . The vector \vec{q} is called the dipole moment of the source. Differentiating equation (2.4.1), we get

$$G'(x, y) = G(x, y) \left[ik + \frac{1}{r(x, y)} \right] \frac{\vec{r}(x, y) \cdot \vec{q}}{r(x, y)}, \quad (2.4.4)$$

where $\vec{r} = x - y$. Clearly, $G'(y, x) = -G'(x, y)$. In the next section we will show how a general solution to the reduced wave equation can be expressed in terms of a surface distribution of point sources and dipoles.

2.5 Integral Relations

Previously we showed that interior and exterior acoustic problems can be formulated as boundary-value problems involving the acoustic wave equation. Many methods for numerically solving acoustic problems involve the reduction of a boundary-value problem for the wave equation to an equivalent integral equation. In this section we will present some of the basic integral relations involving solutions to the acoustic wave equation. We will begin by considering integral relations in the frequency domain since most of the numerical methods are based on a frequency domain formulation. A good discussion of these integral relations is contained in [B.B. Baker and E.T. Copson, *Huygen's Principle*, Oxford University Press (1950)]. An excellent more recent reference is [T.W. Wu, *Boundary Element Acoustics*, WIT Press (2000)].

Interior Problems For an interior problem in a region bounded by a closed surface S we have the integral relations

$$\int_S \left[G(x, \xi) \frac{\partial P}{\partial n}(\xi) - P(\xi) \frac{\partial G}{\partial n}(x, \xi) \right] dS(\xi) = \begin{cases} 0 & x \text{ outside } S \\ \alpha(x) P(x) & x \text{ on } S \\ P(x) & x \text{ inside } S, \end{cases} \quad (2.5.1)$$

where $G(x, \xi)$ is the free-space Green's function defined by

$$G(x, \xi) = \frac{e^{-ik|x-\xi|}}{4\pi|x-\xi|}, \quad (2.5.2)$$

n is the outward unit normal to S , and $|x-\xi|$ is the distance between x and ξ . The function $\alpha(x)$ has the value $\frac{1}{2}$ at points where the surface is smooth, but can take on other values for points that lie on edges, corners, etc. A general expression for $\alpha(x)$ is

$$\alpha(x) = - \int_S \frac{\partial}{\partial n} \left(\frac{1}{4\pi|x-\xi|} \right) dS(\xi) \quad (2.5.3)$$

[T.W. Wu, Boundary Element Acoustics, WIT Press (2000), chapter 2]. Since the normal derivative of P is proportional to the normal velocity V [equation (2.1.14)], equation (2.5.1) can be written

$$\int_S \left[-i\omega\rho G(x, \xi) V(\xi) - P(\xi) \frac{\partial G}{\partial n}(x, \xi) \right] dS(\xi) = \begin{cases} P(x) & x \text{ inside } S \\ \alpha(x)P(x) & x \text{ on } S \\ 0 & x \text{ outside } S. \end{cases} \quad (2.5.4)$$

If the normal velocity V is specified on S , then the middle relation in equation (2.5.4) gives the following integral equation for the surface pressure P :

$$-\alpha(\zeta)P(\zeta) - \int_S P(\xi) \frac{\partial G}{\partial n}(\zeta, \xi) dS(\xi) = i\omega\rho \int_S G(\zeta, \xi) V(\xi) dS(\xi) \quad \zeta \text{ on } S. \quad (2.5.5)$$

Once this integral equation is solved for the surface pressure, the pressure at any interior point can be obtained using the first relation in equation (2.5.4). As with the original boundary-value problem, the solution of this integral equation is not unique at the frequencies corresponding to the resonances of the interior region.

Exterior Problems For the exterior problem in the region exterior to S , we have the integral relations

$$\int_S \left[G(x, \xi) \frac{\partial P}{\partial n}(\xi) - P(\xi) \frac{\partial G}{\partial n}(x, \xi) \right] dS(\xi) = \begin{cases} -P(x) & x \text{ outside } S \\ (\alpha(x) - 1)P(x) & x \text{ on } S \\ 0 & x \text{ inside } S, \end{cases} \quad (2.5.6)$$

or equivalently,

$$\int_S \left[-i\omega\rho G(x, \xi) V(\xi) - P(\xi) \frac{\partial G}{\partial n}(x, \xi) \right] dS(\xi) = \begin{cases} -P(x) & x \text{ outside } S \\ (\alpha(x) - 1)P(x) & x \text{ on } S \\ 0 & x \text{ inside } S. \end{cases} \quad (2.5.7)$$

If the normal velocity V is specified on the boundary S , then the middle relation in equation (2.5.7) provides an integral equation for the surface pressure P , i.e.,

$$(1 - \alpha(\zeta))P(\zeta) - \int_S P(\xi) \frac{\partial G}{\partial n}(\zeta, \xi) dS(\xi) = i\omega\rho \int_S G(\zeta, \xi) V(\xi) dS(\xi) \quad \zeta \text{ on } S. \quad (2.5.8)$$

Once this integral equation is solved for the surface pressure, the pressure at any point in the exterior region can be obtained using the first relation in equation (2.5.7). However, for the exterior problem, there is an infinite discrete set of frequencies f_1, f_2, \dots for which the integral equation does not have a unique solution. These frequencies are the resonance frequencies of the interior problem for the boundary condition $P = 0$ on S . As one might expect, numerical methods based on these integral equations have a problem when the frequency is close to one these interior resonance frequencies. A large volume of literature describes various methods for overcoming this difficulty [G.W. Benthien and H.A. Schenck, *Nonexistence and Nonuniqueness Problems Associated with Integral Equation Methods in Acoustics*]. The resonance frequencies f_1, f_2, \dots are not resonances of the problem of interest as was the case with the interior problem. There are no resonances of the exterior problem. The exterior problem has a unique solution at all frequencies. The interior resonance problem is a mathematical difficulty, not a physical one. What happens at these frequencies is that the integral equation is no longer equivalent to the original exterior acoustic boundary-value problem. This nonuniqueness problem will be discussed in more detail in section 2.6.

2.6 Nonuniqueness of solution to Helmholtz Integral Equation

In this section we will assume for simplicity that the boundary surface is smooth, and hence, that $\alpha(x) = \frac{1}{2}$ for x on the boundary S . If P is the solution of the boundary-value problem

$$\begin{aligned} \Delta P + k^2 P &= 0 && \text{exterior to } S \\ \frac{\partial P}{\partial n} &= q && \text{on } S \\ \lim_{r \rightarrow \infty} r \left(\frac{\partial P}{\partial r} + ikP \right) &= 0 && \text{outgoing radiation condition,} \end{aligned} \quad (2.6.9)$$

then P satisfies the Helmholtz integral equation

$$\frac{1}{2}P(\zeta) - \int_S P(\xi) \frac{\partial G}{\partial n_\xi}(\zeta, \xi) dS(\xi) = \int_S G(\zeta, \xi) q(\xi) dS(\xi) \quad (2.6.10)$$

on S , where

$$G(\zeta, \xi) = \frac{e^{-ikr(\zeta, \xi)}}{4\pi r(\zeta, \xi)}. \quad (2.6.11)$$

For some values of k , the solution of (2.6.10) is not unique. In this section we will investigate the conditions that give rise to this nonuniqueness and the nature of this nonuniqueness when it occurs. We will begin by stating some basic results. If ϕ is a solution of the interior problem

$$\Delta\phi + k^2\phi = 0 \quad \text{interior to } S, \quad (2.6.12)$$

then ϕ satisfies the Helmholtz integral relations

$$\int_S \left(\phi \frac{\partial G}{\partial n} - G \frac{\partial \phi}{\partial n} \right) = \begin{cases} 0 & x \text{ exterior to } S \\ -\frac{1}{2}\phi(x) & x \text{ on } S \\ -\phi(x) & x \text{ interior to } S. \end{cases} \quad (2.6.13)$$

If ψ is a solution of the exterior problem

$$\begin{aligned} \Delta\psi + k^2\psi &= 0 & \text{exterior to } S \\ \lim_{r \rightarrow \infty} r \left(\frac{\partial \psi}{\partial r} + ik\psi \right) &= 0 & \text{outgoing radiation condition,} \end{aligned} \quad (2.6.14)$$

then ψ satisfies the Helmholtz integral relations

$$\int_S \left(\psi \frac{\partial G}{\partial n} - G \frac{\partial \psi}{\partial n} \right) = \begin{cases} 0 & x \text{ interior to } S \\ \frac{1}{2}\psi(x) & x \text{ on } S \\ \psi(x) & x \text{ exterior to } S. \end{cases} \quad (2.6.15)$$

A function D of the form

$$D(x) = \int_S \frac{\partial G(x, \xi)}{\partial n_\xi} \sigma(\xi) dS(\xi) \quad (2.6.16)$$

is called a *double layer potential*. A double layer potential satisfies the wave equation in both the interior and exterior regions. It also satisfies the outgoing radiation condition in the exterior region. If ζ is on the surface S , then we have the following limit relations:

$$\lim_{x \rightarrow \zeta^+} D(x) = \frac{1}{2}\sigma(\zeta) + \int_{\partial V} \frac{\partial G(\zeta, \xi)}{\partial n_\xi} \sigma(\xi) dS(\xi) \quad (2.6.17a)$$

$$\lim_{x \rightarrow \zeta^-} D(x) = -\frac{1}{2}\sigma(\zeta) + \int_{\partial V} \frac{\partial G(\zeta, \xi)}{\partial n_\xi} \sigma(\xi) dS(\xi). \quad (2.6.17b)$$

A double layer potential D also satisfies

$$\lim_{x \rightarrow S^+} \frac{\partial D}{\partial n}(x) = \lim_{x \rightarrow S^-} \frac{\partial D}{\partial n}(x), \quad (2.6.18)$$

i.e., the normal derivative of D is continuous across the boundary surface.

Suppose k_m is a wave number corresponding to an eigenfrequency of the interior Dirichlet problem and ϕ_m is a corresponding eigenmode, i.e., ϕ_m satisfies

$$\Delta\phi_m + k_m^2\phi_m = 0 \quad \text{inside radiating surface } S \quad (2.6.19a)$$

$$\phi_m = 0 \quad \text{on the radiating surface } S. \quad (2.6.19b)$$

Since the exterior Neumann problem is uniquely solvable, let ψ_m be the unique solution of

$$\Delta\psi_m + k^2\psi_m = 0 \quad \text{exterior to radiating surface } S \quad (2.6.20a)$$

$$\frac{\partial\psi_m}{\partial n} = \frac{\partial\phi_m}{\partial n} \quad \text{on radiating surface } S \quad (2.6.20b)$$

$$\lim_{R \rightarrow \infty} R \left(\frac{\partial\psi_m}{\partial R} + ik\psi_m \right) = 0 \quad \text{outgoing radiation condition.} \quad (2.6.20c)$$

It follows from equation (2.6.15) that ψ_m satisfies

$$\int_S \left(\psi_m \frac{\partial G}{\partial n} - G \frac{\partial\psi_m}{\partial n} \right) = \begin{cases} 0 & x \text{ interior to } S \\ \frac{1}{2}\psi_m(x) & x \text{ on } S \\ \psi_m(x) & x \text{ exterior to } S. \end{cases} \quad (2.6.21)$$

It follows from equations (2.6.13) and (2.6.19b) that

$$\int_S G \frac{\partial\phi_m}{\partial n} = 0 \quad \text{on radiating surface } S. \quad (2.6.22)$$

It now follows from equations (2.6.22) and (2.6.20b) that

$$\int_S G \frac{\partial\psi_m}{\partial n} = 0 \quad \text{on radiating surface } S. \quad (2.6.23)$$

Combining the second relation in equation (2.6.21) with equation (2.6.23), gives

$$\int_S \psi_m \frac{\partial G}{\partial n} = \frac{1}{2}\psi_m \quad \text{on radiating surface } S. \quad (2.6.24)$$

It follows from equations (2.6.24) and (2.6.10) that any linear combination of P and ψ_m satisfies the integral equation (2.6.10), i.e., the solution of the integral equation (2.6.10) is nonunique.

We next show that any solution of the integral equation (2.6.10) is a linear combination of P and a function ψ that satisfies

$$\begin{aligned} \Delta\psi + k^2\psi &= 0 && \text{exterior to } S \\ \frac{\partial\psi}{\partial n} &= \frac{\partial\phi}{\partial n} && \text{on } S \\ \lim_{R \rightarrow \infty} R \left(\frac{\partial\psi}{\partial R} + ik\psi \right) &= 0 && \text{outgoing radiation condition} \end{aligned}$$

for some internal Dirichlet eigenfunction ϕ .

Let P' be any solution of equation (2.6.10) and define $\psi = P' - P$. Then ψ satisfies the integral relation

$$\frac{1}{2}\psi(\zeta) = \int_S \frac{\partial G(\zeta, \xi)}{\partial n_\xi} \psi(\xi) dS(\xi) \quad \zeta \text{ on } S. \quad (2.6.25)$$

Since the external Dirichlet problem has a unique solution, we can extend ψ to the exterior region in such a way that it satisfies the wave equation and the outgoing radiation condition. Define ϕ by

$$\phi(x) = \int_S \frac{\partial G(x, \xi)}{\partial n_\xi} \psi(\xi) dS(\xi). \quad (2.6.26)$$

The function ϕ satisfies the wave equation in both the interior and exterior regions and satisfies the outgoing radiation condition as $R \rightarrow \infty$. It follows from equations (2.6.26), (2.6.17a), and (2.6.25) that

$$\begin{aligned} \lim_{x \rightarrow \zeta^+} \phi(x) &= \frac{1}{2}\psi(\zeta) + \int_S \frac{\partial G(\zeta, \xi)}{\partial n_\xi} \psi(\xi) dS(\xi) \\ &= \frac{1}{2}\psi(\zeta) + \frac{1}{2}\psi(\zeta) \\ &= \psi(\zeta). \end{aligned} \quad (2.6.27)$$

Since ϕ satisfies the wave equation and the outgoing radiation condition in the exterior region and coincides with ψ on the boundary, it follows from the uniqueness property of the exterior Dirichlet problem that $\phi = \psi$ in the exterior region. It thus follows from equation (2.6.18) that

$$\lim_{x \rightarrow S^-} \frac{\partial \phi}{\partial n}(x) = \lim_{x \rightarrow S^+} \frac{\partial \phi}{\partial n}(x) = \frac{\partial \psi}{\partial n}. \quad (2.6.28)$$

It follows from equations (2.6.26), (2.6.17b), and (2.6.25) that

$$\begin{aligned} \lim_{x \rightarrow \zeta^-} \phi(x) &= -\frac{1}{2}\psi(\zeta) + \int_S \frac{\partial G(\zeta, \xi)}{\partial n_\xi} \psi(\xi) dS(\xi) \\ &= - \int_S \frac{\partial G(\zeta, \xi)}{\partial n_\xi} \psi(\xi) dS(\xi) + \int_S \frac{\partial G(\zeta, \xi)}{\partial n_\xi} \psi(\xi) dS(\xi) \\ &= 0. \end{aligned} \quad (2.6.29)$$

Thus, ϕ is an internal Dirichlet eigenfunction whose normal derivative coincides with the normal derivative of ψ on the boundary surface S . We have now demonstrated that ψ has the desired properties.

In CHIEF, the nonuniqueness is handled by supplementing the integral equation (2.6.10) with equations of the form

$$\int_S \left(P \frac{\partial G}{\partial n} - Gq \right) = 0 \quad (2.6.30)$$

evaluated at several interior points. It follows from equation (2.6.15) that P satisfies equation (2.6.30) at every interior point. Suppose $P + \psi$ is a solution of the integral equation (2.6.10).

We have seen that ψ can be extended to a solution of the exterior Neumann problem with

$$\frac{\partial \psi}{\partial n} = \frac{\partial \phi}{\partial n} \quad \text{on } S \quad (2.6.31)$$

for some interior Dirichlet eigenfunction ϕ . Since P satisfies equation (2.6.30), it follows that

$$\int_S \left(\frac{\partial G}{\partial n}(P + \psi) - Gq \right) = \int_S \frac{\partial G}{\partial n} \psi \quad \text{interior to } S. \quad (2.6.32)$$

Since ψ satisfies equation (2.6.15), it follows that

$$\int_S \frac{\partial G}{\partial n} \psi = \int_S G \frac{\partial \psi}{\partial n} = \int_S G \frac{\partial \phi}{\partial n} \quad \text{interior to } S. \quad (2.6.33)$$

It follows from the first relation in equation (2.6.13) and the fact that $\phi = 0$ on S that

$$\int_S G \frac{\partial \phi}{\partial n} = \phi \quad \text{interior to } S. \quad (2.6.34)$$

Thus, combining equations (2.6.32) through (2.6.34) gives

$$\int_S \left(\frac{\partial G}{\partial n}(P + \psi) - Gq \right) = \phi \quad \text{interior to } S. \quad (2.6.35)$$

If there is only one independent interior eigenmode at the frequency of interest, then it can be seen from equation (2.6.35) that $P + \psi$ will not satisfy equation (2.6.30) for given normal derivative of P if the interior point is chosen so that the interior eigenfunction does not vanish. If there are m independent interior eigenmodes ϕ_1, \dots, ϕ_m at the frequency of interest, then

$$\phi = \alpha_1 \phi_1 + \dots + \alpha_m \phi_m \quad (2.6.36)$$

for some set of scalars $\alpha_1, \dots, \alpha_m$. Therefore, $P + \psi$ will not satisfy equation (2.6.30) if we choose m interior points x_1, \dots, x_m so that the system of equations

$$\begin{aligned} \alpha_1 \phi_1(x_1) + \dots + \alpha_m \phi_m(x_1) &= 0 \\ &\vdots \\ \alpha_1 \phi_1(x_m) + \dots + \alpha_m \phi_m(x_m) &= 0 \end{aligned}$$

has only the zero solution $\alpha_1 = \dots = \alpha_m = 0$.

2.7 Integral Equation Methods

Many of the numerical methods used for acoustic problems are based on the integral equations presented in section 2.5. The simplest discrete approximation for an integral equation like equation (2.5.8) is the piecewise constant approximation. In this approximation, the boundary surface S is subdivided into a finite number of subareas S_1, S_2, \dots, S_N . On each subarea S_n the pressure is approximated by a single value P_n and the normal velocity is approximated by a single value V_n . With this approximation, the integral equation (2.5.8) becomes

$$(1 - \alpha(\zeta))P(\zeta) - \sum_{n=1}^N P_n \int_{S_n} \frac{\partial G}{\partial n}(\zeta, \xi) dS(\xi) = i\omega\rho \sum_{n=1}^N V_n \int_{S_n} G(\zeta, \xi) dS(\xi). \quad (2.7.1)$$

Evaluating equation (2.7.1) at a set of reference points $\zeta_1, \zeta_2, \dots, \zeta_N$ (one on each subarea) and taking $\alpha = \frac{1}{2}$ (the smooth value), we obtain the system of equations

$$\sum_{n=1}^N A_{mn}P_n = i\omega \sum_{n=1}^N B_{mn}V_n \quad m = 1, 2, \dots, N, \quad (2.7.2)$$

where

$$A_{mn} = \frac{1}{2}\delta_{mn} - \int_{S_n} \frac{\partial G}{\partial n}(\zeta_m, \xi) dS(\xi) \quad (2.7.3)$$

$$B_{mn} = \rho \int_{S_n} G(\zeta_m, \xi) dS(\xi) \quad (2.7.4)$$

and δ_{mn} is the Kronecker delta defined by

$$\delta_{mn} = \begin{cases} 0 & m \neq n \\ 1 & m = n. \end{cases} \quad (2.7.5)$$

In this system of equations we have taken α to be $\frac{1}{2}$ (the smooth value) since it is not necessary or desirable to take the reference points ζ_m on an edge or corner. Usually, ζ_m is taken at the center of the m -th subarea. The system of equations (2.7.2) can be written in the matrix form

$$AP = i\omega BV = B\dot{V}, \quad (2.7.6)$$

where P is an N -vector whose n -th component is P_n , V is an N -vector whose n -th component is V_n , and \dot{V} is an N -vector whose n -th component is $i\omega V_n$. The components of \dot{V} are the Fourier transforms of the surface accelerations on each subarea.

If the velocities V_1, V_2, \dots, V_N are prescribed, then the system of equations (2.7.2) can be solved for the surface pressures P_1, P_2, \dots, P_N . In solving the system of equations for the

surface pressures it is important to take advantage of any geometric symmetries of the radiating surface as they can be used to greatly reduce the computation cost. A general approach to handling symmetry reductions for problems of this type is described in [Benthien, G.W., *Symmetry Reductions*, unpublished notes].

The expression in equation (2.5.7) for the pressure at an arbitrary field point can be approximated using the same discrete approximations, yielding

$$P(x) = \sum_{n=1}^N [A_n(x)P_n + i\omega B_n(x)V_n], \quad (2.7.7)$$

where

$$A_n(x) = \int_{S_n} \frac{\partial G}{\partial n}(x, \xi) dS(\xi) \quad \text{and} \quad B_n(x) = \rho \int_{S_n} G(x, \xi) dS(\xi). \quad (2.7.8)$$

This expression can be used to calculate the pressure at an arbitrary field point x once the surface pressures and normal velocities have been determined. In the next section we will discuss approximations that can be made when the field point is in the far-field of the source.

In the vicinity of one of the frequencies for which the underlying integral equation does not have a unique solution, the system of equations (2.7.2) becomes numerically ill-conditioned. One method of overcoming this difficulty is to add some additional equations obtained by evaluating a discretized version of the last relation in equation (2.5.7) at a selected number of interior points. The overdetermined system of equations is then solved in a least squares sense. A more complete discussion of this approach to solving acoustic problems is contained in [Benthien, Barach, and Hobbs *CHIEF 2004 Users Manual*]. This method as well as a number of other methods for handling this nonuniqueness problem are discussed in the reference [G.W. Benthien and H.A. Schenck, *Nonexistence and Nonuniqueness Problems Associated with Integral Equation Methods in Acoustics*]. It is possible to obtain other approximations using higher order finite element interpolation functions; however, care must be taken to correctly handle nodes lying on edges or corners since the normal velocity is discontinuous at such points.

2.8 Far-Field Approximations

We have seen previously in equation (2.5.7) that the pressure $P(x)$ at an external point x can be written

$$P(x) = \int_S \left[P(\xi) \frac{\partial G}{\partial n}(x, \xi) + i\omega \rho G(x, \xi) V(\xi) \right] dS(\xi), \quad (2.8.1)$$

where G is the free space Green's function, $P(\xi)$ is the surface pressure, and $V(\xi)$ is the surface normal velocity. In this section we are interested in the case where x is far from

the source. Let 0 be an origin located near the radiating body (usually inside the radiating surface S). In addition, let \vec{r} , \vec{R} , and $\vec{\delta}$ be vectors as shown in Figure 2.2. The magnitudes of these vectors will be denoted by r , R , and δ respectively.

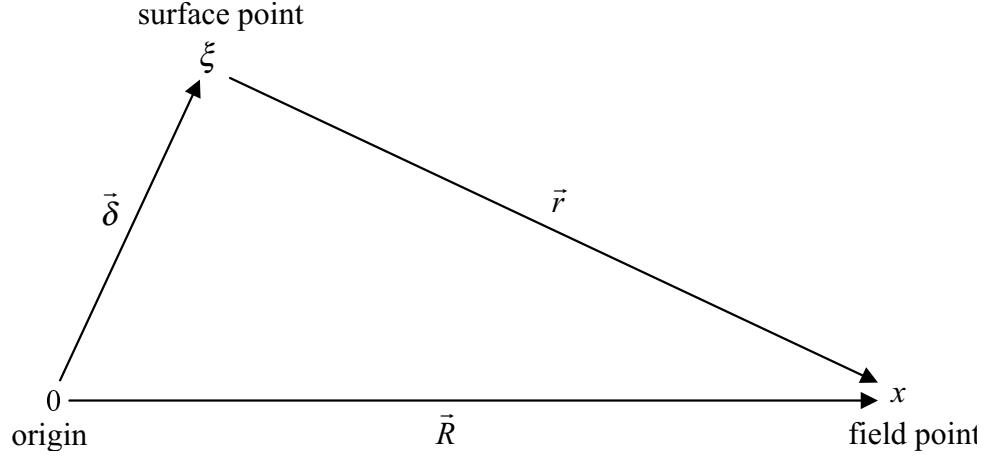


Figure 2.2. Location of points and vectors involved in far-field approximation

Clearly,

$$\vec{r} = \vec{R} - \vec{\delta}. \quad (2.8.2)$$

Moreover, when $R \gg \delta$,

$$\begin{aligned} r^2 &= \vec{r} \cdot \vec{r} = R^2 - 2\vec{R} \cdot \vec{\delta} + \delta^2 \\ &= R^2 \left(1 - 2\frac{\vec{R} \cdot \vec{\delta}}{R^2} + \frac{\delta^2}{R^2} \right) \\ &\doteq R^2 \left(1 - 2\frac{\vec{R} \cdot \vec{\delta}}{R^2} \right). \end{aligned} \quad (2.8.3)$$

By the binomial formula, we have

$$(1 - x)^{1/2} \doteq 1 - \frac{1}{2}x \quad \text{when} \quad |x| \ll 1. \quad (2.8.4)$$

Therefore,

$$r \doteq R \left(1 - \frac{\vec{R} \cdot \vec{\delta}}{R^2} \right) = R - \frac{\vec{R} \cdot \vec{\delta}}{R}. \quad (2.8.5)$$

Using the approximation (2.8.5) in e^{-ikr} and approximating $1/r$ by $1/R$, we have

$$G(x, \xi) \doteq \frac{e^{-ikR}}{4\pi R} e^{ik\vec{R} \cdot \vec{\delta}/R}. \quad (2.8.6)$$

Similarly, $\frac{\partial G}{\partial n}$ can be approximated by

$$\frac{\partial G}{\partial n} \doteq ik \frac{e^{-ikR}}{4\pi R} (\vec{R} \cdot \vec{n}/R) e^{ik\vec{R} \cdot \vec{\delta}/R}. \quad (2.8.7)$$

Substituting the approximations of equations (2.8.6) and (2.8.7) into equation (2.8.1), we obtain

$$P(x) \doteq \frac{e^{-ikR}}{4\pi R} \left[ik \int_S P(\xi) (\vec{R} \cdot \vec{n}/R) e^{ik\vec{R} \cdot \vec{\delta}/R} dS(\xi) + i\omega\rho \int_S V(\xi) e^{ik\vec{R} \cdot \vec{\delta}/R} dS(\xi) \right]. \quad (2.8.8)$$

Note that the expression in brackets in equation (2.8.8) depends on the field point x only through the unit vector \vec{R}/R . Thus, in terms of a spherical coordinate system at the origin, equation (2.8.8) can be written in the form

$$P(R, \theta, \phi) \doteq A(\theta, \phi) \frac{e^{-ikR}}{R}. \quad (2.8.9)$$

Thus, in the far-field, the pressure from any source decays like $1/R$. The beam pattern of the source $B(\theta, \phi)$ is defined by

$$B(\theta, \phi) = |A(\theta, \phi)|/|A(\theta_0, \phi_0)|, \quad (2.8.10)$$

where (θ_0, ϕ_0) is a specified direction (usually the direction of maximum response). As an example, the computation of the far-field pattern of an arbitrary-shaped piston on an infinite plane rigid baffle is described in [Benthien, G.W., *Far-Field Pressure Due to a Planar Piston of Arbitrary Shape*, unpublished notes]

The question remains as to how far one must go out from the source for the far-field approximations to hold. Two restrictions must be satisfied. At low frequencies, the approximation of $1/r$ by $1/R$ is the dominant source of error. A rough rule-of-thumb is that R must be greater than twice the maximum dimension of the source for this approximation to be valid. At higher frequencies, the approximation of the phase term is the dominant source of error. A good rule-of-thumb is that R must be greater than $(\text{maximum dimension})^2/\lambda$ for this approximation to be valid. Thus, a good far-field criterion is

$$R > \max(2D, D^2/\lambda), \text{ where } D = \text{maximum dimension of source}. \quad (2.8.11)$$

2.9 The Kirchhoff Time-Domain Integral Equation

Kirchhoff's integral equation is the time-domain analog of the Helmholtz integral equation. For smooth surfaces, it can be written as

$$\begin{aligned} \frac{1}{2}p(\zeta, t) + \int_S \frac{1}{4\pi r^2} \frac{\partial r}{\partial n_\xi} \left[p(\xi, t - r/c) + \frac{r}{c} \dot{p}(\xi, t - r/c) \right] dS(\xi) = \\ \rho \int_S \frac{1}{4\pi r} a(\xi, t - r/c) dS(\xi), \end{aligned} \quad (2.9.1)$$

where p is the surface pressure and a is the normal surface acceleration. This can be obtained by a Fourier transform of the Helmholtz integral equation if we use the fact that delays in the time domain correspond to complex exponential multipliers in the frequency domain, i.e.,

$$p(t - \tau) \sim e^{-i\omega\tau} P(\omega). \quad (2.9.2)$$

We have written the Kirchhoff integral equation in terms of the normal acceleration instead of the normal velocity as we did in the frequency domain. In the frequency domain, the relation between displacement, velocity, and acceleration only involves multiplication or division by $i\omega$ factors. In the time domain, the relations involve derivatives that are harder to calculate numerically. Note that Kirchhoff's integral equation relates the values of pressure at the present time in terms of values at earlier times. Thus, numerical solutions of this equation are of a recursive nature. Analogous equations can be obtained for field points not on the surface. One of the earliest attempts to solve Kirchhoff's equation numerically was contained in the paper [K.M. Mitzner, *Numerical Solution for Transient Scattering from a Hard Surface—Retarded Potential Technique*, J. Acoust. Soc. Am., vol. 42, no. 2, pp. 391–397 (1967)]. The technique described in this paper has stability problems for very small time steps. An approach for overcoming this stability problem is described in the papers [G. Benthien and S. Hobbs, *Solution of Kirchhoff's Time-Domain Integral Equation in Acoustics*, unpublished notes] and [G. Benthien and S. Hobbs, *Calculation of Acoustic Loading on Transducers in the Time Domain*]. To illustrate this method, we present some calculated results for a sphere that is uniformly excited by an acceleration pulse. The pulse shape consists of one half cycle of a sign wave whose period is 1.25 times the time required for a sound wave to traverse the diameter of the sphere. Figure 2.3 shows a comparison between the numerically calculated surface pressure and an analytical result. The sphere was divided into eight subdivisions in the θ direction and 12 subdivisions in the ϕ direction. The time step was $1/30$ of the time for a sound wave to cross the diameter. The agreement here is quite good. Figure 2.4 is a plot of the error between the analytic and numerical results for the same problem. Note that the error is not random but has a definite periodic pattern. Figure 2.5 shows the numerical evaluation for a field point interior to the sphere (the result should be zero). Here again, we notice the nonrandom nature of the error. Figure 2.6 shows the discrete Fourier transform of the interior point calculations. Note that there are peaks at frequencies that correspond to the frequencies where the Helmholtz integral equation in the frequency domain has a nonunique solution. Thus, the frequencies where the Helmholtz integral equation has nonuniqueness problems shows up in the time domain solutions as an error that does not decay to zero for large times. However, the error in the time domain is not large enough to invalidate the solution. Figure 2.7 shows computed results for the case where the time step is taken to be $1/90$ of the time for a sound wave to cross the diameter. Here, the solution becomes unstable at large times. The problem can be traced to errors in calculating the time derivative of pressure in the Kirchhoff equation. The problem is that the error in the calculated pressure does not go to zero as the time step becomes smaller due to spatial discretization errors. Thus, difference approximations of the derivative tend to amplify these errors for small time steps. The problem can be reduced by incorporating

smoothing in the derivative approximation as one does in approximating the derivative of an empirical function containing noise. One technique is to least-square fit a quadratic to a number of points surrounding the point of interest and use the derivative of this quadratic as the derivative approximation. Figure 2.8 shows the results for the same time step used in Figure 2.7 when a five-point smoothing approximation to the derivative is used. Note the stability of the solution has been greatly improved. A final remark is that the time and spatial variations of the solution are related. Therefore, it probably does not make sense to make the time subdivision finer and finer while keeping the same spatial subdivisions. I believe that any more than 10 time steps for a wave to cross a spatial subdivision will not give much improvement in accuracy, even if stability can be maintained.

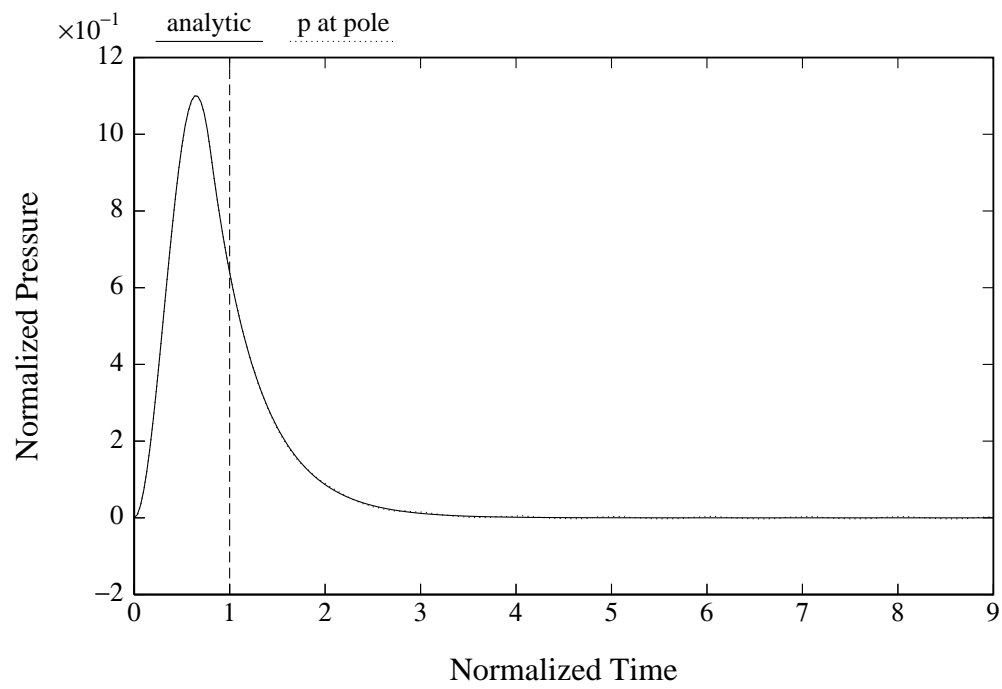


Figure 2.3. Theory vs. numerical for a half sine wave accelerated sphere.

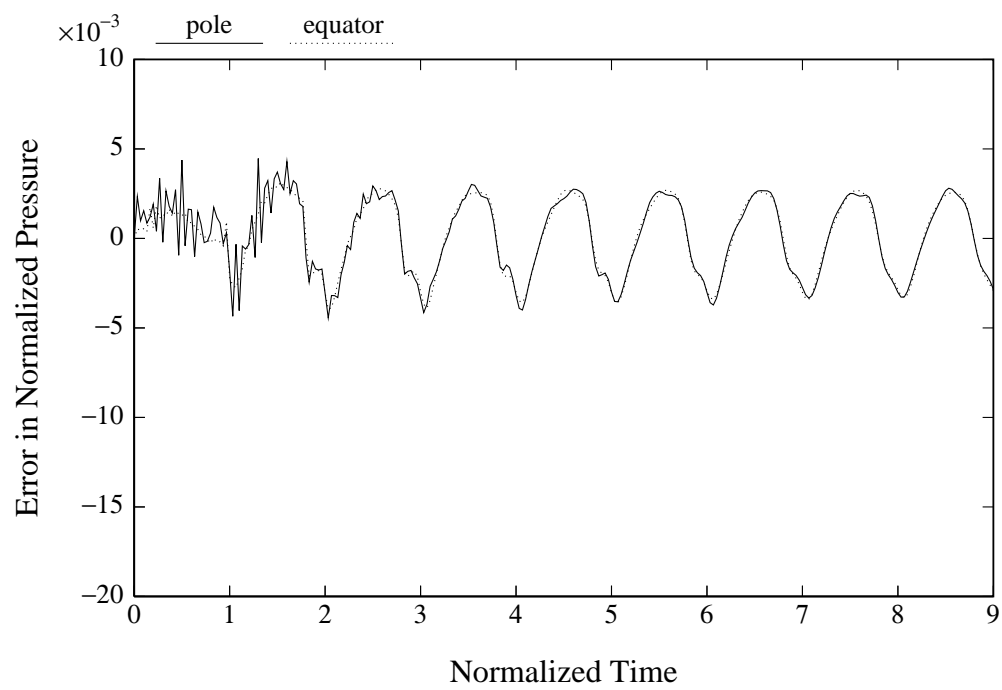


Figure 2.4. Error in surface pressure at pole and equator.

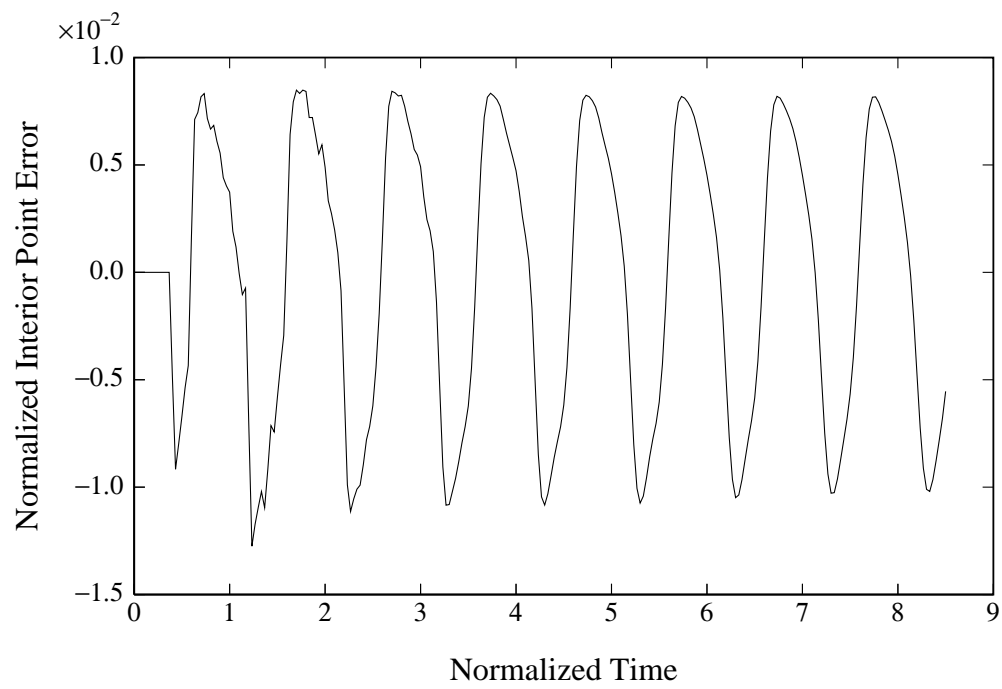


Figure 2.5. Error at interior point vs. normalized time.

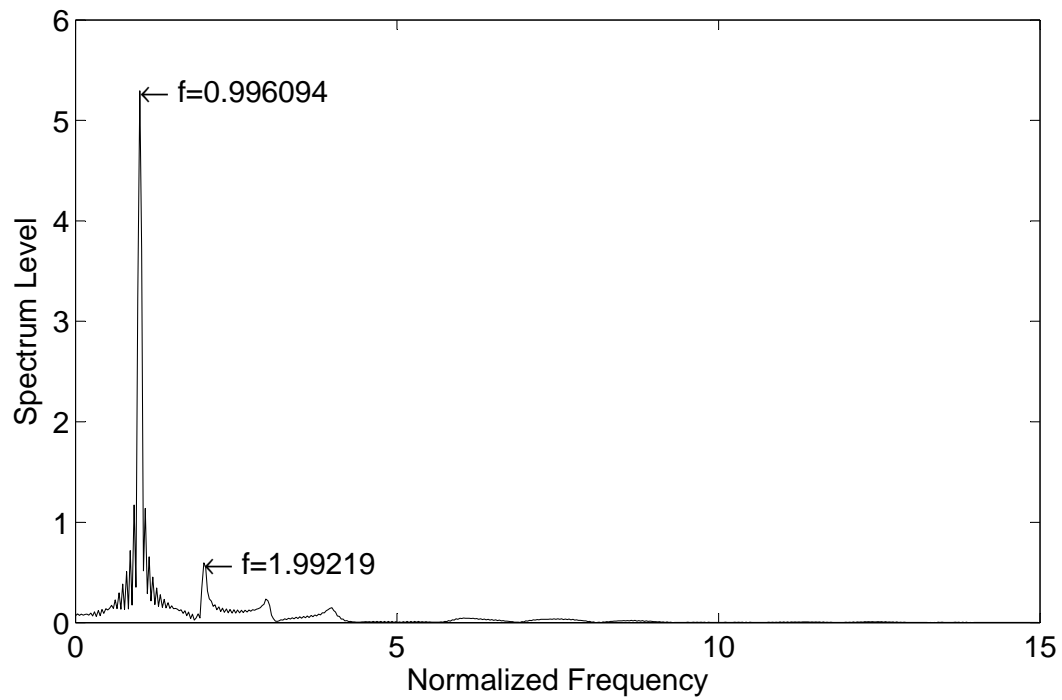


Figure 2.6. Spectrum of interior point error vs. normalized frequency.

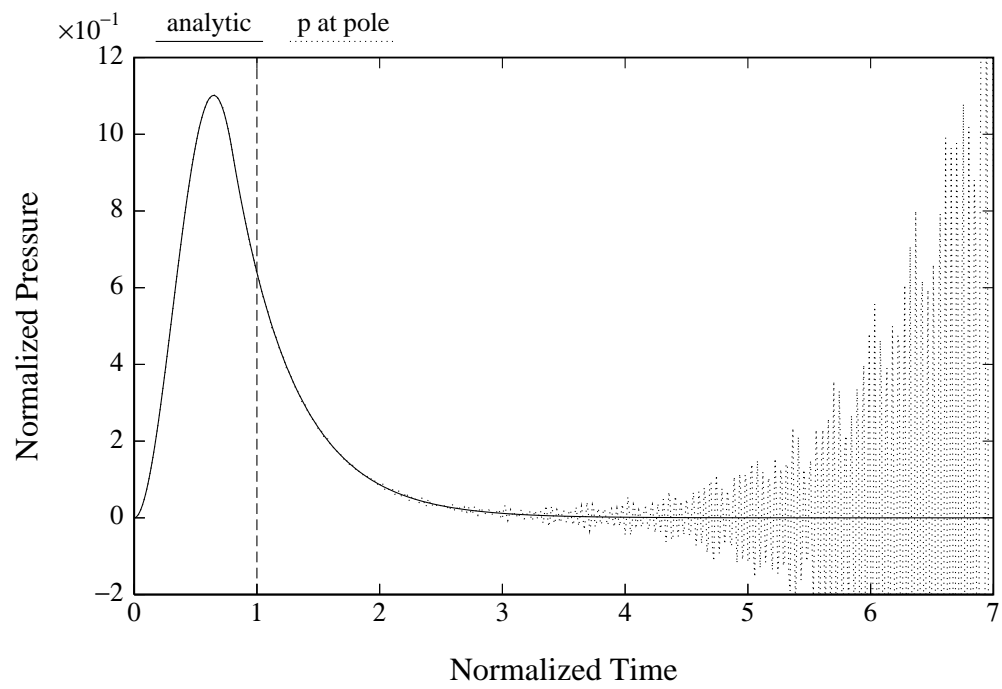


Figure 2.7. Instability due to very small time steps.

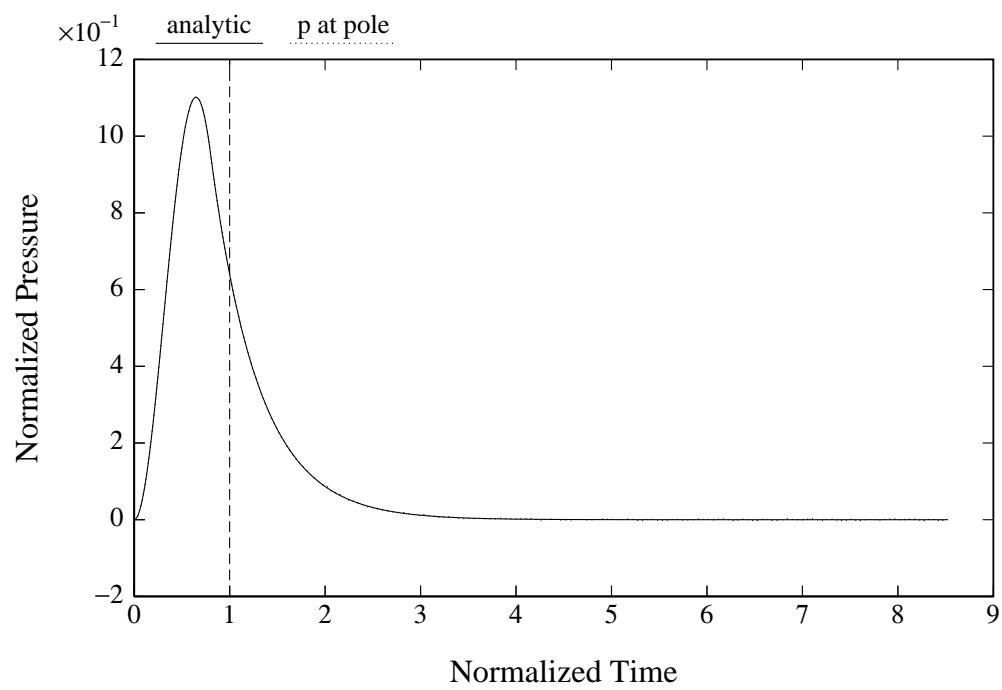


Figure 2.8. Stabilizing effect of derivative smoothing (five-point).

2.10 Infinite Element Methods

An infinite fluid element is similar to a conventional fluid finite element, except one of its dimensions is infinite as shown in Figure 2.9.

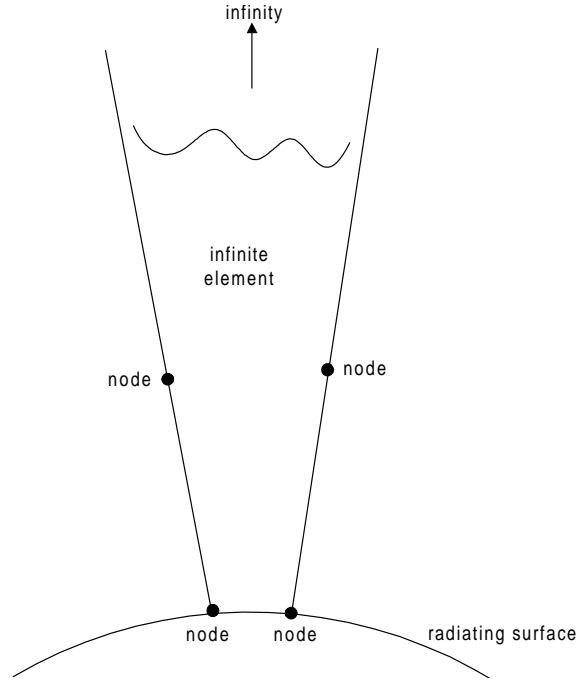


Figure 2.9. A typical infinite element.

The interpolation functions used for this element are like those for conventional finite elements in those directions where the element is finite. The difference is in the infinite direction. The nature of the interpolation in the infinite direction is easiest to see by considering a one-dimensional problem as shown in Figure 2.10. The semi-infinite interval $[a, \infty)$ can be mapped to the finite interval $[-1, 1]$ using the mapping $r \rightarrow \zeta$ defined by

$$\zeta = 1 - \frac{2a}{r} \quad r = \frac{2a}{1 - \zeta}. \quad (2.10.1)$$

On the interval $[-1, 1]$, one can use interpolation functions of the form

$$\phi(\zeta) = P(\zeta)e^{-ik(r-a)} = P(\zeta)e^{-ika\frac{1+\zeta}{1-\zeta}}, \quad (2.10.2)$$

where $P(\zeta)$ is conventional finite element interpolating polynomial that vanishes at $\zeta = 1$ ($r = \infty$). The exponential phase factor is added to account for the time lag inherent in an



Figure 2.10. One-dimensional infinite element.

outgoing acoustic wave. In terms of the variable r , the interpolation functions take the form

$$\phi(r) = P(1 - 2a/r)e^{-ik(r-a)} = \frac{e^{-ikr}}{r} \left(a_0 + a_1 \frac{1}{r} + a_2 \frac{1}{r^2} + \cdots + a_n \frac{1}{r^n} \right) \quad (2.10.3)$$

Thus, we see that the interpolation functions have the correct asymptotic form. This mapping approach can be extended to two and three dimensions. The big advantage of the infinite element approach is that it is easily incorporated into a finite element program for handling fluid-structure interaction problems. A good reference for infinite element methods is [Zienkiewicz, O.C., Emson, C., and Bettess, P., *A Novel Boundary Infinite Element*, International Journal for Numerical Methods in Engineering, vol. 19, pp. 393–404 (1983)].

2.11 Wave Envelope Method

The wave envelope method is similar to the infinite element method. In fact, the same interpolation functions and element geometry can be used in either method. To see the difference between the two methods, we must go back to the derivation of the finite element equations. One common approach in deriving the finite element equations is to use the so-called Galerkin method. In this approach, the unknowns in the underlying differential or integral equations are approximated by finite sums of interpolation functions where the weights in these sums are now the unknowns. The finite element equations are obtained by forming weighted integrals of the resulting approximate equations. For conventional finite elements or infinite elements, the weighting functions are taken to be the same as the interpolation functions. In the wave envelope method, the weighting functions are taken to be the complex conjugates of the interpolation functions. This does not seem to be a big difference, but it leads to finite element equations with a much simpler frequency dependence. In fact the resulting finite element equations have the matrix form

$$(-\omega^2 M + i\omega R + K)U = F, \quad (2.11.1)$$

where the mass matrix M , the damping matrix R , and the stiffness matrix K are independent of frequency. This equation can be easily transformed to the following system of differential equations in the time domain

$$M\ddot{U} + R\dot{U} + KU = F. \quad (2.11.2)$$

Thus, the wave envelope method provides a method for solving acoustic-structure interaction problems in the time domain. The SARA finite element program developed by Bolt, Beranek and Newman for the government is one finite element program that incorporates both conventional infinite elements and wave-envelope elements [Butler, M., Allik, H., et al., *Practical implementation of a p-version wave envelope infinite element for structural acoustic analysis*, Proceedings of the First MIT Conference on Computational Fluid and Solid Mechanics, June 2001]. Two good general references on the wave-envelope method are [Astley, R.J., Macaulay, G.J., Coyette, J-P., and Cremers, L., *Three-dimensional wave-envelope elements of variable order for acoustic radiation and scattering. Part I. Formulation in the frequency domain*, J. Acoust. Soc. Am., **103**(1), pp. 49–63 (1998)] and [Astley, R.J., Macaulay, G.J., Coyette, J-P., and Cremers, L., *Three-dimensional wave-envelope elements of variable order for acoustic radiation and scattering. Part II. Formulation in the time domain*, J. Acoust. Soc. Am., **103**(1), pp. 64–72 (1998)].

2.12 Radiation Boundary Conditions

Another approach to the numerical solution of an exterior acoustic radiation problem is to terminate the semi-infinite exterior region at some distance by a spherical surface and place some kind of radiation boundary conditions on this spherical surface that approximates the outgoing radiation condition. Usually, the fluid region out to the spherical surface is modeled with conventional fluid finite elements. The natural boundary condition on the outer boundary for the fluid finite elements involves specification of integrals of the form

$$\int_S \frac{\partial P}{\partial r} \phi_m dS \quad (2.12.1)$$

where S is a spherical surface of radius R enclosing the radiator and ϕ_m is a finite element interpolation function. Thus, we need radiation conditions on the outer boundary for $\frac{\partial P}{\partial r}$. It can be shown that the pressure field exterior to the spherical surface S can be written as an infinite series in inverse powers of r , i.e.,

$$P(r, \theta, \phi) = e^{-ikr} \sum_{n=1}^{\infty} \frac{F_n(\theta, \phi)}{r^n}. \quad (2.12.2)$$

Bayliss *et al* [Bayliss, Gunzburger and Turkel, *Boundary Conditions for the Numerical Solution of Elliptic Equations in Exterior Regions*, SIAM J. APPL. MATH., Vol. 42, No. 2, April 1982] developed a series of differential operators B_1, B_2, \dots such that B_n operating on

the series in equation (2.12.2) gives zero for the first n terms. The first two of these operators are given by

$$B_1 = \frac{\partial}{\partial r} + ik + \frac{1}{r} \quad (2.12.3)$$

$$B_2 = \left(\frac{\partial}{\partial r} + ik + \frac{3}{r} \right) \left(\frac{\partial}{\partial r} + ik + \frac{1}{r} \right). \quad (2.12.4)$$

The condition $B_1 P = 0$ on the surface $r = R$ can be written

$$\frac{\partial P}{\partial r}(R, \theta, \phi) = - \left(ik + \frac{1}{R} \right) P(R, \theta, \phi). \quad (2.12.5)$$

This condition is called a monopolar condition. It can be shown that $B_1 P = O(1/r^3)$. The condition $B_2 P = 0$ on $r = R$ can be written

$$\begin{aligned} \frac{\partial p}{\partial r}(R, \theta, \phi) = & -(1/R + ik)P(R, \theta, \phi) + \frac{\partial/\partial\theta[\sin\theta(\partial P/\partial\theta)]}{2r^2(1/r + ik)\sin\theta} \Big|_{r=R} \\ & + \frac{1}{2R^2(1/R + ik)\sin^2\theta} \frac{\partial^2 P}{\partial\phi^2}(R, \theta, \phi), \end{aligned} \quad (2.12.6)$$

where $\partial^2 P/\partial r^2$ has been eliminated using the reduced wave equation $\Delta P + k^2 P = 0$. This second order boundary condition is called a dipolar condition. It can be shown that $B_2 P = O(1/r^5)$. When this dipolar boundary condition is substituted into the finite element boundary integrals of equation (2.12.1), integration by parts can be used to eliminate the second order angular derivatives. These radiation boundary conditions have been implemented in the ATILA finite element program and are described in [Bossut and Decarpigny, *Finite element modeling of radiating structures using dipolar damping elements*, J. Acoust. Soc. Am., **86**(4), October 1989].

2.13 An Integral Equation Variational Method

An alternative to the integral equation methods discussed previously is a variational method described in [Ginsberg, J.H., Pierce, A.D., and Wu, X.-F., *A Variational Principle for Sound Radiation from Vibrating Bodies*, Technical Report GTADRL-86-101, Georgia Institute of Technology, November 1986]. In this reference a functional $J(P)$ of the surface pressure P is developed which is stationary with respect to small variations in surface pressure. This functional can be written

$$\begin{aligned} \frac{1}{4\pi} J(P) = & i\omega\rho \int_S P(\zeta) U(\zeta) dS(\zeta) \\ & + \frac{1}{2} k^2 \int_S \int_S [\vec{n}(\zeta) \cdot \vec{n}(\xi)] P(\zeta) P(\xi) G(\zeta, \xi) dS(\xi) dS(\zeta) \\ & - \frac{1}{2} \int_S \int_S [\vec{n}(\zeta) \times \nabla P(\zeta)] \cdot [\vec{n}(\xi) \times \nabla P(\xi)] G(\zeta, \xi) dS(\xi) dS(\zeta), \end{aligned} \quad (2.13.1)$$

where P is the surface pressure, k is the acoustic wavenumber, \vec{n} is the outward unit normal to S , and G is the free-space Green's function defined by

$$G(\zeta, \xi) = \frac{e^{-ikr(\zeta, \xi)}}{4\pi r(\zeta, \xi)}. \quad (2.13.2)$$

The quantity U involves the surface normal velocity V and is defined by

$$U(\zeta) = V(\zeta) + \frac{1}{4\pi} \lim_{\epsilon \rightarrow 0} \int_S V(\xi) \vec{n}(\zeta) \cdot \nabla_x G(x, \xi) dS(\xi) \quad x = \zeta + \epsilon \vec{n}(\zeta). \quad (2.13.3)$$

The condition of stationarity can be written

$$\delta_h J(P) = 0 \quad \text{for all admissible functions } h, \quad (2.13.4)$$

where the variation $\delta_h J$ with respect to h is defined by

$$\delta_h J(P) = \lim_{\epsilon \rightarrow 0} \frac{J(P + \epsilon h) - J(P)}{\epsilon}. \quad (2.13.5)$$

The variation with respect to a function h is the function space analog of the directional derivative, where h plays the role of the direction of the derivative. In view of the definition of J given by equation (2.13.1), the stationarity condition of equation (2.13.4) can be written

$$\begin{aligned} i\omega\rho \int_S h(\zeta) U(\zeta) dS(\zeta) + k^2 \int_S \int_S [\vec{n}(\zeta) \cdot \vec{n}(\xi)] h(\zeta) P(\xi) G(\zeta, \xi) dS(\xi) dS(\zeta) \\ - \int_S \int_S [\vec{n}(\zeta) \times h(\zeta)] \cdot [\vec{n}(\xi) \times \nabla P(\xi)] G(\zeta, \xi) dS(\xi) dS(\zeta) = 0. \end{aligned} \quad (2.13.6)$$

We will assume now that the surface pressure P can be expanded in terms of a set of functions ϕ_n as follows

$$P(\xi) = \sum_{n=1}^N P_n \phi_n(\xi). \quad (2.13.7)$$

Replacing h successively by each ϕ_n and replacing P by the expansion (2.13.7) in equation (2.13.6), leads to a system of N linear equations for the unknown quantities P_n . Once the quantities P_n are determined, the pressure at any point on the surface can be calculated using equation (2.13.7). The functions ϕ_n can be either local interpolation functions like those used in finite element methods or global functions like those involved in Fourier series.

2.14 Doubly Asymptotic Approximations

In this class of approximations an asymptotic approximation valid at low frequencies is smoothly joined to an asymptotic approximation valid at high frequencies. These methods are also referred to as matched asymptotic methods. Two good references for the application of these methods to acoustics are [Felippa, C.A., *Top-Down Derivation of Doubly Asymptotic Approximations for Structure-Fluid Interaction Analysis*, in **Innovative Numerical Analysis for the Engineering Sciences**, edited by R.P. Shaw *et al.* (U.P. of Virginia, Charlottesville, 1980), pp. 79–88.] and [Geers, T.L. and Felippa, C.A., *Doubly asymptotic approximations for vibration analysis of submerged structures*, J. Acoust. Soc. Am., **73** (4), April 1983, pp. 1152–1159.]

Low Frequency Approximations In section 2.7 we showed that the surface integral equation relating pressure and normal velocity or acceleration could be approximated by the system of equations

$$AP = B\dot{V}, \quad (2.14.1)$$

where

$$A_{mn} = \frac{1}{2}\delta_{mn} - \int_{S_n} \frac{\partial G}{\partial n}(\zeta_m, \xi) dS(\xi) \quad (2.14.2)$$

$$B_{mn} = \rho \int_{S_n} G(\zeta_m, \xi) dS(\xi) \quad (2.14.3)$$

and G is the free-space Green's function defined by

$$G(\zeta, \xi) = \frac{e^{-ikr(\zeta, \xi)}}{4\pi r(\zeta, \xi)} \quad r(\zeta, \xi) = \text{distance between } \zeta \text{ and } \xi. \quad (2.14.4)$$

At low frequencies the Green's function G and its normal derivative can be expanded in terms of powers of kr . Various orders of approximation can be obtained by truncating these

power series so that both sides of equation (2.14.1) are approximated by the same degree of polynomial in kr . The first order approximation is given by

$$A^0 P = B^0 \dot{V}, \quad (2.14.5)$$

where

$$A_{mn}^0 = \frac{1}{2} \delta_{mn} - \int_{S_n} \frac{\partial G^0}{\partial n}(\zeta_m, \xi) dS(\xi) \quad (2.14.6)$$

$$B_{mn}^0 = \rho \int_{S_n} G^0(\zeta_m, \xi) dS(\xi) \quad (2.14.7)$$

and G^0 is defined by

$$G^0 = \frac{1}{4\pi r}. \quad (2.14.8)$$

It should be noted that G^0 is the free-space Green's function for Laplace's equation $\Delta P = 0$ which is what the reduced wave equation reduces to at zero frequency. Since the matrices in equation (2.14.5) are independent of frequency, this equation can be transformed to the time-domain equations

$$A^0 p = B^0 \dot{v}. \quad (2.14.9)$$

If we define D to be a diagonal matrix whose diagonal entries are the surface areas of the subareas in our discrete approximation, then equation (2.14.5) can be rearranged to give

$$DP = [D(A^0)^{-1} B^0] \dot{V} \equiv M_F \dot{V}. \quad (2.14.10)$$

The matrix M_F represents the mass loading of the fluid. The approximation given by equation (2.14.10) is called the virtual mass approximation.

The next order of approximation is given by

$$A^0 P = B^0 \dot{V} + C^0 \ddot{V}, \quad (2.14.11)$$

where

$$C^0 = -\frac{\rho}{4\pi c} D. \quad (2.14.12)$$

As before this approximation can be rearranged to give

$$DP = M_F \dot{V} + Q \ddot{V} \quad Q = D(A^0)^{-1} C^0. \quad (2.14.13)$$

It can be argued using energy arguments that only the symmetric part of the mass matrix M_F should be retained in these approximations [DeRuntz, J.A. and Geers, T.L., *Added Mass Computation By The Boundary Integral Method*, International Journal for Numerical Methods in Engineering, Vol. 12, 531–549 (1978)].

High Frequency Approximations At high frequencies the relation between pressure and velocity tends to be local in nature. The simplest approximation is the plane wave approximation

$$p = \rho cv. \quad (2.14.14)$$

We can write this relation in a matrix form like those occurring in the low frequency approximations as follows

$$DP = \rho c DV. \quad (2.14.15)$$

Higher order approximations involve the local curvature of the surface. Consider a small patch of the surface S as shown in Figure 2.11. At a point ξ on the surface patch we set up

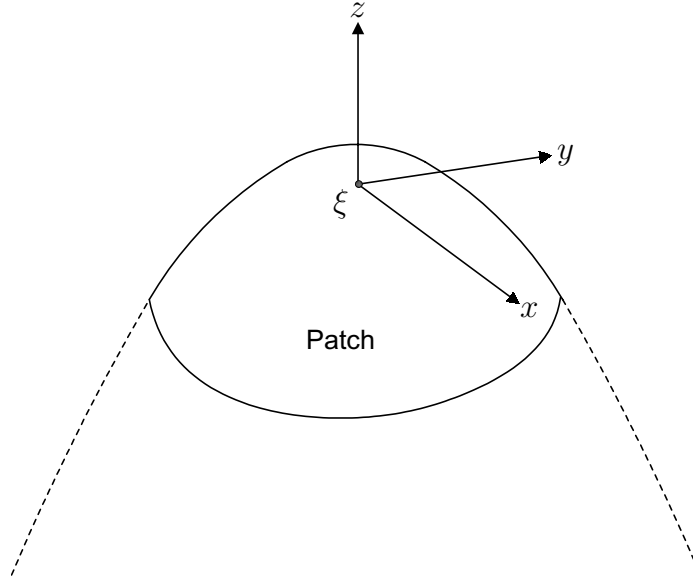


Figure 2.11. Local coordinate system at point of surface patch

a local coordinate system in which the z -axis is in the direction of the outward normal at ξ and the x and y axes are in the tangent plane at ξ . By proper orientation of the x and y axes, the surface patch in the vicinity of ξ can be represented approximately by the equation

$$z = \kappa_x x^2 + \kappa_y y^2, \quad (2.14.16)$$

where κ_x and κ_y are the principal curvatures at ξ . At high frequencies the surface pressure and normal velocity at ξ are approximately related by

$$\dot{p} - c\kappa p = \rho c \dot{v} \quad \kappa = (\kappa_x + \kappa_y)/2. \quad (2.14.17)$$

This approximation is referred to as the curved wave approximation. Clearly, the curved wave approximation reduces to the plane wave approximation when the mean curvature κ is set to zero. For a discretized problem this relation can be written in the matrix form

$$D\dot{P} - cDKP = \rho c \dot{V}, \quad (2.14.18)$$

where K is a diagonal matrix whose diagonal entries are the mean curvatures at the reference points of the subareas of the discretization.

Matching Asymptotic Approximations In this section we will illustrate a general technique for smoothly matching high and low frequency asymptotic approximations. Consider, for example, the matching of the virtual mass approximation at low frequencies and the plane wave approximation at high frequencies. Thus, we want to match the following pair of approximations

$$DP = i\omega M_F V \quad (\text{virtual mass approximation}) \quad (2.14.19a)$$

$$DP = \rho c DV \quad (\text{plane wave approximation}). \quad (2.14.19b)$$

We seek an approximate equation of the form

$$\mathcal{P}_P(i\omega)P = \mathcal{P}_V(i\omega)V, \quad (2.14.20)$$

where \mathcal{P}_P and \mathcal{P}_V are polynomials in $i\omega$ with matrix coefficients. This is the matrix analog of assuming that the impedance is a rational function of $i\omega$. We want to choose these polynomials so that equation (2.14.20) agrees with equation (2.14.19a) at low frequencies and agrees with equation (2.14.19b) at high frequencies. In this case we seek an approximation of the form

$$(I + i\omega A)P = (i\omega B)V, \quad (2.14.21)$$

where the matrices A and B are to be determined. At low frequencies equation (2.14.21) reduces to $P = i\omega BV$ and at high frequencies it reduces to $AP = BV$. Comparing these results to the low and high frequency approximations given in (2.14.19a) and (2.14.19b), we see that

$$B = D^{-1}M_F \quad \text{and} \quad A = \frac{1}{\rho c}B. \quad (2.14.22)$$

Substituting these results into equation (2.14.21) and rearranging produces the approximate relation

$$(\rho c D + i\omega M_F)P = (i\omega \rho c M_F)V \quad (2.14.23)$$

or equivalently

$$M_F \dot{P} + \rho c DP = \rho c M_F \dot{V}. \quad (2.14.24)$$

This approximation is often referred to as DAA₁. Higher order approximations can be obtained similarly and are discussed in the references.

2.15 Array Acoustic Interactions

The acoustic interaction between transducer elements of an array can often be a significant factor in the performance of the array. Acoustic interactions are usually described in terms

of mutual radiation impedances. The concept of mutual radiation impedance was first introduced in connection with arrays of piston radiators. For such arrays the normal velocity of the n -th element can be specified by a single value V_n . The acoustic force on the m -th piston element can be written as a linear combination of the element velocities, i.e.,

$$F_m = \sum_{n=1}^N z_{mn} V_n, \quad m = 1, \dots, N. \quad (2.15.1)$$

The values z_{mn} are called mutual radiation impedances. When $m = n$ the values z_{mm} are called self radiation impedances. Figure (2.12) shows the self radiation impedance for a circular piston of radius a normalized by $\rho c(\pi a^2)$ as a function of the normalized frequency ka . Figure (2.13) shows the mutual radiation impedance between two circular pistons having a center-to-center spacing of d as a function of kd with $ka = 1$. The behavior of the radiation impedances shown in these figures is typical of most radiators. For a few special geometries the radiation impedances z_{mn} can be computed analytically. For example, Pritchard [R.L. Pritchard, *Mutual Acoustic Impedance between Radiators in an Infinite Plane*, J. Acoust.Soc. Am., 32, no. 6, pp. 730–737 (1960)] derived the following expression for the mutual radiation impedance between circular pistons on a plane

$$z_{12} = 2\rho c(\pi a^2) \sum_{m=0}^{\infty} \sum_{n=0}^{\infty} \frac{\Gamma(m+n+1/2)}{\sqrt{\pi} m! n!} \left(\frac{a}{d}\right)^{m+n} J_{m+1}(ka) J_{n+1}(ka) h_{m+n}^{(2)}(kd), \quad (2.15.2)$$

where a is the radius of a piston, d is the center-to-center spacing between pistons, J_n is the Bessel function of the first kind, and $h_n^{(2)}$ is the spherical Hankel function of the second kind. A general technique for calculating mutual radiation impedances of arbitrary shaped pistons on an infinite plane rigid baffle is described in [Benthien, G.W., *Mutual Interaction of Pistons of Arbitrary Shape on a Planar Rigid Baffle*, unpublished notes]. The report [Sherman, C.H., *Mutual Radiation Impedance Between Pistons on Spheres and Cylinders*, USL Research Report 405, November 1958] derives expressions for the mutual radiation impedances between pistons on rigid spherical or cylindrical baffles. For most geometries these radiation impedances can not be obtained analytically and must be computed using numerical approximations to the basic differential or integral equations (finite elements, finite differences, boundary element methods, etc.).

The vibratory motion of many transducers can not be described by a single velocity value. For example, it is generally necessary to use the superposition of a number of modes in order to describe the motion of a flextensional transducer. Therefore, we need to generalize equation (2.15.1) in order to handle arrays of such transducers.

Let $V_n(\cdot)$ denote the normal velocity distribution on the n -th element of an array, and let $P_n(\cdot)$ be the pressure due to the array when the n -th element has the velocity distribution $V_n(\cdot)$ and the other elements have zero velocity. By linearity, the surface pressure $P(\cdot)$ due

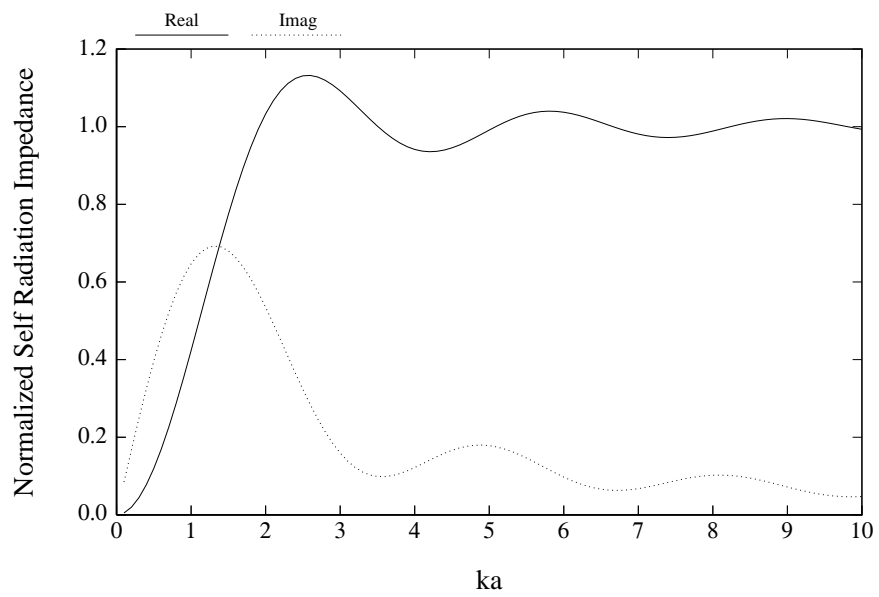


Figure 2.12. Normalized self radiation impedance of a circular piston

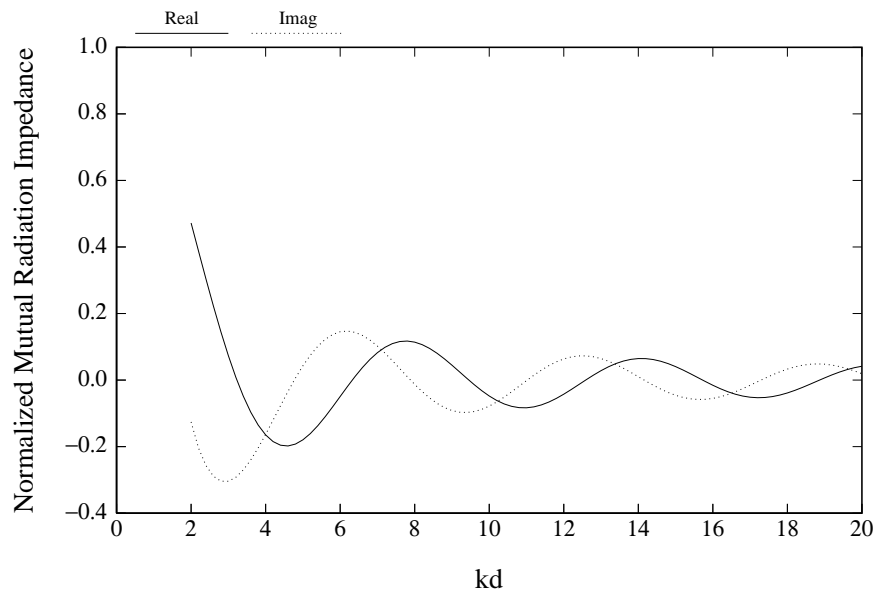


Figure 2.13. Normalized mutual radiation impedance for circular pistons

to the array is given by

$$P(\cdot) = \sum_{n=1}^N P_n(\cdot). \quad (2.15.3)$$

We will assume that there exist functions $\phi_n^1(\cdot), \phi_n^2(\cdot), \dots, \phi_n^M(\cdot)$ such that the velocity distribution on the n -th element can be written

$$V_n(\cdot) = \sum_{q=1}^M V_n^q \phi_n^q(\cdot). \quad (2.15.4)$$

These functions can be normal modes of the radiating structure or they can be interpolation functions related to a finite element description of the structure. For programs like CHIEF that use a piecewise constant representation of the velocity distribution, the functions $\phi_n^q(\cdot)$ have the property that they are identically 1 on one subdivision of the radiating surface of the n -th element and are zero on all the other subdivisions. Furthermore, it will be assumed that the functions $\phi_n^q(\cdot)$ for different elements n are merely translations of each other. Of course, it is desirable to choose the functions $\phi_n^q(\cdot)$ so that only a few are required for each n . If only a few modes are important, then a modal expansion is a good choice. If only a few subdivisions are required for each element, then interpolation functions might be a better choice.

Let $P_n^q(\cdot)$ be the surface pressure due the array when the n -th element has the velocity distribution $\phi_n^q(\cdot)$ and all the other elements have a velocity of zero. By linearity,

$$P_n(\cdot) = \sum_{q=1}^M V_n^q P_n^q(\cdot). \quad (2.15.5)$$

Substituting equation (2.15.5) into equation (2.15.3), we obtain

$$P(\cdot) = \sum_{n=1}^N \sum_{q=1}^M V_n^q P_n^q(\cdot). \quad (2.15.6)$$

Let F_m^r to be the force component defined by

$$F_m^r \equiv \int_{S_m} P(\xi) \phi_m^r(\xi) dS(\xi), \quad (2.15.7)$$

where S_m is the radiating surface of the m -th element. Force components such as this are what is needed in order to couple to structural models such as finite element models. It follows from equation (2.15.6), that

$$F_m^r = \sum_{n=1}^N \sum_{q=1}^M V_n^q \int_{S_m} P_n^q(\xi) \phi_m^r(\xi) dS(\xi). \quad (2.15.8)$$

If we define

$$z_{mn}^{qr} \equiv \int_{S_m} P_n^q(\xi) \phi_m^r(\xi) dS(\xi), \quad (2.15.9)$$

then equation (2.15.8) can be written

$$F_m^r = \sum_{n=1}^N \sum_{q=1}^M z_{mn}^{qr} V_n^q. \quad (2.15.10)$$

If we define

$$\vec{V}_n = \begin{pmatrix} V_n^1 \\ V_n^2 \\ \vdots \\ V_n^M \end{pmatrix} \quad \vec{F}_m = \begin{pmatrix} F_m^1 \\ F_m^2 \\ \vdots \\ F_m^M \end{pmatrix} \quad (2.15.11)$$

and

$$Z_{mn} = \begin{pmatrix} z_{mn}^{11} & \cdots & z_{mn}^{1M} \\ \vdots & & \vdots \\ z_{mn}^{M1} & \cdots & z_{mn}^{MM} \end{pmatrix}, \quad (2.15.12)$$

then equation (2.15.10) can be written in the matrix form

$$\vec{F}_m = \sum_{n=1}^N Z_{mn} \vec{V}_n. \quad (2.15.13)$$

Equation (2.15.13) is the required generalization of equation (2.15.1). In place of F_m we have the M-vector \vec{F}_m ; in place of V_n we have the M-vector \vec{V}_n ; and in place of z_{mn} we have the $M \times M$ matrix Z_{mn} . It can be shown that $Z_{mn} = Z_{nm}$.

The surface pressure distribution P_n^q can be computed numerically using a boundary element method such as CHIEF by placing a velocity distribution ϕ_n^q on the n-th element and zero velocity on the other elements. Once P_n^q is obtained, the mutual impedances can be obtained by evaluating the integrals in equation (2.15.9) using numerical quadrature.

We have expressed the acoustic interactions as a linear relation between forces and velocities. We could just as well have used accelerations or displacements in place of velocities since they only differ by factors of $i\omega$. In the time domain the choice between velocity, acceleration or displacement is more critical since they are not as simply related. Physically, acceleration is more closely related to the generation of acoustic pressures than are velocity or displacement. Recall that acoustic pressures are due to compression of the fluid medium. When a radiating surface moves it is possible for the fluid to flow away without compression. The compression of the fluid is due in large part to the inertia of the fluid. If the radiator accelerates fast enough, the fluid does not have a chance to flow away and therefore compresses. For this

reason acceleration is usually the quantity of choice when working in the time domain. The analog of equation (2.15.13) in terms of accelerations A_n is

$$\vec{F}_m = \sum_{n=1}^N \mathcal{M}_{mn} \vec{A}_n, \quad (2.15.14)$$

where

$$\mathcal{M}_{mn} = \frac{1}{i\omega} Z_{mn} \quad \text{and} \quad A_n = i\omega V_n. \quad (2.15.15)$$

Taking the inverse Fourier transform of equation (2.15.14), we get

$$\vec{f}_m(t) = \sum_{n=1}^N \int_0^t \mu_{mn}(\tau) a_n(t - \tau) d\tau, \quad (2.15.16)$$

where

$$\mu_{mn}(\tau) = \int_{-\infty}^{\infty} \mathcal{M}_{mn}(\omega) e^{i\omega\tau} d\omega. \quad (2.15.17)$$

In obtaining this relation we have used the fact that the Fourier transform of a convolution is the product of the Fourier transforms. We have also assumed that all of the element accelerations a_n are zero for all times t less than zero. The matrix function μ_{mn} is called the mutual acceleration impulse response function. It can be seen from equation (2.15.16) that the force components on the m -th element depend on the past histories of the acceleration components on the other elements. This is because it takes a finite time for sound to travel from one element to another. Figure (2.14) is typical of the behavior that might be expected for a component of the matrix μ_{mn} of impulse responses. These functions usually have a peak at the time corresponding to the time required for sound to travel between the elements. The width of the peak is approximately equal to the time required for sound to travel across the pair of elements.

2.16 Pritchard Approximation

A widely used approximation for mutual radiation impedances was introduced by R.L. Pritchard in a 1960 paper [R.L. Pritchard, *Mutual Acoustic Impedance between Radiators in an Infinite Plane*, J. Acoust.Soc. Am.,32, no. 6, pp. 730–737 (1960)]. In this paper he derived an expression for the mutual radiation impedances between circular pistons in a plane infinite rigid baffle. His general expression was quite complicated involving infinite series and Bessel functions. For low frequencies and large separations, he derived an approximation to his general result which he wrote in a form that allowed generalization to other types of radiators. His approximation can be written in the form

$$z_{mn} = i \operatorname{Real}(z_{11}) \frac{e^{-ikd_{mn}}}{kd_{mn}}, \quad (2.16.1)$$

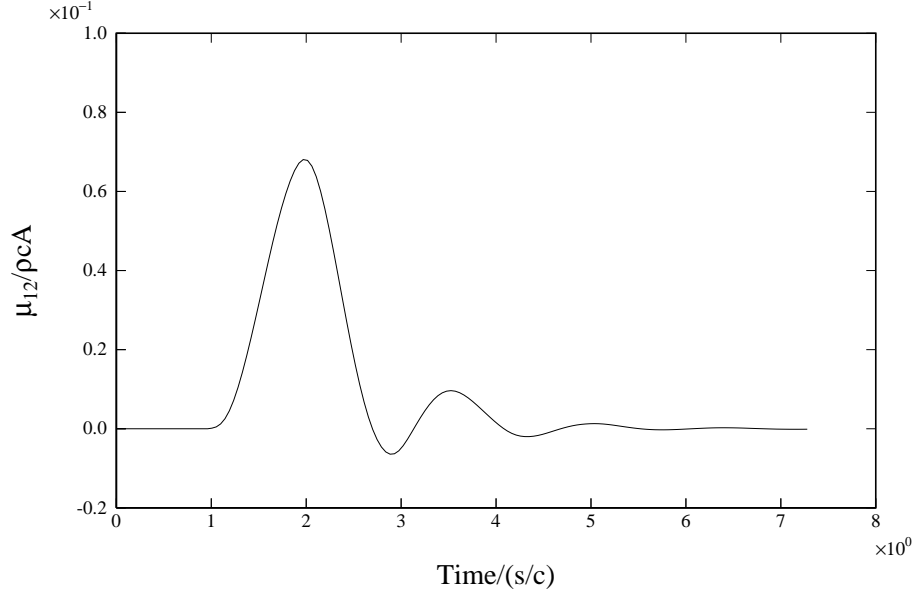


Figure 2.14. Typical mutual acceleration impulse response function

where d_{mn} is the center-to-center separation between the m-th and n-th pistons and z_{11} is the self radiation impedance (assumed to be the same for all elements). This approximation can also be used for problems where the mutual interaction impedance is a matrix as in equation (2.15.13). The generalized form of the approximation is

$$Z_{mn} = i \frac{e^{-ikd_{mn}}}{kd_{mn}} \text{Real}(Z_{11}), \quad (2.16.2)$$

where d_{mn} is now the distance between some reference points associated with each element. This approximation seems to be pretty good at low frequencies even for small separations. Its main drawback is that it doesn't fall off fast enough at higher frequencies. The probable reason for this behavior is that the Pritchard approximation does not include the directivity of the element which is more important at higher frequencies.

2.17 Nearest Neighbor Approximation

The Pritchard approximation computes the mutual impedances from the self impedance. The approximation to be described in this section computes the mutual impedances in terms of a single mutual impedance between an element and its nearest neighbor. Additional information is contained in the reference [G.W. Benthien and D. Barach, *Five Element Array Study*]. In the time domain this approximation amounts to a time shift to account

for the difference in travel time and a scalar multiplier to account for the difference in $1/r$ spreading, i.e.,

$$\mu_{mn}(t) \doteq \frac{d_{12}}{d_{mn}} \mu_{12} \left(t - \frac{d_{mn} - d_{12}}{c} \right). \quad (2.17.1)$$

In the frequency domain this translates to

$$z_{mn}(\omega) \doteq \frac{d_{12}}{d_{mn}} e^{-ik(d_{mn}-d_{12})} z_{12}(\omega). \quad (2.17.2)$$

This approximation seems to agree with the actual mutual interactions over a much larger frequency range than the Pritchard approximation. Figure 2.15 shows a comparison between the Pritchard approximation and a calculation using the boundary element method CHIEF for the interaction of the primary mode between elements 1 and 3 in a line array of Hydroacoustic transducers. In both cases the result was first computed in the frequency domain and then transformed to the time domain. Figure 2.16 shows the same comparison with the Pritchard approximation replaced by the nearest neighbor approximation. It can be seen that the nearest neighbor approximation shows much better agreement.

Figure 2.17 shows a comparison between CHIEF and the Pritchard approximation in the frequency domain. Notice that the Pritchard approximation agrees well at low frequencies, but falls off too slowly at higher frequencies. Figure 2.18 shows the same comparison for the nearest neighbor approximation. Notice that its agreement is quite good at all frequencies.

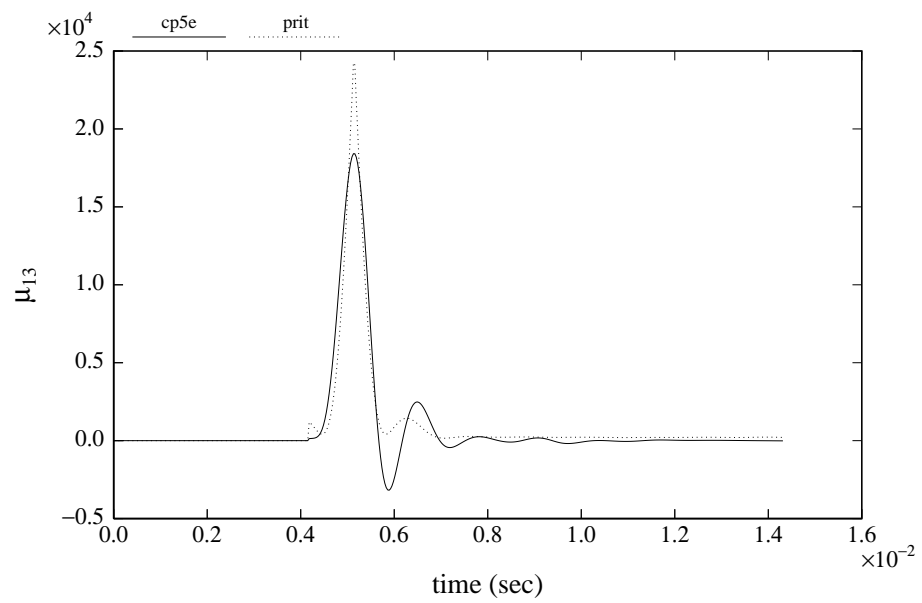


Figure 2.15. Pritchard approximation versus CHIEF in the time domain

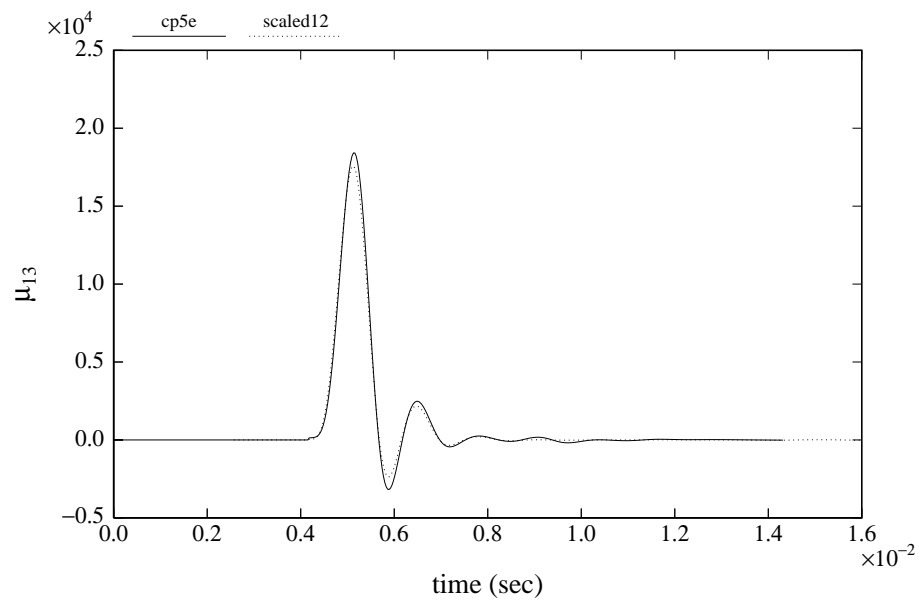


Figure 2.16. Nearest neighbor approximation versus CHIEF in the time domain

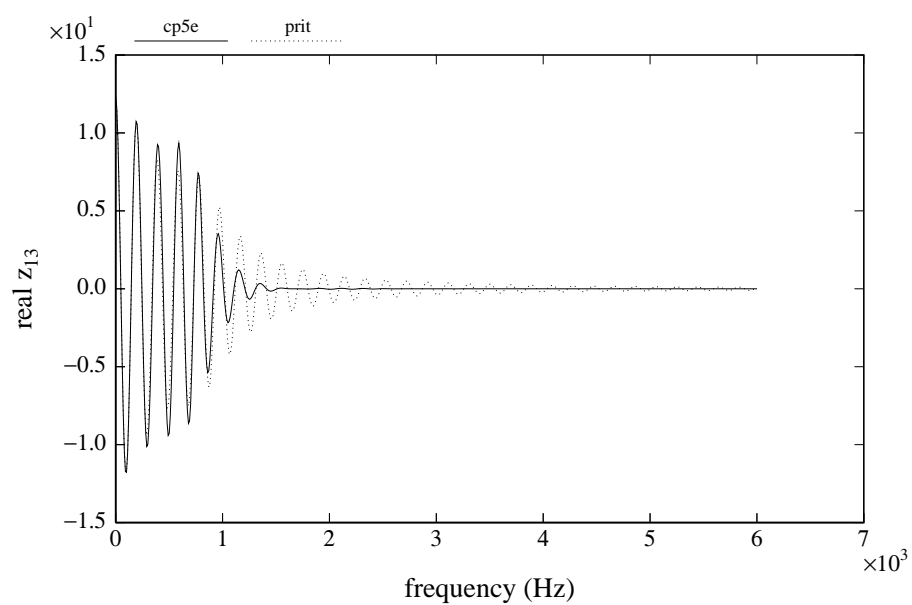


Figure 2.17. Pritchard approximation versus CHIEF in the frequency domain

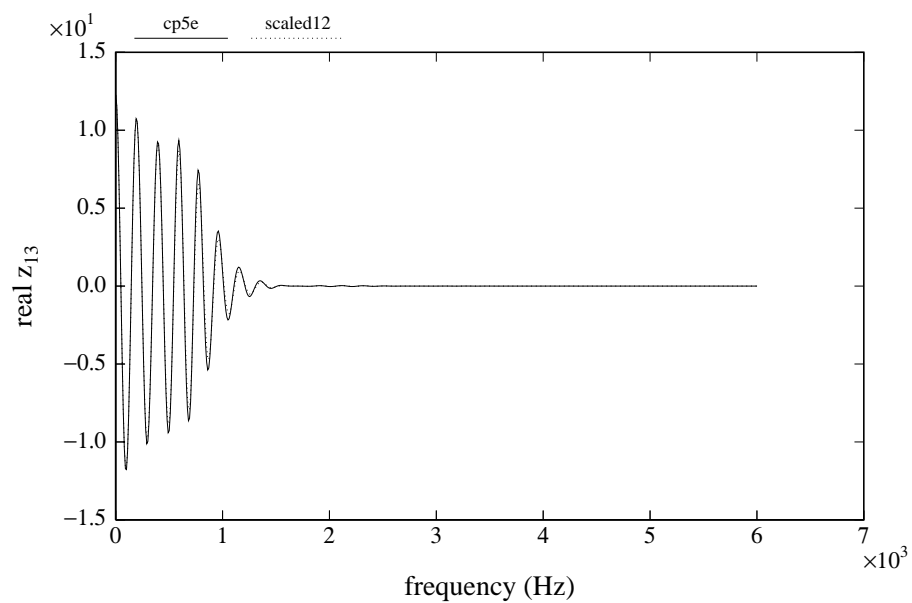


Figure 2.18. Nearest neighbor approximation versus CHIEF in the frequency domain

2.18 T-matrix Approach to Array Interactions

T-matrix methods were first introduced in acoustics to solve scattering problems [Waterman, P., *New Formulation of Acoustic Scattering*, J. Acoust. Soc. Am., **45**(6), 1417–1429 (1969)]. The T-matrix relates coefficients in a spherical harmonic expansion of the incident pressure to the coefficients in a spherical harmonic expansion of the scattered pressure. Several authors have extended the T-matrix method to handle multiple scatterers. See, for example, [Peterson, B. and Ström, S., *Matrix formulation of acoustic scattering from an arbitrary number of scatterers*, J. Acoust. Soc. Am., **56**(3), 771–780 (1974)] and [Varadan, V. V. and Varadan, V. K., *Configurations with finite numbers of scatterers—A self-consistent T-matrix approach*, J. Acoust. Soc. Am., **70**(1), 213–217 (1981)]. Others have extended the T-matrix approach to array interaction problems. See, for example, [Scandrett, C. and Baker, S., *T-matrix approach to array modeling*, Naval Postgraduate School Technical Report, NPS-UW-98-001 (1998)], [Blottman III, J. and Kalinowski, A., *Coupled-field Finite Element/Spherical Harmonic Analysis for Close-Packed Arrays*, presented at the International Congress on Acoustics 2001], and [Scandrett, C. and Baker, S., *Pritchard's Approximation in Array Modeling*, Naval Postgraduate School Technical Report, NPS-UW-99-001 (1999)].

To illustrate some of the concepts involved in applying T-matrix methods to array interaction problems, we will consider here the simple problem of an array of spherical sources as shown in Figure 2.19. For more complicated cases you can refer to the references in this section. Each of the spheres has radius a . We will denote the j -th sphere by S_j and the center of the j -th sphere by x_j . If we are only interested in surface pressures and velocities, it will not be necessary to actually construct the T-matrix. We will, however, make use of spherical harmonic expansions and the spherical harmonic addition theorem as is done in T-matrix methods. The approach taken here follows generally that of the paper [Scandrett, C. L. and Canright, D. R., *Acoustic interactions in arrays of spherical elastic shells*, J. Acoust. Soc. Am., **90**(1), 589–595 (1991)]. However, the notation is more like that used by Varadan in the paper cited above.

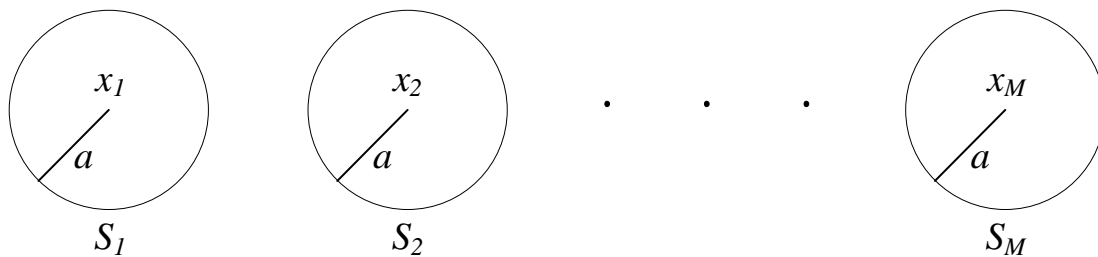


Figure 2.19. An array of spherical radiators.

It follows from the Helmholtz integral formula that

$$\begin{aligned} p(x) &= \sum_{k=1}^M \int_{S_k} \left[p(\sigma) \frac{\partial G(x, \sigma)}{\partial n_\sigma} - \frac{\partial p(\sigma)}{\partial n_\sigma} G(x, \sigma) \right] dS(\sigma) \\ &= \sum_{k=1}^M p_k(x) \quad x \text{ exterior to the array} \end{aligned} \quad (2.18.1)$$

where

$$p_k(x) = \int_{S_k} \left[p(\sigma) \frac{\partial G(x, \sigma)}{\partial n_\sigma} - \frac{\partial p(\sigma)}{\partial n_\sigma} G(x, \sigma) \right] dS(\sigma). \quad (2.18.2)$$

Here $G(x, \sigma)$ is the free-space Green's function. The term $p_k(x)$ is defined and satisfies the acoustic wave equation everywhere exterior to S_k . It also satisfies the outgoing radiation condition at infinity. However, we don't know what boundary conditions to apply to each of the terms p_k ; therefore, we must apply the boundary conditions to the total pressure p .

We will expand each of the terms p_k in terms of spherical harmonics. We will use a notation similar to that used by Varadan [Varadan, V. V. and Varadan, V. K., *Configurations with finite numbers of scatterers—A self-consistent T-matrix approach*, J. Acoust. Soc. Am., **70**(1), 213–217 (1981)]. Define the spherical harmonic function $\psi_{nmp}(x)$ by

$$\psi_{nmp}(x) = \xi_{nm} h_n^{(2)}(kr) Y_{nmp}(\theta, \phi) \quad 0 \leq n < \infty, \quad 0 \leq m \leq n, \quad \sigma = 1, 2 \quad (2.18.3)$$

where

$$Y_{nmp} = P_n^m(\cos \theta) \begin{cases} \cos m\phi & \sigma = 1 \\ \sin m\phi & \sigma = 2 \end{cases} \quad (2.18.4)$$

and

$$\xi_{nm} = \left(\frac{\epsilon_m (2n+1)(n-m)!}{4\pi (n+m)!} \right)^{1/2} \quad \epsilon_0 = 1, \quad \epsilon_m = 2 \text{ for } m > 0. \quad (2.18.5)$$

Here r , θ , and ϕ are the spherical coordinates of the point x relative to a global origin, $h_n^{(2)}$ is the spherical Hankel function of the second kind, and P_n^m is the associated Legendre polynomial.

To simplify the notation we will use a single index “ n ” to represent the triple index “ nmp ”. Thus, we will write $\psi_n(x)$ for $\psi_{nmp}(x)$. In some cases it will be necessary to separate the radial and angular portions of $\psi_n(x)$. It can be seen from equation (2.18.3) that $\psi_n(x)$ can be written as

$$\psi_n(x) = \hat{\psi}_n(|x|) \tilde{\psi}_n(x/|x|) \quad (2.18.6)$$

where $\hat{\psi}_n$ depends only on the radial coordinate and $\tilde{\psi}_n$ depends only on the angular coordinates. The way that the spherical harmonics have been defined, the function $\hat{\psi}_n(|x|)$ is complex and the function $\tilde{\psi}_n(x/|x|)$ is real.

Since $\psi_n(x)$ is defined in terms of the spherical coordinates of x relative to the global origin, we can obtain a spherical harmonic expansion relative to the center x_j by using the functions $\psi_n(x - x_j)$. Thus, $p_j(x)$ has the spherical harmonic expansion

$$p_j(x) = \sum_n a_{jn} \psi_n(x - x_j) \quad (2.18.7)$$

about x_j . Equation (2.18.7) involves an infinite sum over n . However, for numerical purposes, we will truncate this sum at some appropriately high n . This will also be done for all of the spherical harmonic expansions that follow.

Consider now $p_k(x)$, $k \neq j$ for a point x near the sphere S_j . We can expand p_k in terms of spherical harmonics about x_k as follows

$$p_k(x) = \sum_n a_{kn} \psi_n(x - x_k). \quad (2.18.8)$$

We would like to write p_k in terms of spherical harmonics about x_j . To do this we employ the spherical harmonic addition theorem. The details of the addition theorem are somewhat complicated, so we will use the simplified notation employed by Varadan [Varadan, V. V. and Varadan, V. K., *Configurations with finite numbers of scatterers—A self-consistent T-matrix approach*, J. Acoust. Soc. Am., **70**(1), 213–217 (1981)].

$$\psi_n(x - d) = \begin{cases} \sum_m R_{nm}(-d) \psi_m(x) & |x| > |d| \\ \sum_m S_{nm}(-d) \text{Real } \psi_m(x) & |x| < |d|. \end{cases} \quad (2.18.9)$$

The coefficients R_{nm} and S_{nm} involve spherical harmonic functions as well as the Wigner 3-j symbols.

For x near S_j we have

$$x - x_k = (x - x_j) - (x_k - x_j) \quad \text{and} \quad |x - x_j| < |x_k - x_j|, \quad (2.18.10)$$

Therefore, we can use the addition theorem to write

$$\psi_n(x - x_k) = \sum_m S_{nm}(x_j - x_k) \text{Real } \psi_m(x - x_j). \quad (2.18.11)$$

Substituting equation (2.18.11) into equation (2.18.8), we obtain

$$\begin{aligned}
p_k(x) &= \sum_n a_{kn} \sum_n S_{nm}(x_j - x_k) \text{Real } \psi_m(x - x_j) \\
&= \sum_m a_{km} \sum_n S_{mn}(x_j - x_k) \text{Real } \psi_n(x - x_j) \\
&= \sum_n \text{Real } \psi_n(x - x_j) \sum_m a_{km} S_{mn}(x_j - x_k).
\end{aligned} \tag{2.18.12}$$

In obtaining this expression we have interchanged m and n since they are merely summation indices over the same range.

If in equation (2.18.1) we replace $p_j(x)$ by the expression in equation (2.18.7) and $p_k(x)$ ($k \neq j$) by the expression in equation (2.18.12), we obtain

$$p(x) = \sum_n \left\{ a_{jn} \psi_n(x - x_j) + \text{Real } \psi_n(x - x_j) \sum_{\substack{k=1 \\ k \neq j}}^M \sum_m a_{km} S_{mn}(x_j - x_k) \right\}. \tag{2.18.13}$$

To satisfy the boundary condition we need evaluate the normal derivative of p on the surface S_j . Since the normal is in the radial direction, it is only necessary to differentiate the radial part $\hat{\psi}_n$ of each ψ_n in equation (2.18.13). Therefore,

$$\begin{aligned}
\frac{\partial p(\sigma)}{\partial n_\sigma} &= \sum_n \left\{ a_{jn} \hat{\psi}'_n(a) + \text{Real } \hat{\psi}'_n(a) \sum_{\substack{k=1 \\ k \neq j}}^M \sum_m a_{km} S_{mn}(x_j - x_k) \right\} \tilde{\psi}_n \left(\frac{\sigma - x_j}{a} \right) \\
&\quad \text{for } \sigma \text{ on } S_j.
\end{aligned} \tag{2.18.14}$$

where the primes denote differentiation. The normal derivative of p on S_j is related to the normal velocity v_j on S_j through the equation of motion, i.e.,

$$\frac{\partial p(\sigma)}{\partial n_\sigma} = -i\omega \rho v_j(\sigma) \quad \text{for } \sigma \text{ on } S_j \tag{2.18.15}$$

We now expand v_j in terms of the angular spherical harmonics as follows

$$v_j(\sigma) = \sum_n v_{jn} \tilde{\psi}_n \left(\frac{\sigma - x_j}{a} \right). \tag{2.18.16}$$

Combining equations (2.18.14)–(2.18.16), we get

$$-i\omega\rho\sum_n v_{jn}\tilde{\psi}_n\left(\frac{\sigma-x_j}{a}\right)=\sum_n\left\{a_{jn}\hat{\psi}'_n(a)+\text{Real}\hat{\psi}'_n(a)\sum_{\substack{k=1 \\ k\neq j}}^M\sum_m a_{km}S_{mn}(x_j-x_k)\right\}\tilde{\psi}_n\left(\frac{\sigma-x_j}{a}\right). \quad (2.18.17)$$

Since the angular spherical harmonics are orthogonal over the sphere S_j , we can equate coefficients on the two sides of equation (2.18.17) to obtain

$$-i\omega\rho v_{jn}=a_{jn}\hat{\psi}'_n(a)+\text{Real}\hat{\psi}'_n(a)\sum_{\substack{k=1 \\ k\neq j}}^M\sum_m a_{km}S_{mn}(x_j-x_k). \quad (2.18.18)$$

There is an equation like this for each j , $j=1,\dots,M$.

Equation (2.18.18) is a set of linear equations relating the coefficient v_{jn} to the coefficients a_{jn} . We can write this system of equations in matrix form as follows

$$\mathbf{v}=\mathbf{B}\mathbf{a}. \quad (2.18.19)$$

where \mathbf{v} is a vector of the coefficients v_{jn} and \mathbf{a} is a vector of the coefficients a_{jn} . If the velocities are given, this system of equations can be solved for the coefficients a_{jn} . The pressure in the field can then be computed using the expansions (2.18.7) and the summation relation (2.18.1).

Letting the point x in equation (2.18.13) approach a point σ on S_j , we get

$$p(\sigma)=\sum_n\left\{a_{jn}\hat{\psi}_n(a)+\text{Real}\hat{\psi}_n(a)\sum_{\substack{k=1 \\ k\neq j}}^M\sum_m a_{km}S_{mn}(x_j-x_k)\right\}\tilde{\psi}_n\left(\frac{\sigma-x_j}{a}\right) \quad \text{for } \sigma \text{ on } S_j. \quad (2.18.20)$$

The surface pressure p on S_j can be expanded in terms of angular spherical harmonics as follows

$$p(\sigma)=\sum_n p_{jn}\tilde{\psi}_n\left(\frac{\sigma-x_j}{a}\right). \quad (2.18.21)$$

It follows from equations (2.18.20) and (2.18.21) and the orthogonality of the angular spherical harmonics that

$$p_{jn}=a_{jn}\hat{\psi}_n(a)+\text{Real}\hat{\psi}_n(a)\sum_{\substack{k=1 \\ k\neq j}}^M\sum_m a_{km}S_{mn}(x_j-x_k). \quad (2.18.22)$$

This equation can be written in the matrix form

$$\mathbf{p} = \mathbf{H}\mathbf{a} \quad (2.18.23)$$

where \mathbf{p} is a vector of the coefficients p_{jn} and \mathbf{a} is a vector of the coefficients a_{jn} . If the element velocities were not given, it would be necessary to use the transducer element equations to obtain an additional relation involving \mathbf{p} and \mathbf{v} . This additional relation could then be combined with equations (2.18.23) and (2.18.19) to obtain a system of equations to be solved for the coefficients a_{jn} .

2.19 Velocity Control of Arrays

In the early 1960's a large closely-packed planar array of longitudinal vibrators was installed in the bow of a research submarine (the BAYA) as part of the LORAD program. Each element had its own amplifier so that the array could be steered both horizontally and vertically. When the array was first operated, a large number of the amplifiers failed due to overheating. In the design of this array it had been assumed that the velocities of the array elements would track the input drive voltages to the elements. A computer model of the array constructed after the array failure showed that this was not the case. In fact, near resonance, the velocity distribution across the array was so erratic that many of the elements were taking in power instead of radiating it. The erratic velocity distribution was a result of the strong acoustic coupling between array elements and to the sensitivity of the transducers near resonance. In this section we will briefly describe the cure that was implemented for this array. A more complete description can be found in the paper [Carson, D.L., *Diagnosis and Cure of Erratic Velocity Distributions in Sonar Projector Arrays*, J. Acoust. Soc. Am., **34**(9), pp. 1191–1196, September 1962].

For simplicity, we will consider an array of piston radiators in which the motion of each radiating face can be described by a single normal velocity and the acoustic loading on each radiating face can be represented by a single force. The radiation forces are related to the normal velocities by mutual radiation impedances, i.e.,

$$F_m = \sum_{n=1}^N z_{mn} V_n. \quad (2.19.1)$$

We will assume that the transducer elements are all identical and that each element can be described by the pair of equations

$$E_m = \alpha F_m + \beta V_m \quad (2.19.2)$$

$$I_m = \gamma F_m + \delta V_m, \quad (2.19.3)$$

where E_m is the drive voltage for the m -th element, I_m is the drive current for the m -th element, F_m is the acoustic force on the m -th element, and V_m is the normal velocity of the radiating piston surface of the m -th element. Let us assume that the drive voltage is the quantity under our control. Combining equations (2.19.1) and (2.19.2), we obtain

$$E_m = \alpha \sum_{n=1}^N z_{mn} V_n + \beta V_m \quad (2.19.4)$$

$$= (\alpha z_{mm} + \beta) V_m + \alpha \sum_{n \neq m} z_{mn} V_n \quad (2.19.5)$$

$$= \alpha [(z_{mm} + \beta/\alpha) V_m + \sum_{n \neq m} z_{mn} V_n]. \quad (2.19.6)$$

The quantity β/α will be denoted by Z_{sc} since it represents the mechanical impedance looking back into the element when the electrical terminals are shorted. Thus, equation (2.19.6) can be written

$$E_m = \alpha [(z_{mm} + Z_{sc}) V_m + \sum_{n \neq m} z_{mn} V_n]. \quad (2.19.7)$$

Equation (2.19.7) represents a system of N simultaneous linear equations that could be solved for the velocities. If the magnitude of Z_{sc} is large compared to the magnitudes of the mutual impedances, then the velocity V_m will be approximately proportional to the input voltage E_m . Unfortunately, Z_{sc} is usually small near the transducer resonance. Suppose a series tuner Z_T is added as shown in Figure 2.20. The equations for the tuned transducer

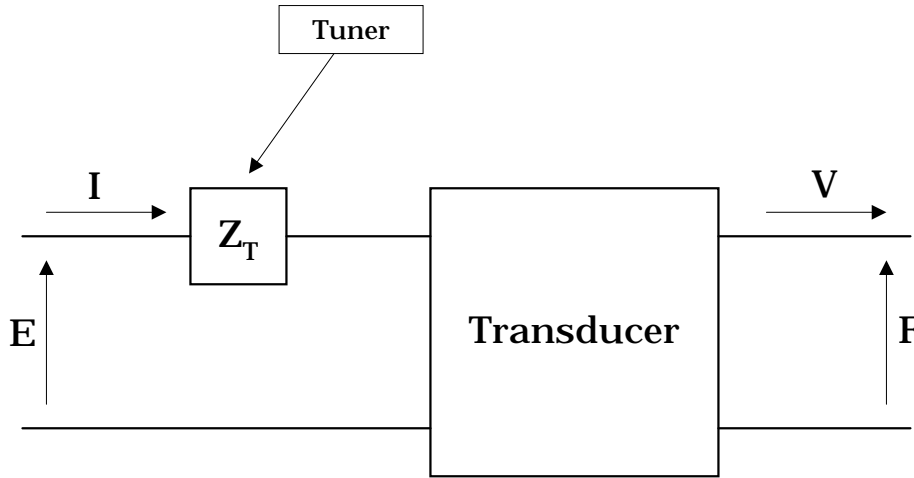


Figure 2.20. Transducer with series tuner

have the same form as those for the untuned transducer if α is replaced by $\alpha + \gamma Z_T$ and β

is replaced by $\beta + \delta Z_T$. In particular

$$Z_{sc} = \frac{\beta + \delta Z_T}{\alpha + \gamma Z_T}. \quad (2.19.8)$$

The tuner is chosen so as to maximize the magnitude of Z_{sc} at some frequency in the band of interest. If there are no losses, then the magnitude of Z_{sc} can be made infinite at one frequency. The short circuit impedance will remain large over some frequency band. In this band we will have velocity control. This velocity control scheme is not affected by a parallel tuning element, so a parallel tuner can be used for further impedance matching. It turns out that a series inductor can be used to tune a piezoelectric device for maximum Z_{sc} and a series capacitor can be used for a magnetic device. Similar results can be obtained for a current drive with a parallel tuner. This approach for velocity control was successful for the LORAD array. A similar problem arose recently in connection with a segmented flexural shell transducer. In this case the segments of a single transducer interacted with each other to produce an anomalous response. The solution of this problem was similar to that used in the LORAD array and is described in the paper [Benthien, G., Gillette, D., and Barach, D., *Control of segment interactions in flexural shell transducers*, presented at the Third Joint Meeting of the Acoustical Society of America and the Acoustical Society of Japan, Honolulu, December 1996]. It can be seen from equation (2.19.7) that it is the sum $Z_{sc} + z_{mm}$ of the short circuit mechanical impedance Z_{sc} and the self radiation impedance z_{mm} that is important in obtaining velocity control by this method. If the array spacing is large or the element radiating faces are sufficiently large in wavelengths, then the magnitude of the self radiation impedance will dominate the magnitude of the mutual radiation impedances and there will be no need to make Z_{sc} large for velocity control. On the other hand, it is possible in some cases for the reactive parts of Z_{sc} and z_{mm} to cancel; thus making the velocity control problem worse.

2.20 Use of Virtual Resistors in Arrays

With multimode transducers (e.g. flexural shell transducers) it is not clear how to generalize the tuning approach to velocity control described previously. In some cases the inclusion of a virtual resistor has been effective in reducing the erratic behavior due to acoustic interactions. A virtual resistor has the damping effect of a real resistor, but does not have the power loss. A feedback loop in the amplifier in effect produces the voltage and current that would be present if there were a real resistor. Figure 2.21 illustrates one feedback scheme for producing a virtual resistor. The current transformer senses the current I and produces a voltage E_1 proportional to this current, i.e.,

$$E_1 = \sigma I. \quad (2.20.1)$$

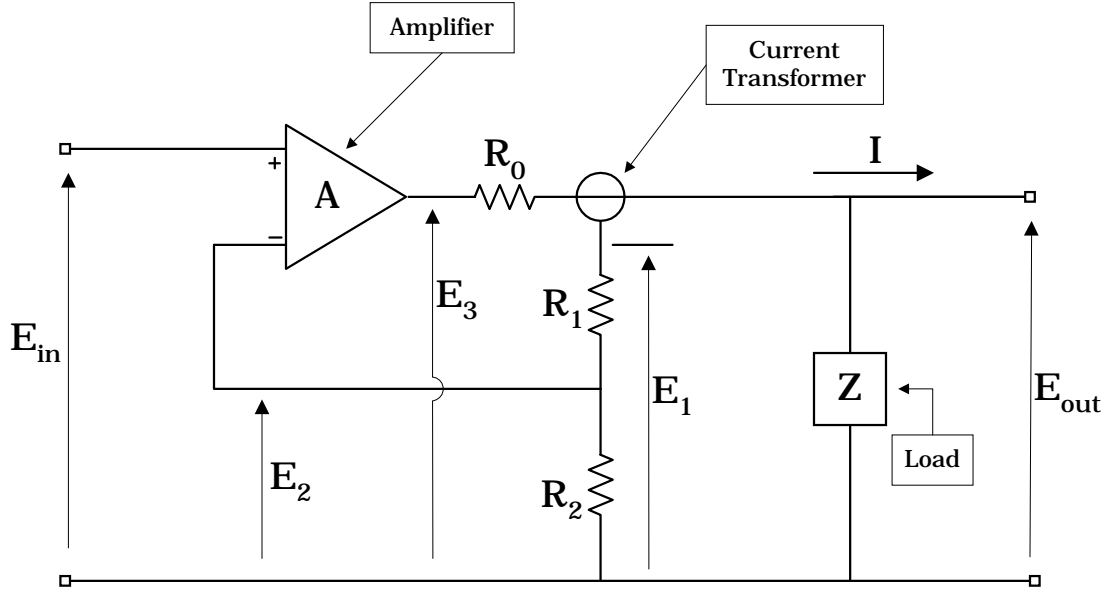


Figure 2.21. Feedback circuit for virtual resistor

The resistors R_1 and R_2 act like a voltage divider, i.e.,

$$E_2 = \frac{R_2 E_1}{R_1 + R_2}. \quad (2.20.2)$$

In this equation we have assumed that there is negligible current in the feedback path. The amplifier has a gain A , i.e.,

$$E_3 = A(E_{in} - E_2). \quad (2.20.3)$$

In addition

$$E_3 = I(R_0 + Z). \quad (2.20.4)$$

and

$$E_{out} = IZ. \quad (2.20.5)$$

Combining equations (2.20.1)–(2.20.5), we obtain

$$\frac{E_{out}}{E_{in}} = \frac{AZ}{R_0 + Z + \sigma R_2 A / (R_1 + R_2)}. \quad (2.20.6)$$

Consider now the simple circuit shown in Figure 2.22. In this circuit we have

$$\frac{E_{out}}{E_{in}} = \frac{AZ}{R_0 + Z + R_s}. \quad (2.20.7)$$

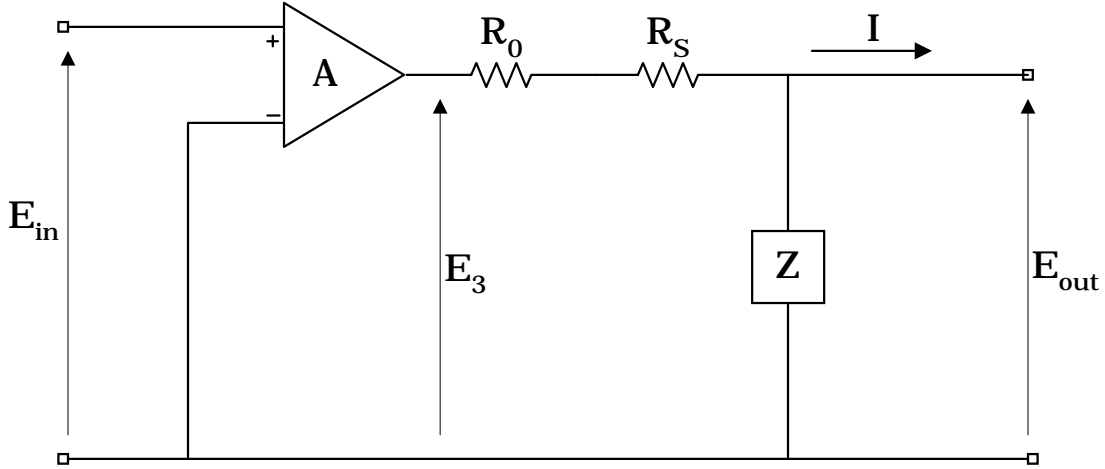


Figure 2.22. Simple amplifier circuit

Comparing equations (2.20.6) and (2.20.7), we see that the simple circuit of figure 2.22 behaves like the feedback circuit of figure 2.21 if we set

$$R_s = \frac{\sigma A R_2}{R_1 + R_2}. \quad (2.20.8)$$

R_s is the desired virtual resistor.

2.21 Acoustic Radiation Modes

Several authors have investigated the concept of acoustic radiation modes which are a complete set of velocity distributions on a radiating surface that radiate power independently. The two papers [Borgiotti, G., *The power radiated by a body in an acoustic fluid and its determination from boundary measurements*, J. Acoust. Soc. Am., **88**(4), pp. 1884–1893 (1990)] and [Photiadis, D., *The relationship of singular value decomposition to wave-vector filtering in sound radiation problems*, J. Acoust. Soc. Am., **88**(2), pp. 1152–1159 (1990)] develop these modes by using a singular value decomposition of the operator relating the surface normal velocity to the far-field pressure. The paper [Sarkissian, A., *Acoustic radiation from finite structures*, J. Acoust. Soc. Am., **90**(1), pp. 574–578 (1991)] develops these modes using an eigenvalue decomposition of the real part of the surface impedance operator. We will use this later approach in our presentation. Typically, the eigenvalues decrease rapidly for large values of the index. Thus, only a few of the modes radiate well to the far-field. The high order weakly radiating modes are called evanescent modes. We will first consider the case of a sphere vibrating axisymmetrically. This problem can be solved

using analytic solutions. Following this we will consider general radiating bodies using the CHIEF numerical formulation.

2.21.1 Axisymmetric sphere problem

Consider a sphere of radius a that is vibrating axisymmetrically. We have seen previously that the pressure exterior to the sphere can be expressed in the form

$$p(r, \theta) = \sum_{n=0}^{\infty} \alpha_n h_n^{(2)}(kr) P_n(\cos \theta) \quad (2.21.1.1)$$

where $h_n^{(2)}(kr)$ is a spherical Hankel function of the second kind and $P_n(\cos \theta)$ is a Legendre polynomial in $\cos \theta$. The Legendre polynomials satisfy the orthogonality relation

$$\int_0^\pi P_m(\cos \theta) P_n(\cos \theta) \sin \theta d\theta = \frac{2}{2n+1} \delta_{mn}. \quad (2.21.1.2)$$

If we define

$$e_n(\theta) = \sqrt{\frac{2n+1}{2}} \sqrt{\frac{1}{2\pi a^2}} P_n(\cos \theta), \quad (2.21.1.3)$$

then the functions e_n satisfy the orthogonality relation

$$\int_S e_m e_n dS = \delta_{mn} \quad (2.21.1.4)$$

where S is the surface of the sphere of radius a . In view of equation (2.21.1.1), the pressure can be expanded in terms of the functions e_n as follows

$$p(r, \theta) = \sum_{n=0}^{\infty} \beta_n h_n^{(2)}(kr) e_n(\theta) \quad (2.21.1.5)$$

where

$$\beta_n = \sqrt{2\pi a^2} \sqrt{\frac{2}{2n+1}} \alpha_n. \quad (2.21.1.6)$$

It follows from the equation of motion that

$$\frac{\partial p}{\partial r}(a, \theta) = k \sum_{n=0}^{\infty} \beta_n h_n^{(2)'}(ka) e_n(\theta) \quad (2.21.1.7)$$

$$= -i\omega \rho v(\theta) \quad (2.21.1.8)$$

where $v(\theta)$ is the normal velocity on the surface S . Solving equations (2.21.1.7)–(2.21.1.8) for $v(\theta)$, we get

$$v(\theta) = \frac{i}{\rho c} \sum_{n=0}^{\infty} \beta_n h_n^{(2)'}(ka) e_n(\theta) \quad (2.21.1.9)$$

$$= \sum_{n=0}^{\infty} v_n e_n(\theta). \quad (2.21.1.10)$$

Due to the orthonormality of the functions e_n , it follows from equations (2.21.1.9)–(2.21.1.10) that

$$v_n = \frac{i}{\rho c} \beta_n h_n^{(2)'}(ka) = \int_S v(\theta) e_n(\theta) dS. \quad (2.21.1.11)$$

Solving equation (2.21.1.11) for β_n , we get

$$\beta_n = \frac{-i\rho c v_n}{h_n^{(2)'}(ka)}. \quad (2.21.1.12)$$

Combining equations (2.21.1.5) and (2.21.1.12), we get

$$p(a, \theta') = -i\rho c \sum_{n=0}^{\infty} v_n \frac{h_n^{(2)}(ka)}{h_n^{(2)'}(ka)} e_n(\theta'). \quad (2.21.1.13)$$

Combining equations (2.21.1.11) and (2.21.1.13), we get

$$p(a, \theta') = \int_S v(\theta) \sum_{n=0}^{\infty} (-i\rho c) \frac{h_n^{(2)}(ka)}{h_n^{(2)'}(ka)} e_n(\theta) e_n(\theta') dS(\theta) \quad (2.21.1.14)$$

$$= \int_S z(\theta, \theta') v(\theta) dS(\theta) \quad (2.21.1.15)$$

where the kernel $z(\theta, \theta')$ is defined by

$$z(\theta, \theta') = -i\rho c \sum_{n=0}^{\infty} \frac{h_n^{(2)}(ka)}{h_n^{(2)'}(ka)} e_n(\theta) e_n(\theta'). \quad (2.21.1.16)$$

If we define

$$z_n = -i\rho c \frac{h_n^{(2)}(ka)}{h_n^{(2)'}(ka)} = r_n + ix_n, \quad (2.21.1.17)$$

then $z(\theta, \theta')$ can be written

$$z(\theta, \theta') = \sum_{n=0}^{\infty} z_n e_n(\theta) e_n(\theta') = r(\theta, \theta') + ix(\theta, \theta'). \quad (2.21.1.18)$$

Clearly

$$r(\theta, \theta') = \sum_{n=0}^{\infty} r_n e_n(\theta) e_n(\theta'). \quad (2.21.1.19)$$

It follows from equation (2.21.1.19) and the orthogonality of the functions e_n that

$$\int_S r(\theta, \theta') e_n(\theta') dS(\theta') = r_n e_n(\theta). \quad (2.21.1.20)$$

Thus, the function e_n is an eigenfunction of the operator r with eigenvalue r_n . The functions e_n are referred to as radiation modes.

The pressure $p_n(\theta)$ due to a velocity distribution $e_n(\theta')$ is given by

$$p_n(\theta) = \int_S z(\theta, \theta') e_n(\theta') dS(\theta') \quad (2.21.1.21)$$

$$= \int_S r(\theta, \theta') e_n(\theta') dS(\theta') + i \int_S x(\theta, \theta') e_n(\theta') dS(\theta') \quad (2.21.1.22)$$

$$= r_n e_n(\theta) + i \int_S x(\theta, \theta') e_n(\theta') dS(\theta'). \quad (2.21.1.23)$$

The average power \mathcal{P}_n radiated by a velocity distribution e_n is given by

$$\mathcal{P}_n = \text{Real} \int_S e_n p_n dS \quad (2.21.1.24)$$

$$= \text{Real} \left[\int_S r_n e_n^2(\theta) dS(\theta) + i \int_S e_n(\theta) dS(\theta) \int_S x(\theta, \theta') e_n(\theta') dS(\theta') \right] \quad (2.21.1.25)$$

$$= r_n \int_S e_n^2(\theta) dS(\theta) = r_n. \quad (2.21.1.26)$$

Thus, the eigenvalue r_n is the power radiated by the mode e_n . Since the kernels r and x are symmetric in their arguments θ and θ' , it follows that the integrals

$$\int_S v^*(\theta) dS(\theta) \int_S r(\theta, \theta') v(\theta') dS(\theta')$$

and

$$\int_S v^*(\theta) dS(\theta) \int_S x(\theta, \theta') v(\theta') dS(\theta')$$

are real. Thus, the average power \mathcal{P} radiated by a velocity distribution v is given by

$$\mathcal{P} = \text{Real} \left[\int_S v^* p dS \right] \quad (2.21.1.27)$$

$$= \text{Real} \left[\int_S v^*(\theta) dS(\theta) \int_S z(\theta, \theta') v(\theta') dS(\theta') \right] \quad (2.21.1.28)$$

$$= \int_S v^*(\theta) dS(\theta) \int_S r(\theta, \theta') v(\theta') dS(\theta'). \quad (2.21.1.29)$$

In view of equations (2.21.1.10) and (2.21.1.20), we have

$$\int_S r(\theta, \theta') v(\theta') dS(\theta') = \sum_{n=0}^{\infty} v_n r_n e_n(\theta). \quad (2.21.1.30)$$

Combining equation (2.21.1.29) with equation (2.21.1.30) and using equation (2.21.1.11), we obtain

$$\mathcal{P} = \sum_{n=0}^{\infty} v_n r_n \int_S v^*(\theta) e_n(\theta) dS(\theta) \quad (2.21.1.31)$$

$$= \sum_{n=0}^{\infty} r_n |v_n|^2. \quad (2.21.1.32)$$

Thus, the modes radiate power independently. In the next section we will generalize these power results for the sphere to more general bodies.

2.21.2 General problem

Consider now a general body with radiating surface S . If we discretize S and use the CHIEF method, we obtain the surface radiation impedance relation

$$F = ZV \quad (2.21.2.1)$$

where F is a column vector whose n -th component is the pressure on the n -th subdivision times the area of the n -th subdivision, V is a column vector whose n -th component is the normal velocity of the n -th subdivision, and Z is a symmetric $N \times N$ complex matrix whose real and imaginary parts are the symmetric matrices R and X . Let E be a real matrix whose columns are the eigenvectors of R , i.e.,

$$RE = E\Lambda \quad , \quad \Lambda = \text{diag}(\lambda_1, \dots, \lambda_N). \quad (2.21.2.2)$$

The values $\lambda_1, \dots, \lambda_N$ are the eigenvalues of R . If E_n is the n -th column of E , then the force vector F_n corresponding to the velocity distribution E_n is given by

$$F_n = ZE_n. \quad (2.21.2.3)$$

The average power \mathcal{P}_n corresponding to the velocity distribution E_n is given by

$$\mathcal{P}_n = \text{Real}(E_n^T F_n) = \text{Real}(E_n^T ZE_n) \quad (2.21.2.4)$$

$$= \text{Real}(E_n^T RE_n + iE_n^T XE_n) \quad (2.21.2.5)$$

$$= E_n^T RE_n = \lambda_n E_n^T E_n = \lambda_n. \quad (2.21.2.6)$$

The velocity V can be expanded in terms of the eigenmodes of R as follows

$$V = E\hat{V} \quad (2.21.2.7)$$

where the components of \hat{V} are the coefficients in this expansion. The average power \mathcal{P} can now be expressed as

$$\mathcal{P} = \text{Real}(V^\dagger Z V) \quad (2.21.2.8)$$

$$= V^\dagger R V = \hat{V}^\dagger E^T R E \hat{V} \quad (2.21.2.9)$$

$$= \hat{V}^\dagger \Lambda \hat{V} = \sum_{n=0}^N \lambda_n |\hat{V}_n|^2. \quad (2.21.2.10)$$

Thus, the modes E_n radiate power independently. As before, we will refer to the column vectors E_n as radiation modes.

We will now show some calculated axisymmetric radiation modes for a circular cylinder with a length-to-diameter ratio of 2 and scaled frequency (kL) values of 0.1, 0.5, 1.0, 2.0, and 5.0. The cylinder was divided into 20 subdivisions that were numbered as shown in figure 2.23. Figure 2.24 shows the logarithm of the eigenvalues of the radiation resistance matrix plotted versus mode index number. The eigenvalues were sorted from largest to smallest. Notice that the eigenvalues decrease very rapidly after a certain point and then level off at a noise floor. Recall that the eigenvalues relate to the radiation efficiency of the modes. As frequency increases there are more modes that have a significant radiation efficiency (eigenvalue). Figures 2.25–2.28 show the first four eigenmodes corresponding to the various frequencies. Notice that the eigenmodes do not change very much with frequency.

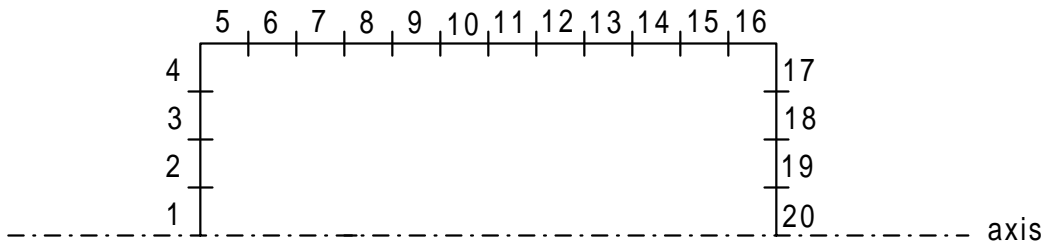


Figure 2.23. Subdivision numbering for cylinder modeled using CHIEF

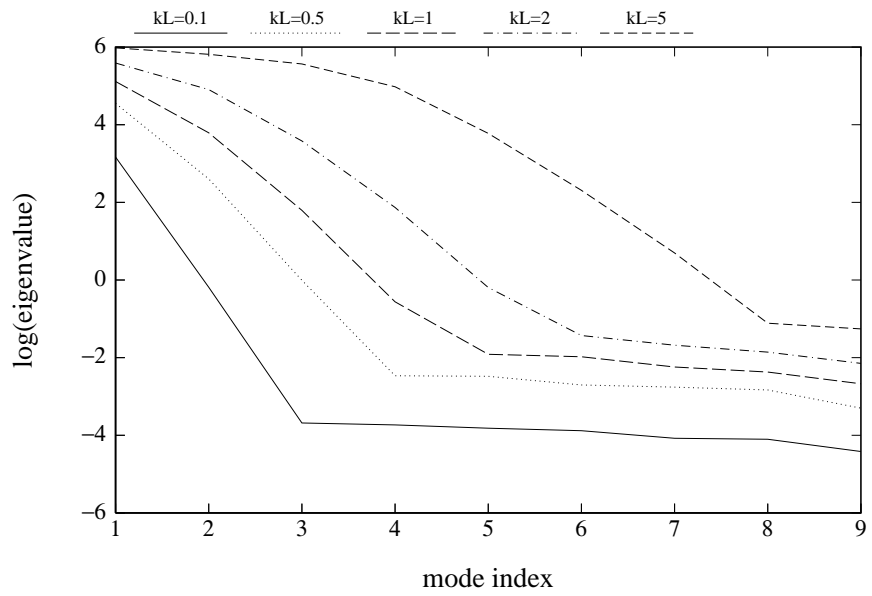


Figure 2.24. Eigenvalues of the radiation resistance matrix

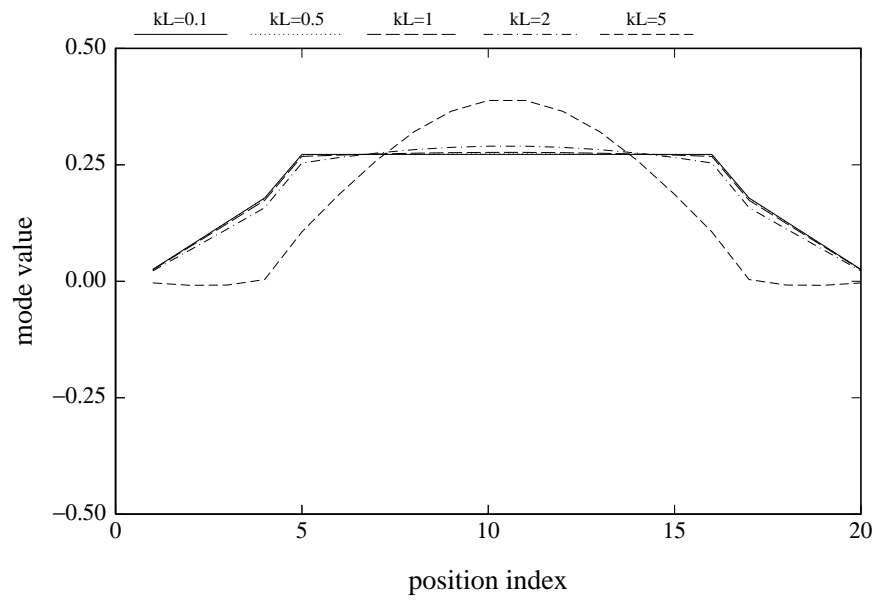


Figure 2.25. First eigenmode of the radiation resistance matrix at various frequencies

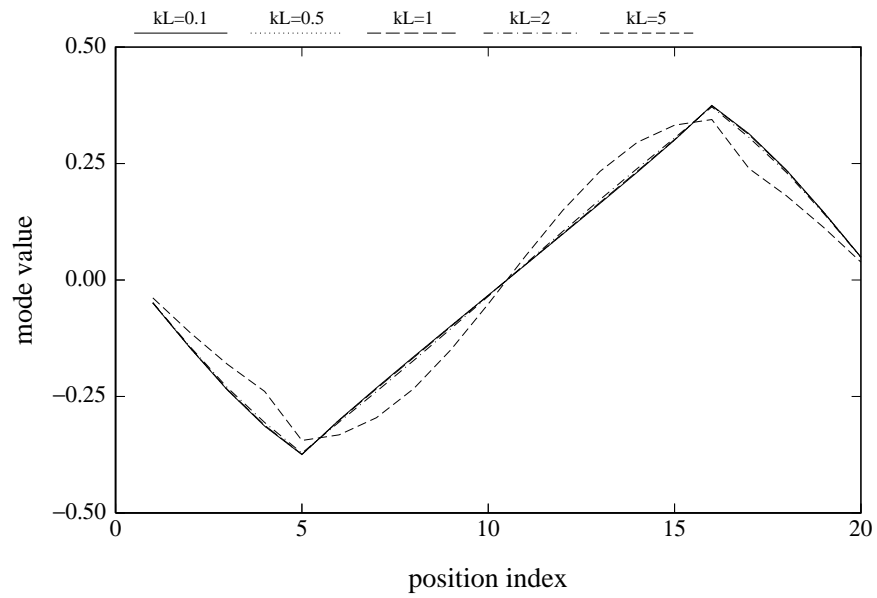


Figure 2.26. Second eigenmode of the radiation resistance matrix at various frequencies

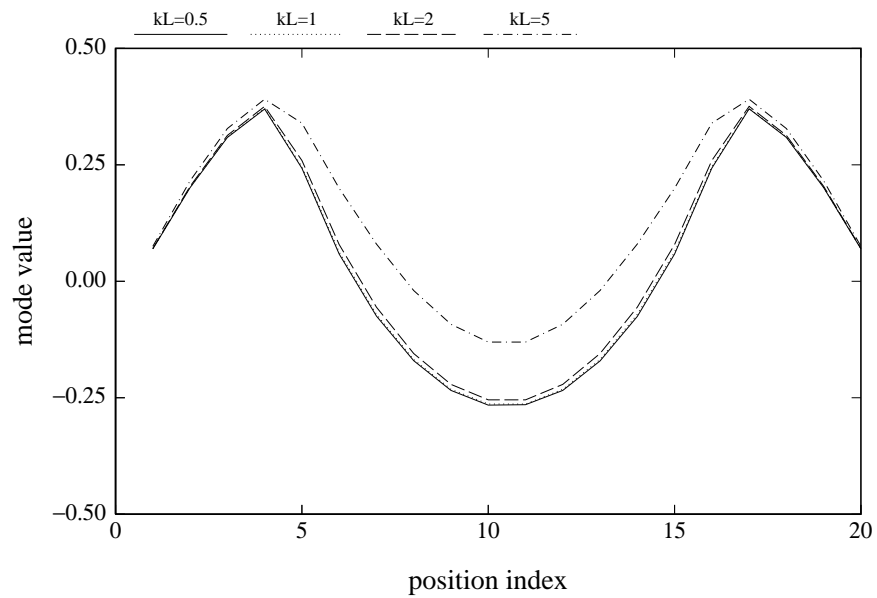


Figure 2.27. Third eigenmode of the radiation resistance matrix at various frequencies

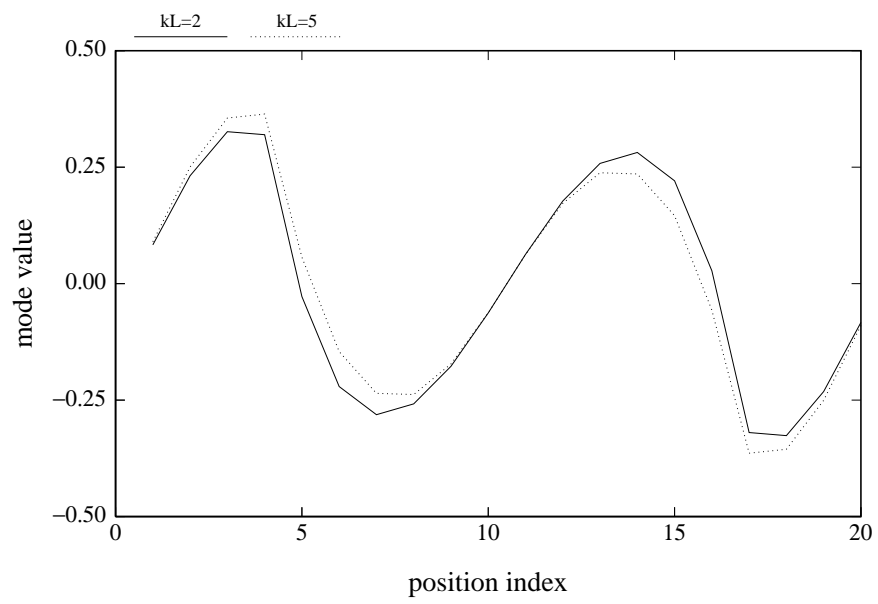


Figure 2.28. Fourth eigenmode of the radiation resistance matrix at various frequencies

Chapter 3

Structural Modeling

This chapter covers the modeling of the structural components of a transducer. This includes the modeling of active components such as piezoelectric or magnetostrictive materials as well as the modeling of purely elastic components. Two classes of models will be discussed. The first class consists of variational based models. The most important representative of this class is the finite element method. The finite element methodology was first developed for elastic structures such as airplane wings and building frames, but it is now recognized that it can be applied to all types of physical problems. Variational methods can also be used to develop simple “lumped parameter” models of transducer components. The second class consists of one-dimensional wave type models. These models are sometimes referred to as “plane wave” models. In many cases these models result in simple analytic expressions for the electrical and mechanical behavior of the components being modeled. Elaborate computer programs have been developed for the interconnection of one-dimensional wave models for various transducer components. One of the earliest of these programs was given the acronym SEADUCER and is described in the reference[Ding, H.H., McCleary, L.E., and Ward, J.A., *Computerized Sonar Transducer Analysis and Design Based on Multiport Network Interconnection Techniques*, NUC Technical Paper 228, April 1973]. It is also possible to intermix one-dimensional wave models of some components with finite element models of other components in the modeling of a transducer.

3.1 Variational Methods

Variational methods form the basis of many of the numerical methods and approximation schemes used in transducer design and analysis. For example, the finite element method used in structural analysis is based on a variational method. The purpose here is not to give an exhaustive treatment of variational methods, but to present enough of the basics so that

the user will understand what is being computed in the variational based numerical methods and will be able to develop simple approximations based on variational principles.

The first topic covered is the conversion between a differential equation formulation of a physical problem and a variational formulation. This is illustrated for a simple boundary-value problem of potential theory. Two basic approaches to variational type problems will be discussed, both of which lead to the same result. The first approach involves constructing a functional defined on a certain class of functions that is stationary at the solution we are seeking, i.e., the first variation of the functional is zero when evaluated at the solution. For the simple potential problem being considered the functional is actually minimized by the solution, but in most problems we can only say that the functional is stationary at the solution. The classical Rayleigh-Ritz method is based on this direct variational approach. The second approach can be thought of as a projection method and is sometimes called the method of weighted residuals. The Galerkin method is an example of this approach. An analogy from ordinary geometry might help to illustrate the two approaches. Consider the problem of finding the point on a plane that is closest to a fixed point not lying on the plane. One approach to solving this problem would be to form the expression for the distance between the fixed point and a general point on the plane, and then to minimize this function using differential calculus. A second approach would be to find the projection of the fixed point onto the plane. Both approaches lead to the same solution.

The second subsection covers some numerical procedures based on variational formulations. In particular finite element type approximations will be discussed. The simple potential problem described in the previous section will be used as an illustration. The third subsection describes the extension of the previous results to steady state dynamic problems. A simple problem from acoustics will be used as an illustration. In later sections these same procedures are used to derive the basic finite element equations for elastic structures, piezoelectric devices, and magnetostrictive devices. The final subsection covers the application of variational methods to the development of simplified models. Simple equivalent circuits as well as simple formulas for resonance frequencies can be obtained from variational principles. A number of examples will be given. I hope to show that variational principles are an excellent starting point for the development of simplified models.

3.1.1 Example Problem

In order to gain some insight into the variational approach we will begin with a simple one-dimensional problem from elastostatics. The problem is to calculate the field inside a spherical capacitor as shown in figure 3.1. It will be assumed that the charge is specified on the outer electrode and that the potential is specified on the inner electrode. It will also be assumed that the electrodes have negligible thickness.

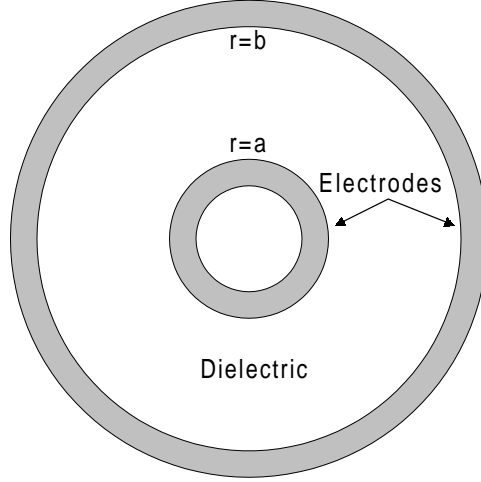


Figure 3.1. A spherical capacitor

The electric field \vec{E} , the electric displacement \vec{D} , and the potential ϕ satisfy the following equations of elastostatics:

$$\mathbf{div} \vec{D} = \rho_e \quad (3.1.1.1)$$

$$\vec{D} = \epsilon \vec{E} \quad (3.1.1.2)$$

$$\vec{E} = -\nabla \phi. \quad (3.1.1.3)$$

Here ρ_e is the free charge density. In our problem ρ_e is zero except on the electrodes. Let S be the outer surface of the dielectric ($r = b$), and let S^+ be a spherical surface inside the outer electrode containing all the charge in its interior. Integrating equation (3.1.1.1) over the region between S and S^+ and using the divergence theorem gives

$$\int_S \vec{D} \cdot \vec{n} + \int_{S^+} \vec{D} \cdot \vec{n} = Q \quad (3.1.1.4)$$

where Q is the total charge on the outer electrode. We assume that the electrodes are perfect conductors so that both \vec{E} and \vec{D} are zero inside the electrodes. Therefore, the second integral in equation (3.1.1.4) vanishes and we have

$$\int_S \vec{D} \cdot \vec{n} = Q. \quad (3.1.1.5)$$

By symmetry, $\vec{D} \cdot \vec{n}$ is constant over S . Thus, equation (3.1.1.5) can be written

$$4\pi b^2 D_r(b) = Q. \quad (3.1.1.6)$$

In view of equations (3.1.1.2)–(3.1.1.3), we can write equation (3.1.1.6) as

$$-4\pi b^2 \epsilon \frac{d\phi}{dr}(b) = Q \quad (3.1.1.7)$$

or

$$b^2 \frac{d\phi}{dr}(b) = \gamma \quad (3.1.1.8)$$

where

$$\gamma = -\frac{Q}{4\pi\epsilon}. \quad (3.1.1.9)$$

On the inner surface ($r = a$), the potential ϕ is constant and has the specified value ζ , i.e.,

$$\phi(a) = \zeta. \quad (3.1.1.10)$$

In the dielectric region ϕ satisfies Laplace's equation. In spherical coordinates Laplace's equation can be written

$$\frac{1}{r^2} \frac{d}{dr} \left(r^2 \frac{d\phi}{dr} \right) = 0 \quad a < r < b. \quad (3.1.1.11)$$

The problem consists of solving the differential equation (3.1.1.11) for ϕ subject to the boundary conditions (3.1.1.8) and (3.1.1.10).

This problem can be solved analytically. The solution has the form

$$\phi(r) = \alpha + \beta \frac{1}{r}. \quad (3.1.1.12)$$

The constants are obtained by applying the boundary conditions in equations (3.1.1.8) and (3.1.1.10). The result is

$$\phi(r) = \zeta + \gamma \left(\frac{1}{a} - \frac{1}{r} \right). \quad (3.1.1.13)$$

Later, when we develop numerical approximations based on variational principles, we will compare the results obtained using those approximations with those obtained using this analytical solution.

In order to formulate a variational principle that is equivalent to the boundary-value problem defined by equations (3.1.1.8)–(3.1.1.11) we define a functional F by

$$F(\psi) = \frac{1}{2} \int_a^b r^2 \left(\frac{d\psi}{dr} \right)^2 dr - \gamma \psi(b) \quad (3.1.1.14)$$

where ψ is any smooth function on the interval (a, b) that satisfies the inner boundary condition $\psi(a) = \zeta$. A functional is like an ordinary function except its argument is a function instead of a number. We will show that of all functions satisfying the potential boundary condition at $r = a$, the solution ϕ of the boundary-value problem (3.1.1.8)–(3.1.1.11) minimizes the functional F . Suppose h is a smooth function satisfying the homogeneous boundary condition $h(a) = 0$. Then

$$F(\phi + h) = F(\phi) + \int_a^b r^2 \frac{d\phi}{dr} \frac{dh}{dr} dr + \frac{1}{2} \int_a^b r^2 \left(\frac{dh}{dr} \right)^2 dr - \gamma h(b). \quad (3.1.1.15)$$

Integrating by parts, we have

$$\int_a^b r^2 \frac{d\phi}{dr} \frac{dh}{dr} dr = b^2 \frac{d\phi}{dr}(b) h(b) - \int_a^b h \frac{1}{r^2} \frac{d}{dr} \left(r^2 \frac{d\phi}{dr} \right) r^2 dr. \quad (3.1.1.16)$$

Since ϕ satisfies Laplace's equation, the preceding equation becomes

$$\int_a^b r^2 \frac{d\phi}{dr} \frac{dh}{dr} dr = b^2 \frac{d\phi}{dr}(b) h(b). \quad (3.1.1.17)$$

Substituting equation (3.1.1.17) into equation (3.1.1.15), we obtain

$$F(\phi + h) = F(\phi) + h(b) \left[b^2 \frac{d\phi}{dr}(b) - \gamma \right] + \frac{1}{2} \int_a^b r^2 \left(\frac{dh}{dr} \right)^2 dr. \quad (3.1.1.18)$$

Since ϕ satisfies the boundary condition (3.1.1.8), this relation becomes

$$F(\phi + h) = F(\phi) + \frac{1}{2} \int_a^b r^2 \left(\frac{dh}{dr} \right)^2 dr \geq F(\phi). \quad (3.1.1.19)$$

Since any function ψ satisfying $\psi(a) = \zeta$ can be written as $\psi = \phi + h$ with $h(a) = 0$, it follows from equation (3.1.1.19) that ϕ minimizes the functional F over all such functions ψ .

We now define the variation $\delta_h F$ of F by

$$\delta_h F(\psi) = \lim_{\lambda \rightarrow 0} \frac{F(\psi + \lambda h) - F(\psi)}{\lambda}. \quad (3.1.1.20)$$

The variation of a functional is analogous to a directional derivative of an ordinary function. It follows from equation (3.1.1.14) that the variation of F is given by

$$\delta_h F(\psi) = \int_a^b r^2 \frac{d\psi}{dr} \frac{dh}{dr} dr - \gamma h(b). \quad (3.1.1.21)$$

Combining equations (3.1.1.16) and (3.1.1.21), we get

$$\delta_h F(\psi) = h(b) \left[b^2 \frac{d\psi}{dr}(b) - \gamma \right] - \int_a^b h \frac{1}{r^2} \frac{d}{dr} \left(r^2 \frac{d\psi}{dr} \right) r^2 dr. \quad (3.1.1.22)$$

If ϕ is the solution of the boundary-value problem given by equations (3.1.1.8)–(3.1.1.11), then it follows that

$$\delta_h F(\phi) = 0 \quad (3.1.1.23)$$

for all h satisfying $h(a) = 0$. This condition is analogous to the derivative of a smooth function being zero at a minimum.

Conversely, suppose $\delta_h F(\phi) = 0$ for all h satisfying $h(a) = 0$. Then, it follows from equation (3.1.1.22) that

$$h(b) \left[b^2 \frac{d\psi}{dr}(b) - \gamma \right] - \int_a^b h \frac{1}{r^2} \frac{d}{dr} \left(r^2 \frac{d\psi}{dr} \right) r^2 dr = 0 \quad (3.1.1.24)$$

for all h such that $h(a) = 0$. It follows from equation (3.1.1.24) that

$$\int_a^b h \frac{1}{r^2} \frac{d}{dr} \left(r^2 \frac{d\psi}{dr} \right) r^2 dr = 0 \quad (3.1.1.25)$$

for all h that satisfy both $h(a) = 0$ and $h(b) = 0$. If we define G by

$$G(r) = \frac{d}{dr} \left(r^2 \frac{d\phi}{dr} \right), \quad (3.1.1.26)$$

then equation (3.1.1.25) can be written

$$\int_a^b h(r) G(r) dr = 0 \quad (3.1.1.27)$$

for all h satisfying $h(a) = h(b) = 0$. We will show that G is identically zero on the interval (a, b) by assuming that it is not true and deriving a contradiction. Assume that G is nonzero for some point \bar{r} in the interval (a, b) . Let us suppose for definiteness that

$$G(\bar{r}) > 0. \quad (3.1.1.28)$$

By continuity, there is some $\delta > 0$ such that

$$G(r) > 0 \quad \text{on the interval } (\bar{r} - \delta, \bar{r} + \delta). \quad (3.1.1.29)$$

Let us define a function \hat{h} by

$$\hat{h} = \begin{cases} e^{-\frac{1}{(r-\bar{r})^2 - \delta^2}}, & \text{for } \bar{r} - \delta < r < \bar{r} + \delta \\ 0, & \text{otherwise.} \end{cases} \quad (3.1.1.30)$$

The function \hat{h} is infinitely differentiable and vanishes at both $r = a$ and $r = b$. It follows from equation (3.1.1.27) that

$$\int_a^b \hat{h}(r) G(r) dr = \int_{\bar{r}-\delta}^{\bar{r}+\delta} \hat{h}(r) G(r) dr = 0. \quad (3.1.1.31)$$

This is a contradiction since \hat{h} and G are strictly positive on the interval $(\bar{r} - \delta, \bar{r} + \delta)$. Therefore, the function G must vanish on the interval (a, b) , i.e.,

$$G(r) = \frac{d}{dr} \left(r^2 \frac{d\phi}{dr} \right) = 0 \quad \text{for } a < r < b. \quad (3.1.1.32)$$

In other words ϕ satisfies Laplace's equation on the interval (a, b) . It follows now from equation (3.1.1.24) that

$$h(b) \left[b^2 \frac{d\psi}{dr}(b) - \gamma \right] = 0 \quad (3.1.1.33)$$

for all h such that $h(a) = 0$. Therefore,

$$b^2 \frac{d\phi}{dr}(b) = \gamma \quad (3.1.1.34)$$

, i.e., ϕ satisfies the boundary condition in equation (3.1.1.8). If, in addition, ϕ satisfies $\phi(a) = \zeta$, then ϕ is a solution of the boundary-value problem given in equations (3.1.1.8)–(3.1.1.11). Notice that the derivative boundary condition in equation (3.1.1.8) follows from the variational equation (3.1.1.23), but that the boundary condition $\phi(a) = \zeta$ must be enforced separately. The derivative boundary condition in equation (3.1.1.8) is called a *natural boundary condition*.

It follows from equation (3.1.1.21) that the condition $\delta_h F(\phi) = 0$ is equivalent to the relation

$$\int_a^b r^2 \frac{d\phi}{dr} \frac{dh}{dr} dr - \gamma h(b) = 0 \quad \text{for all } h \text{ such that } h(a) = 0. \quad (3.1.1.35)$$

We will now show that this relation could have been arrived at by a different procedure. Let h be an arbitrary smooth function such that $h(a) = 0$. Then it follows from Laplace's equation [equation (3.1.1.11)] that

$$\int_a^b h \frac{d}{dr} \left(r^2 \frac{d\phi}{dr} \right) dr = 0 \quad a < r < b. \quad (3.1.1.36)$$

Integrating equation (3.1.1.36) by parts, we get

$$h r^2 \frac{d\phi}{dr} \Big|_a^b - \int_a^b r^2 \frac{d\phi}{dr} \frac{dh}{dr} dr = 0. \quad (3.1.1.37)$$

Combining the boundary conditions $\phi(a) = \zeta$ and $b^2 \frac{d\phi}{dr}(b) = \gamma$ with equation (3.1.1.37), we obtain equation (3.1.1.35). This approach is usually called Galerkin's method. It has the advantage that it is not necessary to construct an appropriate functional for the problem. Equation (3.1.1.35) will be the starting point for the numerical approximations to be discussed in the next section.

3.1.2 Variational Based Numerical Methods

In this section we continue with the simple potential problem described in the previous section as we consider variational based numerical approximations. The starting point will be the

integral relation of equation (3.1.1.35) which we obtained both by a variational argument and by Galerkin's method. This relation states that

$$\int_a^b r^2 \frac{d\phi}{dr} \frac{dh}{dr} dr - \gamma h(b) = 0 \quad \text{for all } h \text{ such that } h(a) = 0. \quad (3.1.2.1)$$

We will consider approximations to ϕ of the form

$$\phi(r) = \phi_a(r) + \sum_{n=1}^N \phi_n \chi_n(r) \quad (3.1.2.2)$$

where $\phi_a(r)$ is a function satisfying $\phi_a(a) = \zeta$ and $\chi_1(r), \dots, \chi_N(r)$ are prescribed functions satisfying $\chi_n(a) = 0$ for all n . One possibility for the function $\phi_a(r)$ is the constant function defined by $\phi_a(r) \equiv \zeta$. The functions χ_n could be powers of $r - a$ or trigonometric functions such as $\sin[n\pi(r - a)/(b - a)]$. The class of methods known as finite element methods are based on piecewise polynomial approximation. Let us consider the simplest approximation of this type, namely piecewise-linear approximation. To construct this approximation we divide the interval (a, b) into a finite number of subdivisions by choosing distinct points $r_0 = a, r_1, \dots, r_N = b$ in the interval. In finite element terminology the points r_n are called *nodes* and the intervals between adjacent nodes are called *elements*. It can be shown that any piecewise linear function on (a, b) can be expressed as a linear combination of piecewise linear functions χ_0, \dots, χ_N having the property

$$\chi_n(r) = \begin{cases} 1 & r = r_n \\ 0 & r = r_m, m \neq n. \end{cases} \quad (3.1.2.3)$$

One such function is shown in figure 3.2. For obvious reasons the functions χ_n are sometimes

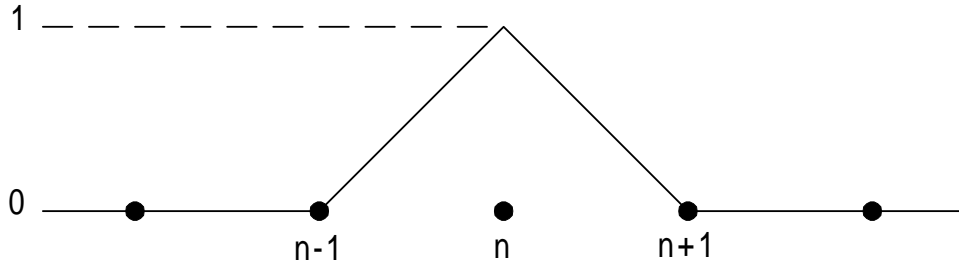


Figure 3.2. Piecewise-linear interpolation function

called *hat functions*. At the ends of the interval only one half of the hat function is used. We approximate ϕ by

$$\phi(r) = \zeta \chi_0(r) + \sum_{n=1}^N \phi_n \chi_n(r) \quad (3.1.2.4)$$

where we have taken $\phi_a = \zeta\chi_0(r)$. Because the hat functions χ_n have the local property of equation (3.1.2.3), it follows that ϕ_n is the value of the approximation to ϕ at r_n .

In addition to approximating ϕ as in equation (3.1.2.2) we also restrict the class of functions h for which equation (3.1.2.1) is required to hold. Corresponding to the piecewise-linear approximation, we require equation (3.1.2.1) to hold for all piecewise-linear functions h such that $h(a) = 0$. Since any piecewise-linear function h satisfying $h(a) = 0$ can be written as a linear combination of χ_1, \dots, χ_N , it is sufficient to require

$$\int_a^b r^2 \frac{d\phi}{dr} \frac{d\chi_m}{dr} dr - \gamma\chi_m(b) = 0 \quad \text{for } m = 1, \dots, N. \quad (3.1.2.5)$$

Substituting equation (3.1.2.2) into equation (3.1.2.5), we get

$$\int_a^b r^2 \left(\frac{d\phi_a}{dr} + \sum_{n=1}^N \phi_n \frac{d\chi_n}{dr} \right) \frac{d\chi_m}{dr} dr - \gamma\chi_m(b) = 0 \quad (3.1.2.6)$$

or

$$\sum_{n=1}^N \phi_n \int_a^b r^2 \frac{d\chi_m}{dr} \frac{d\chi_n}{dr} dr = \gamma\chi_m(b) - \int_a^b r^2 \frac{d\chi_m}{dr} \frac{d\phi_a}{dr} dr \quad m=1, \dots, N. \quad (3.1.2.7)$$

This equation can be written in the matrix form

$$K\Phi = F \quad (3.1.2.8)$$

where Φ is a column vector whose n -th component is ϕ_n , K is a matrix with components

$$K_{mn} = \int_a^b r^2 \frac{d\chi_m}{dr} \frac{d\chi_n}{dr} dr, \quad (3.1.2.9)$$

and F is a column vector whose m -th component is given by

$$F_m = \gamma\chi_m(b) - \int_a^b r^2 \frac{d\chi_m}{dr} \frac{d\phi_a}{dr} dr. \quad (3.1.2.10)$$

In finite element terminology the matrix K is called the *stiffness matrix* and the vector F is called the *load vector*.

Figure 3.3 shows a comparison of the finite element solution with the analytic solution for the case where $a = 1$, $b = 5$, $\zeta = 0$, $\gamma = 1$, and $N = 20$. Notice that the agreement is quite good. The maximum error over the interval is 1.1%. Of course the error gets smaller with more subdivisions.

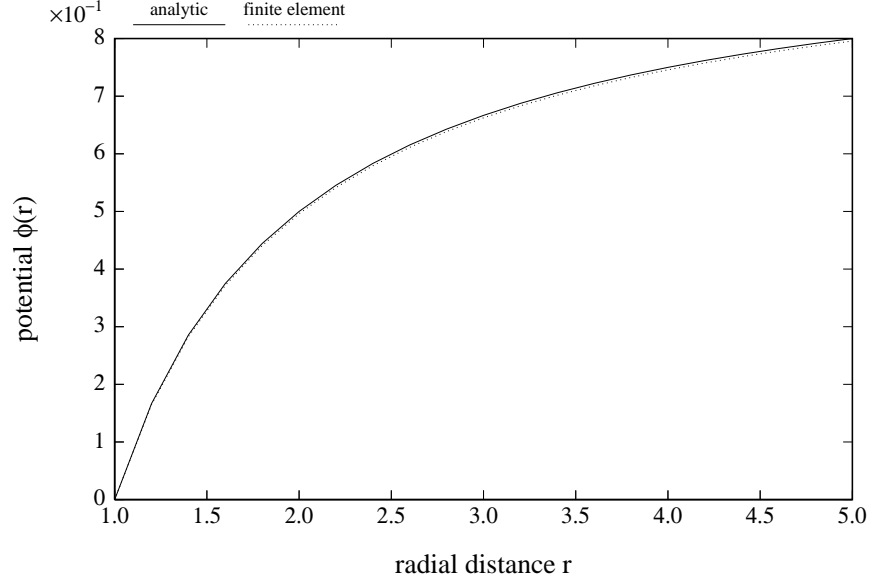


Figure 3.3. Potential distribution in a spherical capacitor with inner radius 1.0 and outer radius 5.0

3.1.3 Example Dynamic Problem

The example problem we have been considering is a static problem. Let us now consider a simple steady-state dynamic problem. Many of the details will be omitted since they are almost identical to those of the potential problem considered previously. Suppose we have the same region between the spherical surfaces $r = a$ and $r = b$ that now contains a fluid such as water. Suppose also that the surface $r = a$ is vibrating sinusoidally at the angular frequency ω with a uniform normal acceleration \dot{v} and that the acoustic pressure p is zero on the inner surface $r = a$. This problem leads to the boundary-value problem

$$\frac{1}{r^2} \frac{d}{dr} \left(r^2 \frac{dp}{dr} \right) + k^2 p = 0 \quad a < r < b \quad (3.1.3.1)$$

$$p(a) = 0 \quad (3.1.3.2)$$

$$\frac{dp}{dr}(b) = -\rho \dot{v} \quad (3.1.3.3)$$

for the acoustic pressure p . Here ρ is the fluid density, $k = \omega/c$ is the acoustic wavenumber, and c is the sound velocity in the fluid. Notice that this boundary-value problem is very similar to the potential boundary-value problem considered previously. The major difference is the addition of the term $k^2 p$ to the Laplacian in equation (3.1.3.1). It can be shown that the solution of this problem is given by

$$p(r) = \frac{1}{r} (\alpha \cos kr + \beta \sin kr) \quad (3.1.3.4)$$

where

$$\alpha = \frac{\rho b^2 \dot{v} \sin ka}{kb \cos k(b-a) - \sin k(b-a)} \quad (3.1.3.5)$$

$$\beta = \frac{-\rho b^2 \dot{v} \cos ka}{kb \cos k(b-a) - \sin k(b-a)}. \quad (3.1.3.6)$$

This problem can be converted to a variational problem in the same manner as for the potential problem considered previously. The appropriate functional for this problem is

$$F(p) = \frac{1}{2} \int_a^b r^2 \left(\frac{dp}{dr} \right)^2 dr - \frac{1}{2} k^2 \int_a^b r^2 p^2 dr + \rho b^2 \dot{v} p(b). \quad (3.1.3.7)$$

This functional is defined on the class of smooth functions p satisfying the inner boundary condition $p(a) = 0$. In this case the functional F is not minimized by the solution of the boundary-value problem, but it can be shown that the variation of F is zero at the solution, i.e.,

$$\delta_h F(p) = 0 \quad \text{for all } h \text{ such that } h(a) = 0. \quad (3.1.3.8)$$

This leads to the integral relation

$$\int_a^b r^2 \frac{dp}{dr} \frac{dh}{dr} dr - k^2 \int_a^b r^2 p h dr + \rho b^2 \dot{v} h(b) = 0$$

for all h such that $h(a) = 0$. (3.1.3.9)

This relation could also have been arrived at by Galerkin's method. As before, applying piecewise linear approximation to this problem leads to the finite element equation

$$(-\omega^2 M + K)P = F \quad (3.1.3.10)$$

where P is a column vector with n -th component p_n , F is a column vector with components

$$F_m = -\rho b^2 \dot{v} \chi_m(b), \quad (3.1.3.11)$$

and M and K are matrices with components

$$M_{mn} = \frac{1}{c^2} \int_a^b r^2 \chi_m \chi_n dr \quad (3.1.3.12)$$

$$K_{mn} = \int_a^b r^2 \frac{d\chi_m}{dr} \frac{d\chi_n}{dr} dr. \quad (3.1.3.13)$$

The functions χ_m are the piecewise linear hat functions described previously. In finite element terminology M is called the *mass matrix*, K is called the *stiffness matrix*, and F is called the *load vector*. It can be shown that the mass matrix M is positive definite, i.e., all its eigenvalues are positive. The matrix K is positive semidefinite, i.e., its eigenvalues are positive or zero.

3.1.4 Nodes vs. elements

So far we have taken a nodal point-of-view in the development of finite element approximations. As the name “finite element method” suggests, the element concept plays an important part in the implementation of these approximations. How are the element view-point and the nodal view-point related? The equation and variable numbering is clearly based on nodes. The computation of the finite element matrices, however, is usually performed on an element basis. Because of the local nature of the interpolation functions (e.g., the “hat” functions) used in finite element methods, the integrand corresponding to the m,n -th matrix component is nonzero only on those elements containing both the m -th and the n -th nodes. Thus, the m,n -th component can be written as a sum of integrals over those elements containing both the m -th and n -th nodes. In the simple one-dimensional scalar problems we have been considering, only the diagonal matrix terms involve more than a one element sum. However, in multidimensional problems, other matrix entries can involve sums of integrals over several elements. The integrals are usually first computed over each element for those nodes contained in the element. In this way an element matrix is constructed. The entries of the element matrix can then be added into appropriate positions in the global matrix to complete the process. This later process is called matrix assembly. Once the finite element matrices are assembled, then the matrix equations can be solved for the unknown nodal variables. Special methods are employed in the solution process since the finite element matrices are very sparse (again due to the local nature of the interpolation functions). One of the most common solution procedures used in finite element programs is the *frontal method*. This method actually combines the solution and assembly procedures. In the common solution procedures (those based on Gaussian elimination), a multiple of one equation is added to other equations so as to zero out the entries below the diagonal in the column corresponding to the equation being used. In this manner the original system of equations is reduced to a triangular system that can be easily solved by back substitution. In the frontal method the element matrices corresponding to different elements are sequentially brought into memory and the appropriate entries of the global matrix formed. At each stage some of the global matrix elements will be complete and others will be only partially complete. As soon as all the entries corresponding to some node are complete, multiples of the equation corresponding to this node are added to equations corresponding to nodes contained in other elements in memory as in the normal solution procedure. Some of the matrix components modified by this procedure are not yet complete. However, since both the solution procedure and the assembly procedure merely add quantities to these matrix components, the order in which this is done is not important. Those elements that are not complete will be completed at a later stage. Once all the equations corresponding to the nodes of an element are completed, this element can be removed from consideration. Thus, at any stage of the frontal method, usually only a few elements are being worked on in the computer. The efficiency and storage involved in the frontal method is dependent on the order in which the elements are introduced and not on the nodal numbering. It is obviously desirable to have only a few elements involved at any one time.

3.2 Interpolation Schemes

An important part of the finite element approximation technique is the selection of a set of independent interpolation functions $\phi_1(x), \phi_2(x), \dots, \phi_N(x)$ such that an unknown function u can be represented by a sum of the form

$$u(x) = \sum_{n=1}^N u_n \phi_n(x). \quad (3.2.1)$$

Such a set of interpolation functions is called a *basis* for the interpolation scheme. We have already mentioned the “hat” functions corresponding to piecewise linear interpolation. Usually, the basis of interpolation functions has the property that the n -th interpolation takes on the value 1 at the n -th node and takes on the value 0 at all the other nodes. Because of this local property, the only interpolation functions that are nonzero on a particular element are those corresponding to nodes contained in the element. Clearly, the global interpolation functions can be determined if we know their behavior on each element.

Consider a one-dimensional line element with endpoints x_n and x_{n+1} ($x_{n+1} > x_n$). For piecewise linear interpolation, the two basis functions that are nonzero on this element are

$$\phi_n(x) = \frac{x - x_{n+1}}{x_n - x_{n+1}} \quad \phi_{n+1}(x) = \frac{x - x_n}{x_{n+1} - x_n}. \quad (3.2.2)$$

Since element sizes may vary, it is common to define the interpolation functions on the standard interval $[-1,1]$. The two basis functions for this interval are

$$\hat{\phi}_1(\xi) = \frac{1}{2}(1 - \xi) \quad \hat{\phi}_2(\xi) = \frac{1}{2}(1 + \xi). \quad (3.2.3)$$

The basis functions on this normalized interval are related to the real basis functions by

$$\phi_n(x) = \hat{\phi}_1\left(\frac{x - \frac{1}{2}(x_n + x_{n+1})}{\frac{1}{2}(x_{n+1} - x_n)}\right) \quad (3.2.4)$$

$$\phi_{n+1}(x) = \hat{\phi}_2\left(\frac{x - \frac{1}{2}(x_n + x_{n+1})}{\frac{1}{2}(x_{n+1} - x_n)}\right). \quad (3.2.5)$$

If we wanted to expand our unknowns in terms of piecewise quadratic functions, we would add a center node to the element as shown in figure 3.4. The following three functions would

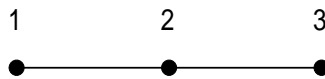


Figure 3.4. One-dimensional quadratic element

serve as normalized basis functions for this type of interpolation

$$\hat{\phi}_1(\xi) = \frac{1}{2}\xi(\xi - 1) \quad \hat{\phi}_2(\xi) = 1 - \xi^2 \quad \hat{\phi}_3(\xi) = \frac{1}{2}\xi(\xi + 1). \quad (3.2.6)$$

The basis functions for any element can be obtained by the same translation and scaling used for the linear elements, i.e.,

$$\xi = \frac{x - \frac{1}{2}(x_n + x_{n+1})}{\frac{1}{2}(x_{n+1} - x_n)}. \quad (3.2.7)$$

The two-dimensional analog of the piecewise linear one-dimensional element is the bilinear element shown in figure 3.5.

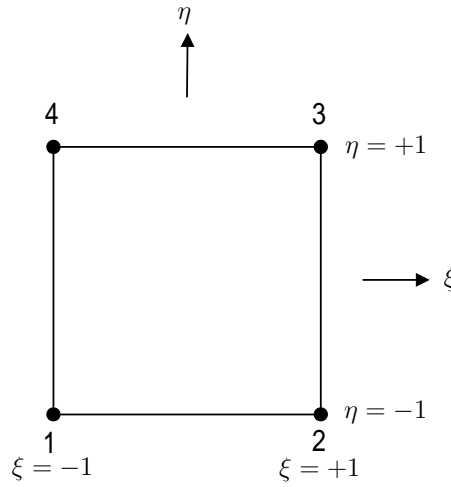


Figure 3.5. Two-dimensional bilinear element

The normalized basis functions for this element are

$$\hat{\phi}_1(\xi, \eta) = \frac{1}{4}(\xi - 1)(\eta - 1) \quad \hat{\phi}_2(\xi, \eta) = \frac{1}{4}(\xi + 1)(1 - \eta) \quad (3.2.8)$$

$$\hat{\phi}_3(\xi, \eta) = \frac{1}{4}(\xi + 1)(\eta + 1) \quad \hat{\phi}_4(\xi, \eta) = \frac{1}{4}(1 - \xi)(\eta + 1). \quad (3.2.9)$$

The variables ξ and η can be mapped to a rectangular region corresponding to the element by applying a one-dimensional translation and scaling to each coordinate separately. A two-dimensional quadratic element is shown in figure 3.6.

This element is called a serendipity element. The normalized basis functions for this element

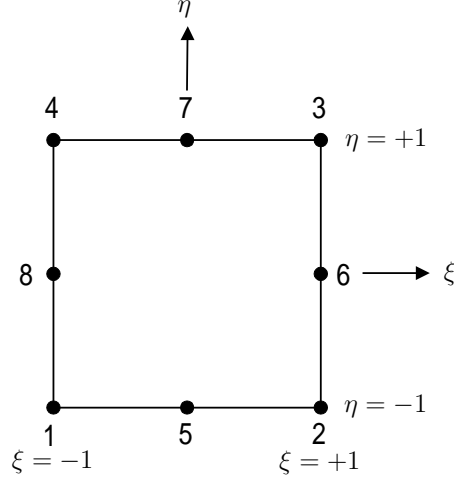


Figure 3.6. A two dimensional quadratic element

are

$$\hat{\phi}_1(\xi, \eta) = \frac{1}{4}\xi\eta(\xi - 1)(\eta - 1) \quad \hat{\phi}_2(\xi, \eta) = \frac{1}{4}\xi\eta(\xi + 1)(\eta - 1) \quad (3.2.10)$$

$$\hat{\phi}_3(\xi, \eta) = \frac{1}{4}\xi\eta(\xi + 1)(\eta + 1) \quad \hat{\phi}_4(\xi, \eta) = \frac{1}{4}\xi\eta(\xi - 1)(\eta + 1) \quad (3.2.11)$$

$$\hat{\phi}_5(\xi, \eta) = \frac{1}{2}\eta(\xi^2 - 1)(1 - \eta) \quad \hat{\phi}_6(\xi, \eta) = \frac{1}{2}\xi(\xi + 1)(1 - \eta^2) \quad (3.2.12)$$

$$\hat{\phi}_7(\xi, \eta) = \frac{1}{2}\eta(1 - \xi^2)(\eta + 1) \quad \hat{\phi}_8(\xi, \eta) = \frac{1}{2}\xi(\eta^2 - 1)(1 - \xi). \quad (3.2.13)$$

The serendipity element is quadratic, but it is not complete in the sense that there are quadratic functions on this region that can not be represented in terms of the eight $\hat{\phi}$ functions. The element can be made complete by adding a ninth node in the center as shown in figure 3.7. This element is called a Lagrange element. The normalized basis functions for

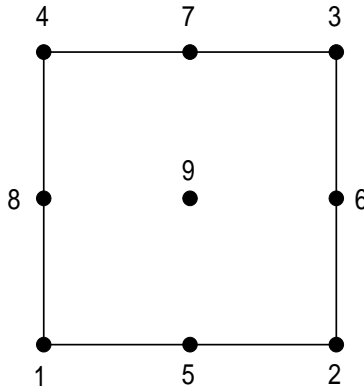


Figure 3.7. A complete two-dimensional quadratic element

this element are the basis functions for the serendipity element plus the ninth basis function

$$\hat{\phi}_9(\xi, \eta) = (1 - \xi^2)(1 - \eta^2). \quad (3.2.14)$$

Three-dimensional elements can be defined in a similar manner. There is an eight node linear element, a twenty node serendipity type quadratic element, and a 27 node Lagrange type quadratic element.

So far we have considered elements that are line intervals or planar rectangles. To handle more complex regions we can use the finite element basis functions to approximate the geometry. If $\vec{x}_1, \dots, \vec{x}_N$ are nodes in an element, then the mapping

$$\vec{x}(\xi, \eta) = \sum_{n=1}^N \vec{x}_n \hat{\phi}_n(\xi, \eta) \quad (3.2.15)$$

is an approximate representation of the geometry in the vicinity of the nodes. An example of this type of mapping is shown in figure 3.8.

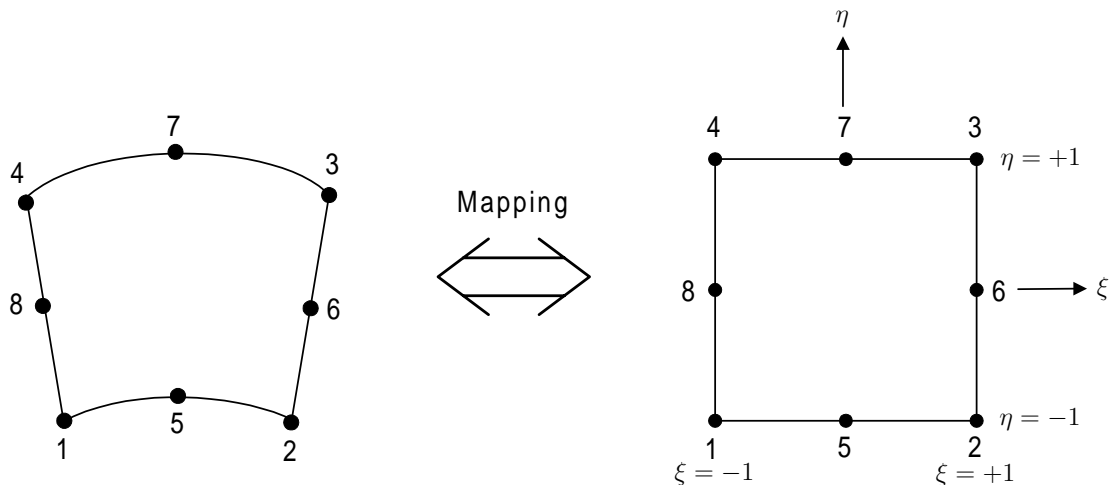


Figure 3.8. Geometry defined using finite element interpolation functions

An element in which both the geometry and the unknown functions are approximated using the same interpolation functions is called an *isoparametric* element.

3.3 Structural Finite Elements

In this section we will develop the basic finite element equations for an elastic continuum. The interior forces in an elastic continuum are described in terms of a vector area density

function \vec{t} called the stress vector. Given a point x in the body, a surface containing x , and a vector \vec{n} normal to the surface at x , the stress vector $\vec{t}(x)$ is the force per unit area of the positive side of the surface on the negative side. The positive side is the side into which the normal \vec{n} points. The stress tensor T is a linear transformation having the property

$$\vec{t} = T\vec{n}. \quad (3.3.1)$$

The basic equation of motion can be written in terms of the stress tensor as follows

$$\mathbf{div} T = \rho \frac{\partial^2 \vec{u}}{\partial t^2} \quad \text{in } \mathcal{V} \quad (3.3.2)$$

where ρ is the mass density, \vec{u} is the displacement vector, and \mathcal{V} is the volume occupied by the elastic material.

The strain tensor S is defined to be the symmetric part of the displacement gradient, i.e.,

$$S = \hat{\nabla} \vec{u} \equiv \frac{1}{2}(\nabla \vec{u} + \nabla \vec{u}^T). \quad (3.3.3)$$

The stress tensor and the strain tensor are related through the constitutive equation

$$T = C(S) \quad (3.3.4)$$

where C is a linear function.

Let $\vec{\psi}_1, \dots, \vec{\psi}_N$ be a basis of linearly independent vector interpolation functions on \mathcal{V} . In the finite element method these basis functions are piecewise polynomial functions each of which is nonzero at one node and zero at all the other nodes. The displacement \vec{u} is approximated by

$$\vec{u}(x) = \sum_{n=1}^N U_n \vec{\psi}_n(x). \quad (3.3.5)$$

In this approximation the displacement is completely determined by the values U_1, \dots, U_N . Substituting equation (3.3.5) into equation (3.3.3), we get

$$S(x) = \sum_{n=1}^N U_n \hat{\nabla} \vec{\psi}_n(x). \quad (3.3.6)$$

Thus, the constitutive relation of equation (3.3.4) becomes

$$T = \sum_{n=1}^N U_n C(\hat{\nabla} \vec{\psi}_n) \quad (3.3.7)$$

Following Galerkin's method, we take the dot product of equation (3.3.2) with each of the interpolation functions $\vec{\psi}_n$ and integrate over the volume V to obtain

$$\int_{\mathcal{V}} \mathbf{div} T \cdot \vec{\psi}_m = \int_{\mathcal{V}} \rho \frac{\partial^2 \vec{u}}{\partial t^2} \cdot \vec{\psi}_m \quad m = 1, \dots, N. \quad (3.3.8)$$

We have the following product rule for differentiation

$$\begin{aligned}\mathbf{div}(T\vec{\psi}_m) &= \mathbf{div} T \cdot \vec{\psi}_m + T \cdot \nabla \vec{\psi}_m \\ &= \mathbf{div} T \cdot \vec{\psi}_m + T \cdot \hat{\nabla} \vec{\psi}_m.\end{aligned}\quad (3.3.9)$$

The last equality in (3.3.9) follows from the fact that T is symmetric and hence that

$$T \cdot \nabla \vec{\psi}_m = T \cdot \nabla \vec{\psi}_m^T. \quad (3.3.10)$$

Combining equations (3.3.8)–(3.3.9) and making use of the divergence theorem, we get

$$\begin{aligned}\int_{\mathcal{V}} \mathbf{div} T \cdot \vec{\psi}_m &= \int_{\mathcal{V}} \mathbf{div}(T\vec{\psi}_m) - \int_{\mathcal{V}} T \cdot \hat{\nabla} \vec{\psi}_m \\ &= \int_{\partial\mathcal{V}} T\vec{\psi}_m \cdot \vec{n} - \int_{\mathcal{V}} T \cdot \hat{\nabla} \vec{\psi}_m \\ &= \int_{\partial\mathcal{V}} \vec{\psi}_m \cdot T\vec{n} - \int_{\mathcal{V}} T \cdot \hat{\nabla} \vec{\psi}_m \\ &= \int_{\partial\mathcal{V}} \vec{t} \cdot \vec{\psi}_m - \int_{\mathcal{V}} T \cdot \hat{\nabla} \vec{\psi}_m \\ &= \int_{\mathcal{V}} \rho \frac{\partial^2 \vec{u}}{\partial t^2} \cdot \vec{\psi}_m\end{aligned}$$

or

$$\int_{\mathcal{V}} \rho \frac{\partial^2 \vec{u}}{\partial t^2} \cdot \vec{\psi}_m + \int_{\mathcal{V}} T \cdot \hat{\nabla} \vec{\psi}_m = \int_{\partial\mathcal{V}} \vec{t} \cdot \vec{\psi}_m \quad m = 1, \dots, N \quad (3.3.11)$$

where we used the fact that $\vec{t} = T\vec{n}$.

Substituting equations (3.3.5) and (3.3.7) into equation (3.3.11), we get

$$\begin{aligned}\sum_{n=1}^N \ddot{U}_n \int_{\mathcal{V}} \rho \vec{\psi}_m \cdot \vec{\psi}_n + \sum_{n=1}^N U_n \int_{\mathcal{V}} C^E(\hat{\nabla} \vec{\psi}_n) \cdot \hat{\nabla} \vec{\psi}_m \\ = \int_{\partial\mathcal{V}} \vec{t} \cdot \vec{\psi}_m \quad m = 1, \dots, N.\end{aligned}\quad (3.3.12)$$

Equation (3.3.12) can be written in the matrix form

$$M\ddot{U} + KU = F \quad (3.3.13)$$

where U is a column vector with n -th component U_n . The matrices M and K have components given by

$$M_{mn} = \int_{\mathcal{V}} \rho \vec{\psi}_m \cdot \vec{\psi}_n \quad (3.3.14)$$

$$K_{mn} = \int_{\mathcal{V}} C^E(\hat{\nabla} \vec{\psi}_n) \cdot \hat{\nabla} \vec{\psi}_m. \quad (3.3.15)$$

F is a column vector with components

$$F_m = \int_{\partial V} \vec{t} \cdot \vec{\psi}_m. \quad (3.3.16)$$

In finite element terminology M is called the *mass matrix*, K is called the *stiffness matrix*, and F is called the *load vector*. In the frequency domain equation (3.3.13) becomes

$$(-\omega^2 M + K)U = F. \quad (3.3.17)$$

The frequencies ω_n for which the homogeneous equation

$$(-\omega^2 M + K)U = 0 \quad (3.3.18)$$

has a nonzero solution are called *eigenfrequencies*. The corresponding nonzero solutions are called *eigenmodes*. Clearly, if U is an eigenmode, then any scalar multiple of U is also an eigenmode. It can be shown that the eigenmodes corresponding to distinct eigenfrequencies are orthogonal relative to the mass matrix, i.e.,

$$U_m^T M U_n = 0 \quad \text{for } m \neq n. \quad (3.3.19)$$

Therefore, there exists a matrix E , whose columns are eigenmodes, such that

$$E^T M E = I \quad \text{and} \quad E^T K E = \Omega \quad (3.3.20)$$

where Ω is the diagonal matrix $\text{diag}(\omega_1^2, \dots, \omega_N^2)$ of the squares of the eigenfrequencies. Multiplying equation (3.3.17) by E^T and defining \hat{U} by $E\hat{U} = U$, we obtain

$$(-\omega^2 I + \Omega)\hat{U} = \hat{F} \quad (3.3.21)$$

where $\hat{F} = E^T F$. Thus, the finite element equations become uncoupled when expressed in terms of the eigenmodes. Solving equation (3.3.21) for \hat{U} , we obtain

$$U = E(-\omega^2 I + \Omega)^{-1} E^T F. \quad (3.3.22)$$

The inverse in this equation is easy to compute since the matrix is diagonal. Thus, equation (3.3.22) represents an efficient computational form for calculating the solution at a large number of frequencies.

3.4 Fluid Finite Elements

Consider a region \mathcal{V} containing a perfect fluid. The acoustic pressure p in \mathcal{V} satisfies the Helmholtz wave equation

$$\Delta p + k^2 p = 0 \quad (3.4.1)$$

where $k = \omega/c$ is the acoustic wave number. Let χ_1, \dots, χ_N be a basis of interpolation functions for p over \mathcal{V} . Then p can be approximated by

$$p(x) = \sum_n P_n \chi_n(x). \quad (3.4.2)$$

Following the Galerkin procedure, we multiply equation (3.4.1) by χ_m and integrate over \mathcal{V} to obtain

$$\int_{\mathcal{V}} \chi_m \Delta p + k^2 \int_{\mathcal{V}} \chi_m p = 0 \quad m = 1, \dots, N. \quad (3.4.3)$$

We have the following product rule for differentiation

$$\mathbf{div}(\chi_m \nabla p) = \chi_m \Delta p + \nabla \chi_m \cdot \nabla p. \quad (3.4.4)$$

Substituting equation (3.4.4) into equation (3.4.3), we get

$$\int_{\mathcal{V}} \mathbf{div}(\chi_m \nabla p) - \int_{\mathcal{V}} \nabla \chi_m \cdot \nabla p + k^2 \int_{\mathcal{V}} \chi_m p = 0. \quad (3.4.5)$$

Application of the divergence theorem to equation (3.4.5) produces

$$-\frac{\omega^2}{c^2} \int_{\mathcal{V}} \chi_m p + \int_{\mathcal{V}} \nabla \chi_m \cdot \nabla p = \int_{\partial \mathcal{V}} \chi_m \frac{\partial p}{\partial n} \quad (3.4.6)$$

where $\partial \mathcal{V}$ is the boundary of \mathcal{V} . Substitution of equation (3.4.2) into equation (3.4.6) gives the system of equations

$$-\frac{\omega^2}{c^2} \sum_n P_n \int_{\mathcal{V}} \chi_m \chi_n + \sum_n P_n \int_{\mathcal{V}} \nabla \chi_m \cdot \nabla \chi_n = \int_{\partial \mathcal{V}} \chi_m \frac{\partial p}{\partial n} \quad m = 1, \dots, N. \quad (3.4.7)$$

This system of equations can be written in the matrix form

$$(-\omega^2 M^f + K^f) P = F^f \quad (3.4.8)$$

where

$$M_{mn}^f = \frac{1}{c^2} \int_{\mathcal{V}} \chi_m \chi_n \quad (3.4.9)$$

$$K_{mn}^f = \int_{\mathcal{V}} \nabla \chi_m \cdot \nabla \chi_n \quad (3.4.10)$$

$$F_m^f = \int_{\partial \mathcal{V}} \chi_m \frac{\partial p}{\partial n}. \quad (3.4.11)$$

Suppose that the region \mathcal{V} shares a boundary surface \mathcal{S} with an elastic structure. The force vector F^f can be decomposed into two parts as follows

$$F^f = F^s + F^o \quad (3.4.12)$$

where

$$F_m^s = \int_{\mathcal{S}} \chi_m \frac{\partial p}{\partial n} \quad F_m^o = \int_{\mathcal{S}^o} \chi_m \frac{\partial p}{\partial n} \quad (3.4.13)$$

and \mathcal{S}^o is the portion of \mathcal{V} outside of \mathcal{S} . It follows from the equation of motion for the fluid that

$$\frac{\partial p}{\partial n} = \omega^2 \rho \vec{u} \cdot \vec{n} \quad (3.4.14)$$

where \vec{u} is the particle displacement, ρ is the fluid density, and \vec{n} is the outward unit normal to \mathcal{S} . The displacement u within the structure can be approximated in terms of the vector interpolation functions $\vec{\psi}_r$ as follows

$$\vec{u} = \sum_r U_r \vec{\psi}_r. \quad (3.4.15)$$

Combining equations (3.4.14) and (3.4.15), we get

$$\frac{\partial p}{\partial n} = \omega^2 \rho \sum_r U_r \vec{\psi}_r \cdot \vec{n}. \quad (3.4.16)$$

Thus, F_m^s becomes

$$F_m^s = \int_{\mathcal{S}} \chi_m \frac{\partial p}{\partial n} = \omega^2 \rho \sum_r U_r \int_{\mathcal{S}} \chi_m \vec{\psi}_r \cdot \vec{n}. \quad (3.4.17)$$

This equation can be written in the matrix form

$$F^s = \omega^2 \rho L^T U \quad (3.4.18)$$

where U is the column vector of structural displacement degrees of freedom and L is the matrix defined by

$$L_{rm} = \int_{\mathcal{S}} \chi_m \vec{\psi}_r \cdot \vec{n}. \quad (3.4.19)$$

Combining equations (3.4.8), (3.4.12), (3.4.13), and (3.4.18), we get

$$(-\omega^2 M^f + K^f)P - \omega^2 \rho L^T U = F^o. \quad (3.4.20)$$

The finite element equations for the structure can be written in the matrix form

$$(-\omega^2 M + K)U = F^{\text{rad}} + F^d \quad (3.4.21)$$

where F^{rad} is the load vector corresponding to the acoustic loading and F^d is the load vector corresponding to other structural forces. The load vector F^{rad} has the components

$$F_m^{\text{rad}} = \int_s \vec{t} \cdot \vec{\psi}_m \quad (3.4.22)$$

where \vec{t} is the stress vector. The stress vector is related to the pressure by

$$\vec{t} = -p\vec{n}. \quad (3.4.23)$$

Thus,

$$F_m^{\text{rad}} = - \int_s p \vec{\psi}_m \cdot \vec{n}. \quad (3.4.24)$$

Combining equations (3.4.2) and (3.4.24), we obtain

$$F_m^{\text{rad}} = - \sum_n P_n \int_s \chi_n \vec{\psi}_m \cdot \vec{n}. \quad (3.4.25)$$

Equation (3.4.25) can be written in the matrix form

$$F^{\text{rad}} = -LP. \quad (3.4.26)$$

Combining this equation with the structural finite element equation (3.4.21), we get

$$(-\omega^2 M + K)U + LP = F^d. \quad (3.4.27)$$

If we divide equation (3.4.20) by $-\omega^2 \rho$, then we have the pair of equations

$$(-\omega^2 M + K)U + LP = F^d \quad (3.4.28)$$

$$L^T U - \frac{1}{\omega^2 \rho} (-\omega^2 M^f + K^f) P = -\frac{1}{\omega^2 \rho} F^o \quad (3.4.29)$$

describing the interaction of fluid and structure. These equations can be combined into the large matrix equation

$$\begin{bmatrix} -\omega^2 M + K & L \\ L^T & -\frac{1}{\omega^2 \rho} (-\omega^2 M^f + K^f) \end{bmatrix} \begin{pmatrix} U \\ P \end{pmatrix} = \begin{pmatrix} F^d \\ -\frac{1}{\omega^2 \rho} F^o \end{pmatrix} \quad (3.4.30)$$

We divided through by $-\omega^2 \rho$ in order to make the final matrix symmetric. If it was desired to transform the equations into the time domain, then it would be better to write the equations in the form

$$\left(-\omega^2 \begin{bmatrix} M & 0 \\ \rho L^T & M^f \end{bmatrix} + \begin{bmatrix} K & L \\ 0 & K^f \end{bmatrix} \right) \begin{pmatrix} U \\ P \end{pmatrix} = \begin{pmatrix} F^d \\ F^o \end{pmatrix}. \quad (3.4.31)$$

In this form the matrices are not symmetric.

Many finite element programs use interface elements to construct the coupling matrix L . The unknown load vector F^o can be eliminated using some kind of radiation condition or by attaching an infinite fluid element.

3.5 Piezoelectric Finite Elements

Many finite element packages now contain elements for piezoelectric ceramic materials. In this paper I will develop the basic finite element equations for these materials. It will be assumed that the materials are linear, homogeneous and have sufficiently high dielectric constant so that fringing of the electric field can be neglected. The basic approach employed will be the Galerkin method. The Galerkin method is a projection method that in most cases is equivalent to the Rayleigh-Ritz variational procedure. Figure 3.9 shows a piece of piezoelectric material with its associated foil electrodes. It will be assumed that the foils are

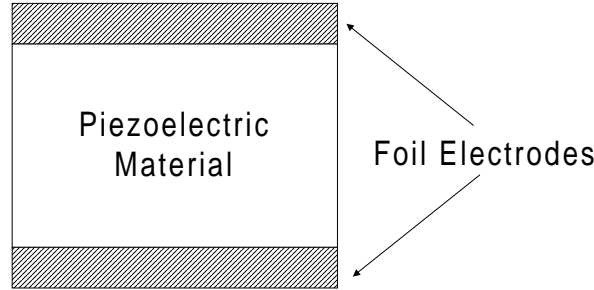


Figure 3.9. Piezoelectric material with electrodes

perfect conductors and have negligible thickness.

3.5.1 Mechanical Equations

The interior forces in an elastic continuum are described in terms of a vector area density function \vec{t} called the stress vector. Given a point x in the body, a surface containing x , and a vector \vec{n} normal to the surface at x , the stress vector $\vec{t}(x)$ is the force per unit area of the positive side of the surface on the negative side. The positive side is the side into which the normal \vec{n} points. The stress tensor T is a linear transformation having the property

$$\vec{t} = T\vec{n}. \quad (3.5.1.1)$$

The basic equation of motion can be written in terms of the stress tensor as follows

$$\mathbf{div} T = \rho \frac{\partial^2 \vec{u}}{\partial t^2} \quad \text{in } \mathcal{V} \quad (3.5.1.2)$$

where ρ is the mass density, \vec{u} is the displacement vector, and \mathcal{V} is the volume occupied by the piezoelectric material.

The strain tensor S is defined to be the symmetric part of the displacement gradient, i.e.,

$$S = \hat{\nabla} \vec{u} \equiv \frac{1}{2}(\nabla \vec{u} + \nabla \vec{u}^T). \quad (3.5.1.3)$$

The stress tensor and the strain tensor are related through the constitutive equations to be described later.

3.5.2 Electrical Equations

The electric field \vec{E} and the magnetic induction \vec{B} are related by Maxwell's equation

$$\text{curl } \vec{E} = -\frac{\partial \vec{B}}{\partial t}. \quad (3.5.2.1)$$

In this paper we will make the quasistatic assumption that magnetic effects are negligible, i.e., $\partial \vec{B} / \partial t = 0$. It follows that

$$\text{curl } \vec{E} = 0. \quad (3.5.2.2)$$

Equation (3.5.2.2) implies the existence of a scalar potential ϕ such that

$$\vec{E} = -\nabla \phi. \quad (3.5.2.3)$$

The electric displacement vector \vec{D} satisfies Maxwell's equation

$$\text{div } \vec{D} = \rho_e \quad (3.5.2.4)$$

where ρ_e is the free charge density.

3.5.3 Constitutive Equations

The linear constitutive equations for a piezoelectric material have the form

$$T = C^E(S) - e^\dagger(\vec{E}) \quad (3.5.3.1)$$

$$\vec{D} = e(S) + \epsilon^S(\vec{E}) \quad (3.5.3.2)$$

where C^E , e , and ϵ^S are linear functions and e^\dagger is the transpose of e . The transpose is defined by the property

$$e(S) \cdot \vec{E} = S \cdot e^\dagger(\vec{E}) \quad \text{for all } S \text{ and } E. \quad (3.5.3.3)$$

3.5.4 Interpolation Functions

Let $\vec{\psi}_1, \dots, \vec{\psi}_N$ be a basis of linearly independent vector interpolation functions on \mathcal{V} . In the finite element method these basis functions are piecewise polynomial functions each of which

is nonzero at one node and zero at all the other nodes. The displacement \vec{u} is approximated by

$$\vec{u}(x) = \sum_{n=1}^N U_n \vec{\psi}_n(x). \quad (3.5.4.1)$$

In this approximation the displacement is completely determined by the values U_1, \dots, U_N .

Let χ_1, \dots, χ_M be a basis of scalar interpolation functions. The electric potential ϕ is approximated by

$$\phi(x) = \sum_{n=1}^M \phi_n \chi_n(x). \quad (3.5.4.2)$$

In this approximation the potential ϕ is completely determined by the values ϕ_1, \dots, ϕ_M .

Combining equations (3.5.1.3) and (3.5.4.1), we get

$$S(x) = \sum_{n=1}^N U_n \hat{\nabla} \vec{\psi}_n(x). \quad (3.5.4.3)$$

Combining equations (3.5.2.3) and (3.5.4.2), we get

$$\vec{E}(x) = - \sum_{n=1}^M \phi_n \nabla \chi_n(x). \quad (3.5.4.4)$$

Substituting equations (3.5.4.3)–(3.5.4.4) into the constitutive equations (3.5.3.1)–(3.5.3.2), we get

$$T = \sum_{n=1}^N U_n C^E (\hat{\nabla} \vec{\psi}_n) + \sum_{n=1}^M \phi_n e^\dagger (\nabla \chi_n) \quad (3.5.4.5)$$

$$\vec{D} = \sum_{n=1}^N U_n e (\hat{\nabla} \vec{\psi}_n) - \sum_{n=1}^M \phi_n \epsilon^S (\nabla \chi_n). \quad (3.5.4.6)$$

3.5.5 Finite Element Equations

Taking the dot product of equation (3.5.1.2) with each of the interpolation functions $\vec{\psi}_n$ and integrating over \mathcal{V} , we obtain

$$\int_{\mathcal{V}} \text{div } T \cdot \vec{\psi}_m = \int_{\mathcal{V}} \rho \frac{\partial^2 \vec{u}}{\partial t^2} \cdot \vec{\psi}_m \quad m = 1, \dots, N. \quad (3.5.5.1)$$

We have the following product rule for differentiation

$$\begin{aligned}\mathbf{div}(T\vec{\psi}_m) &= \mathbf{div} T \cdot \vec{\psi}_m + T \cdot \nabla \vec{\psi}_m \\ &= \mathbf{div} T \cdot \vec{\psi}_m + T \cdot \hat{\nabla} \vec{\psi}_m.\end{aligned}\tag{3.5.5.2}$$

The last equality in (3.5.5.2) follows from the fact that T is symmetric and hence that

$$T \cdot \nabla \vec{\psi}_m = T \cdot \nabla \vec{\psi}_m^T.\tag{3.5.5.3}$$

Combining equations (3.5.5.1)–(3.5.5.2) and making use of the divergence theorem, we get

$$\begin{aligned}\int_{\mathcal{V}} \mathbf{div} T \cdot \vec{\psi}_m &= \int_{\mathcal{V}} \mathbf{div}(T\vec{\psi}_m) - \int_{\mathcal{V}} T \cdot \hat{\nabla} \vec{\psi}_m \\ &= \int_{\partial\mathcal{V}} T\vec{\psi}_m \cdot \vec{n} - \int_{\mathcal{V}} T \cdot \hat{\nabla} \vec{\psi}_m \\ &= \int_{\partial\mathcal{V}} \vec{\psi}_m \cdot T\vec{n} - \int_{\mathcal{V}} T \cdot \hat{\nabla} \vec{\psi}_m \\ &= \int_{\partial\mathcal{V}} \vec{t} \cdot \vec{\psi}_m - \int_{\mathcal{V}} T \cdot \hat{\nabla} \vec{\psi}_m \\ &= \int_{\mathcal{V}} \rho \frac{\partial^2 \vec{u}}{\partial t^2} \cdot \vec{\psi}_m\end{aligned}$$

or

$$\int_{\mathcal{V}} \rho \frac{\partial^2 \vec{u}}{\partial t^2} \cdot \vec{\psi}_m + \int_{\mathcal{V}} T \cdot \hat{\nabla} \vec{\psi}_m = \int_{\partial\mathcal{V}} \vec{t} \cdot \vec{\psi}_m \quad m = 1, \dots, N\tag{3.5.5.4}$$

where we used the fact that $\vec{t} = T\vec{n}$. Substituting equations (3.5.4.1) and (3.5.4.5) into equation (3.5.5.4), we get

$$\begin{aligned}\sum_{n=1}^N \ddot{U}_n \int_{\mathcal{V}} \rho \vec{\psi}_m \cdot \vec{\psi}_n + \sum_{n=1}^N U_n \int_{\mathcal{V}} C^E(\hat{\nabla} \vec{\psi}_n) \cdot \hat{\nabla} \vec{\psi}_m \\ + \sum_{n=1}^M \phi_n \int_{\mathcal{V}} e^\dagger(\nabla \chi_n) \cdot \hat{\nabla} \vec{\psi}_m = \int_{\partial\mathcal{V}} \vec{t} \cdot \vec{\psi}_m \quad m = 1, \dots, N.\end{aligned}\tag{3.5.5.5}$$

Equation (3.5.5.5) can be written in the matrix form

$$M\ddot{U} + KU + K^c\Phi = F\tag{3.5.5.6}$$

where U is a column vector with n -th component U_n and Φ is a column vector with n -th

component ϕ_n . The matrices M , K , and K^c have components given by

$$M_{mn} = \int_{\mathcal{V}} \rho \vec{\psi}_m \cdot \vec{\psi}_n \quad (3.5.5.7)$$

$$K_{mn} = \int_{\mathcal{V}} C^E(\hat{\nabla} \vec{\psi}_n) \cdot \hat{\nabla} \vec{\psi}_m \quad (3.5.5.8)$$

$$\begin{aligned} K_{mn}^c &= \int_{\mathcal{V}} e^\dagger(\nabla \chi_n) \cdot \hat{\nabla} \vec{\psi}_m \\ &= \int_{\mathcal{V}} e(\hat{\nabla} \vec{\psi}_m) \cdot \nabla \chi_n. \end{aligned} \quad (3.5.5.9)$$

F is a column vector with components

$$F_m = \int_{\partial \mathcal{V}} \vec{t} \cdot \vec{\psi}_m. \quad (3.5.5.10)$$

Referring to figure 3.9, we will assume that the volume \mathcal{V} extends slightly into the foils. Since the electric field and electric displacement are zero inside a perfect conductor, it follows that $\vec{D} \cdot \vec{n} = 0$ on the portion of the boundary of \mathcal{V} that lies in the foils. Since we are also assuming that there is no fringing of the electric field, it follows that $\vec{D} \cdot \vec{n} = 0$ on the entire boundary $\partial \mathcal{V}$ of \mathcal{V} . Multiplying equation (3.5.2.4) by each of the interpolation functions χ_m and integrating over \mathcal{V} , we get

$$\int_{\mathcal{V}} \chi_m \mathbf{div} \vec{D} = \int_{\mathcal{V}} \rho_e \chi_m \quad m = 1, \dots, M. \quad (3.5.5.11)$$

We have the following product rule for differentiation

$$\mathbf{div}(\chi_m \vec{D}) = \chi_m \mathbf{div} \vec{D} + \nabla \chi_m \cdot \vec{D}. \quad (3.5.5.12)$$

Combining equations (3.5.5.11)–(3.5.5.12) and making use of the divergence theorem, we get

$$\begin{aligned} \int_{\mathcal{V}} \chi_m \mathbf{div} \vec{D} &= \int_{\mathcal{V}} \mathbf{div}(\chi_m \vec{D}) - \int_{\mathcal{V}} \nabla \chi_m \cdot \vec{D} \\ &= \int_{\partial \mathcal{V}} \chi_m \vec{D} \cdot \vec{n} - \int_{\mathcal{V}} \nabla \chi_m \cdot \vec{D} \\ &= \int_{\mathcal{V}} \rho_e \chi_m. \end{aligned}$$

Since $\vec{D} \cdot \vec{n} = 0$ on $\partial \mathcal{V}$, it follows that

$$-\int_{\mathcal{V}} \nabla \chi_m \cdot \vec{D} = \int_{\mathcal{V}} \rho_e \chi_m \quad m = 1, \dots, M. \quad (3.5.5.13)$$

Substituting equation (3.5.4.6) into equation (3.5.5.13), yields

$$\sum_{n=1}^N U_n \int_{\mathcal{V}} \nabla \chi_m \cdot e(\hat{\nabla} \vec{\psi}_n) - \sum_{n=1}^M \phi_n \int_{\mathcal{V}} \nabla \chi_m \cdot \epsilon^S(\nabla \chi_n) = - \int_{\mathcal{V}} \rho_e \chi_m \quad m = 1, \dots, M. \quad (3.5.5.14)$$

Equation (3.5.5.14) can be written in the matrix form

$$(K^c)^T U + K^e \Phi = Q \quad (3.5.5.15)$$

where K^e is the matrix with components

$$K_{mn}^e = - \int_{\mathcal{V}} \nabla \chi_m \cdot \epsilon^S(\nabla \chi_n) \quad (3.5.5.16)$$

and Q is a column vector with components

$$Q_m = - \int_{\mathcal{V}} \rho_e \chi_m. \quad (3.5.5.17)$$

Equations (3.5.5.6) and (3.5.5.15) can be combined to give

$$\begin{pmatrix} M & 0 \\ 0 & 0 \end{pmatrix} \begin{pmatrix} \ddot{U} \\ \ddot{\Phi} \end{pmatrix} + \begin{pmatrix} K & K^c \\ (K^c)^T & K^e \end{pmatrix} \begin{pmatrix} U \\ \Phi \end{pmatrix} = \begin{pmatrix} F \\ Q \end{pmatrix}. \quad (3.5.5.18)$$

Equation (3.5.5.18) is the basic finite element equation for piezoelectric materials. The usual finite element interpolation functions χ_m have the property

$$\chi_m(x_n) = \begin{cases} 0 & m \neq n \\ 1 & m = n \end{cases} \quad (3.5.5.19)$$

where the x_n 's are the nodes in the model. Since the free charge is concentrated on the foils, it follows from equation (3.5.5.17) that $Q_m = 0$ when x_m does not lie on one of the foils. Furthermore, the sum of the Q_m over all the nodes on a single foil is the charge on that foil. Since the foils are perfect conductors, the potentials ϕ_n are the same for all nodes on a single foil, and this constant value is the potential on that foil.

In modeling a stack of piezoelectric ceramic slabs, it is necessary to consider that the polarization is reversed on adjacent slabs. The reversal of polarization can be accomplished by replacing e by $-e$ in the constitutive equations (3.5.3.1) and (3.5.3.2).

3.6 Magnetostrictive Finite Elements

Recently there has been renewed interest in magnetostrictive drivers due to the discovery of some new rare-earth magnetostrictive materials (particularly Terfenol-D). These new materials have a coupling coefficient as high as that of piezoelectric ceramics and allow much larger strains. The high strain capability along with a lower Young's modulus make these materials attractive for low frequency, high power transducers. From a modeling standpoint these materials pose some special challenges. Since the magnetic permeability of these materials is small (only 2 to 3 times that of a vacuum), the magnetic field is not well confined to the material, i.e., fringing can not be neglected. Thus, in a finite element model, the magnetic domain must be larger than the elastic domain. In addition, these materials are highly nonlinear and can only be considered linear around some dc bias.

As far as I know, the only general purpose finite element program that allows for magnetostrictive materials with low magnetic permeability is the ATILA program developed by ISEN (l'Institut Supérieur d'Electronique du Nord) for the French Navy. The theory behind the ATILA implementation is described in the doctoral thesis [F. Claeysen, *Conception et réalisation de transducteurs sonar basse fréquence à base d'alliages magnétostrictifs Terres rares-Fer*, Thesis n. 89 ISAL 0065, INSA Lyon Fr. (1989)]. This section is largely based on this thesis and represents my interpretation of the theoretical basis behind the method used by ATILA to model magnetostrictive materials.

3.6.1 Magnetic Potential

Let \mathcal{V}_M denote the magnetic region where the magnetic field is considered significant, and let \mathcal{V}_E denote the elastic region. We will assume that the magnetostrictive material is excited by a finite number of coils where the current in the k -th coil is denoted by I_k . Figure 3.10 shows a coil surrounding a magnetostrictive bar and a magnetic return path.

Let H^s be the magnetic field generated by the coils *in vacuo*. Then

$$H^s = \sum_k I_k \hat{H}_k \quad (3.6.1.1)$$

where \hat{H}_k is the *in vacuo* magnetic field corresponding to unit current in the k -th coil and zero current in the remaining coils. \hat{H}_k can be calculated using the Biot-Savart law

$$\hat{H}_k = \frac{1}{4\pi} \int_{V_k^c} \frac{\hat{J}_k \times \vec{r}}{r^3} dV \quad (3.6.1.2)$$

where \vec{r} is a vector from the integration point to the field point, r is the magnitude of \vec{r} , V_k^c is the volume occupied by the k -th coil, and \hat{J}_k is the current density corresponding to a

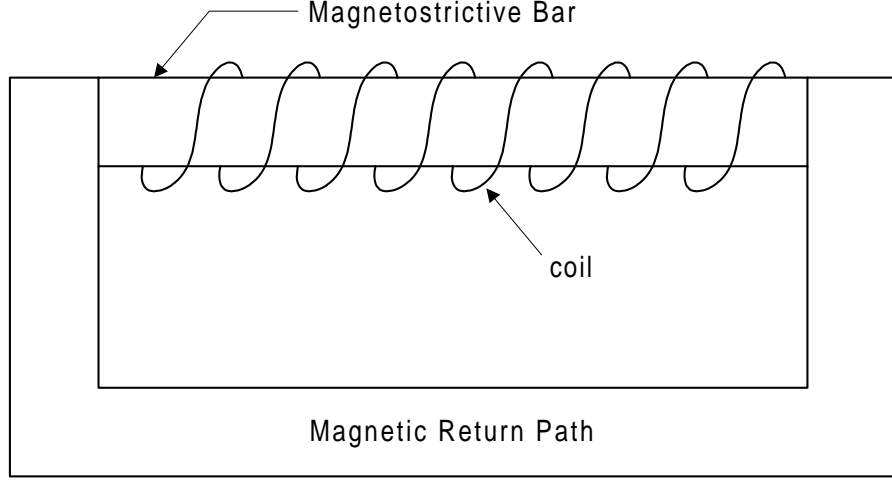


Figure 3.10. A magnetostrictive bar surrounded by a coil with its return path

unit current in the k -th coil and zero current in the other coils. The residual magnetic field H^r is defined by

$$H^r = H - H^s. \quad (3.6.1.3)$$

Since both H and H^s satisfy Maxwell's equation $\text{curl } H = J$, it follows from equation (3.6.1.3) that

$$\text{curl } H^r = 0. \quad (3.6.1.4)$$

Therefore, there exists a scalar magnetic potential ϕ such that

$$H^r = -\nabla\phi. \quad (3.6.1.5)$$

It follows from equations (3.6.1.5) and (3.6.1.3) that

$$H = H^s - \nabla\phi = \sum_k I_k \hat{H}_k - \nabla\phi. \quad (3.6.1.6)$$

3.6.2 Basic Equations

The stress tensor T and the displacement u obey Cauchy's equation of motion

$$\mathbf{div } T = \rho \ddot{u} = -\omega^2 \rho u \quad (3.6.2.1)$$

in the region \mathcal{V}_E occupied by elastic materials. The magnetic induction B satisfies Maxwell's equation

$$\mathbf{div } B = 0 \quad (3.6.2.2)$$

in the magnetic region \mathcal{V}_M which includes the elastic region \mathcal{V}_E . The elastic and magnetic fields are assumed to satisfy the linear constitutive equations

$$T = C^H(S) - e^\dagger(H) \quad (3.6.2.3)$$

$$B = e(S) + \mu^S(H) \quad (3.6.2.4)$$

where C^H , e , and μ^S are linear functions; e^\dagger denotes the transpose of the function e ; and S is the strain tensor defined by

$$S = \frac{1}{2}(\nabla u + \nabla u^T). \quad (3.6.2.5)$$

We will use the notation $\hat{\nabla}$ for the symmetric part of the gradient operator ∇ . Thus, the strain is given by

$$S = \hat{\nabla} u. \quad (3.6.2.6)$$

The constitutive equations (3.6.2.4) can also be used for non-magnetostrictive materials. For materials that are not magnetostrictive, the coupling function e is zero. For nonelastic magnetic materials both C^H and e are zero.

3.6.3 Interpolation Functions

Let $\psi_1, \psi_2, \dots, \psi_N$ be a set of independent vector interpolation functions on the region \mathcal{V}_E such that the displacement u can be approximated by

$$u(x) \doteq \sum_{n=1}^N U_n \psi_n(x) \quad x \in \mathcal{V}_E. \quad (3.6.3.1)$$

In finite element models, the interpolation functions are piecewise polynomials. Using the form of interpolation shown in equation (3.6.3.1) allows the unknown function u to be replaced by the N values U_1, \dots, U_N . We will let U denote the column vector whose n -th component is U_n . The vector U is one of the basic variables in the finite element model.

Let $\chi_1, \chi_2, \dots, \chi_M$ be a set of independent scalar interpolation functions such that the magnetic potential ϕ can be approximated by

$$\phi(x) \doteq \sum_{r=1}^M \phi_r \chi_r(x) \quad x \in \mathcal{V}_M. \quad (3.6.3.2)$$

Again, we will let Φ denote the column vector whose r -th component is ϕ_r . The vector Φ is another one of the basic variables in the finite element model. If we substitute equation (3.6.3.2) into equation (3.6.1.6), then we obtain the following approximation for the magnetic field H

$$H(x) \doteq \sum_k I_k \hat{H}_k - \sum_{r=1}^M \phi_r \nabla \chi_r(x). \quad (3.6.3.3)$$

The current column vector I with k -th component I_k is another one of the basic variables in the finite element model. Referring to equation (3.6.1.1), we see that the functions \hat{H}_k play the role of interpolation functions for H^s .

3.6.4 Elastic Finite Element Equations

Taking the dot product of the equation of motion (3.6.2.1) by the interpolation function ψ_m and integrating over \mathcal{V}_E , we get

$$\int_{\mathcal{V}_E} \psi_m \cdot \mathbf{div} T = -\omega^2 \int_{\mathcal{V}_E} \rho \psi_m \cdot u \quad \text{for each } m. \quad (3.6.4.1)$$

In view of the product rule

$$\mathbf{div}(T\psi_m) = \mathbf{div} T \cdot \psi_m + \hat{\nabla} \psi_m \cdot T, \quad (3.6.4.2)$$

equation (3.6.4.1) can be written

$$\int_{\mathcal{V}_E} \mathbf{div}(T\psi_m) - \int_{\mathcal{V}_E} \hat{\nabla} \psi_m \cdot T = -\omega^2 \int_{\mathcal{V}_E} \rho \psi_m \cdot u \quad \text{for each } m. \quad (3.6.4.3)$$

Making use of the divergence theorem, equation (3.6.4.3) can be written

$$-\omega^2 \int_{\mathcal{V}_E} \rho \psi_m \cdot u + \int_{\mathcal{V}_E} \hat{\nabla} \psi_m \cdot T = \int_{\partial \mathcal{V}_E} \psi_m \cdot T n \quad \text{for each } m \quad (3.6.4.4)$$

where $\partial \mathcal{V}_E$ is the boundary surface of the region \mathcal{V}_E and n is the outward unit normal vector to $\partial \mathcal{V}_E$. Substituting the constitutive equation (3.6.2.3) for T into equation (3.6.4.4), we get

$$\begin{aligned} -\omega^2 \int_{\mathcal{V}_E} \rho \psi_m \cdot u + \int_{\mathcal{V}_E} \hat{\nabla} \psi_m \cdot C^H(\hat{\nabla} u) - \int_{\mathcal{V}_E} \hat{\nabla} \psi_m \cdot e^\dagger(H) = \\ \int_{\partial \mathcal{V}_E} \psi_m \cdot T n \quad \text{for each } m. \end{aligned} \quad (3.6.4.5)$$

Substituting equations (3.6.3.3) and (3.6.3.1) into equation (3.6.4.5), we get

$$\begin{aligned} -\omega^2 \sum_{n=1}^N U_n \int_{\mathcal{V}_E} \rho \psi_m \cdot \psi_n + \sum_{n=1}^N U_n \int_{\mathcal{V}_E} \hat{\nabla} \psi_m \cdot C^H(\hat{\nabla} \psi_n) \\ - \sum_k I_k \int_{\mathcal{V}_E} \hat{\nabla} \psi_m \cdot e^\dagger(\hat{H}_k) + \sum_{r=1}^M \phi_r \int_{\mathcal{V}_E} \hat{\nabla} \psi_m \cdot e^\dagger(\nabla \chi_r) = \\ \int_{\partial \mathcal{V}_E} \psi_m \cdot T n \quad \text{for each } m. \end{aligned} \quad (3.6.4.6)$$

This equation can be written in the matrix form

$$(-\omega^2 M + K^{uu})U + K^{u\phi}\Phi + K^{uI}I = F \quad (3.6.4.7)$$

where the matrices M , K^{uu} , $K^{u\phi}$, and K^{uI} are defined by

$$M = \left[\int_{\mathcal{V}_E} \rho \psi_m \cdot \psi_n \right] \quad (3.6.4.8)$$

$$K^{uu} = \left[\int_{\mathcal{V}_E} \hat{\nabla} \psi_m \cdot C^H(\hat{\nabla} \psi_n) \right] \quad (3.6.4.9)$$

$$K^{u\phi} = \left[\int_{\mathcal{V}_E} \hat{\nabla} \psi_m \cdot e^\dagger(\nabla \chi_r) \right] \quad (3.6.4.10)$$

$$K^{uI} = \left[\int_{\mathcal{V}_E} \hat{\nabla} \psi_m \cdot e^\dagger(\hat{H}_k) \right] \quad (3.6.4.11)$$

and the vector F is defined by

$$F = \left[\int_{\partial \mathcal{V}_E} \psi_m \cdot Tn \right]. \quad (3.6.4.12)$$

3.6.5 Magnetic Finite Element Equations

Multiplying equation (3.6.2.2) by the interpolation function χ_q and integrating over \mathcal{V}_M , we get

$$\int_{\mathcal{V}_E} \chi_q \mathbf{div} B = 0 \quad \text{for each } q. \quad (3.6.5.1)$$

In view of the product rule

$$\mathbf{div}(\chi_q B) = \chi_q \mathbf{div} B + \nabla \chi_q \cdot B, \quad (3.6.5.2)$$

equation (3.6.5.1) can be written

$$\int_{\mathcal{V}_M} \nabla \chi_q \cdot B = \int_{\mathcal{V}_M} \mathbf{div}(\chi_q B) = \int_{\partial \mathcal{V}_M} \chi_q (B \cdot n) \quad \text{for each } q. \quad (3.6.5.3)$$

In the above equation we have made use of the divergence theorem. Substituting the constitutive equation (3.6.2.4) for B into equation (3.6.5.3), gives

$$\int_{\mathcal{V}_M} \nabla \chi_q \cdot e(\hat{\nabla} u) + \int_{\mathcal{V}_M} \nabla \chi_q \cdot \mu^S(H) = \int_{\partial \mathcal{V}_M} \chi_q (B \cdot n) \quad \text{for each } q. \quad (3.6.5.4)$$

Substituting equations (3.6.3.3) and (3.6.3.1) into equation (3.6.5.4), we get

$$\begin{aligned} \sum_{n=1}^N U_n \int_{\mathcal{V}_E} \nabla \chi_q \cdot e(\hat{\nabla} \psi_n) + \sum_k I_k \int_{\mathcal{V}_M} \nabla \chi_q \cdot \mu^S(\hat{H}_k) \\ - \sum_{r=1}^M \phi_r \int_{\mathcal{V}_M} \nabla \chi_q \cdot \mu^S(\nabla \chi_r) = \int_{\partial \mathcal{V}_M} \chi_q B \cdot n \quad \text{for each } q. \end{aligned} \quad (3.6.5.5)$$

In this equation we have used the fact that the displacement is zero outside of the elastic region \mathcal{V}_E . Equation (3.6.5.5) can be written in the matrix form

$$(K^{u\phi})^T U + K^{\phi\phi} \Phi + K^{\phi I} I = Q \quad (3.6.5.6)$$

where

$$K^{\phi\phi} = \left[- \int_{\mathcal{V}_M} \nabla \chi_q \cdot \mu^S(\nabla \chi_r) \right] \quad (3.6.5.7)$$

$$K^{\phi I} = \left[\int_{\mathcal{V}_M} \nabla \chi_q \cdot \mu^S(\hat{H}_k) \right] \quad (3.6.5.8)$$

$$Q = \left[\int_{\partial \mathcal{V}_M} \chi_q B \cdot n \right]. \quad (3.6.5.9)$$

3.6.6 Current Finite Element Equations

Since the magnetic induction vector B satisfies $\mathbf{div} B = 0$, there exists a vector potential A such that

$$B = \text{curl } A. \quad (3.6.6.1)$$

In view of the product rule

$$\mathbf{div}(\hat{H}_p \times A) = A \cdot \text{curl } \hat{H}_p - \hat{H}_p \cdot \text{curl } A \quad (3.6.6.2)$$

and the fact that \hat{H}_p satisfies Maxwell's equation

$$\text{curl } \hat{H}_p = \hat{J}_p, \quad (3.6.6.3)$$

we have

$$B \cdot \hat{H}_p = A \cdot \hat{J}_p - \mathbf{div}(\hat{H}_p \times A). \quad (3.6.6.4)$$

Integrating equation (3.6.6.4) over all space and making use of the divergence theorem, we obtain

$$\int B \cdot \hat{H}_p = \int A \cdot \hat{J}_p - \lim_{r \rightarrow \infty} \int_{S_r} \hat{H}_p \times A \cdot \hat{r} \quad (3.6.6.5)$$

where S_r is a sphere of radius r and \hat{r} is a unit vector in the radial direction. Since \hat{H}_p decays like $1/r^2$ and A decays like $1/r$, it follows that the limit in equation (3.6.6.5) is zero. Thus,

$$\int B \cdot \hat{H}_p = \int A \cdot \hat{J}_p. \quad (3.6.6.6)$$

Since \hat{J}_p is zero outside of the p -th coil, we have

$$\int A \cdot \hat{J}_p = \sum_l \int_{\mathcal{V}_l^p} A \cdot \hat{J}_p \quad (3.6.6.7)$$

where \mathcal{V}_l^p is the volume of the l -th loop in the p -th coil. We will assume that A is approximately constant over the cross-section of each wire loop. Since \hat{J}_p corresponds to a unit current in the p -th coil, equation (3.6.6.7) can be approximated by

$$\int A \cdot \hat{J}_p = \sum_l \oint_{\mathcal{C}_l^p} A \cdot ds \quad (3.6.6.8)$$

where \mathcal{C}_l^p is the curve defining the centerline of the l -th loop in the p -th coil. By Stoke's theorem we have

$$\oint_{\mathcal{C}_l^p} A \cdot ds = \int_{S_l^p} \text{curl } A \cdot n \quad (3.6.6.9)$$

where S_l^p is the area bounded by \mathcal{C}_l^p and n is normal to this area. Since $\text{curl } A = B$, combination of equations (3.6.6.6)–(3.6.6.9) gives

$$\int B \cdot \hat{H}_p = \sum_l \int_{S_l^p} B \cdot n \equiv q_p. \quad (3.6.6.10)$$

Substituting the constitutive equation (3.6.2.4) into equation (3.6.6.10), we obtain

$$\int_{\mathcal{V}_E} e(\hat{\nabla} u) \cdot \hat{H}_p + \int_{\mathcal{V}_M} \mu^S(H) \cdot \hat{H}_p = q_p. \quad (3.6.6.11)$$

Substituting equations (3.6.3.3) and (3.6.3.1) into equation (3.6.6.11), we get

$$\begin{aligned} \sum_{n=1}^N U_n \int_{\mathcal{V}_E} e(\hat{\nabla} \psi_n) \cdot \hat{H}_p + \sum_k I_k \int_{\mathcal{V}_M} \mu^S(\hat{H}_k) \cdot \hat{H}_p \\ + \sum_{r=1}^M \phi_r \int_{\mathcal{V}_M} \mu^S(\nabla \chi_r) \cdot \hat{H}_p = q_p. \end{aligned} \quad (3.6.6.12)$$

Equation (3.6.6.12) can be written in the matrix form

$$(K^{uI})^T U + K^{II} I + (K^{\phi I})^T \Phi = -q \quad (3.6.6.13)$$

where

$$K^{II} = \left[\int_{\mathcal{V}_M} \mu^S(\hat{H}_k) \cdot \hat{H}_p \right] \quad (3.6.6.14)$$

$$q = \left[\sum_l \int_{S_l^p} B \cdot n \right] = \text{fluxes through coils.} \quad (3.6.6.15)$$

3.6.7 Summary of Finite Element Equations

The finite element equations given in (3.6.4.7), (3.6.5.6), and (3.6.6.13) can be combined into the single matrix equation

$$\begin{pmatrix} -\omega^2 M + K^{uu} & K^{u\phi} & K^{uI} \\ (K^{u\phi})^T & K^{\phi\phi} & K^{\phi I} \\ (K^{uI})^T & (K^{\phi I})^T & K^{II} \end{pmatrix} \begin{pmatrix} U \\ \Phi \\ I \end{pmatrix} = \begin{pmatrix} F \\ Q \\ q \end{pmatrix} \quad (3.6.7.1)$$

where

$$M = \left[\int_{\mathcal{V}_E} \rho \psi_m \cdot \psi_n \right] \quad (3.6.7.2)$$

$$K^{uu} = \left[\int_{\mathcal{V}_E} \hat{\nabla} \psi_m \cdot C^H(\hat{\nabla} \psi_n) \right] \quad (3.6.7.3)$$

$$K^{u\phi} = \left[\int_{\mathcal{V}_E} \hat{\nabla} \psi_m \cdot e^\dagger(\nabla \chi_r) \right] \quad (3.6.7.4)$$

$$K^{uI} = \left[\int_{\mathcal{V}_E} \hat{\nabla} \psi_m \cdot e^\dagger(\hat{H}_k) \right] \quad (3.6.7.5)$$

$$K^{\phi I} = \left[\int_{\mathcal{V}_M} \nabla \chi_q \cdot \mu^S(\hat{H}_k) \right] \quad (3.6.7.6)$$

$$K^{\phi\phi} = \left[- \int_{\mathcal{V}_M} \nabla \chi_q \cdot \mu^S(\nabla \chi_r) \right] \quad (3.6.7.7)$$

$$K^{II} = \left[\int_{\mathcal{V}_M} \mu^S(\hat{H}_k) \cdot \hat{H}_p \right] \quad (3.6.7.8)$$

and

$$F = \left[\int_{\partial \mathcal{V}_E} \psi_m \cdot T n \right] \quad (3.6.7.9)$$

$$Q = \left[\int_{\partial \mathcal{V}_M} \chi_q B \cdot n \right] \quad (3.6.7.10)$$

$$q = \left[\sum_l \int_{S_l^p} B \cdot n \right] = \text{fluxes through coils.} \quad (3.6.7.11)$$

The flux through a coil is related to the voltage on the coil. The electric field E satisfies Maxwell's equation

$$\text{curl } E = -\dot{B} = -i\omega B. \quad (3.6.7.12)$$

Integrating the normal component of equation (3.6.7.12) over the surface S_l^p bounded by the l -th loop of the p -th coil and using Stoke's theorem, gives

$$\int_{S_l^p} \text{curl } E \cdot n = \oint_{\mathcal{C}_l^p} E \cdot ds = -i\omega \int_{S_l^p} B \cdot n. \quad (3.6.7.13)$$

Thus, the voltage V_p on the p -th coil is given by

$$V_p = \sum_l \oint_{\mathcal{C}_l^p} E \cdot ds = -i\omega \sum_l \int_{S_l^p} B \cdot n = -i\omega q_p. \quad (3.6.7.14)$$

3.7 Variational Approximations

In addition to forming the basis of many computational schemes, variational methods can also serve as a starting point for developing simple approximations. In this section we will show how the variational methods we have discussed previously can be used to develop simple models for transducer components and their equivalent circuit representation. The stationary nature of variational functionals near the solution means that fairly crude approximations for the displacement shape can produce quite accurate approximations for such quantities as stored energy and resonance frequencies. Simple models will be developed for two example problems. The first example problem is the longitudinal vibration of a cylindrical bar. The second example problem is the longitudinal vibration of a stack of piezoelectric ceramic pieces having nonuniform material properties. In both cases we will develop simple equivalent circuits representing the models.

3.7.1 Longitudinal Vibration of a Cylindrical Bar

Consider a cylindrical elastic bar with its axis in the x -direction as shown in figure 3.11.

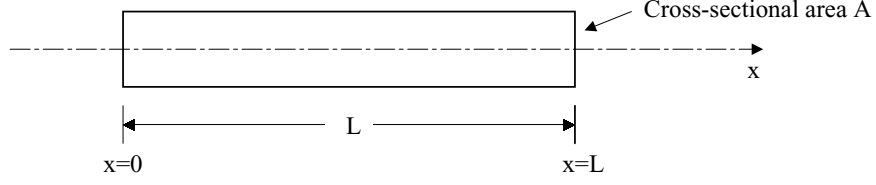


Figure 3.11. An elastic bar

It will be assumed that all quantities have only an x dependence and that all vector components not in the x -direction are zero. With these assumptions the equation of motion becomes

$$T'_{xx} = \rho \ddot{u}_x \quad (3.7.1.1)$$

where T is the stress tensor and u is the displacement. It will be assumed that u_x varies linearly along the bar, i.e.,

$$u(x) = u_0 \phi_0(x) + u_L \phi_L(x) \quad (3.7.1.2)$$

where ϕ_0 and ϕ_L are linear interpolation functions defined by

$$\phi_0(x) = 1 - x/L \quad (3.7.1.3)$$

$$\phi_L(x) = x/L. \quad (3.7.1.4)$$

Following Galerkin's method we multiply equation (3.7.1.1) by each interpolation function and integrate from 0 to L . This gives

$$\int_0^L T'_{xx} \phi_0 dx = \int_0^L \rho \ddot{u}_x \phi_0 dx \quad (3.7.1.5)$$

$$\int_0^L T'_{xx} \phi_L dx = \int_0^L \rho \ddot{u}_x \phi_L dx. \quad (3.7.1.6)$$

Integrating these equations by parts gives

$$T_{xx} \phi_0 \Big|_0^L - \int_0^L T_{xx} \phi'_0 dx = \rho \int_0^L \ddot{u}_x \phi_0 dx \quad (3.7.1.7)$$

$$T_{xx} \phi_L \Big|_0^L - \int_0^L T_{xx} \phi'_L dx = \rho \int_0^L \ddot{u}_x \phi_L dx \quad (3.7.1.8)$$

or equivalently

$$\rho \int_0^L \ddot{u}_x \phi_0 dx + \int_0^L T_{xx} \phi'_0 dx = -T_{xx}(0) \quad (3.7.1.9)$$

$$\rho \int_0^L \ddot{u}_x \phi_L dx + \int_0^L T_{xx} \phi'_L dx = T_{xx}(L). \quad (3.7.1.10)$$

The constitutive equation for the elastic bar can be approximated by

$$T_{xx} = Y u'_x \quad (3.7.1.11)$$

where Y is Young's modulus for the material. Substituting equation (3.7.1.11) into equations (3.7.1.9)–(3.7.1.10), we obtain

$$\rho \int_0^L \ddot{u}_x \phi_0 dx + Y \int_0^L u'_x \phi'_0 dx = -T_{xx}(0) \quad (3.7.1.12)$$

$$\rho \int_0^L \ddot{u}_x \phi_L dx + Y \int_0^L u'_x \phi'_L dx = T_{xx}(L). \quad (3.7.1.13)$$

Combining equation (3.7.1.2) with equations (3.7.1.12)–(3.7.1.13), we get

$$\begin{aligned} \rho \ddot{u}_0 \int_0^L \phi_0^2 dx + \rho \ddot{u}_L \int_0^L \phi_0 \phi_L dx \\ + Y u_0 \int_0^L (\phi'_0)^2 dx + Y u_L \int_0^L \phi'_0 \phi'_L dx = -T_{xx}(0) \end{aligned} \quad (3.7.1.14)$$

$$\begin{aligned} \rho \ddot{u}_0 \int_0^L \phi_0 \phi_L dx + \rho \ddot{u}_L \int_0^L \phi_L^2 dx \\ + Y u_0 \int_0^L \phi'_0 \phi'_L dx + Y u_L \int_0^L (\phi'_L)^2 dx = T_{xx}(L). \end{aligned} \quad (3.7.1.15)$$

It is easily verified that

$$\begin{aligned} \int_0^L \phi_0^2 dx = \int_0^L \phi_L^2 dx = \frac{L}{3} \quad \text{and} \quad \int_0^L \phi_0 \phi_L dx = \frac{L}{6} \\ \int_0^L (\phi'_0)^2 dx = \int_0^L (\phi'_L)^2 dx = \frac{1}{L} \quad \text{and} \quad \int_0^L \phi'_0 \phi'_L dx = -\frac{1}{L}. \end{aligned}$$

Using these relations, equations (3.7.1.14)–(3.7.1.15) can be written

$$\frac{\rho L}{3} \ddot{u}_0 + \frac{\rho L}{6} \ddot{u}_L + \frac{Y}{L} u_0 - \frac{Y}{L} u_L = -T_{xx}(0) \quad (3.7.1.16)$$

$$\frac{\rho L}{6} \ddot{u}_0 + \frac{\rho L}{3} \ddot{u}_L - \frac{Y}{L} u_0 + \frac{Y}{L} u_L = T_{xx}(L) \quad (3.7.1.17)$$

In the frequency domain equations (3.7.1.16)–(3.7.1.17) can be written

$$i\omega \rho \frac{L}{3} v_0 + i\omega \rho \frac{L}{6} v_L + \frac{Y}{i\omega L} v_0 - \frac{Y}{i\omega L} v_L = -T_{xx}(0) \quad (3.7.1.18)$$

$$i\omega \rho \frac{L}{6} v_0 + i\omega \rho \frac{L}{3} v_L - \frac{Y}{i\omega L} v_0 + \frac{Y}{i\omega L} v_L = T_{xx}(L) \quad (3.7.1.19)$$

where v_0 and v_L are the velocities at the two ends of the bar. These equations can be represented by the equivalent circuit where $M = \rho AL$ is the mass of the bar and $C = L/(YA)$ is the compliance of the bar.

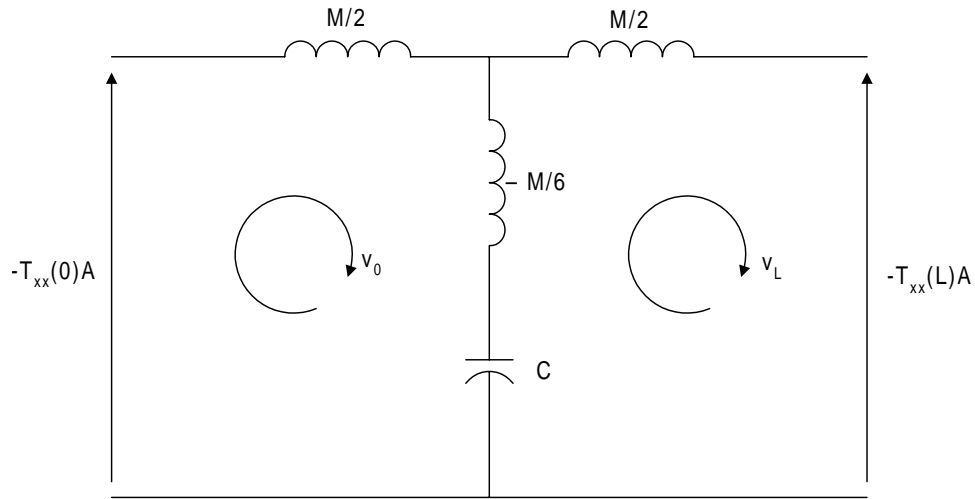


Figure 3.12. Equivalent circuit for the longitudinal vibration of a bar

3.7.2 Vibration of a Ceramic Stack with Nonuniform Material Properties

Consider a stack of ceramic pieces as shown in figure 3.13. Each ceramic piece has a thin

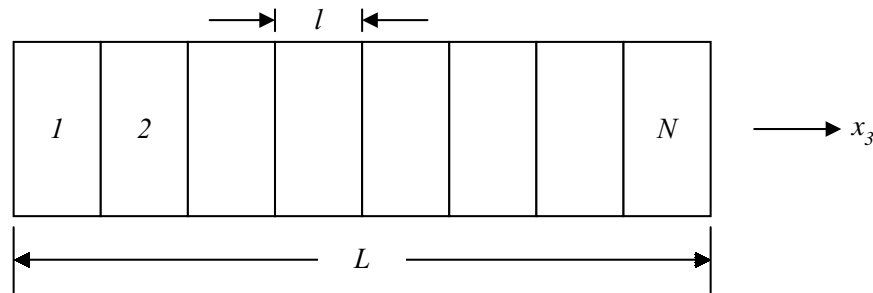


Figure 3.13. Stack of Ceramic Pieces

electrode on each of the parallel surfaces orthogonal to the x_3 direction. The pieces in the stack are arranged so that the polarization directions alternate between $\pm x_3$. Thus, any two adjacent pieces have opposite polarization directions. The ceramic pieces are wired in parallel with every other electrode at zero potential. In the approximate model it will be assumed that all variables have only an x_3 spatial dependence and have components only in the x_3 direction. This assumption leads to the following one-dimensional equations for a

ceramic piece

$$T'_{33} = \rho \ddot{u}_3 = i\omega \rho v_3 \quad \text{Balance of momentum} \quad (3.7.2.1)$$

$$S_{33} = u'_3 \quad \text{Strain-displacement relation} \quad (3.7.2.2)$$

$$S_{33} = s_{33}^E T_{33} + d_{33} \mathcal{E}_3 \quad \text{Constitutive relation} \quad (3.7.2.3)$$

$$\mathcal{D}_3 = d_{33} T_{33} + \epsilon_{33}^T \mathcal{E}_3 \quad \text{Constitutive relation} \quad (3.7.2.4)$$

where u_3 is the x_3 component of displacement, T_{33} is the 33-component of the stress tensor T , ρ is the density, S_{33} is the 33-component of the strain tensor S , \mathcal{E}_3 is the 3-component of the electric field, \mathcal{D}_3 is the 3-component of the electric displacement, and s_{33}^E , d_{33} , ϵ_{33}^T are material constants. Moreover, \square' denotes differentiation with respect to x_3 . It will be assumed that the density, length, and cross-sectional area of each ceramic piece are the same, but that s_{33}^E , d_{33} , and ϵ_{33}^T vary from piece to piece. Let $s_{33}^E(n)$, $d_{33}(n)$, and $\epsilon_{33}^T(n)$ denote the parameters for the n -th piece.

Assume that the displacement u_3 varies linearly across the stack, i.e.,

$$u_3(x_3) \doteq u_0 \psi_0(x_3) + u_1 \psi_1(x_3) \quad (3.7.2.5)$$

where u_0 and u_1 are the displacements at the left and right ends of the stack respectively and ψ_0 , ψ_1 are the linear interpolation functions on $0 \leq x_3 \leq L$ defined by

$$\psi_0(x) = 1 - x/L \quad (3.7.2.6)$$

$$\psi_1(x) = x/L. \quad (3.7.2.7)$$

Following Galerkin's method, we multiply equation (3.7.2.1) by ψ_n and integrate from 0 to L . This yields

$$\int_0^L T'_{33} \psi_n dx_3 = i\omega \rho \int_0^L v_3 \psi_n dx_3 \quad n = 0, 1. \quad (3.7.2.8)$$

Integrating equation (3.7.2.8) by parts, we get

$$i\omega \rho \int_0^L v_3 \psi_n dx_3 + \int_0^L T_{33} \psi'_n dx_3 = T_{33} \psi_n \Big|_0^L \quad n = 0, 1. \quad (3.7.2.9)$$

It follows from equations (3.7.2.2) and (3.7.2.3) that

$$T_{33} = \frac{1}{s_{33}^E} u'_3 - \frac{d_{33}}{s_{33}^E} \mathcal{E}_3. \quad (3.7.2.10)$$

Substituting equation (3.7.2.10) into equation (3.7.2.9), we get

$$i\omega \rho \int_0^L v_3 \psi_n dx_3 + \int_0^L \frac{1}{s_{33}^E} u'_3 \psi'_n dx_3 - \int_0^L \frac{d_{33}}{s_{33}^E} \mathcal{E}_3 \psi'_n dx_3 = T_{33} \psi_n \Big|_0^L \quad n = 0, 1. \quad (3.7.2.11)$$

Assume that the potential varies approximately linearly across each ceramic piece. Then the electric field \mathcal{E}_3 is approximately constant in each ring. The voltage E on each ring is given approximately by

$$E \doteq \mathcal{E}_3 l. \quad (3.7.2.12)$$

It follows from equations (3.7.2.5)–(3.7.2.7) that

$$v_3 = v_0 \psi_0 + v_1 \psi_1 \quad (3.7.2.13)$$

$$\psi'_0 = -\frac{1}{L} \quad (3.7.2.14)$$

$$\psi'_1 = \frac{1}{L} \quad (3.7.2.15)$$

$$u'_3 = \frac{u_1 - u_0}{L}. \quad (3.7.2.16)$$

Moreover,

$$\int_0^L \psi_0^2 dx_3 = \int_0^L \psi_1^2 dx_3 = \frac{L}{3} \quad (3.7.2.17)$$

and

$$\int_0^L \psi_0 \psi_1 dx_3 = \frac{L}{6}. \quad (3.7.2.18)$$

Substituting equations (3.7.2.12)–(3.7.2.18) into each of the equations that make up equation (3.7.2.11), we get

$$i\omega\rho\left(v_0\frac{L}{3} + v_1\frac{L}{6}\right) - \frac{u_1 - u_0}{L^2} \int_0^L \frac{1}{s_{33}^E} dx_3 + \frac{E}{lL} \int_0^L \frac{d_{33}}{s_{33}^E} dx_3 = -T_{33}(0) \quad (3.7.2.19)$$

$$i\omega\rho\left(v_0\frac{L}{6} + v_1\frac{L}{3}\right) + \frac{u_1 - u_0}{L^2} \int_0^L \frac{1}{s_{33}^E} dx_3 - \frac{E}{lL} \int_0^L \frac{d_{33}}{s_{33}^E} dx_3 = T_{33}(L). \quad (3.7.2.20)$$

Since the polarization direction changes from piece to piece, the constant d_{33} changes sign from piece to piece. However, the voltage E also changes sign in the same way. In equations (3.7.2.19)–(3.7.2.20) the parameter d_{33} always occurs in the combination Ed_{33} . Therefore, it is not necessary change the signs from piece to piece. If we define

$$Y_{33}^E(n) = \frac{1}{s_{33}^E(n)} \quad \text{and} \quad \phi(n) = \frac{d_{33}(n)A}{s_{33}^E(n)l}, \quad (3.7.2.21)$$

then the integrals in equations (3.7.2.19)–(3.7.2.20) can be written

$$\int_0^L \frac{1}{s_{33}^E} dx_3 = l \sum_{n=1}^N \frac{1}{s_{33}^E(n)} = l \sum_{n=1}^N Y_{33}^E(n) \quad (3.7.2.22)$$

$$\int_0^L \frac{d_{33}}{s_{33}^E} dx_3 = l \sum_{n=1}^N \frac{d_{33}(n)}{s_{33}^E(n)} = \frac{l^2}{A} \sum_{n=1}^N \phi(n). \quad (3.7.2.23)$$

If we define

$$\bar{Y}_{33}^E = \frac{1}{N} \sum_{n=1}^N Y_{33}^E(n) \quad (3.7.2.24)$$

$$\bar{\phi} = \frac{1}{N} \sum_{n=1}^N \phi(n), \quad (3.7.2.25)$$

then

$$\int_0^L \frac{1}{s_{33}^E} dx_3 = L \bar{Y}_{33}^E \quad (3.7.2.26)$$

$$\int_0^L \frac{d_{33}}{s_{33}^E} dx_3 = \frac{lL}{A} \bar{\phi}. \quad (3.7.2.27)$$

Thus, equations (3.7.2.19)–(3.7.2.20) can be written

$$i\omega\rho\left(v_0\frac{L}{3} + v_1\frac{L}{6}\right) - \frac{u_1 - u_0}{L} \bar{Y}_{33}^E + \frac{\bar{\phi}E}{A} = -T_{33}(0) \quad (3.7.2.28)$$

$$i\omega\rho\left(v_0\frac{L}{6} + v_1\frac{L}{3}\right) + \frac{u_1 - u_0}{L} \bar{Y}_{33}^E - \frac{\bar{\phi}E}{A} = T_{33}(L). \quad (3.7.2.29)$$

If we define

$$M = \rho LA \quad (3.7.2.30)$$

$$\bar{K} = \frac{\bar{Y}_{33}^E A}{L} \quad (3.7.2.31)$$

and

$$F_0 = -T_{33}(0)A \quad (3.7.2.32)$$

$$F_1 = -T_{33}(L)A, \quad (3.7.2.33)$$

then equations (3.7.2.28)–(3.7.2.29) become

$$\left(i\omega\frac{M}{3} + \frac{\bar{K}}{i\omega}\right)v_0 + \left(i\omega\frac{M}{6} - \frac{\bar{K}}{i\omega}\right)v_1 + \bar{\phi}E = F_0 \quad (3.7.2.34)$$

$$\left(-i\omega\frac{M}{6} + \frac{\bar{K}}{i\omega}\right)v_0 - \left(i\omega\frac{M}{3} + \frac{\bar{K}}{i\omega}\right)v_1 + \bar{\phi}E = F_1. \quad (3.7.2.35)$$

The electric displacement $\vec{\mathcal{D}}$ satisfies Maxwell's equation

$$\mathbf{div} \vec{\mathcal{D}} = \rho_e \quad (3.7.2.36)$$

where ρ_e is the free-charge density. In the ceramic there is no free-charge, and hence

$$\mathbf{div} \vec{\mathcal{D}} = 0. \quad (3.7.2.37)$$

Since we are assuming that $\vec{\mathcal{D}}$ has only a 3-component, it follows that \mathcal{D}_3 is constant in a ceramic piece. Applying the divergence theorem to equation (3.7.2.36) for a small cylindrical volume with axis in the x_3 -direction that contains the charge on the electrode and has one face in the ceramic and the other inside the electrode, we get

$$\mathcal{D}_3 = \frac{Q}{A} = \frac{I}{i\omega A}. \quad (3.7.2.38)$$

Here Q is the positive charge on the electrode and I is the current into the electrode. Combining this relation with equation (3.7.2.4), we obtain

$$\begin{aligned} I &= i\omega d_{33}AT_{33} + i\omega\epsilon_{33}^T\mathcal{E}_3 \\ &= i\omega d_{33}AT_{33} + i\omega\left(\frac{\epsilon_{33}^T A}{l}\right)E. \end{aligned} \quad (3.7.2.39)$$

If we now combine equation (3.7.2.39) with equation (3.7.2.10), we get

$$\begin{aligned} I &= i\omega d_{33}A\left(\frac{1}{s_{33}^E}u'_3 - \frac{d_{33}}{s_{33}^E}\frac{E}{l}\right) + i\omega\left(\frac{\epsilon_{33}^T A}{l}\right)E \\ &= i\omega\frac{d_{33}A}{s_{33}^E}u'_3 + i\omega\left(\epsilon_{33}^T - \frac{d_{33}^2}{s_{33}^E}\right)\frac{A}{l}E \\ &= \frac{d_{33}A}{s_{33}^E L}(v_1 - v_0) + i\omega\frac{(\epsilon_{33}^T - d_{33}^2/s_{33}^E)A}{l}E. \end{aligned} \quad (3.7.2.40)$$

If we define

$$C_0 = \frac{(\epsilon_{33}^T - d_{33}^2/s_{33}^E)A}{l}, \quad (3.7.2.41)$$

then equation (3.7.2.40) can be written

$$I = \frac{\phi}{N}(v_1 - v_0) + i\omega C_0 E. \quad (3.7.2.42)$$

Thus, for the n -th ring we have

$$I(n) = \frac{\phi(n)}{N}(v_1 - v_0) + i\omega C_0(n)E. \quad (3.7.2.43)$$

A reversal of the polarization direction changes the signs of $I(n)$, $\phi(n)$, and E . Thus, equation (3.7.2.43) remains valid for either polarization direction. Summing equation (3.7.2.43) over n , we get

$$I = \sum_{n=1}^N I(n) = \left(\frac{1}{N} \sum_{n=1}^N \phi(n) \right) (v_1 - v_0) + i\omega \sum_{n=1}^N C_0(n) E \quad (3.7.2.44)$$

where I is the total current into the stack. If we define

$$\bar{C}_0 = \frac{1}{N} \sum_{n=1}^N C_0(n), \quad (3.7.2.45)$$

then equation (3.7.2.44) can be written

$$I = \bar{\phi}(v_1 - v_0) + i\omega N \bar{C}_0 E. \quad (3.7.2.46)$$

In summary, the equations for the stack can be written

$$\begin{aligned} \left(i\omega \frac{M}{3} + \frac{\bar{K}}{i\omega} \right) v_0 + \left(i\omega \frac{M}{6} - \frac{\bar{K}}{i\omega} \right) v_1 + \bar{\phi} E &= F_0 \\ \left(-i\omega \frac{M}{6} + \frac{\bar{K}}{i\omega} \right) v_0 - \left(i\omega \frac{M}{3} + \frac{\bar{K}}{i\omega} \right) v_1 + \bar{\phi} E &= F_1. \\ \bar{\phi}(v_1 - v_0) + i\omega N \bar{C}_0 E &= I \end{aligned}$$

where

$$\begin{aligned} M &= \rho AL \\ \bar{K} &= \frac{\bar{Y}_{33}^E A}{L} \\ \bar{\phi} &= \frac{1}{N} \sum_{n=1}^N \phi(n) \\ \bar{C}_0 &= \frac{1}{N} \sum_{n=1}^N C_0(n) \end{aligned}$$

and

$$\begin{aligned} F_0 &= -T_{33}(0)A \\ F_1 &= -T_{33}(L)A. \end{aligned}$$

These equations can be represented by the following equivalent circuit

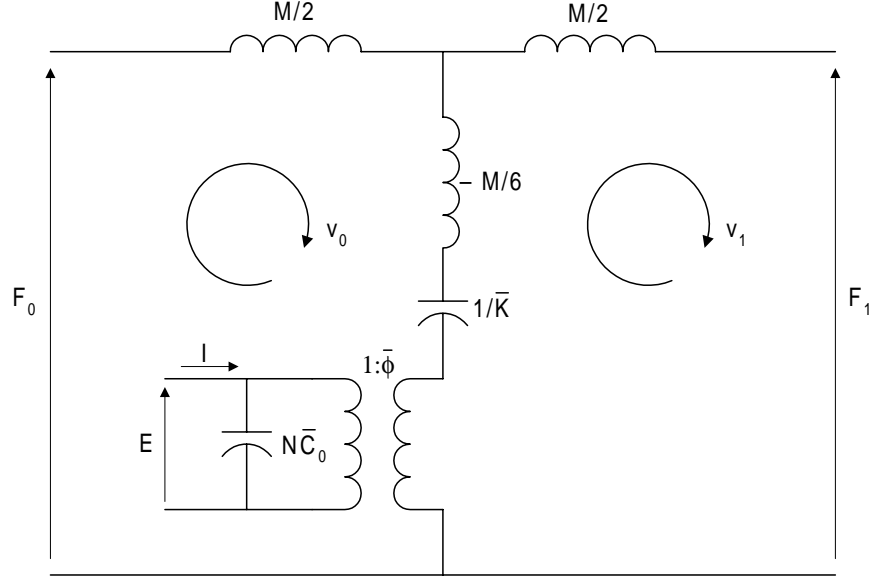


Figure 3.14. Equivalent circuit for a ceramic stack with nonidentical pieces

3.8 One-dimensional (plane wave) Model of a Piezoelectric Rod

In this section we will develop a one-dimensional model for a piezoelectric ceramic rod polarized in the length direction. Figure 3.15 shows a piezoelectric ceramic rod of length L polarized in the x_3 direction. The rod is electroded on the ends as shown. The voltage and current at the electrical terminals are denoted by E and I . Since the piezoelectric material is polarized, the orientation of E and I relative to the direction of polarization is important. It will be assumed that there is no variation of any of the physical quantities in the x_1 and x_2 directions. For this reason the model we are developing is also called a plane wave model.

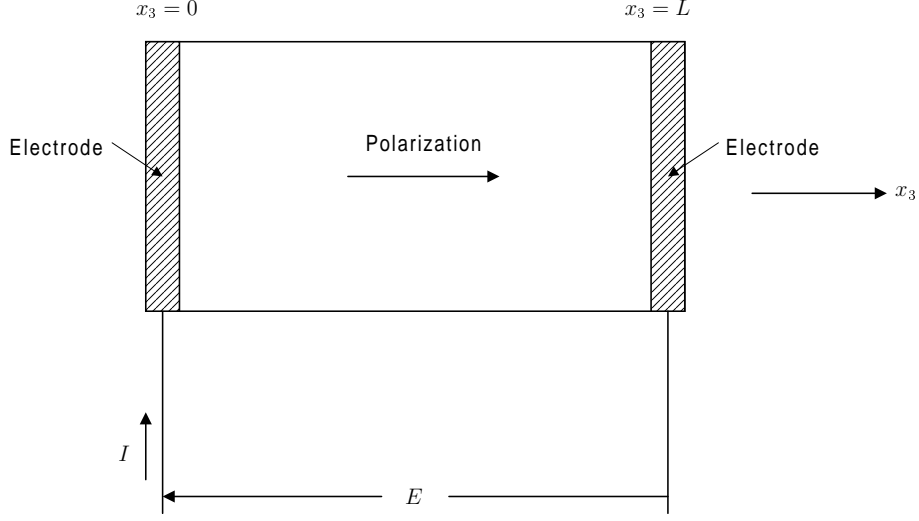


Figure 3.15. Piezoelectric ceramic rod polarized in the axial direction

In addition, it will be assumed that there is no fringing of the electric field, i.e., the electric field is confined to the piezoelectric material. Derivatives with respect to x_3 will be denoted by a prime, i.e., $\frac{d\Box}{dx_3} = \Box'$. With the above assumptions the equation of motion becomes

$$T'_{33} = -\omega^2 \rho u_3 \quad (3.8.1)$$

where ρ is the density of the material, T_{33} is the 33-component of the stress tensor, and u_3 is the 3-component of the displacement.

The constitutive equations can be written

$$S_{33} = S_{33}^D T_{33} + g_{33} \mathcal{D}_3 \quad (3.8.2)$$

$$\mathcal{E}_3 = -g_{33} T_{33} + \frac{1}{\epsilon_{33}^T} \mathcal{D}_3 \quad (3.8.3)$$

where S_{33} is the 33-component of the strain tensor, \mathcal{D}_3 is the 3-component of electric displacement, and \mathcal{E}_3 is the 3-component of electric field. The strain is related to displacement by

$$S_{33} = u'_3. \quad (3.8.4)$$

The electric displacement \mathcal{D} satisfies Maxwell's equation

$$\mathbf{div} \mathcal{D} = \rho_e \quad (3.8.5)$$

where ρ_e is the free charge density. The charge density is positive for positive charge and negative for negative charge. Since the piezoelectric ceramic material is a dielectric, there

is no free charge inside the ceramic rod. All of the free charge is confined to the electrodes. Thus, it follows from equation (3.8.5) that

$$\mathcal{D}'_3 = 0 \quad \text{inside the piezoelectric rod} \quad (3.8.6)$$

and hence \mathcal{D}_3 is constant along the length of the rod. If we assume that the electrodes are perfect conductors, then \mathcal{D} vanishes inside the electrodes. Since we are assuming no fringing, \mathcal{D} vanishes outside the rod. We will also assume that \mathcal{D}_3 is constant across the cross-section of the rod.

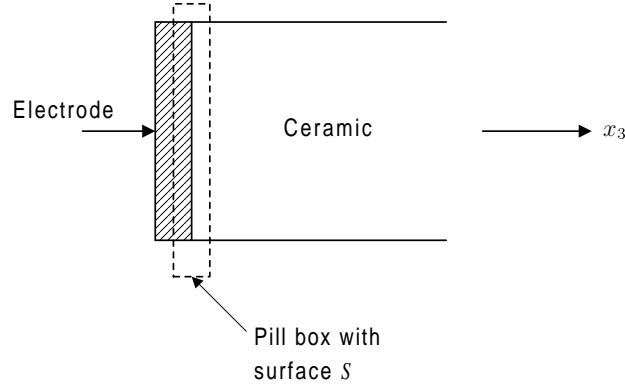


Figure 3.16. Pill box surrounding interface between piezoelectric material and electrode

If we integrate equation (3.8.5) over the volume of the pill box shown in figure 3.16 and apply the divergence theorem, we obtain

$$\int_S \mathcal{D} \cdot n = Q \quad (3.8.7)$$

where Q is the charge on the electrode, S is the surface of the pill box, and n is the outward normal to S . In view of the assumptions we have made concerning \mathcal{D} , equation (3.8.7) becomes

$$Q = \int_S \mathcal{D} \cdot n \doteq \mathcal{D}_3 A \quad (3.8.8)$$

where A is the cross-sectional area of the rod. The current I is the time derivative of the charge Q . Thus,

$$\mathcal{D}_3 = \frac{Q}{A} = \frac{I}{i\omega A}. \quad (3.8.9)$$

Solving the constitutive equation (3.8.2) for T_{33} and making use of equation (3.8.4), we get

$$T_{33} = \frac{1}{S_{33}^D} u'_3 - \frac{g_{33}}{S_{33}^D} \mathcal{D}_3. \quad (3.8.10)$$

Substituting equation (3.8.10) into equation (3.8.3), we get

$$\mathcal{E}_3 = -\frac{g_{33}}{S_{33}^D} u'_3 + \left(\frac{1}{\epsilon_{33}^T} + \frac{g_{33}^2}{S_{33}^D} \right) \mathcal{D}_3. \quad (3.8.11)$$

Since we are neglecting magnetic effects, the electric field is given by the gradient of a potential, i.e.,

$$\mathcal{E} = -\nabla\phi. \quad (3.8.12)$$

Therefore,

$$\int_0^L \mathcal{E}_3 dx_3 = \phi_0 - \phi_L = E \quad (3.8.13)$$

where ϕ_0 is the potential at $x_3 = 0$, ϕ_L is the potential at $x_3 = L$, and E is the terminal voltage as shown in figure 3.15. Integrating equation (3.8.11) over the length of the rod and making use of equation (3.8.13), we get

$$\begin{aligned} E &= -\frac{g_{33}}{S_{33}^D} [u_3(L) - u_3(0)] + \left(\frac{1}{\epsilon_{33}^T} + \frac{g_{33}^2}{S_{33}^D} \right) \mathcal{D}_3 L \\ &= -\frac{g_{33}}{i\omega S_{33}^D} [v_3(L) - v_3(0)] + \left(\frac{1}{\epsilon_{33}^T} + \frac{g_{33}^2}{S_{33}^D} \right) \frac{IL}{i\omega A} \end{aligned} \quad (3.8.14)$$

where v_3 is the velocity in the 3-direction. Let us define

$$\epsilon_{LC} = \left(\frac{1}{\epsilon_{33}^T} + \frac{g_{33}^2}{S_{33}^D} \right)^{-1} \quad (3.8.15)$$

$$C_0 = \frac{\epsilon_{LC} A}{L} \quad (3.8.16)$$

$$\mathcal{N} = \frac{g_{33} C_0}{S_{33}^D}. \quad (3.8.17)$$

Then, equation (3.8.14) becomes

$$E = -\frac{\mathcal{N}}{i\omega C_0} [v_3(L) - v_3(0)] + \frac{I}{i\omega C_0}. \quad (3.8.18)$$

Substituting equation (3.8.4) into equation (3.8.2), we get

$$u'_3 = S_{33}^D T_{33} + g_{33} \mathcal{D}_3. \quad (3.8.19)$$

Differentiating equation (3.8.19) and making use of equations (3.8.1) and (3.8.6), we get

$$u''_3 = -\omega^2 \rho S_{33}^D u_3$$

or equivalently

$$u''_3 + k^2 u_3 = 0 \quad (3.8.20)$$

where

$$k^2 = \omega^2 \rho S_{33}^D = \frac{\omega^2}{c^2} \quad , \quad c^2 = \frac{1}{\rho S_{33}^D}. \quad (3.8.21)$$

Thus, u_3 satisfies a one-dimensional wave equation. Clearly, v_3 satisfies this same wave equation, i.e.,

$$v_3'' + k^2 v_3 = 0. \quad (3.8.22)$$

The general solution of equation (3.8.22) has the form

$$v_3(x_3) = \alpha \sin(kx_3) + \beta \cos(kx_3). \quad (3.8.23)$$

Evaluating equation (3.8.23) at $x_3 = 0$ and $x_3 = L$, we get

$$v_3(0) = \beta \quad (3.8.24)$$

$$v_3(L) = \alpha \sin(kL) + \beta \cos(kL). \quad (3.8.25)$$

Solving equations (3.8.24)–(3.8.25), we get

$$\beta = v_3(0) \quad (3.8.26)$$

$$\alpha = \frac{v_3(L) - v_3(0) \cos(kL)}{\sin(kL)}. \quad (3.8.27)$$

Differentiating equation (3.8.23), we obtain

$$v_3'(x_3) = k(\alpha \cos kx_3 - \beta \sin kx_3). \quad (3.8.28)$$

Evaluating equation (3.8.28) at $x_3 = 0$ and $x_3 = L$, we get

$$v_3'(0) = k\alpha \quad (3.8.29)$$

$$v_3'(L) = k(\alpha \cos kL - \beta \sin kL). \quad (3.8.30)$$

Equation (3.8.10) can be written

$$T_{33} = \frac{1}{i\omega S_{33}^D} v_3' - \frac{g_{33}}{S_{33}^D} \frac{I}{i\omega A}. \quad (3.8.31)$$

Substituting equation (3.8.29) into equation (3.8.31), we get

$$T_{33}(0) = \frac{k\alpha}{i\omega S_{33}^D} - \frac{g_{33}}{S_{33}^D} \frac{I}{i\omega A}. \quad (3.8.32)$$

It is easily verified from the definitions in equation (3.8.21) that

$$\frac{k}{\omega S_{33}^D} = \rho c. \quad (3.8.33)$$

It follows from the definition given in equation (3.8.17) that

$$\frac{g_{33}}{S_{33}^D} = \frac{\mathcal{N}}{C_0}. \quad (3.8.34)$$

Combining equations (3.8.32)–(3.8.34), we get

$$T_{33}(0) = -i\rho c\alpha - \frac{\mathcal{N}I}{i\omega C_0 A}. \quad (3.8.35)$$

Substituting equation (3.8.27) into equation (3.8.35) and rearranging terms, we obtain

$$-T_{33}(0)A = -i\rho cA[v_3(0)\cot(kL) - v_3(L)\csc(kL)] + \frac{\mathcal{N}}{i\omega C_0}I. \quad (3.8.36)$$

In a similar manner it can be shown that

$$-T_{33}(L)A = i\rho cA[v_3(L)\cot(kL) - v_3(0)\csc(kL)] + \frac{\mathcal{N}}{i\omega C_0}I. \quad (3.8.37)$$

If we define impedances z_1 and z_2 by

$$z_1 = i\rho cA \tan(\tfrac{1}{2}kL) \quad z_2 = \frac{\rho cA}{i \sin(kL)}, \quad (3.8.38)$$

then equations (3.8.36)–(3.8.37) can be written

$$-T_{33}(0)A = (z_1 + z_2)v_3(0) - z_2v_3(L) + \frac{\mathcal{N}}{i\omega C_0}I \quad (3.8.39)$$

$$-T_{33}(L)A = z_2v_3(0) - (z_1 + z_2)v_3(L) + \frac{\mathcal{N}}{i\omega C_0}I \quad (3.8.40)$$

Equations (3.8.39)–(3.8.40) together with equation (3.8.18) can be represented by the equivalent circuit shown in figure 3.17.

The equations for a nonpiezoelectric elastic rod are the same as those given in equations (3.8.39)–(3.8.40) with the last term in each equation omitted, i.e.,

$$-T_{33}(0)A = (z_1 + z_2)v_3(0) - z_2v_3(L) \quad (3.8.41)$$

$$-T_{33}(L)A = z_2v_3(0) - (z_1 + z_2)v_3(L) \quad (3.8.42)$$

The equivalent circuit for an elastic rod is shown in figure 3.18.

Let us now consider the case of two piezoelectric pieces placed end to end and connected electrically in parallel as shown in figure 3.19. Notice that the polarization is in opposite directions in the two pieces. There are a number of sign changes that occur when the

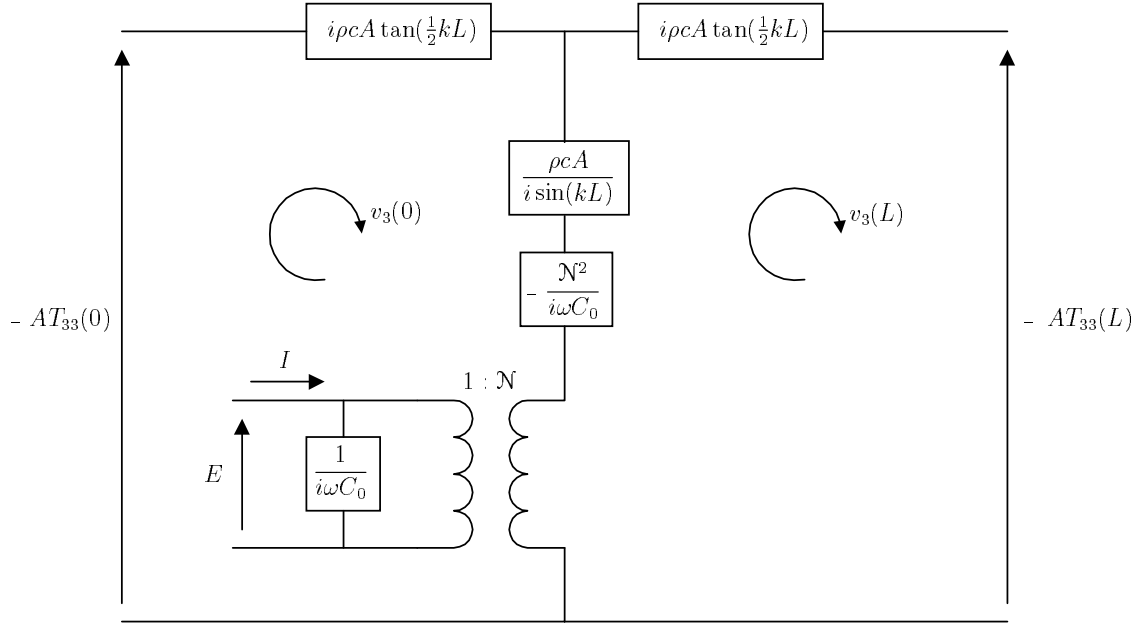


Figure 3.17. Equivalent circuit for a piezoelectric ceramic rod

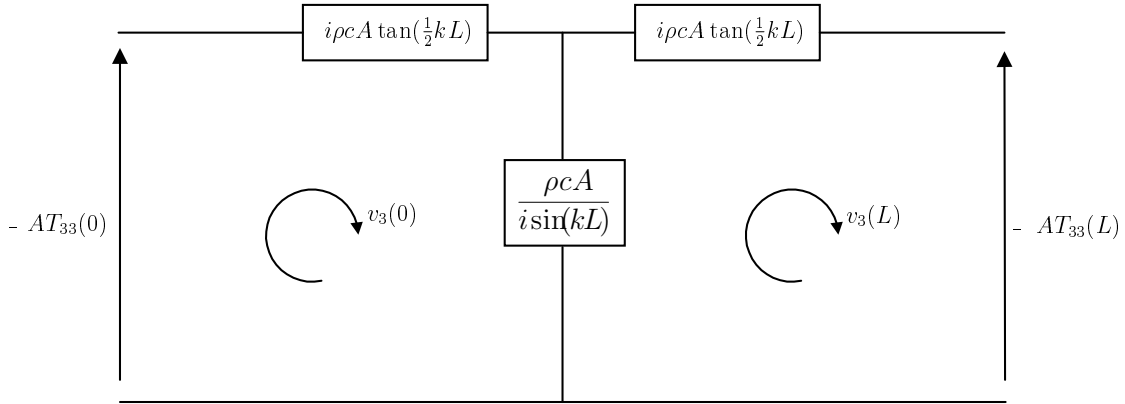


Figure 3.18. Equivalent circuit for an elastic rod

polarization is in the negative x_3 -direction, but as we will see these sign changes always occur in pairs. The equations for the second piece are exactly the same as for the first piece if they are referred to an axis pointing in the negative x_3 -direction. Thus, we need to see what happens when the direction of the x_3 -axis is reversed. The constitutive equations as usually presented assume that the x_3 -axis is the direction of polarization. If we reverse this axis the sign of g_{33} changes. However, the sign of \mathcal{D}_3 also changes. Thus, the product $g_{33}\mathcal{D}_3$ remains unchanged. The stress component T_{33} is given by $T_{33} = \vec{e}_3 \cdot T \vec{e}_3$. Thus,

if the direction of \vec{e}_3 is reversed, the component T_{33} remains unchanged. Similarly, the strain component S_{33} remains unchanged when the axes are reversed. It follows that the constitutive relation (3.8.2) has the same form when the x_3 -axis is reversed. In the second constitutive equation \mathcal{E}_3 , \mathcal{D}_3 , and g_{33} change sign when the x_3 -axis is reversed. Thus, the second constitutive equation (3.8.3) also has the same form when the axes are reversed. The quantity $v_3(L) - v_3(0)$ occurring in equation (3.8.18) remains unchanged since the direction of e_3 reverses and the roles of the endpoints 0 and L interchange. Similarly, in equations (3.8.39)–(3.8.40) the roles of 0 and L are interchanged and the velocities v_3 change signs leaving the form of the two equations unchanged. Thus, we can use the same equations for the two pieces with the variables meaning the same thing in both.

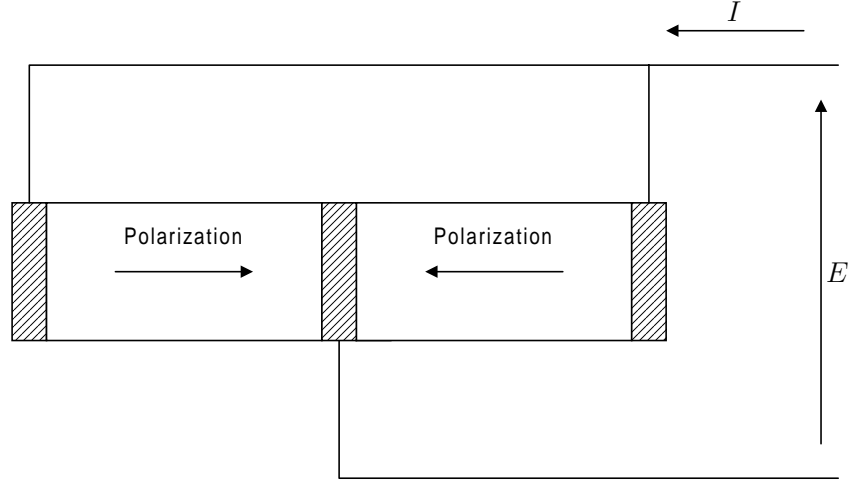


Figure 3.19. Two ceramic pieces connected electrically in parallel

3.9 One-dimensional Model of a Magnetostrictive Rod

In this article we will develop a one-dimensional model for a magnetostrictive rod biased in the length direction. Figure 3.20 shows a magnetostrictive rod of length L biased in the x_3 direction. The magnetic path is completed by a material having a very high magnetic permeability. Thus, the magnetic field \mathcal{H} vanishes in this portion of the magnetic path. The voltage and current at the electrical terminals are denoted by E and I . Since the magnetostrictive material is biased, the orientation of E and I relative to the bias direction is important. It is also important which direction the coil is wound around the rod. We will assume that there is no variation of any of the physical quantities in the x_1 and x_2 directions. For this reason the model we are developing is also called a plane wave model.

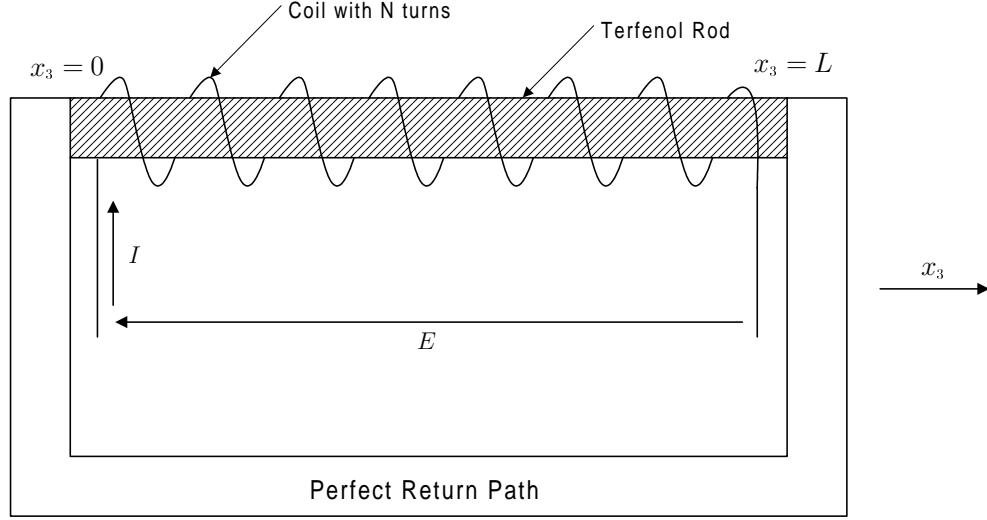


Figure 3.20. Magnetostrictive rod biased in the axial direction

In addition, it will be assumed that there is no fringing of the magnetic field, i.e., the magnetic field is confined to the magnetostrictive material. Derivatives with respect to x_3 will be denoted by a prime, i.e., $\frac{d\Box}{dx_3} = \Box'$. With the above assumptions the equation of motion becomes

$$T'_{33} = -\omega^2 \rho u_3 \quad (3.9.1)$$

where ρ is the density of the material, T_{33} is the 33-component of the stress tensor, and u_3 is the 3-component of the displacement.

The constitutive equations can be written

$$S_{33} = S_{33}^B T_{33} + g_{33} \mathcal{B}_3 \quad (3.9.2)$$

$$\mathcal{H}_3 = -g_{33} T_{33} + \frac{1}{\mu_{33}^T} \mathcal{B}_3 \quad (3.9.3)$$

where S_{33} is the 33-component of the strain tensor, \mathcal{H}_3 is the 3-component of the magnetic field, and \mathcal{B}_3 is the 3-component of the magnetic induction. The strain is related to displacement by

$$S_{33} = u'_3. \quad (3.9.4)$$

The magnetic induction \mathcal{B} satisfies Maxwell's equation

$$\text{div } \mathcal{B} = 0. \quad (3.9.5)$$

Because of equation (3.9.5) and the plane wave assumption, the magnetic induction \mathcal{B} is perpendicular to the cross-section of the magnetic path and is constant along the path. In particular,

$$\mathcal{B}'_3 = 0 \quad \text{in the magnetostrictive rod.} \quad (3.9.6)$$

Solving the constitutive equation (3.9.2) for T_{33} and making use of equation (3.9.4), we get

$$T_{33} = \frac{1}{S_{33}^B} u_3' - \frac{g_{33}}{S_{33}^B} \mathcal{B}_3. \quad (3.9.7)$$

Substituting equation (3.9.7) into equation (3.9.3), we get

$$\mathcal{H}_3 = -\frac{g_{33}}{S_{33}^B} u_3' + \left(\frac{1}{\mu_{33}^T} + \frac{g_{33}^2}{S_{33}^B} \right) \mathcal{B}_3. \quad (3.9.8)$$

Differentiating equation (3.9.7) and making use of equations (3.9.1) and (3.9.6), we get

$$u_3'' = -\omega^2 \rho S_{33}^B u_3$$

or equivalently

$$u_3'' + k^2 u_3 = 0 \quad \text{inside the magnetostrictive rod} \quad (3.9.9)$$

where

$$k^2 = \omega^2 \rho S_{33}^B = \frac{\omega^2}{c^2}, \quad c^2 = \frac{1}{\rho S_{33}^B}. \quad (3.9.10)$$

Thus, u_3 satisfies a one-dimensional wave equation. Clearly, v_3 satisfies this same wave equation, i.e.,

$$v_3'' + k^2 v_3 = 0 \quad \text{inside the magnetostrictive rod.} \quad (3.9.11)$$

The general solution of equation (3.9.11) has the form

$$v_3(x_3) = \alpha \sin(kx_3) + \beta \cos(kx_3). \quad (3.9.12)$$

Evaluating equation (3.9.12) at $x_3 = 0$ and $x_3 = L$, we get

$$v_3(0) = \beta \quad (3.9.13)$$

$$v_3(L) = \alpha \sin(kL) + \beta \cos(kL). \quad (3.9.14)$$

Solving equations (3.9.13)–(3.9.14), we get

$$\beta = v_3(0) \quad (3.9.15)$$

$$\alpha = \frac{v_3(L) - v_3(0) \cos(kL)}{\sin(kL)}. \quad (3.9.16)$$

Differentiating equation (3.9.12), we obtain

$$v_3'(x_3) = k(\alpha \cos kx_3 - \beta \sin kx_3). \quad (3.9.17)$$

Evaluating equation (3.9.17) at $x_3 = 0$ and $x_3 = L$, we get

$$v_3'(0) = k\alpha \quad (3.9.18)$$

$$v_3'(L) = k(\alpha \cos kL - \beta \sin kL). \quad (3.9.19)$$

Equation (3.9.7) can be written

$$T_{33} = \frac{1}{i\omega S_{33}^B} v_3' - \frac{g_{33}}{S_{33}^B} \mathcal{B}_3. \quad (3.9.20)$$

Substituting equation (3.9.18) into equation (3.9.20), we get

$$T_{33}(0) = \frac{k\alpha}{i\omega S_{33}^B} - \frac{g_{33}}{S_{33}^B} \mathcal{B}_3. \quad (3.9.21)$$

It is easily verified from the definitions in equation (3.9.10) that

$$\frac{k}{\omega S_{33}^B} = \rho c. \quad (3.9.22)$$

Combining equations (3.9.21)–(3.9.22), we get

$$T_{33}(0) = -i\rho c\alpha - \frac{g_{33}}{S_{33}^B} \mathcal{B}_3. \quad (3.9.23)$$

Substituting equation (3.9.16) into equation (3.9.23) and rearranging terms, we obtain

$$-T_{33}(0)A = -i\rho cA[v_3(0) \cot(kL) - v_3(L) \csc(kL)] + \frac{g_{33}A}{S_{33}^B} \mathcal{B}_3. \quad (3.9.24)$$

In a similar manner it can be shown that

$$-T_{33}(L)A = i\rho cA[v_3(L) \cot(kL) - v_3(0) \csc(kL)] + \frac{g_{33}A}{S_{33}^B} \mathcal{B}_3. \quad (3.9.25)$$

If we define impedances z_1 and z_2 by

$$z_1 = i\rho cA \tan(\tfrac{1}{2}kL) \quad z_2 = \frac{\rho cA}{i \sin(kL)}, \quad (3.9.26)$$

then equations (3.9.24)–(3.9.25) can be written

$$-T_{33}(0)A = (z_1 + z_2)v_3(0) - z_2v_3(L) + \frac{g_{33}A}{S_{33}^B} \mathcal{B}_3 \quad (3.9.27)$$

$$-T_{33}(L)A = z_2v_3(0) - (z_1 + z_2)v_3(L) + \frac{g_{33}A}{S_{33}^B} \mathcal{B}_3. \quad (3.9.28)$$

We will now show that the magnetic induction \mathcal{B}_3 can be related to the voltage E at the terminals of the coil. Consider a loop of wire as shown in figure 3.21. Let \mathcal{C} be a closed path that is along the centerline of the wire. By Stoke's theorem,

$$\oint_{\mathcal{C}} \mathcal{E} \cdot d\mathbf{l} = \int_S \text{curl } \mathcal{E} \cdot \mathbf{n} dS \quad (3.9.29)$$

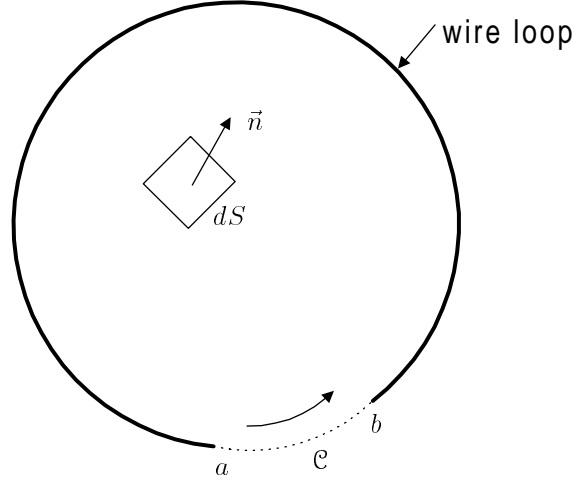


Figure 3.21. A single loop of wire

where \mathcal{E} is the electric field and S is the surface area bounded by \mathcal{C} . Since \mathcal{E} vanishes inside the wire, it follows that

$$\oint_{\mathcal{C}} \mathcal{E} \cdot d\mathbf{l} = \oint_{\mathcal{C}_{ab}} \mathcal{E} \cdot d\mathbf{l} \quad (3.9.30)$$

where \mathcal{C}_{ab} is the portion of the path \mathcal{C} that lies outside the wire. We assume that outside the wire \mathcal{E} satisfies $\text{curl } \mathcal{E} = 0$, and hence that \mathcal{E} can be written as the gradient of a potential, i.e.,

$$\mathcal{E} = -\nabla\phi \quad \text{outside wire.} \quad (3.9.31)$$

Thus,

$$\oint_{\mathcal{C}} \mathcal{E} \cdot d\mathbf{l} = - \oint_{\mathcal{C}_{ab}} \nabla\phi \cdot d\mathbf{l} = \phi_a - \phi_b \quad (3.9.32)$$

where ϕ_a is the potential at a and ϕ_b is the potential at b . The electric field and the magnetic induction satisfy Maxwell's equation

$$\text{curl } \mathcal{E} = -\dot{\mathcal{B}} = -i\omega\mathcal{B}. \quad (3.9.33)$$

Substituting equation (3.9.33) into equation (3.9.29), we get

$$\oint_{\mathcal{C}} \mathcal{E} \cdot d\mathbf{l} = -i\omega \int_S \mathcal{B} \cdot \mathbf{n} dS. \quad (3.9.34)$$

As a result of the plane wave assumption, equation (3.9.34) can be approximated by

$$\oint_{\mathcal{C}} \mathcal{E} \cdot d\mathbf{l} = -i\omega A\mathcal{B} \cdot \mathbf{n} \quad (3.9.35)$$

where A is the area of the surface region S . Equations (3.9.32) and (3.9.35) can be combined to give

$$\phi_a - \phi_b = -i\omega A \mathcal{B} \cdot \mathbf{n}. \quad (3.9.36)$$

Applying equation (3.9.36) to each loop of the coil, it follows that

$$E = i\omega N \mathcal{B}_3 A \quad (3.9.37)$$

or

$$\mathcal{B}_3 = \frac{E}{i\omega N A}. \quad (3.9.38)$$

Let us now integrate the magnetic field \mathcal{H} around the path shown in figure 3.22. By Stoke's

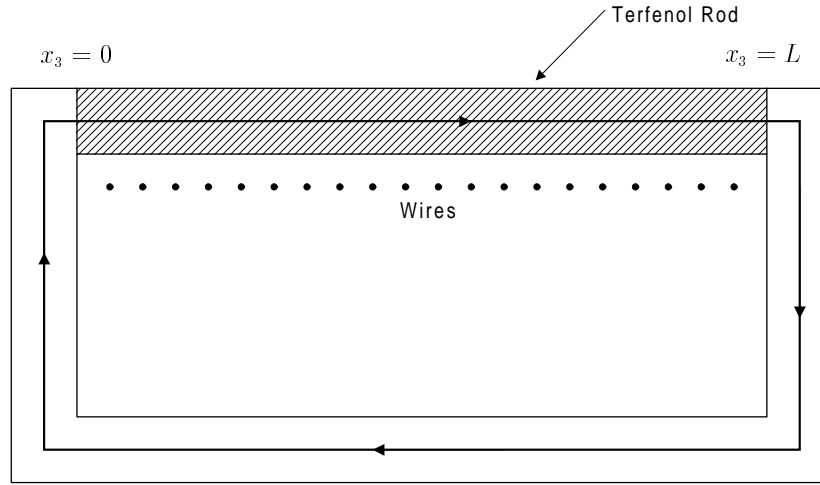


Figure 3.22. Integration path for the magnetic field

theorem,

$$\oint \mathcal{H} \cdot d\mathbf{l} = \int_{S'} \text{curl } \mathcal{H} \cdot \boldsymbol{\nu} dS \quad (3.9.39)$$

where S' is the surface bounded by the path and $\boldsymbol{\nu}$ is the normal to S' pointing into the paper. The magnetic field \mathcal{H} and the current density \mathcal{J} satisfy Maxwell's equation

$$\text{curl } \mathcal{H} = \mathcal{J}. \quad (3.9.40)$$

Combining equations (3.9.39)–(3.9.40), we get

$$\oint \mathcal{H} \cdot d\mathbf{l} = \int_{S'} \mathcal{J} \cdot \boldsymbol{\nu} dS. \quad (3.9.41)$$

The only current passing through S' is in the wires. Thus, equation (3.9.41) becomes

$$\oint \mathcal{H} \cdot d\mathbf{l} = NI. \quad (3.9.42)$$

Since the magnetic field \mathcal{H} vanishes in the return path, equation (3.9.42) can be written

$$\int_0^L \mathcal{H}_3 dx_3 = NI. \quad (3.9.43)$$

Integrating equation (3.9.8) from 0 to L and making use of equation (3.9.43), we get

$$\int_0^L \mathcal{H}_3 dx_3 = -\frac{g_{33}}{i\omega S_{33}^B} [v_3(L) - v_3(0)] + \left(\frac{1}{\mu_{33}^T} + \frac{g_{33}^2}{S_{33}^B} \right) \mathcal{B}_3 L. \quad (3.9.44)$$

Combining equations (3.9.43)–(3.9.44), we get

$$I = -\frac{g_{33}}{i\omega N S_{33}^B} [v_3(L) - v_3(0)] + \left(\frac{1}{\mu_{33}^T} + \frac{g_{33}^2}{S_{33}^B} \right) \frac{L}{N} \mathcal{B}_3. \quad (3.9.45)$$

We can now combine equations (3.9.27)–(3.9.28), (3.9.38), and (3.9.45) to obtain

$$-T_{33}(0)A = (z_1 + z_2)v_3(0) - z_2v_3(L) + \frac{g_{33}}{i\omega N S_{33}^B} E \quad (3.9.46)$$

$$-T_{33}(L)A = z_2v_3(0) - (z_1 + z_2)v_3(L) + \frac{g_{33}}{i\omega N S_{33}^B} E. \quad (3.9.47)$$

$$I = -\frac{g_{33}}{i\omega N S_{33}^B} [v_3(L) - v_3(0)] + \left(\frac{1}{\mu_{33}^T} + \frac{g_{33}^2}{S_{33}^B} \right) \frac{L}{i\omega N^2 A} E. \quad (3.9.48)$$

Define

$$\mu_{LC} = \left(\frac{1}{\mu_{33}^T} + \frac{g_{33}^2}{S_{33}^B} \right)^{-1} \quad (3.9.49)$$

$$L_{LC} = \frac{\mu_{LC} N^2 A}{L} \quad (3.9.50)$$

$$G = \frac{g_{33} L_{LC}}{N S_{33}^B}. \quad (3.9.51)$$

Then equations (3.9.46)–(3.9.48) can be written

$$-T_{33}(0)A = (z_1 + z_2)v_3(0) - z_2v_3(L) + \frac{G}{i\omega L_{LC}} E \quad (3.9.52)$$

$$-T_{33}(L)A = z_2v_3(0) - (z_1 + z_2)v_3(L) + \frac{G}{i\omega L_{LC}} E. \quad (3.9.53)$$

$$I = -\frac{G}{i\omega L_{LC}} [v_3(L) - v_3(0)] + \frac{1}{i\omega L_{LC}} E. \quad (3.9.54)$$

These equations can be represented by the equivalent circuit shown in figure 3.23. This circuit makes use of a gyrator. The behavior of a gyrator is shown in figure 3.24.

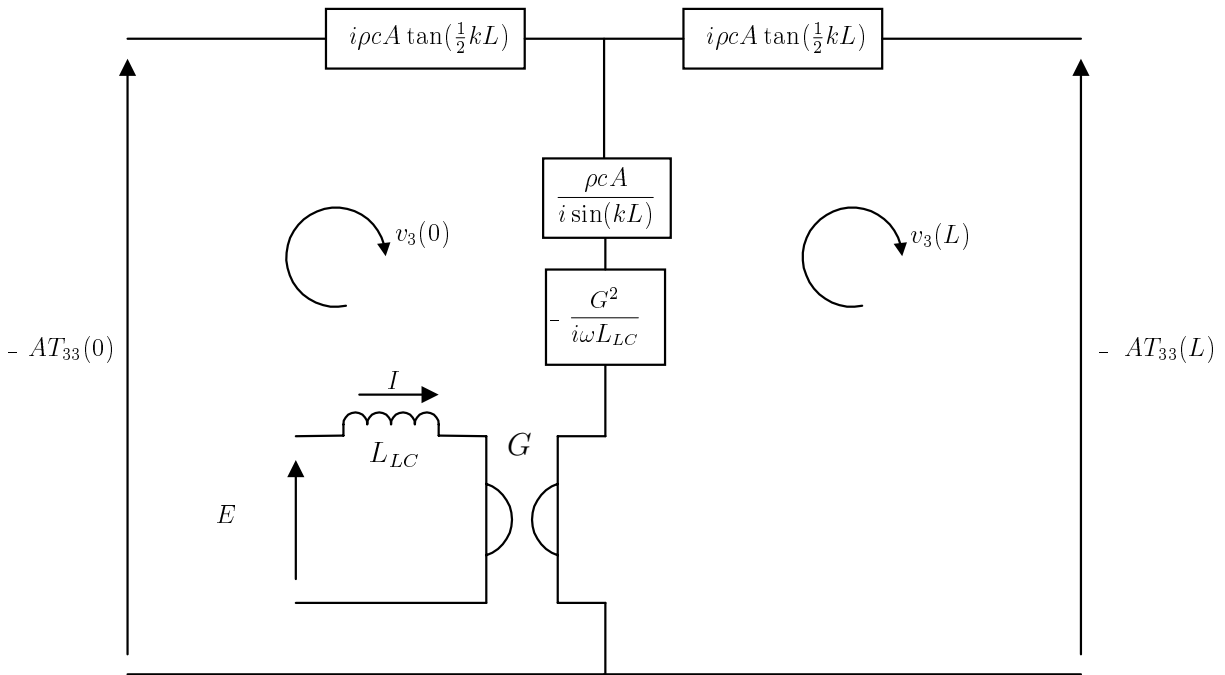


Figure 3.23. Equivalent circuit for a magnetostrictive rod

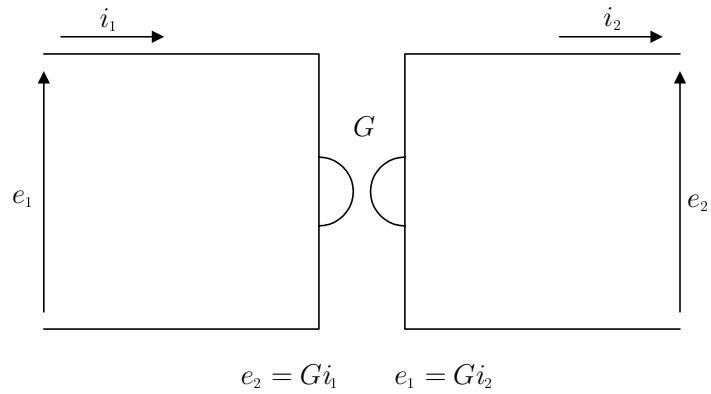


Figure 3.24. Description of a gyrator

Consider next a pair of magnetostrictive rods connected electrically in series as shown in figure 3.25. The DC bias field is in the x_3 -direction in one of the rods and in the negative

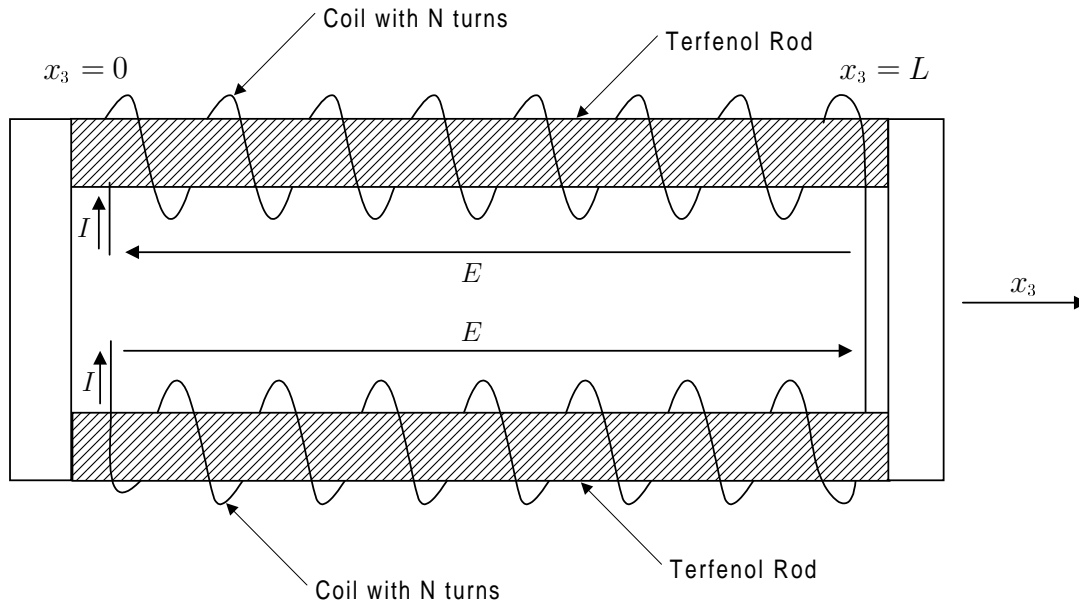


Figure 3.25. Two magnetostrictive rods connected electrically in series

x_3 -direction for the other rod. As in the piezoelectric case the sign changes that occur when the direction of the x_3 -axis is reversed are such that the same equations can be used for both of the rods. Since the two rods are connected electrically in series, the currents in the two coils are the same. However, the magnetostrictive case is different from the piezoelectric case in that the magnetic coupling between the two rods also forces the voltages across the two coils to be the same. It should also be noted that the terminal voltage is $2E$.

3.10 Cascading of Plane Wave Segments

Many transduction devices are made up of multiple segments connected end-to-end as shown in figure 3.26. For example, piezoelectric ceramic drivers often consist of a stack of ceramic pieces cemented together and connected electrically in parallel. In this section we will show

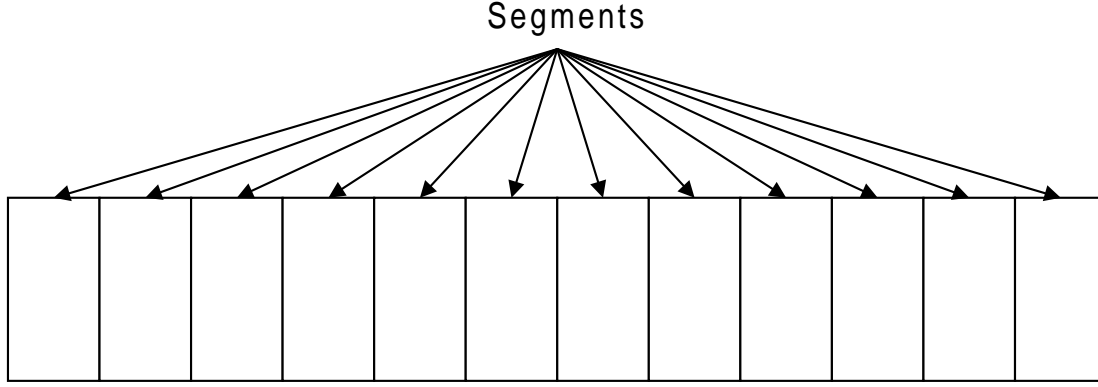


Figure 3.26. A multisegment device

ways of taking the plane wave models of the individual segments and combining them to obtain an overall model of the segmented device. To be more specific I will write the equations for the piezoelectric case, but the magnetostrictive case is done in the same manner.

The equations for a piezoelectric ceramic piece have the form

$$F_L = Z_{11}v_L + Z_{12}v_R + \alpha I \quad (3.10.1)$$

$$F_R = -Z_{12}v_L - Z_{11}v_R + \alpha I \quad (3.10.2)$$

$$E = -\alpha(v_R - v_L) + Z_0 I \quad (3.10.3)$$

where F_L is the value of $-AT_{33}$ on the left end, v_L is the 3-component of velocity on the left end, F_R is the value of $-AT_{33}$ on the right end, v_R is the 3-component of velocity on the right end, E is the voltage, and I is the current. Solving equation (3.10.3) for I , we obtain

$$I = \frac{1}{Z_0}E + \frac{\alpha}{Z_0}v_R - \frac{\alpha}{Z_0}v_L \quad (3.10.4)$$

Substituting equation (3.10.4) into equations (3.10.1)–(3.10.2), we get

$$F_L = \left(Z_{11} - \frac{\alpha^2}{Z_0} \right) v_L + \left(Z_{12} + \frac{\alpha^2}{Z_0} \right) v_R + \frac{\alpha}{Z_0} E \quad (3.10.5)$$

$$F_R = \left(-Z_{12} - \frac{\alpha^2}{Z_0} \right) v_L + \left(-Z_{11} + \frac{\alpha^2}{Z_0} \right) v_R + \frac{\alpha}{Z_0} E. \quad (3.10.6)$$

These equations have the form

$$F_L = Z'_{11}v_L + Z'_{12}v_R + \alpha'E \quad (3.10.7)$$

$$F_R = -Z'_{12}v_L - Z'_{11}v_R + \alpha'E. \quad (3.10.8)$$

We have chose to represent these equations in terms of the voltage E since E is constant for each piece when they are connected in parallel. For the magnetostrictive case we would generally use the magnetic flux $\mathcal{B}A$ since this quantity is constant around a magnetic path.

If we solve equation (3.10.8) for v_L , we obtain

$$v_L = -\frac{1}{Z'_{12}}F_R - \frac{Z'_{11}}{Z'_{12}}v_R + \frac{\alpha'}{Z'_{12}}E. \quad (3.10.9)$$

Substituting equation (3.10.9) into equation (3.10.7), we obtain

$$F_L = -\frac{Z'_{11}}{Z'_{12}}F_R + \left(Z'_{12} - \frac{(Z'_{11})^2}{Z'_{12}}\right)v_R + \alpha'\left(1 + \frac{Z'_{11}}{Z'_{12}}\right)E. \quad (3.10.10)$$

Equations (3.10.9)–(3.10.10) can be written in the matrix form

$$\begin{pmatrix} F_L \\ v_L \end{pmatrix} = \begin{pmatrix} A_{11} & A_{12} \\ A_{21} & A_{22} \end{pmatrix} \begin{pmatrix} F_R \\ v_R \end{pmatrix} + E \begin{pmatrix} \beta_1 \\ \beta_2 \end{pmatrix} \quad (3.10.11)$$

where

$$A_{11} = -\frac{Z'_{11}}{Z'_{12}} \quad (3.10.12)$$

$$A_{12} = Z'_{12} - \frac{(Z'_{11})^2}{Z'_{12}} \quad (3.10.13)$$

$$A_{21} = -\frac{1}{Z'_{12}} \quad (3.10.14)$$

$$A_{22} = -\frac{Z'_{11}}{Z'_{12}} \quad (3.10.15)$$

$$\beta_1 = \alpha'\left(1 + \frac{Z'_{11}}{Z'_{12}}\right) \quad (3.10.16)$$

$$\beta_2 = \frac{\alpha'}{Z'_{12}}. \quad (3.10.17)$$

It is easily verified that the matrix A has the properties

$$A_{22} = A_{11} \quad \text{and} \quad \det A = 1. \quad (3.10.18)$$

Suppose now that we have two pieces that are cemented end-to-end and that the electrical terminals are connected in parallel. Then, we can write a matrix equation like equation

(3.10.11) for each of the pieces, i.e.,

$$x_L^{(1)} = A^{(1)}x_R^{(1)} + Eb^{(1)} \quad (3.10.19)$$

$$x_L^{(2)} = A^{(2)}x_R^{(2)} + Eb^{(2)} \quad (3.10.20)$$

where x_L and x_R are column vectors of length 2 containing the appropriate F and v components. By continuity of velocity and the stress tensor, we have

$$x_R^{(1)} = x_L^{(2)}. \quad (3.10.21)$$

Thus, equations (3.10.19)–(3.10.20) can be combined to give

$$x_L^{(1)} = A^{(1)}A^{(2)}x_R^{(2)} + E(b^{(1)} + A^{(1)}b^{(2)}). \quad (3.10.22)$$

If the pieces are identical, then the above relation becomes

$$x_L^{(1)} = A^2x_R^{(2)} + E(I + A)b. \quad (3.10.23)$$

It can be easily verified that for n pieces, we have

$$x_L^{(1)} = A^n x_R^{(n)} + E(I + A + \cdots + A^{n-1})b. \quad (3.10.24)$$

We will next show a couple of ways to raise a matrix to the n -th power. Let E be a matrix whose columns are the eigenvectors of A . Then

$$AE = E\Lambda \quad (3.10.25)$$

where Λ is a diagonal matrix of the eigenvalues of A . It follows from equation (3.10.25) that

$$A = E\Lambda E^{-1}. \quad (3.10.26)$$

Thus,

$$A^n = (E\Lambda E^{-1})(E\Lambda E^{-1}) \cdots (E\Lambda E^{-1}) \quad (3.10.27)$$

$$= E\Lambda^n E^{-1}. \quad (3.10.28)$$

Since Λ is a diagonal matrix, raising it to the n -th power only involves raising the diagonal entries to the n -th power. Moreover, it is also true that

$$I + A + \cdots + A^{n-1} = E(I + \Lambda + \cdots + \Lambda^{n-1})E^{-1}. \quad (3.10.29)$$

A second way of computing these powers is to use the Cayley-Hamilton Theorem. This theorem states that a matrix satisfies its own characteristic equation. The characteristic equation of the 2×2 matrix A is given by

$$\lambda^2 - \text{tr}(A)\lambda + \det(A) = 0. \quad (3.10.30)$$

Thus, A satisfies

$$A^2 - \operatorname{tr}(A)A + \det(A)I = 0 \quad (3.10.31)$$

or equivalently,

$$A^2 = \operatorname{tr}(A)A - \det(A)I. \quad (3.10.32)$$

Suppose for some m , we have

$$A^m = \alpha_m A + \beta_m I. \quad (3.10.33)$$

Then

$$A^{m+1} = \alpha_m A^2 + \beta_m A = (\beta_m + \operatorname{tr}(A)\alpha_m)A - \alpha_m \det(A)I. \quad (3.10.34)$$

It follows by induction that equation (3.10.33) holds for all m . Moreover, it follows from equation (3.10.34) that α_m and β_m satisfy the recurrence relation

$$\alpha_{m+1} = \beta_m + \operatorname{tr}(A)\alpha_m \quad (3.10.35)$$

$$\beta_{m+1} = -\det(A)\alpha_m. \quad (3.10.36)$$

The starting values for this recursion are

$$\alpha_0 = 0 \quad \text{and} \quad \beta_0 = 1. \quad (3.10.37)$$

Moreover, we also have

$$I + A + \cdots + A^{n-1} = (\alpha_0 + \alpha_1 + \cdots + \alpha_{n-1})A + (\beta_0 + \beta_1 + \cdots + \beta_{n-1})I. \quad (3.10.38)$$

Chapter 4

Structure-Acoustic Coupling

The coupling of structural models to acoustic models depends on the type of models being used. Infinite element acoustic models, for example, fit naturally into the finite element program structure and thus need no special discussion of coupling. In this chapter we will discuss the coupling of finite element type structural models to integral equation type acoustic models. In order to keep the discussion relatively simple we will restrict the discussion to CHIEF type acoustic models. Some of the details for models employing higher order interpolation will be different, but the general approach is the same. An early and still excellent reference on the subject of acoustic-structure coupling is the paper [Wilton, D.T., *Acoustic Radiation and Scattering from Elastic Structures*, International Journal for Numerical Methods in Engineering, Vol. **13**, 123–138(1978)]. A more recent reference is [Benthien, G.W. and Schenck, H.A., *Structure-Acoustic Coupling*, Boundary Element Methods in Acoustics, Ciskowski, R.D. and Brebbia, C.A. (Eds), Computational Mechanics Publications, Elsevier Applied Science, Chapter 6 (1991) (prepublication draft copy)].

Recall that the finite element equations can be written in the matrix form

$$(-\omega^2 M + K)U = F \quad (4.1)$$

where M is the mass matrix, K is the stiffness matrix, U is a vector of the displacement degrees of freedom, and F is the load vector. For structure immersed in a fluid, the load vector can be decomposed into an acoustic load vector F^{rad} and a load vector F^D corresponding to other forces that drive the structure as shown below

$$(-\omega^2 M + K)U = F^{\text{rad}} + F^D. \quad (4.2)$$

Recall also that the components of the load vector F are given by

$$F_m = \int_{\partial V} \vec{t} \cdot \vec{\psi}_m \quad (4.3)$$

where ∂V is the boundary of the structure, \vec{t} is the stress vector on ∂V , and $\vec{\psi}_m$ is the m -th finite element interpolation function. In particular,

$$F_m^{\text{rad}} = \int_S \vec{t} \cdot \vec{\psi}_m \quad (4.4)$$

where S is the radiating surface of the structure. On the fluid side of the surface S the stress vector is given by

$$\vec{t} = -p\vec{n} \quad (4.5)$$

where p is the acoustic pressure and \vec{n} is the outward normal to S . Substituting equation (4.5) into equation (4.4), we get

$$F_m^{\text{rad}} = - \int_S p \vec{\psi}_m \cdot \vec{n}. \quad (4.6)$$

If the surface S is subdivided into CHIEF subdivisions S_1, \dots, S_N and the pressure is assumed to be approximately constant on each subdivision, then equation (4.6) becomes

$$F_m^{\text{rad}} = - \sum_n p_n \int_{S_n} p \vec{\psi}_m \cdot \vec{n}. \quad (4.7)$$

If we define a coupling matrix C by

$$C_{mn} = \frac{1}{S_n} \int_{S_n} p \vec{\psi}_m \cdot \vec{n}, \quad (4.8)$$

then equation (4.7) becomes

$$F_m^{\text{rad}} = - \sum_n p_n S_n C_{mn}. \quad (4.9)$$

Equation (4.9) can be written in the matrix form

$$F^{\text{rad}} = -CDP \quad (4.10)$$

where D is a diagonal matrix whose diagonals are the surface areas S_n .

Next we need to enforce continuity of normal velocity across the radiating boundary S . Since the interpolation used in the acoustic problem by CHIEF is different from that used in the finite element method for the structure, it is impossible to enforce exact continuity at every point of S . Instead we enforce continuity in an average sense over each subdivision S_n , i.e.,

$$v_n = \frac{1}{S_n} \int_{S_n} \vec{v} \cdot \vec{n} = \frac{i\omega}{S_n} \int_{S_n} \vec{u} \cdot \vec{n}. \quad (4.11)$$

Here v_n is the CHIEF normal velocity on the n -th subdivision, \vec{v} is the velocity vector, and \vec{u} is the displacement vector. In the finite element method the displacement \vec{u} is approximated in terms of the interpolation functions $\vec{\psi}_m$ by

$$\vec{u} = \sum_m U_m \vec{\psi}_m. \quad (4.12)$$

Substituting equation (4.12) into equation (4.11), we obtain

$$v_n = i\omega \sum_m U_m \frac{1}{S_n} \int_{S_n} \vec{\psi}_m \cdot \vec{n}. \quad (4.13)$$

This equation can be written in the matrix form

$$V = i\omega C^T U. \quad (4.14)$$

From the CHIEF acoustic model we have the following relation between the vector P of surface pressures and the vector V of surface normal velocities

$$AP = BV. \quad (4.15)$$

Solving the finite element equation (4.1) for U , we get

$$U = (-\omega^2 M + K)^{-1} F^{\text{rad}} + (-\omega^2 M + K)^{-1} F^D. \quad (4.16)$$

Multiplying equation (4.16) by $i\omega C^T$ and making use of equation (4.14), we obtain

$$V = i\omega C^T (-\omega^2 M + K)^{-1} F^{\text{rad}} + i\omega C^T (-\omega^2 M + K)^{-1} F^D. \quad (4.17)$$

In view of equation (4.10) the above equation becomes

$$V = -i\omega C^T (-\omega^2 M + K)^{-1} C D P + i\omega C^T (-\omega^2 M + K)^{-1} F^D. \quad (4.18)$$

Substituting equation (4.18) into the CHIEF equation (4.15) and rearranging terms, we obtain

$$[A + i\omega B C^T (-\omega^2 M + K)^{-1} C D] P = i\omega B C^T (-\omega^2 M + K)^{-1} F^D. \quad (4.19)$$

If this equation is solved for the surface pressure vector P , then the surface velocity vector V can be obtained from equation (4.18). Once the surface pressures and velocities are known, then the pressure can be calculated anywhere in the field using the Helmholtz integral relation. If the solution is needed at many frequencies and the finite element mass and stiffness matrices are frequency independent, then it is efficient to use the eigenvalue/eigenvector relation

$$(-\omega^2 M + K)^{-1} = E(-\omega^2 I + \Omega)^{-1} E^T \quad (4.20)$$

where E is a matrix whose columns are the finite element eigenmodes and Ω is a diagonal matrix whose diagonal elements are the corresponding eigenfrequencies.

Chapter 5

Electrical Interconnections

Often in transducer arrays there will be a combination of series and parallel electrical interconnection of elements either to shade the array or to modify the input impedance. For example, the elements might be partitioned into groups with the elements within the groups connected in series and the groups connected in parallel. Such electrical interconnections allow the elements to interact electrically as well as acoustically. In this section we will show how all such series-parallel electrical interconnections can be reduced to two basic operations that can be easily implemented on a computer.

Typically, our models of a transducer can be reduced to a linear relationship involving the input voltage and current and the acoustic force and normal velocity degrees of freedom. For an array we can arrange these equations in the form

$$\begin{pmatrix} \vec{E} \\ \vec{F} \end{pmatrix} = \begin{pmatrix} A_1 & A_2 \\ A_3 & A_4 \end{pmatrix} \begin{pmatrix} \vec{I} \\ \vec{V} \end{pmatrix} \quad (5.1)$$

where \vec{E} is a vector of the input voltages to all the array elements, \vec{I} is a vector of the input currents to all the elements, \vec{F} is a vector of all the acoustic force degrees of freedom for all the array elements, and \vec{V} is a vector of all the acoustic normal velocity degrees of freedom for all the elements. The matrix in equation (5.1) will be referred to as the transfer matrix.

When two transducers are connected in series the currents to the elements are equated and the voltages are added. When two transducers are connected in parallel the voltages to the elements are equated and the currents are added. These are similar operations with the roles of voltages and currents interchanged. Let us look at series interconnections first. Equating currents amounts to adding two columns of the transfer matrix of equation (5.1) and then eliminating the two original columns. Adding the corresponding voltages amounts to adding the corresponding rows and then eliminating the original rows. Paralleling elements or groups can be performed with the same operations once the roles of voltage and current have been

interchanged. Equation (5.1) can be written in the alternate form

$$\begin{pmatrix} \vec{I} \\ \vec{F} \end{pmatrix} = \begin{pmatrix} A_1^{-1} & -A_1^{-1}A_2 \\ A_3A_1^{-1} & A_4 - A_3A_1^{-1}A_2 \end{pmatrix} \begin{pmatrix} \vec{E} \\ \vec{V} \end{pmatrix} \quad (5.2)$$

in which the positions of \vec{E} and \vec{I} have been interchanged. Paralleling can be accomplished by applying the same row and column additions described previously to this other form of the transfer matrix. Obviously, it is not necessary to interchange all the voltages and currents as shown in equation (5.2). Only the ones being paralleled need to be interchanged. The other voltages and currents can be lumped with the forces and velocities. Thus, series-parallel interconnections amount to two basic matrix operations

1. Adding appropriate rows and columns of the matrix and eliminating the originals being added;
2. Interchanging the roles of voltage and current as shown in equation (5.2).

These matrix operations are easily implemented on a computer.

Chapter 6

Material Parameters

Table 6.1 gives rough elastic parameters for various materials that might be used in a transducer. The purpose in providing these values is to provide a starting point for a modeler when no measured values are available. A good reference for material properties of elastomers, fill fluids, and adhesives is [Capps, R.N., Thompson, C.M., and Weber, F.J., *Handbook of Sonar Transducer Passive Materials*, NRL Memorandum Report 4311, October 1981].

Table 6.1. Properties of Transducer Materials

Material	Density (Kg/m ³)	Young's Modulus (N/m ²)	Poisson's Ratio
Alnico	7.0×10^3	17.0×10^{10}	0.32
Alumina	3.6×10^3	27.0×10^{10}	0.33
Aluminum	2.7×10^3	7.2×10^{10}	0.33
Beryllium-Copper	8.2×10^3	22.5×10^{10}	0.33
Brass	8.5×10^3	9.7×10^{10}	0.33
Cork	0.24×10^3	0.006×10^{10}	
Copper	8.5×10^3	12.0×10^{10}	0.35
Glass	2.4×10^3	6.5×10^{10}	0.25
Gold	19.3×10^3	7.8×10^{10}	0.38
Lead	11.3×10^3	1.7×10^{10}	0.43
Lucite	1.2×10^3	0.40×10^{10}	0.40

<i>continued from previous page</i>			
Material	Density (Kg/m ³)	Young's Modulus (N/m ²)	Poisson's Ratio
Magnesium	1.7×10^3	4.3×10^{10}	0.32
Nickel	8.8×10^3	21.0×10^{10}	0.33
Nylon	1.1×10^3	0.36×10^{10}	0.40
Platinum	21.4×10^3	17.0×10^{10}	0.32
Polyethylene	0.90×10^3	0.076×10^{10}	0.44
Polystyrene	1.1×10^3	0.53×10^{10}	0.40
Polyvinyl Chloride	1.35×10^3	0.28×10^{10}	0.40
Quartz	2.2×10^3	7.0×10^{10}	0.20
Rubber (hard)	1.1×10^3	0.23×10^{10}	0.49
Rubber (soft)	0.95×10^3	0.0005×10^{10}	0.49
Rubber (rho-c)	1.03×10^3	0.0001×10^{10}	0.49
Silver	10.5×10^3	7.7×10^{10}	0.37
Stainless Steel	7.9×10^3	19.6×10^{10}	0.30
Steel	7.7×10^3	20.0×10^{10}	0.30
Tin	7.2×10^3	5.0×10^{10}	0.33
Titanium	4.4×10^3	11.6×10^{10}	0.32
Tungsten	19.0×10^3	36.0×10^{10}	0.33
Zinc	7.1×10^3	9.3×10^{10}	0.27

Table 6.2 gives some rough values for piezoelectric ceramic parameters. All values in this table are given in metric units.

Table 6.2. Properties of Piezoelectric Ceramic Materials

Parameter	BaTiO ₃	PZT-4	PZT-8	PZT-5
ρ	5550	7500	7600	7750
S_{11}^E	8.6×10^{-12}	12.3×10^{-12}	11.1×10^{-12}	16.4×10^{-12}
S_{12}^E	-2.6×10^{-12}	-4.1×10^{-12}	-3.7×10^{-12}	-5.7×10^{-12}
S_{13}^E	-2.7×10^{-12}	-5.3×10^{-12}	-4.8×10^{-12}	-7.2×10^{-12}

<i>continued from previous page</i>				
Parameter	BaTiO ₃	PZT-4	PZT-8	PZT-5
S_{33}^E	9.1×10^{-12}	15.5×10^{-12}	13.9×10^{-12}	18.8×10^{-12}
S_{44}^E	22.2×10^{-12}	39.0×10^{-12}	32.3×10^{-12}	47.5×10^{-12}
S_{66}^E	22.4×10^{-12}	32.7×10^{-12}	29.6×10^{-12}	44.3×10^{-12}
d_{15}	242×10^{-12}	496×10^{-12}	330×10^{-12}	584×10^{-12}
d_{31}	-58×10^{-12}	-123×10^{-12}	-93×10^{-12}	-171×10^{-12}
d_{33}	149×10^{-12}	289×10^{-12}	218×10^{-12}	374×10^{-12}
ϵ_{11}^T	11.5×10^{-9}	13.1×10^{-9}	11.4×10^{-9}	15.3×10^{-9}
ϵ_{33}^T	10.6×10^{-9}	11.5×10^{-9}	8.85×10^{-9}	15.0×10^{-9}
S_{11}^D	8.3×10^{-12}	11.0×10^{-12}	10.1×10^{-12}	14.5×10^{-12}
S_{12}^D	-2.9×10^{-12}	-5.4×10^{-12}	-4.7×10^{-12}	-7.7×10^{-12}
S_{13}^D	-1.9×10^{-12}	-2.2×10^{-12}	-2.5×10^{-12}	-3.0×10^{-12}
S_{33}^D	7.0×10^{-12}	8.2×10^{-12}	8.5×10^{-12}	9.5×10^{-12}
S_{44}^D	17.1×10^{-12}	20.2×10^{-12}	22.7×10^{-12}	25.2×10^{-12}
S_{66}^D	22.4×10^{-12}	32.7×10^{-12}	29.6×10^{-12}	44.3×10^{-12}
g_{15}	21.0×10^{-3}	37.9×10^{-3}	28.9×10^{-3}	38.2×10^{-3}
g_{31}	-5.5×10^{-3}	-10.7×10^{-3}	-10.5×10^{-3}	-11.4×10^{-3}
g_{33}	14.1×10^{-3}	25.1×10^{-3}	24.6×10^{-3}	24.9×10^{-3}

Chapter 7

Specific Projector types

In this chapter we will discuss the modeling of three types of projector that are currently of high interest to the Navy—the Terfenol-driven class VII flextensional transducer, the slotted cylinder projector, and the hydroacoustic projector. The models for these transducers use many of the methods described in previous sections. The models discussed are applied to real transducers of the appropriate type so that computed results can be compared to measured results on the real devices. This comparison helps to ensure that the models do not neglect any significant physical mechanisms. Many details of the models are discussed in Navy reports that are not included on the CD-ROM since they contain military critical material.

7.1 Class VII Terfenol Driven Flextensional Projector

The Navy has had an interest in Terfenol-D magnetostrictive drivers due to this materials high strain capability and its relatively low elastic modulus. The high strain capability allows these drivers to be driven at high levels to get higher source levels. The low elastic modulus allows resonant devices to be built at lower frequencies. A class VII flextensional is attractive because, unlike the class IV flextensional, it provides more stress on the driver with increased depth. This increased stress means that the manufacturer does not have to highly stress the shell and driver during construction. A sufficient static stress is applied to the driver at depth, where it is most needed. Figure 7.1 shows a typical Terfenol-driven class VII flextensional transducer.

The modeling of this transducer is discussed in the report [Hobbs, S.L. and Gillette, D., Terfenol-D Dogbone Projector Modeling Report, SPAWAR Systems Center, San Diego Technical Report 1775, May 1998]. The model for the Terfenol drivers is based on the one-dimensional plane wave theory discussed in section 3.7 of this handbook. The driver model

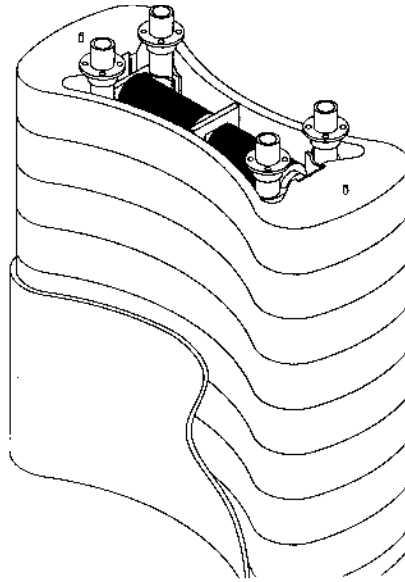


Figure 7.1. An eight segment Terfenol class VII flextensional transducer.

is coupled to a finite element model of the flextensional shell and a CHIEF model for the acoustic radiation. The above report also discusses how to model the series-parallel electrical interconnection of the various half-stacks. Modeling the electrical interconnections is complicated by the constraints placed on the voltages of the half-stacks in a complete magnetic path by the magnetic coupling. The report also discusses the effects of material parameter variations with applied static stress due to depth changes. Comparisons are made with transducer measurements made at Lake Senneca. Comparisons are also made between the plane wave model for a Terfenol driver and an ATILA finite element model.

7.2 Slotted Cylinder Projector

The Navy has had an interest in Slotted Cylinder Projectors because they can produce high acoustic output at low frequencies with a fairly compact device. Figure 7.2 shows a generic Slotted Cylinder Projector (SCP). As the ceramic material expands and contracts, the sides of the SCP vibrate much like a tuning fork. The motion is greatest near the slot.

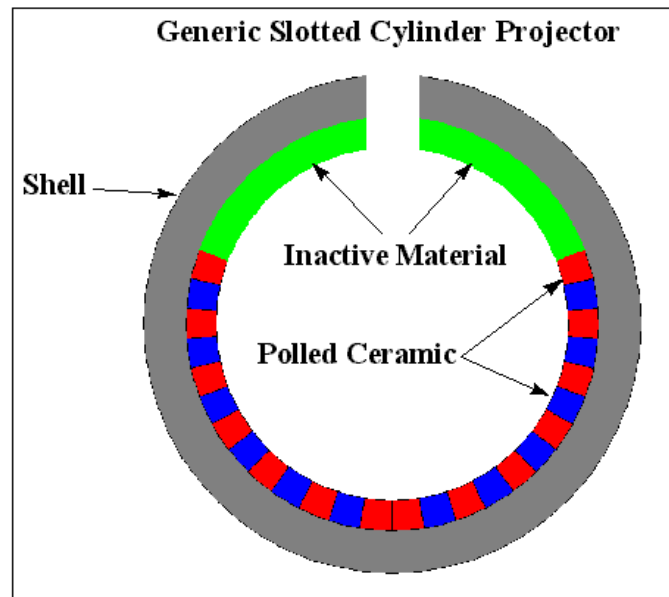


Figure 7.2. Generic slotted cylinder projector.

The modeling of Slotted Cylinder Projectors is discussed in the report [DeJaco, J., Benthien, G., Barach, D., and Gillette, D., *Electroacoustic Modeling of Slotted Cylinder Projector Transducers*, SPAWAR Systems Center, San Diego Technical Document 3047, January 1999]. This report also provides experimental validation of the modeling results. Additional experimental data are contained in the report [DeJaco, J.F., *Sanders Scale Advanced Slotted Cylinder Projector (SSASCP) Single Element Seneca Lake Test Report*, SPAWAR Systems Center, San Diego Technical Document 2965, September 1997].

7.3 Hydroacoustic Projector

Hydroacoustic projectors have been of interest to the Navy because they can produce high acoustic output at low frequencies. Figure 7.3 shows a generic hydroacoustic projector. The flow from a pump to the drive cavity is modulated by a sliding control valve. The flow modulation varies the pressure in the drive cavity. The drive cavity is connected to radiating diaphragms by drive pistons. The varying pressure in the drive cavity produces a force on the drive pistons that, in turn, force the diaphragms to vibrate. These devices are inherently nonlinear because the pressure drop across the control valve is proportional to the square of the flow through the valve.

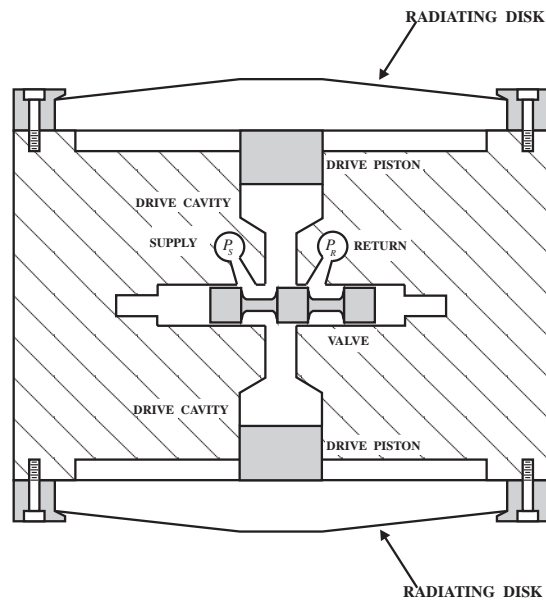


Figure 7.3. Generic hydroacoustic projector

The time-domain modeling of hydroacoustic projectors and arrays is discussed in the report [Benthien, G.W. and Barach, D., [Time-Domain Model for a Hydroacoustic Transducer Array](#), NRaD Technical Report 1654, May 1994]. This report also provides experimental validation of the modeling results.

Chapter 8

Transducer Modelling Contributions of Ralph Woollett

Dr. Ralph Woollett was involved in underwater transducer modelling at the New London Laboratory of the Naval Underwater Systems Center from 1947 to 1984. He was truly one of the pioneers in the modeling of underwater transducers. On this CD-ROM we have included three publications of his work that illustrate the breadth of his modeling expertise and are still important references on the subjects covered. The first publication included is [\[Woollett, R.S., Sonar Transducer Fundamentals, Naval Underwater Systems Center\]](#). The first part of this document covers general transducer theory while the second part goes in to more detail on longitudinal vibrators. The second publication included on this CD-ROM is [\[Woollett, R.S., The Flexural Bar Transducer, Naval Underwater Systems Center\]](#). This publication is still considered the definitive work on this subject. The third publication included is [\[Woollett, R.S., *Theory of the Piezoelectric Flexural Disk Transducer with Applications to Underwater Sound*, USL Research Report No. 490, 1960\]](#). Again this report is foundational in the modeling of flexural disk transducers. Of course we can not capture all of Ralph's contributions in just three publications, but it is hoped that these will provide a useful starting place.

Chapter 9

Lead Magnesium Niobate as an Active Sonar Material

Dr. Steven M. Pilgrim

New York State College of Ceramics at Alfred University

Introduction

Lead Magnesium Niobate ($\text{Pb}(\text{Mg}_{1/3}, \text{Nb}_{2/3})\text{O}_3$ or PMN) is the parent perovskite compound for a number of ceramic drive materials. In all cases, the PMN is the majority of the composition; however, various additional elements are added to modify the properties. These elements are most commonly shown as equivalent perovskite additions (PbTiO_3 , SrTiO_3 , BaTiO_3) or as site-dopants (La^{3+} , Fe^{2+} , etc.) Thus, from a materials composition standpoint they are similar to the better known $\text{Pb}(\text{Zr}, \text{Ti})\text{O}_3$ ceramics.

The primary addition to PMN is usually PT. This is used to increase the Curie temperature (material indicator of the phase transition) to meet the desired operating temperature. Small additions of PT (<15 mol%) provide electrostrictive materials with use temperatures at or below 25°C. As more PT is added the electrostrictive use temperature increases. With the addition of sufficient PT (nominally 35 mol%) the material provides its best performance in a piezoelectric mode. Both modes are used for transducers.

Chemistry and Synthesis

PMN is a perovskite (like PZT and BaTiO_3) ceramic. Commonly formed by mixed oxide synthesis with a columbite precursor, it follows conventional ceramic processing routes. It can be viewed as a face centered array of oxygen anions and A-site (primarily lead with Ba, Sr, La dopants) with interstitial B-site cations (primarily Mg and Nb with Ti, Zr, Fe dopants). Depending on the dopants the materials range from pale yellow, to cream to brown in color. A deleterious pyrochlore phase is sometimes noted during synthesis--this is usually bright yellow and degrades the electrical, mechanical, and electromechanical properties of the ceramic.

The chemical similarity with PZT results in a gross agreement of the mechanical and physical properties. Regardless of dopants, the PMN's are poor in tension, of high density, and thermally stable. Characteristic strengths range from 45 to 66 MPa with fracture toughness values near $0.64 \text{ MPa}\cdot\text{m}^{1/2}$ (Ewart 1998). Depending on the composition and use temperature, they may be used as piezoelectrics or electrostrictors

The primary compositions lie in the ternary of PMN, PT with either BT, ST or lanthanum (Yan 1989, Pilgrim 1992, Gupta 1998). The compositions are generally: piezoelectric (EDO and TRS; 65PMN-35PT), high-temperature (85°C EDO), electrostrictive (Lockheed-Martin, TRS, EDO, Unilator, BM Hi-Tech; 90PMN-10PT).

Density and Thermal

The PMN-based materials have an approximate density between 8.1 g/cm³ (nominally 5% higher than a PZT) for the electrostrictive varieties and 7.85 g/cm³ for the piezoelectric varieties. In thermal performance there is little difference between them and PZT. They have a heat capacity of ~0.35 J/g°C and generally lower thermal expansions (~2.3 ppm/°C) (Barber 1997). Since, when in use, the materials display ∞m symmetry there are multiple coefficients needed to define the thermal conductivity and thermal expansions. Specifically, the transverse properties differ from the longitudinal values.

Important Differences from PZT

Background and Origin of Effects

Electrostrictive materials in the purest sense include all materials in the world — *everything* is electrostrictive. "Electrostriction" in a material is commonly defined as a mechanical deformation with an applied electrical stimulus. This could be from either an applied electric field or from an induced polarization. Since all materials possess atoms, ions, or molecules, or domains which are polarized or polarizable, application of an electrical excitation distorts the charge distribution which is then coupled to distortion of the actual dimensions. In short, the deformation, or strain, of the material results from distortion of the bond lengths, bond angles, electron distribution functions, or electric dipoles with an applied electric stress. In paraelectric, cubic materials the relationship of strain and electric field should be perfectly quadratic if the material is a linear dielectric (strain as the square of electric field). However, since few materials are linear dielectrics at high fields, the more appropriate description is based on dielectric displacement (nominally polarization). The electrical nonlinearity is shown in Fig. 1 for medium field excitations.

In this case, the primary relationship of interest is between electric field E and dielectric displacement D. This development is well described in various texts including Nye 1979. As shown in Eq. (1), the dielectric displacement is the sum of the polarization of free space and the polarization of the material

$$D = \epsilon_0 E + P \quad \text{Eq. (1)}$$

where ϵ = the permittivity of free space (8.854×10^{-12} F/m); P = polarization (C/m²).

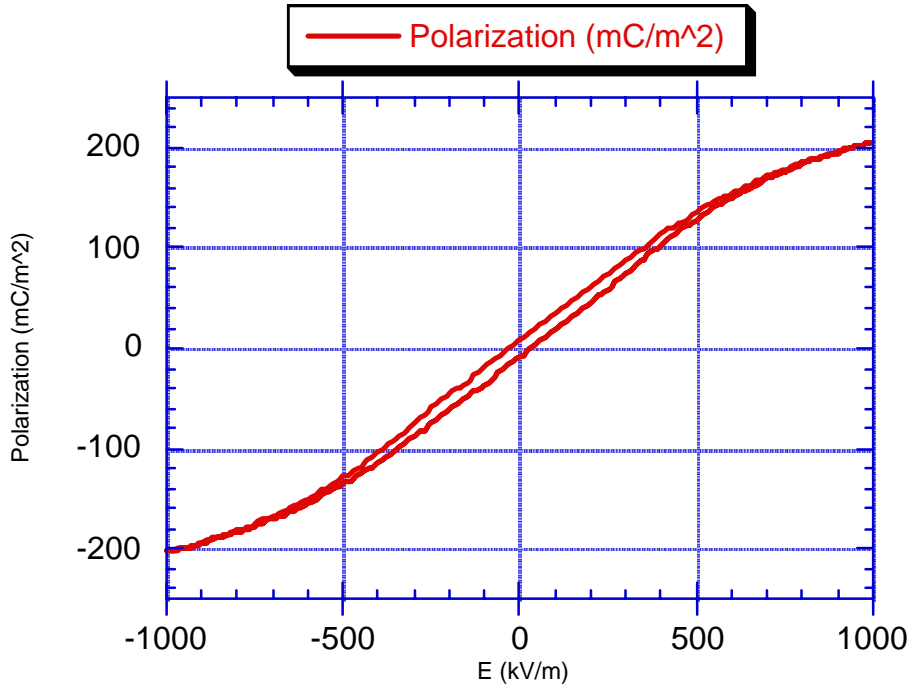


Figure 1. Polarization as a function of field for a PMN-based electrostrictor.

Since polarization is also dependent on E , its relationship may be defined through use of a dielectric susceptibility function χ , as in Eq. (2).

$$P = \epsilon_0 \chi E \quad \text{Eq. (2)}$$

Note that χ may be a function of E ; it is not necessarily a constant for high values of E . Combining Eqs. (1) and (2) provides a relationship between the dielectric displacement and the applied electric field as shown in Eq. (3).

$$D = (\epsilon_0 + \epsilon_0 \chi) E = \epsilon_0 (1 + \chi) E \quad \text{Eq. (3)}$$

In this case, the term $(1 + \chi)$ when normalized by ϵ_0 is commonly called the "dielectric constant" or the "relative permittivity" of the material. Since the term, $1 + \chi$, is dependent on the electric field for nonlinear dielectrics, the term "relative permittivity" is generally preferred. Regardless of terminology, Eq. (3) provides a functional relationship between the induced dielectric displacement and the applied electric field which can be used to define electrostriction.

Following the Devonshire phenomenology (1954), Gibbs Free Energy Approach, and the experimental behavior of materials under high electric field, the most relevant operational definition of electrostriction is the quadratic relationship between electric and mechanical variables (shown in Figs. 2 and 3). This leads to Eqs. 4 and 5 when using electric field as the drive variable and to Eq. 6 when using polarization.

$$S = ME^2 \quad \text{Eq. (4)}$$

$$S = Q[\epsilon_0(1+\chi)E]^2 \quad \text{Eq. (5)}$$

where S is strain and E is electric field.

This is shown graphically in Fig. 2.

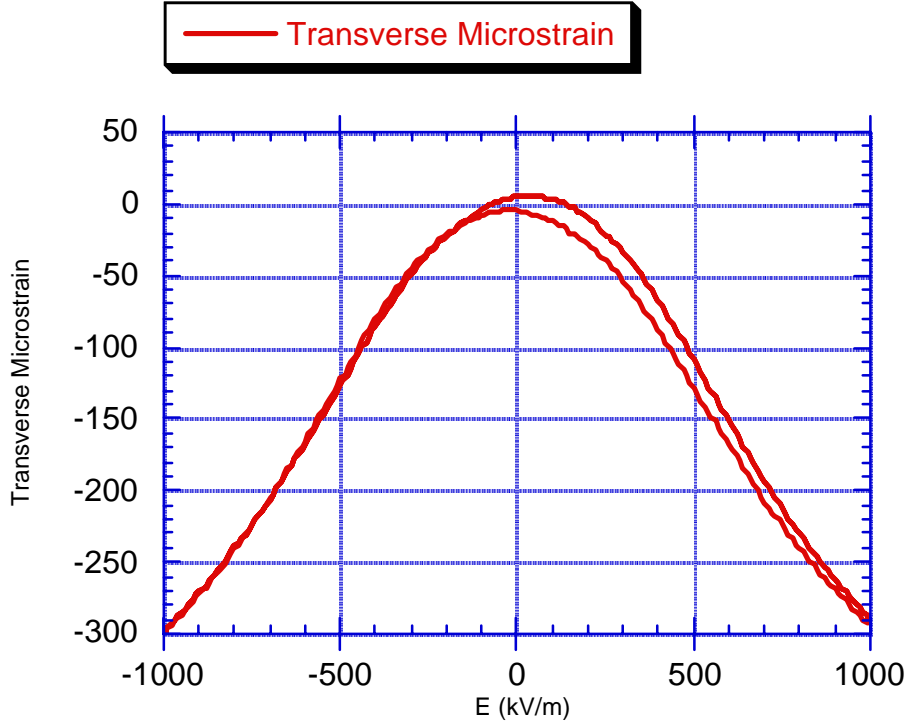


Figure 2. Transverse strain as a function of field for a PMN-based electrostrictor (same composition as Fig. 1).

On first examination, Eqs. 4 and 5 and Fig. 2 seem to state that strain is quadratically dependent on applied electric field. However, one must note that Eq. 5 shows the explicit dependence of M on χ , whose nonlinearity is displayed in Fig. 1. Thus, M is a function of E for a nonlinear dielectric. Secondly, since any material clearly has an upper maximum in strain, Eq. (4) must go to a finite limit for high values of E . Since E is unbounded, this limitation must come through the M term. In fact both of these effects are attributable to the saturation of the induced polarization at high electric field values. When the field dependence of χ , and consequently of M , is minimal, M may be considered as an effective constant. This simplifies the electrical engineering considerations of drive, but is not applicable at high electric fields.

From a materials and physics standpoint, it is preferable to work with Q and D , which are a constant and a state variable, respectively.

$$S = QD^2 \quad \text{Eq. (6)}$$

where S =mechanical strain (dimensionless)
 D =induced dielectric displacement (C/m^2)
 Q =electrostrictive Q coefficient (C^2/m^4).

This provides a view of the phenomena as shown in Fig. 3.

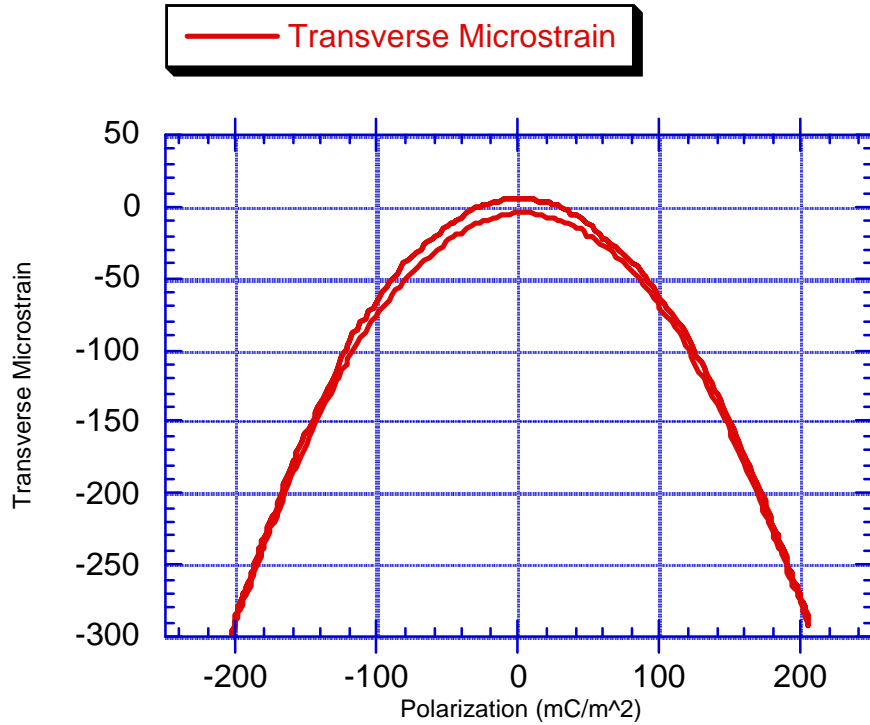


Figure 3. Transverse strain as a function of polarization for a PMN-based electrostrictor (same composition as Figs. 1 and 2).

This makes dielectric displacement (or its near equivalent, polarization) the operative independent drive variable for generating and determining the electrostrictive strain. A similar class of materials (less widespread, but better known) is that of the piezoelectric ceramics. Typified by PZT, these materials show a primarily linear relationship ($S=gD$) between strain and dielectric displacement. However, since *all* materials are electrostrictive the true relationship for piezoelectrics actually includes an electrostrictive term (Eq. 7):

$$S=gD+QD^2 \quad (\text{Eq. 7})$$

Under practical operating conditions for piezoelectrics, the quadratic component is sufficiently small to be neglected or results in an acceptably low level of harmonic generation. Under practical operating conditions for electrostrictors, the linear component is sufficiently small to be neglected. The co-existence of both effects can be noted in Fig. 4.

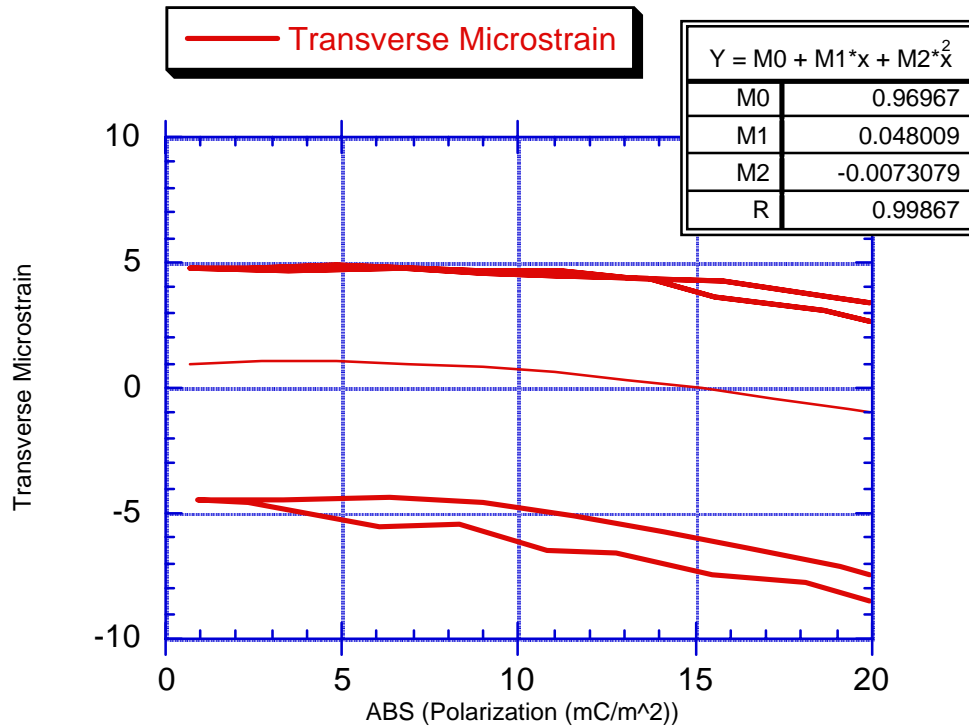


Figure 4. Transverse strain as a function of absolute polarization for a PMN-based electrostrictor (same composition as Figs. 1, 2, and 3). Note M0 defines the absolute error of the measurement. M1 corresponds to the g coefficient of 48 mV.m/N and M2 corresponds to the Q coefficient of 0.0073 m⁴/C².

For most materials, the electrostrictive effect under modest to moderately high fields (~0.1 to 5 MV/m) is very small (Sundar 1992). The values of Q are relatively constant by structure type. In fact, the electrostrictive strain may be several orders of magnitude less than the strain resulting from a 1°C temperature differential — apparently relegating electrostriction to the realm of academic curiosity. However, the usefulness of electrostriction is clear from an examination of Eq. (4). In essence, the level of electrostriction can be improved by: a) increasing the drive field or b) increasing the M coefficient. Since the drive field is normally constrained by system considerations relating to breakdown of insulation, maximum voltage of the system, or corona issues, increasing the M coefficient is the primary avenue of approach. Viewed in the context of Eq. 5 this corresponds to increasing χ . Thus, materials with large values of dielectric displacement have much larger values of electrostrictive strain.

Note that in general the dielectric displacement and the electrostrictive coefficient are inversely proportional. However, since the strain has a quadratic dependence on dielectric displacement, the presence of a large dielectric displacement in a material is desirable.

Ideally, the best practical electrostrictor would meet a minimum of five criteria:

- it would possess a very large dielectric displacement (D)
- it would display a linear electrical response for ease of use
- it would have a large coefficient between strain and dielectric displacement field (Q)
- it would have a high breakdown field
- it would maintain these properties over a wide range of environmental conditions.

These criteria may be extended and modified (Wilson 1985). The first and second criteria are met exceptionally well by the ceramic capacitor materials (Herbert 1985 and Jaffe 1971). Some capacitor materials in the BaTiO₃ and related perovskite families have dielectric displacements and relative permittivities that are 1000 times those of other materials. Materials that meet criterion one fail on criterion two; however, the perovskites are predictably nonlinear. Large values of Q are apparently inconsistent with large values of D, since $QD \sim \text{constant}$. Large, field-induced *piezoelectric* strains are present in the Pb(Zr,Ti)O₃ and related perovskite piezoelectrics (Jona 1962 and Jaffe 1971) for a several hundred degree temperature range. Regardless, the perovskites do have high breakdown fields ($>20\text{MV/m}$). All of the properties are somewhat temperature dependent since the maximal response comes from the proximity of a phase transition.

Relationship between Electrostriction and Piezoelectricity

In the preceding discussion, we have considered electrostrictive strains as resulting from an *induced* dielectric displacement. However, in the materials which most closely approximate the ideal electrostrictor there is often a spontaneous polarization which is reorientable within the material, i.e., the materials are ferroelectric. This is the case for BaTiO₃, Pb(Zr,Ti)O₃, and many of the related perovskites (Jona 1962, Lines 1977, Jaffe 1971, Nomura 1981, Ikeda 1990). This adds complexity to Eqs. 1 – 7. Since the materials are not isotropic in properties and the electric excitation is not limited to a single direction, all of our previous equations must be presented in tensor form (Nye 1979). Using the tensor forms, adding the spontaneous polarizations, and following the basic phenomenological approach of Devonshire (1954) converts Eq. 7 to:

$$S_{ij} = Q_{ijkl} P_k^S P_l^S + 2Q_{ijkl} P_k^S P_l' + Q_{ijkl} P_k' P_l' \quad (\text{Eq. 8})$$

and Eq. 5 to:

$$S_{ij} = Q_{ijkl} P_k^S P_l^S + 2Q_{ijkl} P_k^S \chi_{lm} E_m + Q_{ijkl} \chi_{lm} E_m \chi_{kp} E_p \quad (\text{Eq. 9}).$$

Note that P^S and P' are the spontaneous and induced polarizations. These are nearly equivalent to the spontaneous and induced dielectric displacements since they lack only the contribution from free space.

For materials without a spontaneous polarization (e.g., wholly nonpiezoelectric materials and ferroelectrics in their paraelectric state and therefore $P^S=0$) these equations may be simplified by setting all of the P^S terms to zero in Eqs. (8) and (9). Note once again that the Q_{ijkl} coefficients are constants; whereas the associated M_{ijmp} coefficients include the field dependence of the dielectric susceptibility.

In piezoelectric materials, P^s is nonzero; the piezoelectric coefficients, e.g., g_{lij} , can be equated with specific functions of the general Eqs. (8) and (9) as shown in Eq. (10) for the effective piezoelectric coefficient g_{lij} :

$$\frac{\partial S_{ij}}{\partial P_l} = 2Q_{ijkl}P_k^s + 2Q_{ijkl}P_k' = g_{lij} \quad \text{Eq. (10)}$$

Since $Q_{ijkl}=Q_{jikl}$ from the energy constraints on strain and $Q_{ijkl}=Q_{ijlk}$ from the independent nature of the applied polarizations, Eq. 10. actually incorporates a great deal of information. Note that Q_{ijkl} are not tensors of the same form as the stiffness or compliance (stiffness and compliance lack the equivlance between the 'ijkl' and 'ijlk' terms). This gives the change in strain component S_{ij} with induced polarization as referred to the material state absent all spontaneous and induced strains. The effective strain is in fact the sum of two parts: a strain resulting from the spontaneous strain and one resulting from an induced polarization in the material.

Examining Eq. 10 shows clearly that the true piezoelectric coefficient is directly related to the electrostrictive Q coefficient by Eq. (11a and 11b). Eq. 10 also gives the contribution to the coefficient from the spontaneous polarization—for piezoelectrics this is the remanent polarization. The associated strain is the dimensional change accompanying original poling.

$$\frac{\partial S_{ij}}{\partial P_l} = g_{lij} \quad \text{Eq. (11a)} \quad g_{lij} = 2Q_{ijkl}P_k' \quad \text{Eq. (11b)}$$

Thus via phenomenology and the attendant energy considerations, the origins of piezoelectricity clearly lie in electrostriction. However, since this awareness of the joint origin of the two effects is relatively recent there are significant differences in notation and convention. Following the IEEE standards of 1987, the polar axis for a piezoelectric is assigned to the '3' or z-axis. Thus for a piezoelectric ceramic the coefficients are g_{333} , $g_{311}=g_{322}$, g_{113} , and g_{232} . Since the first two subscripts come from the strain, these are usually contracted following the convention: 11 to 1, 22 to 2, 33 to 3, 23 to 4, 13 to 5 and 12 to 6. This gives the familiar four coefficients: g_{33} , $g_{31}=g_{32}$, g_{15} , and g_{24} . The convention for electrostrictors is different from this. In the electrostrictive case, the polarized axis is usually given as the '1' or z-axis. Since only one polarization is typically applied (the one along the z-axis, this results in only four Q coefficients for an electrostrictive ceramic: Q_{1111} , $Q_{2211}=Q_{3311}$, $Q_{1211}=Q_{1311}=Q_{2111}=Q_{3111}$, and $Q_{2311}=Q_{3211}$. These are the longitudinal, transverse and two shear components, respectively. Contracting the strain subscripts and reducing the polarization subscripts to a single value yields Q_{11} , Q_{12} , Q_{16} , and Q_{14} (note that the subscripts are permutable in pairs). These Q_{ij} 's are direct analogs to the piezoelectric g coefficients listed above.

By convention, the longitudinal coefficient relating a uniaxial strain to a parallel electric excitation for piezoelectrics is a '33' coefficient whereas that for an electrostrictor it is a

'11' coefficient. The transverse components are '31' and '12' for piezoelectrics and electrostrictors, respectively.

In summary, electrostriction and piezoelectricity are fundamentally similar effects. Materials primarily exhibiting one effect may be superior to the other for a given application (see Yamashita 1996).

Relaxor Nature of PMN-based Electrostrictors

Since a large induced polarization over a wide range of temperatures is vital to generating a practical, electrostrictive strain, capacitor materials were obvious choices for electrostrictors. In particular, the class of relaxor ferroelectrics has special appeal. As ferroelectrics they possess a paraelectric high-temperature phase and a piezoelectric low-temperature phase (Lines and Glass). However, their behavior is significantly different from other ferroelectrics in three important ways: the peak in the permittivity versus temperature curve is frequency dependent (Fig. 5), the peak is broad and diffuse (Fig. 5), and the dielectric loss is frequency dependent. These departures from normal ferroelectric behavior were first noted by Smolenskii and Isupov when considering the relaxors for capacitor uses (Smolenskii 1958, Isupov 1956). Cross further details the behavior and origins of relaxor ferroelectrics (1987).

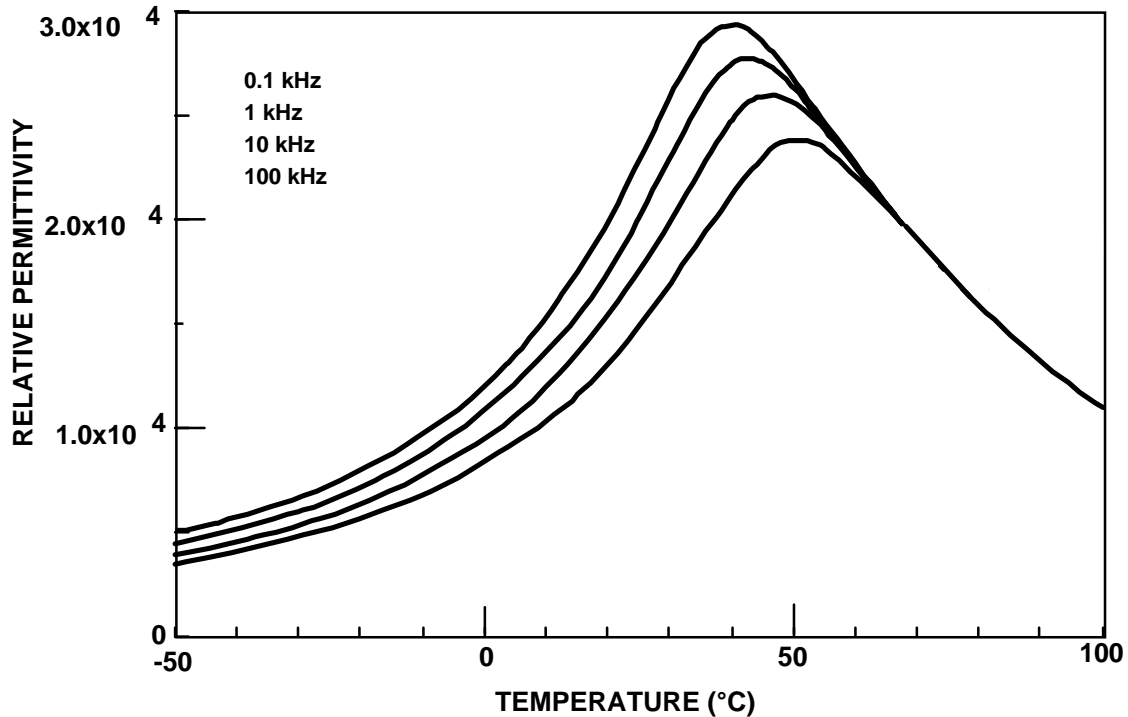


Figure 5. Weak-field dielectric response of a PMN-based electrostrictor showing the frequency dispersion and decrease in permittivity with increasing frequency (after Pilgrim 1992).

Following Smolenskii (1958) most explanations of relaxor behavior turn on the presence and ordering of micropolar or microheterogeneous regions within a perovskite (Reinecke 1977, Chen 1989, Viehland 1990). The details of these approaches and explanations fall outside our subject; however, the characteristics and outgrowths of the relaxor behavior are important. They will be discussed as typical properties.

Summary of Practical Differences Between PZT and PMN-based Materials

In a previous chapter, the performance of the various Navy piezoelectrics has been presented in detail. The properties of the PMN-based materials are very similar to those of the piezoelectrics for mechanical and thermal properties. The primary differences are in the electromechanical response of the materials. These arise from: the proximity of the use temperature and the transition temperature (T_{\max}), the basic differences in mechanism, and the present state of PMN development. In approximate terms, the important electromechanical relationships are shown in Table I.

Table I. Electromechanical Properties of Electroactive PMN Ceramics

		PMN electrostrictor	PMN piezoelectric (EDO)
T_{\max} or Curie Temperature($^{\circ}\text{C}$)		25-40	170
Longitudinal Strain (ppm@1MV/m)		1000-1200 ($M_{11}E_1$)	730 (d_{33})
Transverse Strain (ppm@1MV/m)		-400 ($M_{21}E_1$)	-312 (d_{31})
Relative Dielectric Constant (RT @ 1 kHz)	K_3^T	8,000-25,000	5500
Dissipation factor (%)	DF; $\tan\delta$	1-3	2
Mechanical Q	Q_m	100	70
Coupling (k_{33})	k_{33}	0.55	0.72
Coupling	k_{31}	0.25	0.35
Hysteresis (strain / field)		<3%	Not reported
Modulus (MPa @ 0.5 MV/m)	Y_{33}^E	70-90	55
Frequency Constant	(N_t kHz-in)	~50	71
Aging (per time decade in K_3^T)		Not applicable	1.5%
Aging (per time decade in N_t)		Not reported	0.4%
Aging (per time decade in k_{33})		Not applicable	0.4%
Piezoelectric constant (mV.m/N)	g_{33}	Minimal	15.6
Piezoelectric constant (mV.m/N)	g_{31}	Minimal	-6.4
Electrostrictive constant (m^4/C^2)	Q_{1122}	-0.65×10^{-3}	Not applicable
Electrostrictive constant (m^4/C^2)	Q_{1111}	1.7×10^{-3}	Not applicable

(major references Zhang 1989, EDO 1998, Gupta 1998, Pilgrim various)

Note that as the T_{\max} approaches the use temperature the temperature dependence of the listed properties will increase. It will also be more difficult to utilize the properties at higher electric fields without field-induced changes. The electrostrictive compositions are operated very near their T_{\max} values. This results in improved strain and hysteresis properties (see subsequent sections); however, it also restricts optimal response to specific temperature and stress regions.

PMN Compositions

As described above, the PMN materials are presently made in two distinct types: piezoelectric and electrostrictive. The piezoelectric compositions (EDO Western) are used principally as higher strain analogs of $\text{Pb}(\text{Zr}_{1-x}\text{Ti}_x)\text{O}_3$. They have lower T_{\max} values and higher strains. Their base composition is a solid solution of ~65% $\text{Pb}(\text{Mg}_{1/3}\text{Nb}_{2/3})\text{O}_3$ with ~35% PbTiO_3 ; this provides advantages for some applications.

However, the majority of makers are involved in electrostrictive compositions (EDO, Lockheed-Martin, TRS Ceramics, and Unilator). These materials have the requisite induced polarizations with adequate Q coefficients and a range of temperature dependent properties. Specifically, most interest in electrostrictors for practical use has centered around ceramics based on solid solutions of ~85 to 93% $\text{Pb}(\text{Mg}_{1/3}\text{Nb}_{2/3})\text{O}_3$ as a solid solution with ~15 to 7% PbTiO_3 and various other perovskite additions (nominally 1 to 5%) (BaTiO_3 , SrTiO_3) or dopants, lanthanum, europium, gadolinium, etc. These materials may also include a variety of dopant packages, analogous to those used for piezoelectric ceramics, to improve properties (Jang 1979, Uchino 1981, Uchino 1986, Wheeler 1991, Winzer 1989, Takeuchi 1990, Pilgrim 1992). They are primarily described by their acronyms: PMN for $\text{Pb}(\text{Mg}_{1/3}\text{Nb}_{2/3})\text{O}_3$, PT for PbTiO_3 , ST for SrTiO_3 , and BT for BaTiO_3 . Each of these systems has particular advantages from both practical and performance standpoints.

The solid solutions display relaxor behavior to varying degrees (Jang 1978, Yan 1989a, Yan 1989b, Pilgrim 1992). Of these base systems, the PMN-PT one has been more easily and reliably reproduced. It also blends the low-transition PMN with the high-transition PT to conveniently yield transition temperatures near room temperature. Further selection of suitable perovskite additions to control other characteristics of performance have concentrated on BT and ST for the PMN-PT systems (Uchino 1986, Wheeler 1991, Winzer 1988).

Lockheed Martin, as a successor to Martin Marietta Laboratories, has developed a sequence of "Generations" of PMN based electrostrictors (Generation 4 is under development in 1998). These are PMN-PT-BT materials or PMN-PT-ST materials. Lockheed Martin materials have compositions given by a seven character code. This follows the composition $(1-y)[(1-x)\text{PMN}-x\text{PT}]+y\text{RT}$. The composition code leads with a

letter: 'B' or 'b' if RT is BaTiO₃ and 'S' or 's' if RT is Sr TiO₃. Thus a B250141 would be 0.975[0.859PMN-0.141PT]-0.025BT.

Material Properties

From a practical point-of-view the parameters and properties which are most important to actual application of an electrostrictor are those related to the frequency and temperature dependence of the energy use, energy conversion, and induced strain. For actual material or device selection these important parameters should be quantified under use conditions. However, they are often improperly extrapolated from different test conditions. Proper test conditions for the materials are vital to predicting the behavior of resulting devices (Carlson 1987, Winzer 1988, Hom 1994, Brown 1996). One *must* remember that the relaxors do not show a linear response with applied field, nor are their properties independent of frequency.

Typical properties used to characterize electrostrictive materials for quality control include: density, phase purity, weak-field peak permittivity, and weak-field dielectric loss, temperature of maximum permittivity (T_{\max}), and diffuseness. These are important to the response of the electrostrictive *material*, but may not be indicative of the material's actual performance in a *device*. Density is usually determined from an x-ray powder diffraction pattern following standard procedures (Snyder 1992). This gives densities of approximately 8000 kg/m³. Phase purity is also generally determined from the x-ray pattern by ratioing the intensities of the primary perovskite peak to the sum of the intensities of the primary perovskite and pyrochlore peaks. This provides a rough guide to the pyrochlore level; however, the ideal material will be a phase pure perovskite, i.e., no pyrochlore.

Weak-field Properties

Weak-field or dielectric properties, relative permittivity, dielectric loss, and T_{\max} are determined directly from automated measurements of dielectric behavior as functions of temperature and frequency (see Fig. 5). These are frequently termed 'Curie' runs and are typically conducted while cooling the material at 1 to 4°C/min in an automated system. Values corresponding to the important points on the curve are then determined (T_{\max} is the temperature of maximum permittivity, typically taken at 1 kHz). Diffuseness, δ , is also a dielectric parameter; however, its derivation from Fig. 5 is more involved. Beginning with the supposition that relaxors could be considered as an assemblage of individual, normal ferroelectrics, Smolenskii (1958) defined the diffuseness parameter, δ according to Eq. 12. Smolenskii also set forth a power law approximation which was valid when $\delta \gg T - T_{\max}$ as shown in Eq. 13. The diffuseness characterizes the breadth of the diffuse phase transition in a reproducible and quantifiable way. However, improper use of Eq. 13 has, as outlined by Pilgrim (1990), resulted in doubtful conclusions regarding the effects of specific dopants, compositions, and grain sizes on the weak field properties of relaxors. Overall, Eq. 12 is preferred.

$$\epsilon_{\max} = \epsilon_e \frac{(T - T_{\max})^2}{2\delta^2} \quad \text{Eq. (12)}$$

$$\frac{1}{\epsilon} = \frac{1}{\epsilon_{\max}} \left(1 + \frac{(T - T_{\max})^2}{2\delta^2} \right) \quad \text{Eq. (13)}$$

As a summary of the weak-field dielectric properties for various recent PMN-PT materials see Table II. Additional details for a wide variety of recent material compositions made under reproducible conditions are available in the literature.

Table II. Weak-field Properties of the Lockheed-Martin Generation 3 Materials

Sample	T _{max} (°C)	K _{max} @ T _{max}	Loss Tangent @ T _{max}
b300100 - pellet	22.5	22083	0.0413
- plate	24.3	22089	0.0425
b250090 - pellet	20.3	21307	0.0426
- plate	21.7	19845	0.0392
b250075 - pellet	13.6	21790	0.0442
- plate	16.1	20167	0.0417
s250075 - pellet	8.2	19019	0.0385
- plate	8.3	19811	0.0413
s250090 - pellet	15.6	19930	0.0400
- plate	15.9	21916	0.0444
s400090 - pellet	3.4	22994	0.0404
- plate	5.1	17419	0.0385
s400110 - pellet	14.3	18597	0.0375
- plate	17.6	15131	0.0314
b500100 - pellet	16.6	17492	0.0392
- plate	18.7	18908	0.0408

From MML TR 92-23c, "Development of Advanced Active Sonar Materials and Their Microstructure / Property Relations," Martin Marietta Laboratories under N66001-91-C-6012 (1991).

Additional data to show the possible variations in weak-field properties can also be found in Table III.

Table III. Weak-field dielectric properties of PMN-PT-BT, ST compositions.

Sample	K@25°C @ 1 kHz	D@25°C @ 1 kHz	K@T _{max} @ 1 kHz	D@ T _{max} @ 1 kHz	T _{max} (°C) @ 5 Hz	T _{max} (°C) @ 1 kHz
B200120	10359	0.0190	24983	0.0327	41.1	41.7
B125650	23103	0.0239	23390	0.045	10.7	17.9
B125775	16738	0.0197	22579	0.0394	14.3	21.6
B125900	13499	0.0199	22829	0.0276	24.0	30.6
B250115	17003	0.1127	18089	0.0835	26.7	32.8
B250141	12648	0.0746	19723	0.0385	38.0	45.0
B250640	19399	0.0083	21550	0.046	4.0	12.0
B250900	15065	0.0201	21316	0.035	14.5	16.9
S200120	14861	0.0671	17113	0.035	27.9	33.9
S125650	17679	0.0079	19434	0.0422	3.8	10.0
S125775	20610	0.0225	21191	0.0447	8.3	16.7
S125900	22186	0.0747	23100	0.048	18.8	27.3
S250115	17460	0.0347	17519	0.0396	11.8	19.8
S250141	16033	0.0708	18003	0.0353	30.3	38.1
S250640	14485	0.0017	19089	0.0446	-4.2	3.6
S250900	16063	0.0092	17229	0.0398	1.8	10.8
N910900	13008	0.0743	16476	0.0354	29.1	35.9

From MML TR 90-66c, "Electrostrictors for Active Sonar, Martin Marietta Laboratories under N00014-89-C-2357 (Oct 1990).

In general, the weak-field dielectric properties can be scaled to the desired frequency of use. This process is shown in Fig. 6.

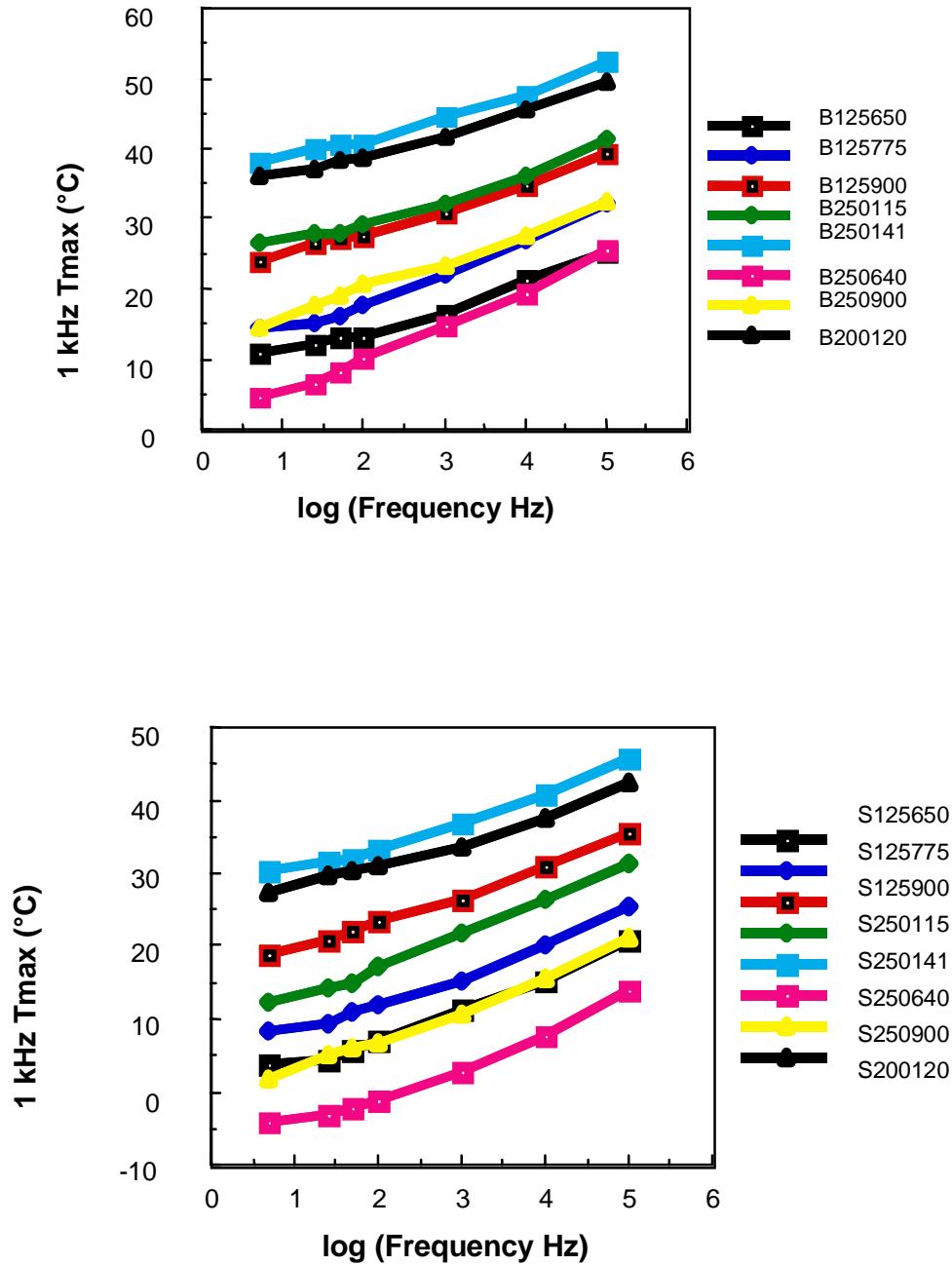


Figure 6. Frequency dependence of T_{max} for various PMN-PT-BT, ST compositions. From MML TR 90-66c, "Electrostrictors for Active Sonar," Martin Marietta Laboratories under N00014-89-C-2357 (Oct 1990).

High-field Properties

Weak-field properties are ideal for quality control during manufacturing and as *necessary* checks on the performance of devices. However, they are not *sufficient* to characterize or predict the performance of a relaxor electrostrictor at high electric fields. This requires measurement of polarization and strain as functions of applied electric field. Typically these measurements are made at low frequency (~0.1 to 500 Hz) for applied fields of 1 MV/m at various temperatures (see Figs. 1, 2, 3). Salient features of such measurements are: the peak polarization, peak strain, and the average hysteresis. The peak values are those at maximum positive excitation, with peak strain usually taken as the maximum positive strain. These are obtained with minimal data reduction. Average hysteresis denotes the average separation of the increasing and decreasing arms of the loop normalized by the maximum response. Thus, the product of H_{ave} for polarization and the maximum field-excitation is directly proportional to the energy loss on cycling. H_{ave} is defined for both y-variables, polarization and strain, via Eq. (14).

$$H_{ave} = \frac{\sum_{i=1}^n (y_i^{dec} - y_i^{inc})}{n} \cdot \frac{100}{y_{max}} \quad \text{Eq. 14}$$

The coefficient M_{12} can also be determined from the instantaneous slope of Fig. 2 while the coefficient ϵ_{11} is the instantaneous slope of Fig. 1. Q_{12} can be determined from the data shown in Fig. 4 as shown in the inset or from Fig. 7. Note that each arm of the loop generates a single line. For an ideal electrostrictor, all four lines will be collinear. Deviations from the fit line as shown in Fig. 8, indicate the presence of piezoelectric components or errors in determining the zero origin.

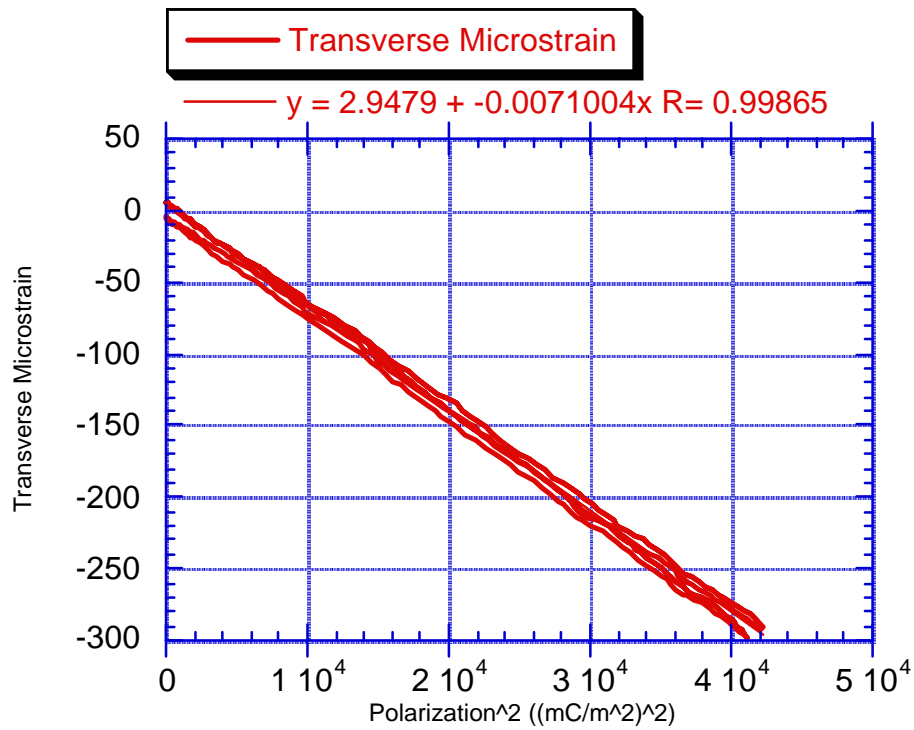


Figure 7. Method for determining the Q_{12} as the slope.

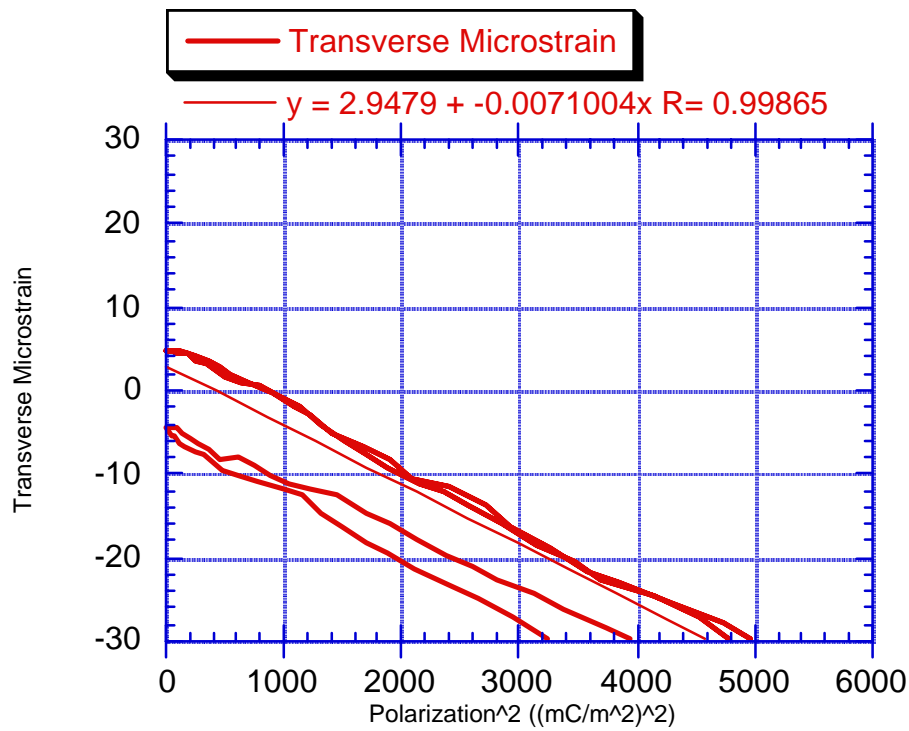


Figure 8. Enlargement of the intercept region from Fig. 7, illustrating the close fit.

Another way to view the electromechanical performance is by determining the data of Figs. 1 and 2 as a function of temperature. This generates a sequence of curves as shown in Fig. 9.

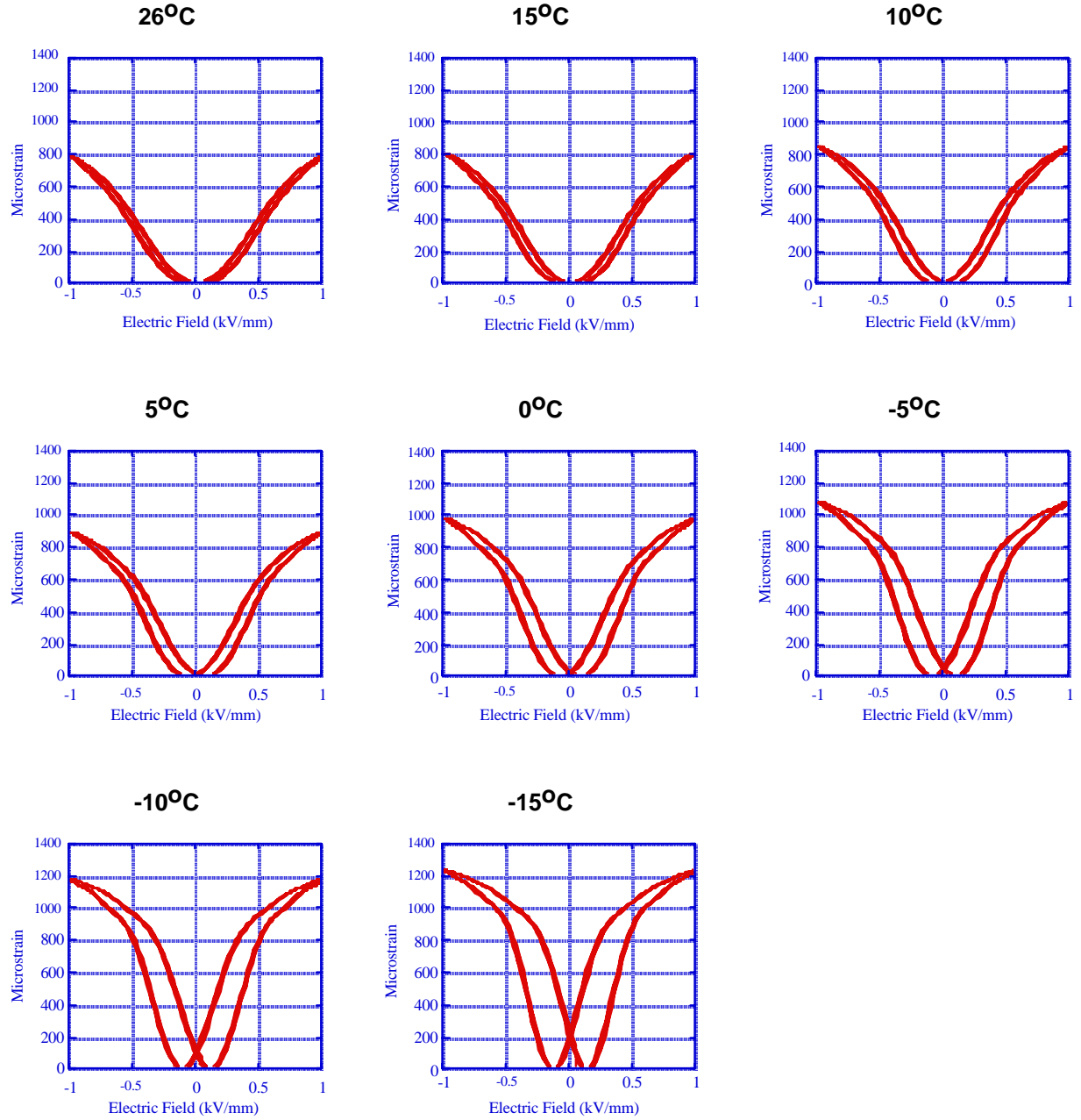


Figure 9. Longitudinal strain vs Electric Field with temperature for a modified B400090 (PM-3). Note that contrary to convention, all strain is included as positive (from Bridger 1998).

For better visualization, the peak strain values and the corresponding hysteresis values can be combined to provide a materials selection chart (see Fig. 10 and Figs. 11-14).

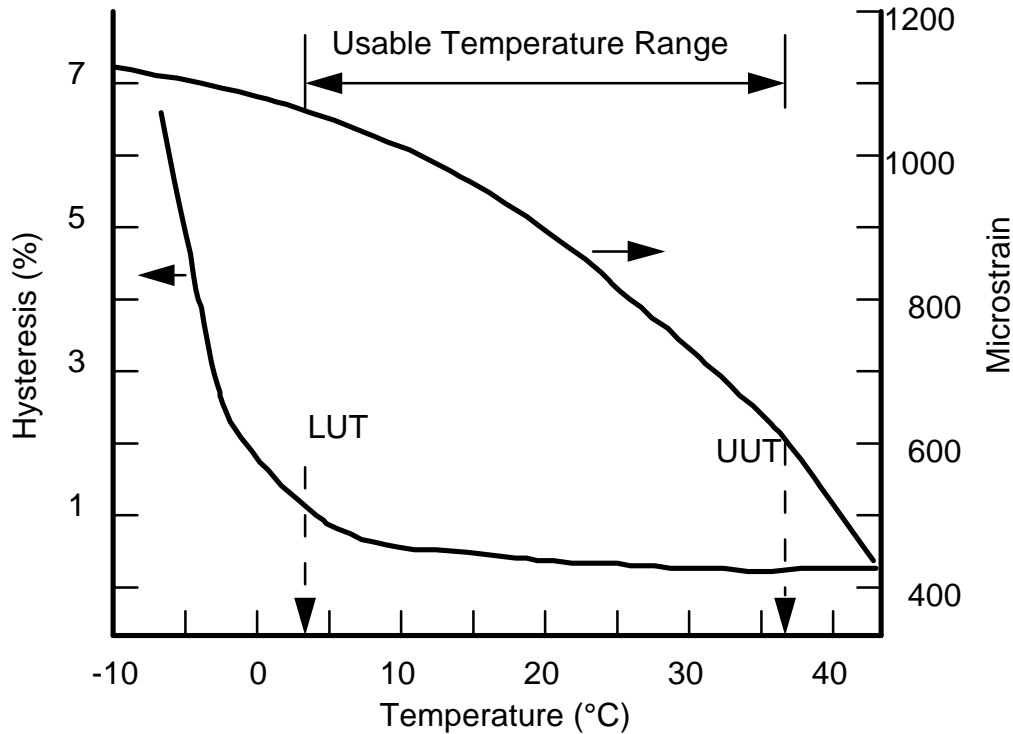


Figure 10. Schematic determination of lower and upper use temperatures (LUT and UUT) from electromechanical data.

Essentially, the LUT is fixed by the increase in either the strain or polarization hysteresis associated with the transition of most of the material to piezoelectric behavior. A second potential LUT occurs at the temperature defined by the increase in the dielectric loss. It is expected that these LUTs are relatively close together; however, this has not been completely verified. The LUT defined by strain has been shown to occur at or below the LUT defined by polarization; the dielectric loss LUT is generally higher than either of the other two. The LUT has been defined by an increase of 50% in the average polarization or strain hysteresis between two successive 5°C temperature steps measured at the desired frequency. The upper use temperature (UUT) is set by the reduction in strain below the acceptable threshold or by the onset of an increase in dielectric loss from conductivity (analogous to that found in traditional piezoelectrics). Since there is no qualitative lower limit on strain, and strain decreases relatively smoothly with increasing temperature, the UUT is set by the application.

This performance of strain with temperature may also be a function of frequency, although it is difficult to separate the frequency effect from the effect of heating—both result in behavior as shown in Fig. 11.

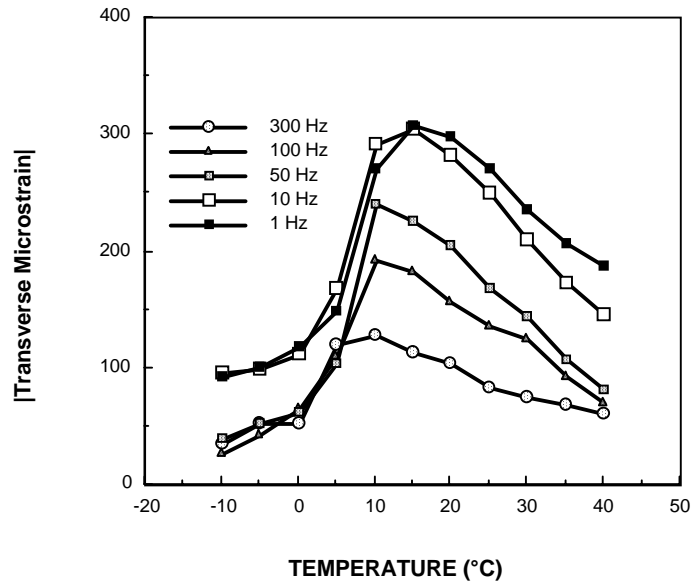


Figure 11. Frequency dependence of electromechanical properties of Lockheed Martin Generation 2 S250141 (from Pilgrim 1993).

The performance of the materials is also composition dependent. This is shown in Figs. 12, 13, and 14 for the Lockheed-Martin ‘Generation 3’ materials.

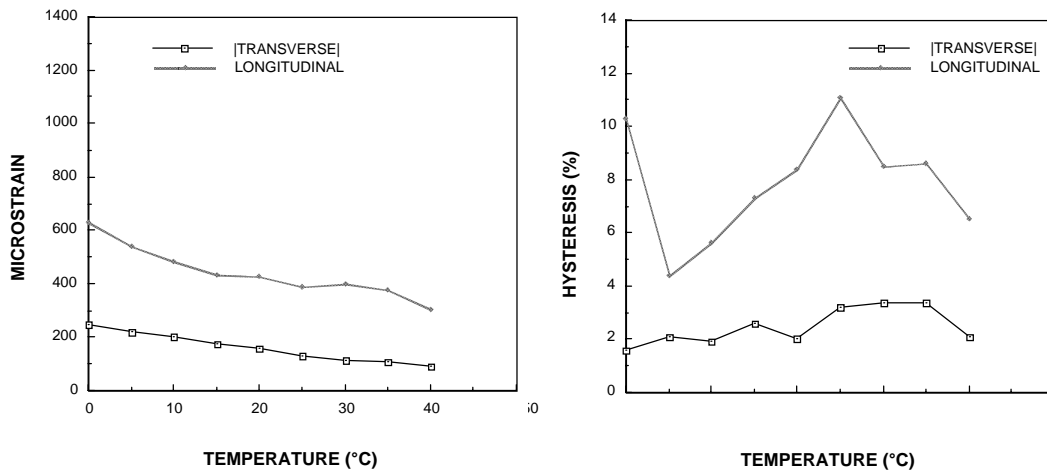


Figure 12. Induced strain and hysteresis for Lockheed Martin Generation 3 S250075 composition (1 Hz) (from Pilgrim MML TR 92-2c (1992)).

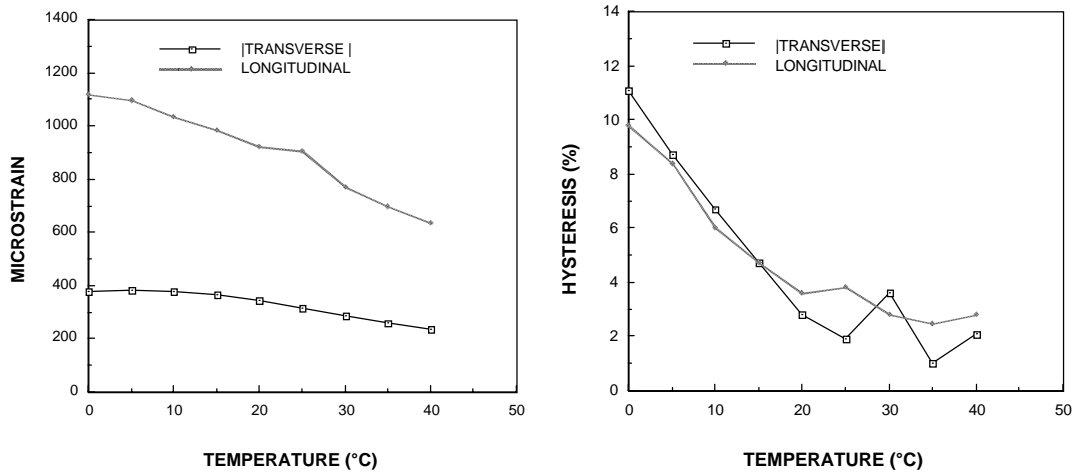


Figure 13. Induced strain and hysteresis for Lockheed Martin Generation 3 S250141 composition (1 Hz) (from Pilgrim MML TR 92-2c (1992)).

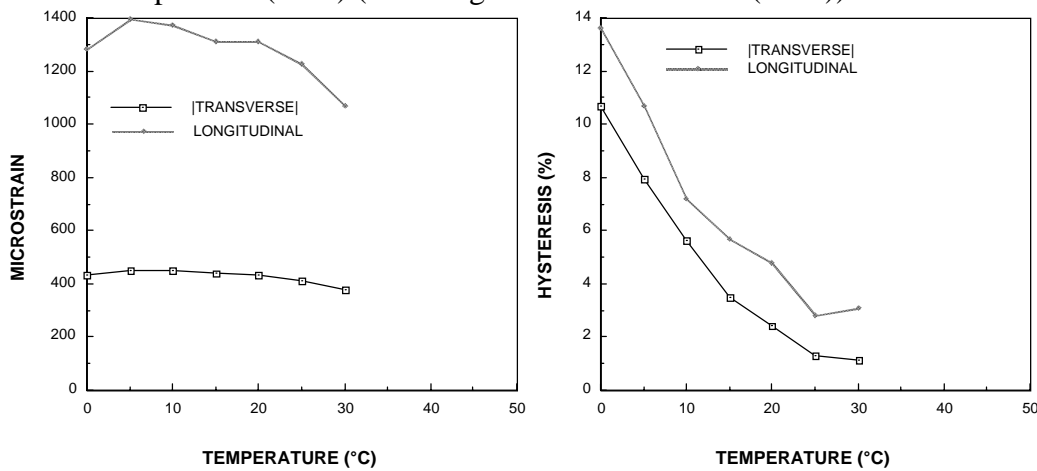


Figure 14. Induced strain and hysteresis for Lockheed Martin Generation 3 B250051 composition (1 Hz) (from Pilgrim MML TR 92-2c (1992)).

Aging of Properties

Figs. 12-14 from “Development of Advanced Active Sonar Materials and Their Microstructure / Property Relations” MML TR 92-2c N66001-91-C-6012 (Jan 1992). In addition to the temperature and expected compositional dependence, some researchers have noted time varying responses in both the weak- and high-field behavior of the perovskites and electrostrictors (Schulze 1988, Pan 1989, Sutherland 1990, Leary 1998). These 'aging' effects occur in both the high-field and weak-field properties. The effect is noted by the decrease in the material response with time. This is shown in Figs. 15 and 16, for high- and weak-fields respectively. The ‘aging’ phenomenon can be prevented with proper processing and care (Sutherland 1990, Ritter 1994).

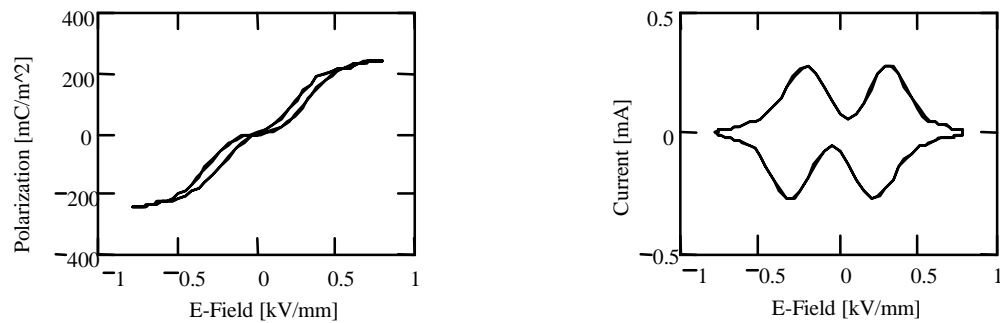


Figure 15. High-field aging in a PMN-PT-ST at 1 Hz after 5 days (from Leary 1998).

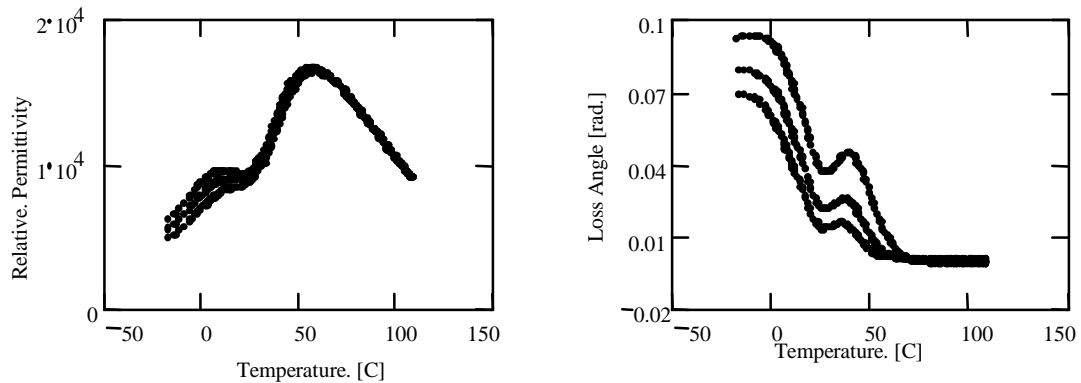


Figure 16. Weak-field aging in a PMN-PT-ST at 1, 10, and 100 kHz after 5 days (from Leary 1998).

Universal Properties Based on Reduced Temperature

In the absence of aging, the materials show remarkable unity of response, i.e., Figs. 12, 13, and 14 and the other Lockheed Martin Generation 3 materials can be overlaid if the response is plotted versus reduced temperature. This is shown in Figs. 17, 18, 19, and 20 for the Lockheed Martin Generation 3 materials. Note that in all cases the T_{\max} for 1 kHz has been used. Substitution of the frequency-corrected T_{\max} further improves the results.

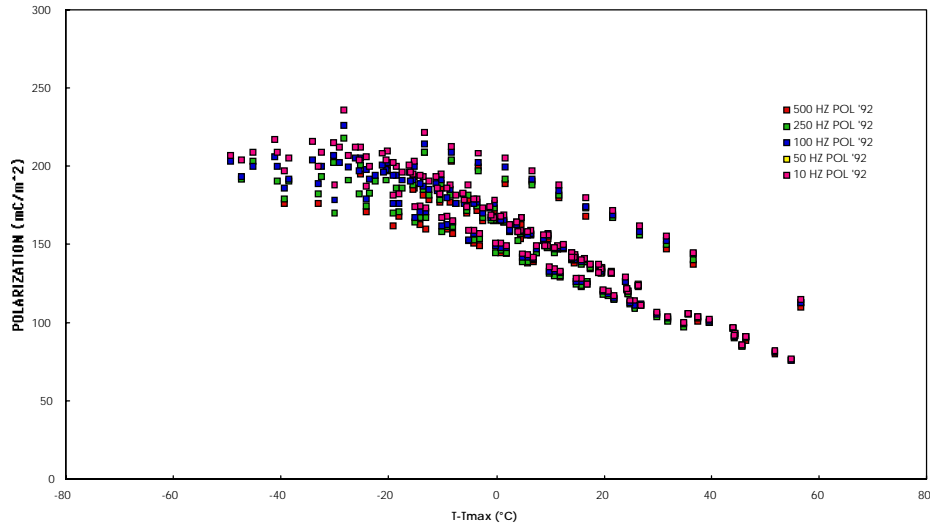


Figure 17. Polarization commonality for Generation 3 Lockheed Martin materials (from N66001-91-C-6012).

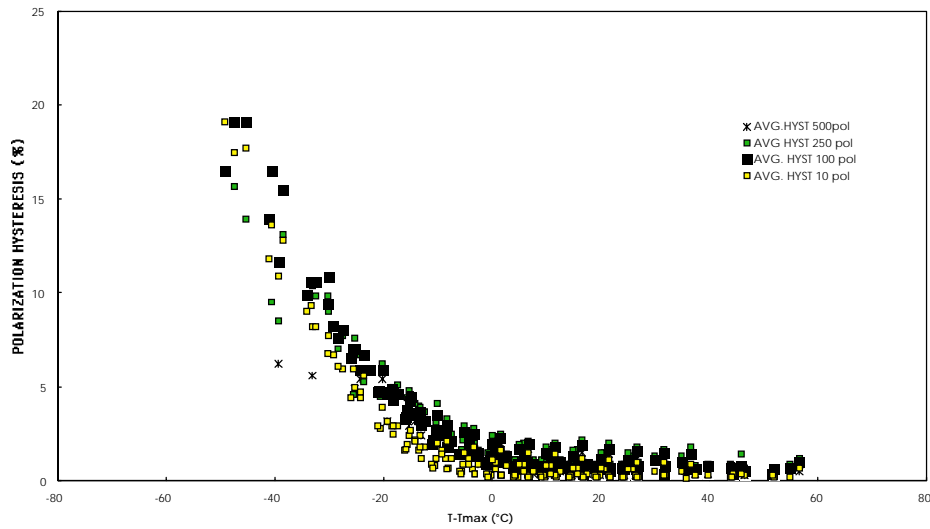


Figure 18. Polarization hysteresis commonality for Generation 3 Lockheed Martin materials (from N66001-91-C-6012).

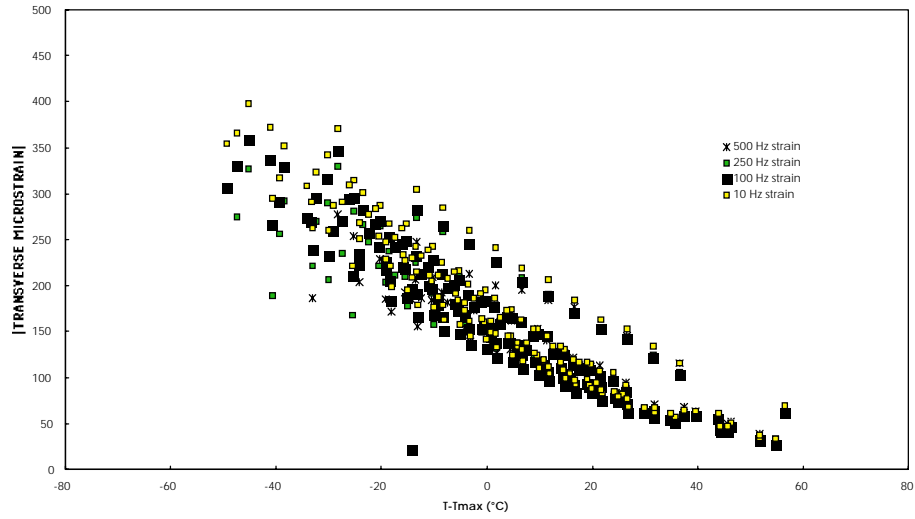


Figure 19. Transverse microstrain commonality for Generation 3 Lockheed Martin materials (from N66001-91-C-6012).

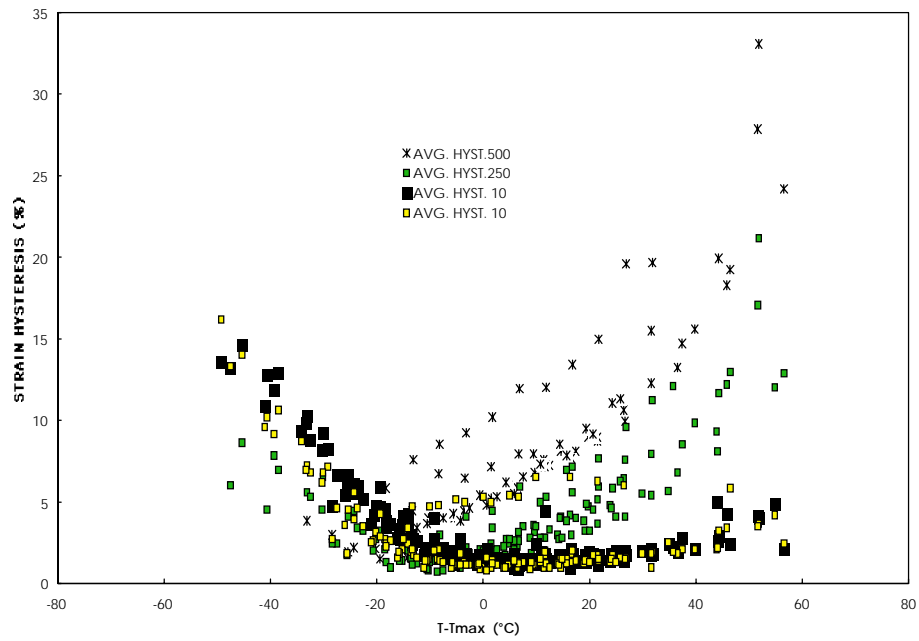


Figure 20. Transverse microstrain hysteresis commonality for Generation 3 Lockheed Martin materials (from N66001-91-C-6012).

Electromechanical Q_{ijkl}

Data as shown in Figs. 17-20 can be used to determine the electromechanical Q_{ijkl} . In the transverse case, this yields the Q_{12} values if the instantaneous strain is divided by the square of the instantaneous polarization. More commonly, the peak strain is divided by the square of the peak polarization to yield a “ Q_{eff} ”. Thus, Q_{eff} (Eq. 14 and Eq. 15) includes any piezoelectric components of the strain response and is not a true measure of transverse Q (Q_{12}). Equation 14 shows the effective response of the material as the sum a true piezoelectric portion (from ‘g’) and the underlying electrostriction. The magnitude of the piezoelectric contribution is scaled by ‘x’, the fraction of the material that shows piezoelectric activity. Above the transition, ‘x’ should be zero and the material should be electrostrictive. As the transition is approached ‘x’ should increase and Q_{ijkl} should diverge from Q_{eff} . As shown in Fig. 21, Q_{eff} is constant for measurements at 1 Hz. However, (the 'knee' temperature) and Q_{eff} are apparently frequency dependent. This is shown for an S250141 plate, Lockheed Martin Generation 1 material in the figures.

The change in Q_{eff} is more abrupt and distinct than the change visible in either the strain or polarization plots. In general, Q_{eff} increases in magnitude at lower temperatures. This effect is more pronounced at lower frequency. This effect has been attributed to the onset of piezoelectric contributions and to heating in the Generation 1 materials (Pilgrim 1992).

$$\epsilon_{ij} = xg_{kij}P_k + Q_{klj}P_kP_l = Q_{eff}P_kP_l \quad (\text{Eq. 14})$$

where

$$xg_{kij}/P_l + Q_{klj} = Q_{eff} \quad (\text{Eq. 15})$$

The piezoelectric g, leftmost term in Eq. 15, should become more important at lower frequency for a given temperature, since the soft piezoelectric regions can pole during the measurement. For relaxors with broad phase transitions a portion of the material can be piezoelectrically activated at correspondingly high temperatures. Consequently, there will be a piezoelectric contribution (xg/P) to Q_{eff} at low frequency. This contribution should increase the magnitude of Q_{eff} , shift the 'knee' to higher temperatures, and broadens the transition.

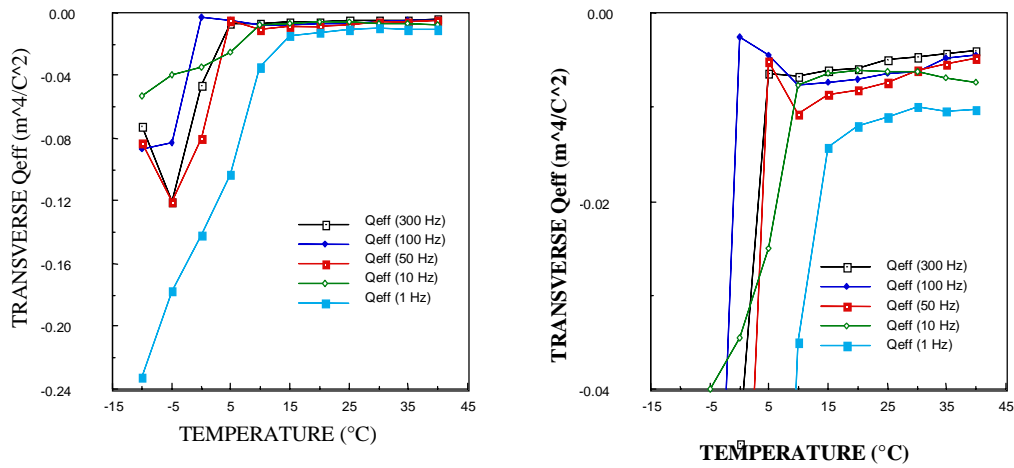


Figure 21. Frequency effects on Q_{eff} for a Lockheed Martin Generation 1 S250141 on the field interval 0-0.5 MV/m (adapted from Pilgrim 1992 and “Development of Advanced Active Sonar Materials and Their Microstructure-Property Relations” MML TR 91-33c N62190-91-M-0322 (June 1991)).

This effect is another manifestation of the piezoelectric contribution noted in Fig. 2. However, the frequency dependence is not necessarily a general phenomenon in the PMN-materials under all conditions of temperature, field, and frequency. In fact, the diminishing effect at higher frequencies suggests that the frequency dispersion would be less at higher temperatures. This has been confirmed for the Lockheed Martin Generation 3 materials (Fig. 22). Note that the frequency dependence has been wholly removed by using reduced frequency as the x-axis—this leaves a frequency independent Q_{eff} .

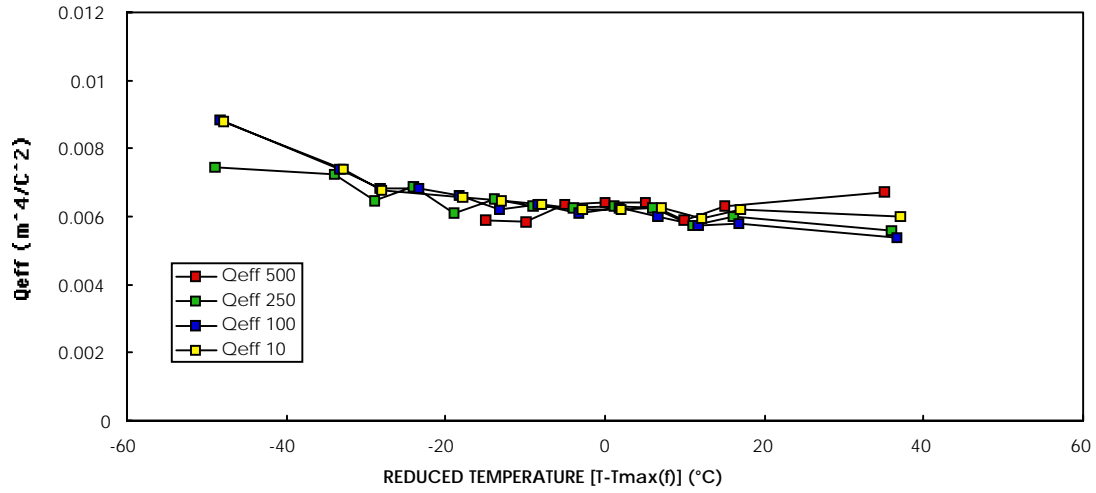


Figure 22. Effective electromechanical Q for a Lockheed Martin Generation 3 B300100 (from MML TM 93-01 N66001-91-C-6012).

Electromechanical Coupling

Determination of electromechanical coupling in electrostrictors is based on the same principles as for piezoelectrics (Berlincourt 1968, Tsuchiya 1981, IEEE 1987). However, the frequency dependence, field dependence and need for a bias field make it more difficult to experimentally determine the appropriate coefficients. Direct application of the IEEE equations, results in an underestimation of the coupling coefficient (c.f. Kelly 1997). This arises from neglecting the electrostrictive terms and also from the frequency dependence of the properties. Despite these limitations, the IEEE standard equations can be modified to determine coupling (see Eq. 16 from Hom 1994).

$$k_{33}^2 = \frac{kQ_{3333}^2 P_B^4}{s_{3333}^P \left(P_B \ln \left(\frac{P_s + P_B}{P_s - P_B} \right) + P_s \ln \left(1 - \left(P_B / P_s \right)^2 \right) + \frac{\epsilon_a}{k} \arctan h^2 \left(\frac{P_B}{P_s} \right) \right)} \quad (\text{Eq. 16})$$

where the ‘P’ values are determined from the polarization response, ‘k’ is permittivity, ‘s’ is stiffness and ‘h’ is an empirical fit parameter. Application of this model yields the characteristic coupling for electrostrictors (Figs. 23 and 24). This constitutive approach accommodates the nonlinearities and the prestress dependence. It can be extended to predict the stress and modulus of the materials (Brown 1996, Hom 1994, Hom 1994). Alternative models to those of Hom are also available (Piquette 1997 and Robinson 1996). A modified method based directly on the energy balance can also be applied—this is more

convenient to determine, but provides equivalent results to Hom 1994 (see Fig. 25 from Leary 1997). Quasistatic measurement of coupling may also be done *in-situ* (Janus 1997).

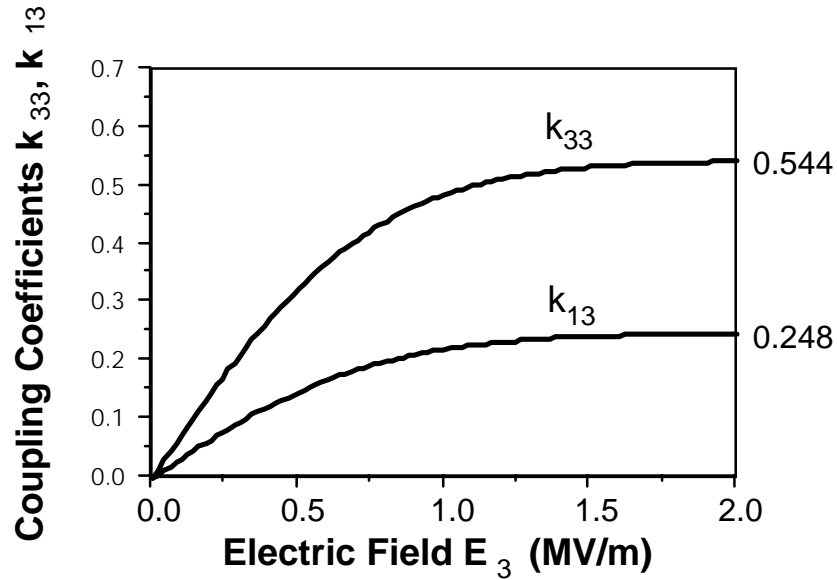


Figure 23. The quasi-static coupling coefficients versus applied electric field for Lockheed Martin Generation 3 b250077 PMN at 5°C without bias voltage or prestress (Hom 1994).

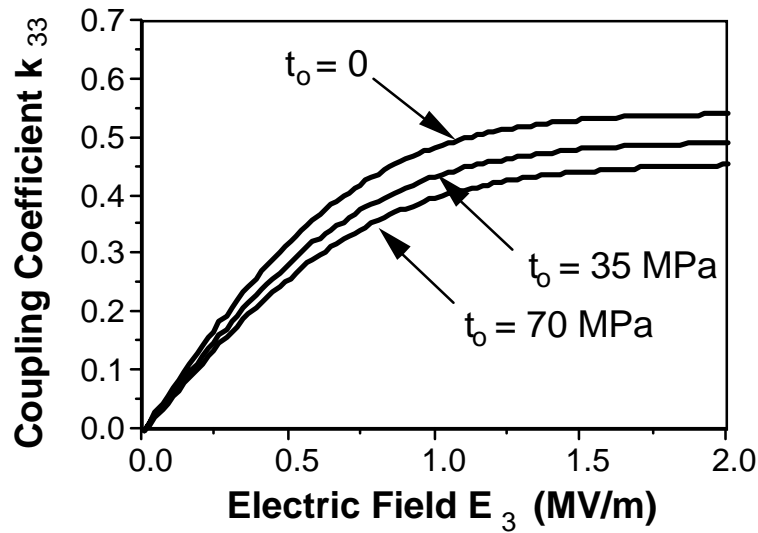


Figure 24. The longitudinal coupling coefficient versus applied electric field for Lockheed Martin Generation 3 b250077 PMN at 5°C without bias voltage at various levels of compressive pre-stress (Hom 1994).

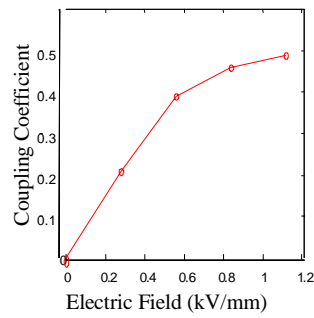
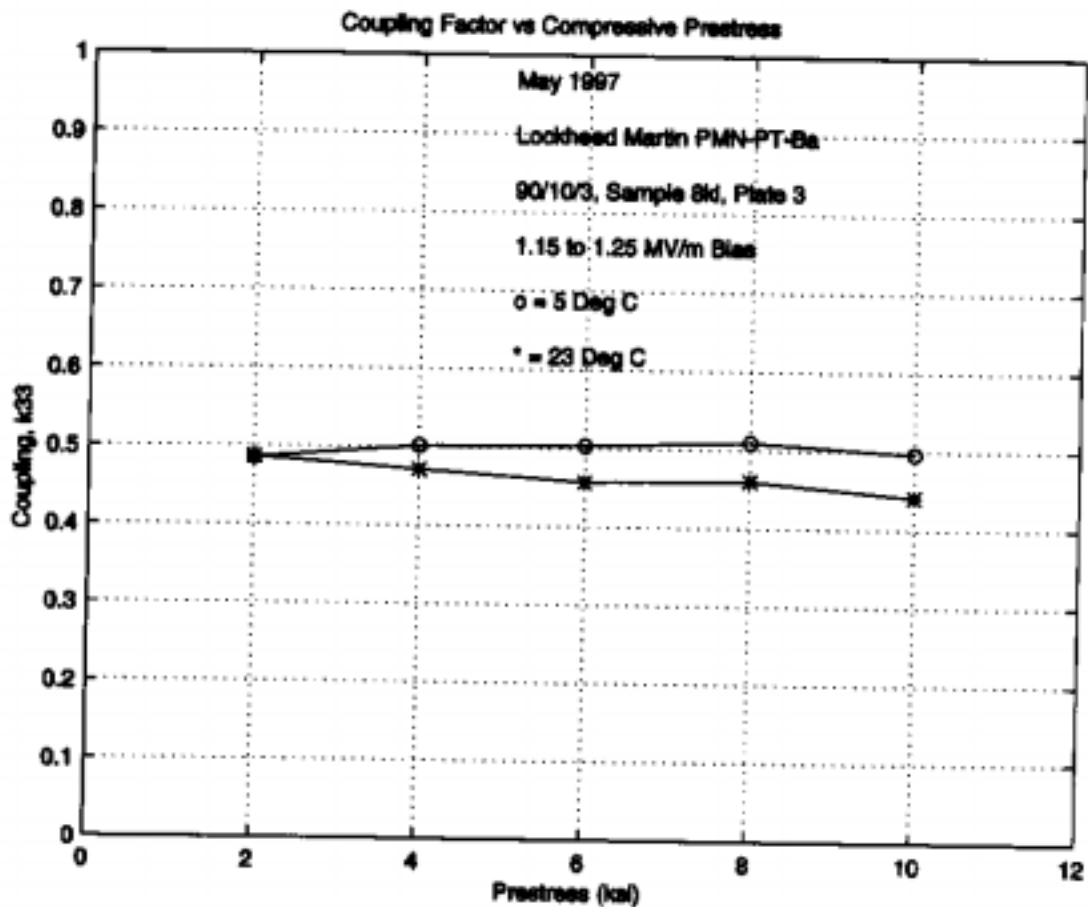


Figure 25. Coupling as a function of ac drive field at room temperature for a Lockheed Martin Generation 2 PMN-PT-ST (after Leary 1997).

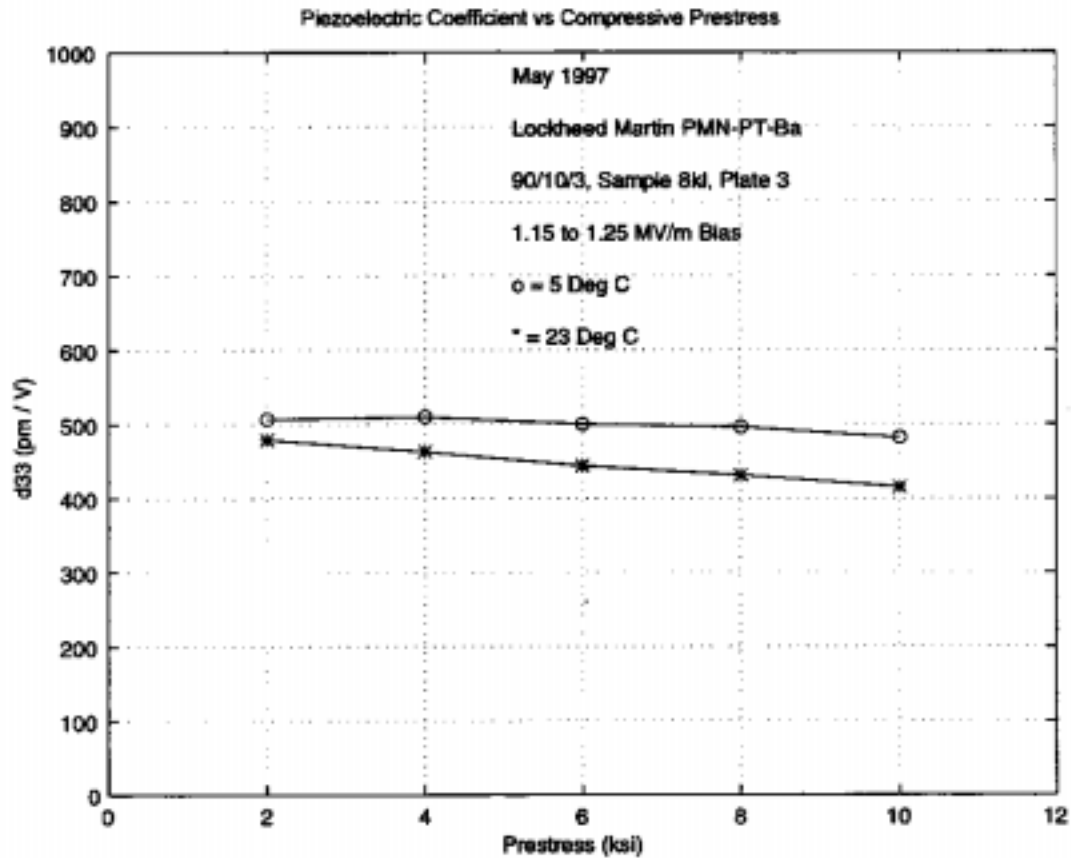
Stress Effects

Although a great deal of work has been done, there are few complete data sets available. Three of the more complete are in Rittenmyer 1998, Janus 1997, and Brown 1996. Figs. 26, 27, 28, 29, 30, 31, and 32 are taken from Janus 1997. While the specific values and critical temperatures of electrostrictive PMN's will vary with composition, the general behaviors are anticipated to remain constant.



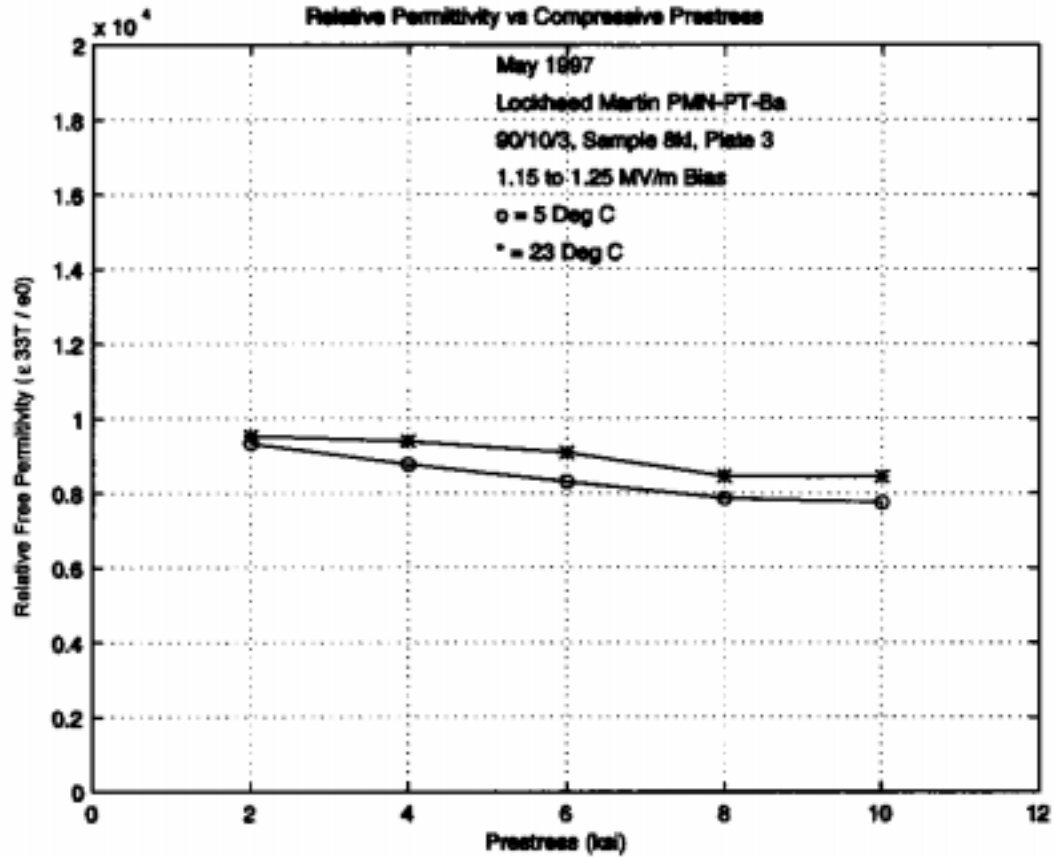
This plot summarizes the variation in coupling coefficient, k_{33} , with compressive stress. The results demonstrate that this material achieves a large-signal coupling factor, k_{33} , between 0.49 and 0.51 at the temperature at which it was designed to operate, 5° C. When compared with the data at 23° C, k_{33} is shown to be slightly enhanced at this lower temperature.

Figure 26. from R.S. Janus, M.B. Moffett, and J.M. Powers, "Large Signal Characterization of PMN-PT-Ba (90/10/3)," *NUWC-NPT Reprint Report 10,860* (1997). [Lockheed Martin Generation 3 B300100].



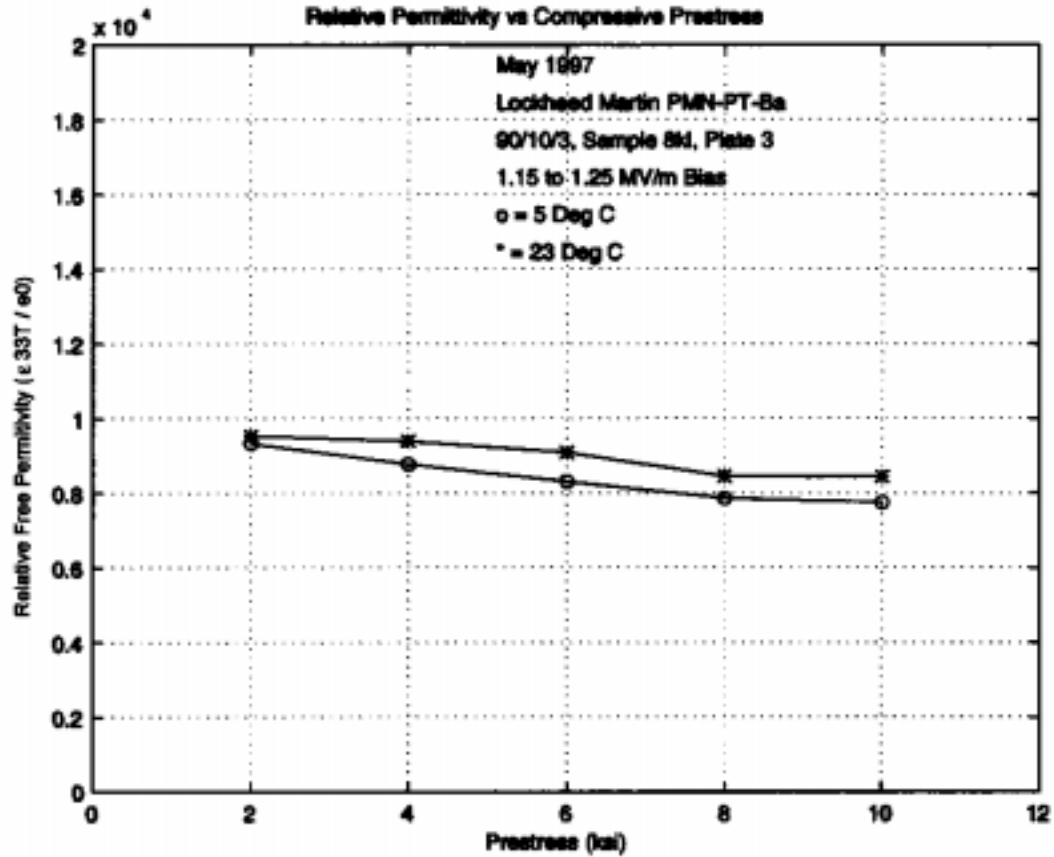
k_{33} is derived from the piezoelectric coefficient, d_{33} , elastic compliance, s_{33}^E , and electrical permittivity, ϵ_{33}^T : $k_{33}^2 = d_{33}^2 / (s_{33}^E \epsilon_{33}^T)$. Values for these three parameters that were used to compute the corresponding k_{33} are shown in this and the two following plots.

Figure 27. from R.S. Janus, M.B. Moffett, and J.M. Powers, "Large Signal Characterization of PMN-PT-Ba (90/10/3)," *NUWC-NPT Reprint Report 10,860* (1997). [Lockheed Martin Generation 3 B300100].



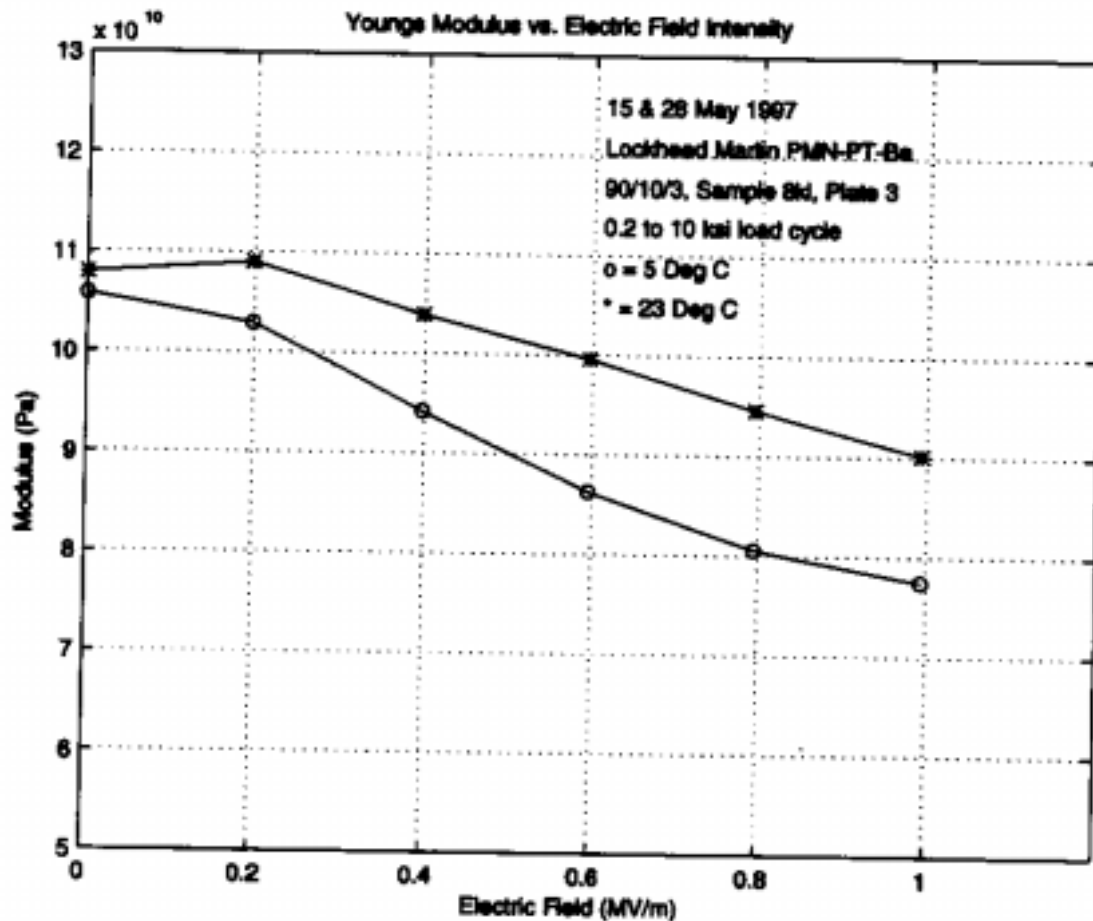
Here ϵ_{33}^T has been normalized by the permittivity of free space, ϵ_0 .

Figure 28. from R.S. Janus, M.B. Moffett, and J.M. Powers, "Large Signal Characterization of PMN-PT-Ba (90/10/3)," *NUWC-NPT Reprint Report 10,860* (1997). [Lockheed Martin Generation 3 B300100].



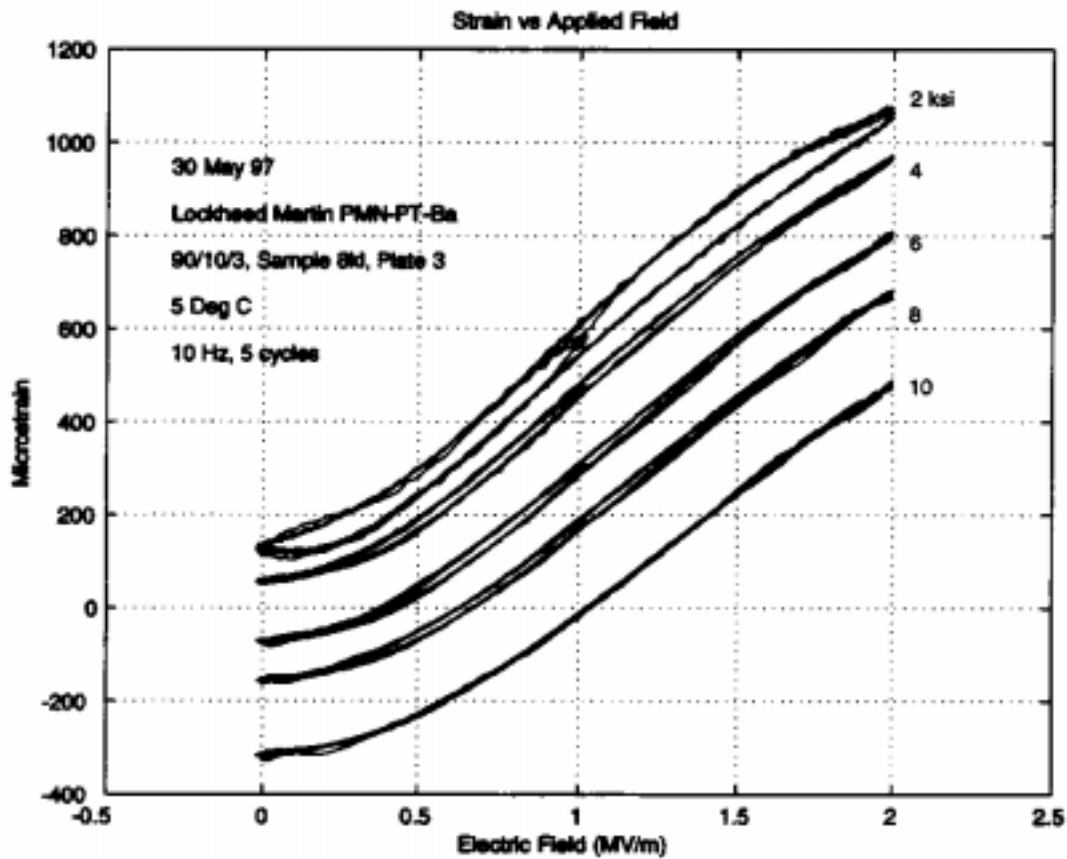
Here ϵ_{33}^T has been normalized by the permittivity of free space, ϵ_0 .

Figure 29. from R.S. Janus, M.B. Moffett, and J.M. Powers, "Large Signal Characterization of PMN-PT-Ba (90/10/3)," *NUWC-NPT Reprint Report 10,860* (1997). [Lockheed Martin Generation 3 B300100].



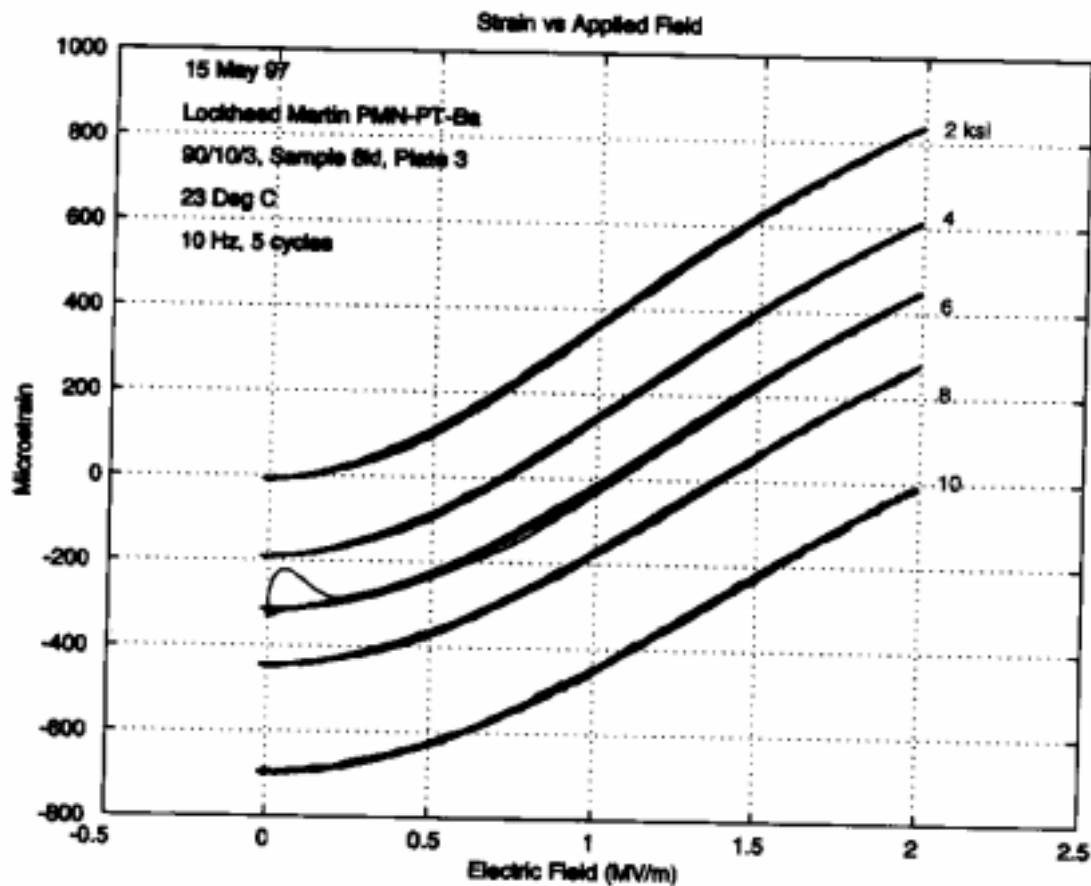
The line pressure to the pneumatic cylinder was ramped up and down to sweep the mechanical bias between 0.2 and 10 ksi while maintaining a constant electric field across the sample. Stress and strain data were simultaneously recorded and plotted against each other to obtain Young's modulus (i.e., $1 / s_{33}E$). The resultant values of Young's modulus versus electric field are shown in this plot.

Figure 30. from R.S. Janus, M.B. Moffett, and J.M. Powers, "Large Signal Characterization of PMN-PT-Ba (90/10/3)," *NUWC-NPT Reprint Report 10,860* (1997). [Lockheed Martin Generation 3 B300100].



The PMN sample was driven with 5 cycle, 10 Hz sinusoidal pulses on a 1 MV/m dc pedestal to reach a peak field of 2 MV/m. The values of d_{33} were computed from the slopes of the hysteresis loops of strain, S_3 , versus electric field, E_3 , $d_{33} = \Delta S_3 / \Delta E_3$. This is a composite plot of the loops taken at 5° C for prestresses of 2, 4, 6, 8, and 10 ksi. The slopes were determined between the endpoints at 0.5 and 2 MV/m. These large signal data represent the drive levels that are required for actual sonar operation.

Figure 31. from R.S. Janus, M.B. Moffett, and J.M. Powers, "Large Signal Characterization of PMN-PT-Ba (90/10/3)," *NUWC-NPT Reprint Report 10,860* (1997). [Lockheed Martin Generation 3 B300100].



This second set of strain versus field loops was taken to determine d_{33} at 23° C. Each loop is averaged from 10 data records.

Figure 32. from R.S. Janus, M.B. Moffett, and J.M. Powers, "Large Signal Characterization of PMN-PT-Ba (90/10/3)," *NUWC-NPT Reprint Report 10,860* (1997). [Lockheed Martin Generation 3 B300100].

Harmonic Effects and Considerations

The electrostrictors produce strain at a doubled frequency; however, the materials are usually run with an applied dc-bias which results in unipolar excitation. This is shown in the preceding figures and in Figs. 33 and 34 (Leary 1998).

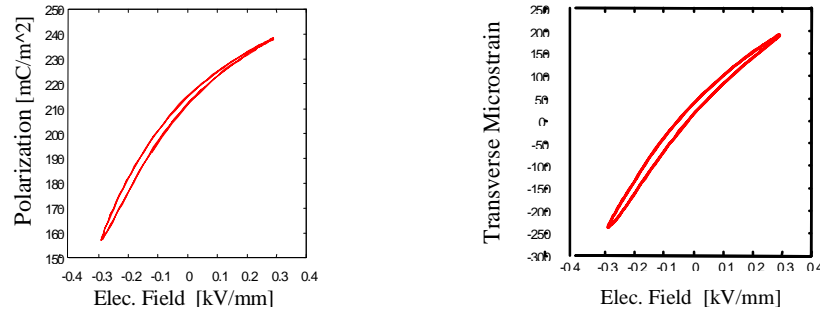


Figure 33 and Figure 34. Polarization and strain as a function of applied ac field for a Lockheed Martin Generation 2 PMN-PT-ST. The dc bias field (= 0.7 kV/mm) was subtracted from the field values (after Leary 1997).

In a transducer, the amplitude of the harmonics will be reduced through the action of the shell or radiator. In practice an optimum bias level must be selected for each material/transducer pair to ensure that harmonic distortion is below the acceptable threshold. Since the deviations from linearity are comparable to existing piezoelectrics this has not proven to be a major problem. Passaro in Winzer 1994, shows that Lockheed Martin Generation 3 materials had 3rd harmonics that were more than 35 dB down for a bias of 0.7 MV/m and drive amplitudes of 0.5 MV/m (~225 transverse microstrain @ 1 kHz). The comparative value for Morgan Matroc PZT-8 (Navy III) was -54.5 dB at zero bias and 5MV/m drive amplitude (~110 transverse microstrain @ 1 kHz). The electrical and mechanical powers stay in phase under unipolar use (see Fig 35 from Leary 1997).

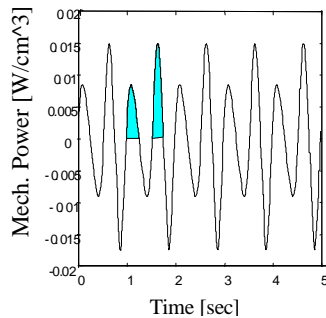


Figure 35. Electrical and mechanical power signals for dc biased case. [Lockheed Martin PMN-PT-ST Generation 2 from Leary 1997].

Mechanical Q and Imittance Behavior

The mechanical Q of the materials is illustrated in Fig. 36. There is some bias-field dependence. The minimum in the Qm curve corresponds to the broad transition from electrostrictive to piezoelectric behavior

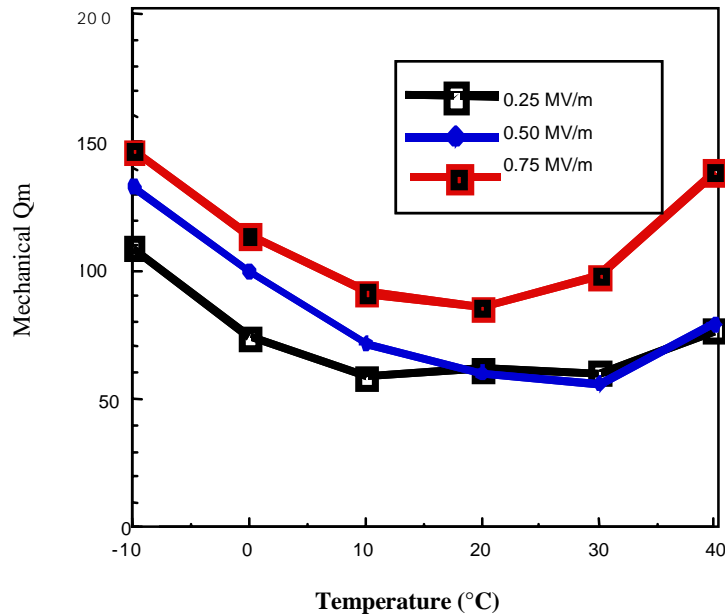


Figure 36. Mechanical quality factor (Qm) for a B200120 sample. “Development of Advanced Active Sonar Materials and Their Microstructure / Property Relations” [from Pilgrim et al. MML TR 92-2c N66001-91-C-6012 (Jan 1992)].
References

Under bias conditions, the electrostrictive compositions mimic the familiar behavior of piezoelectrics (IEEE 1987). There is some variation in the electrical response of the materials with bias field and amplitude. However, this effect is quantifiable and does not lead to the generation of undesirable harmonics. There is some movement in the resonance frequency with bias as noted in Fig. 37 from Leary 1998.

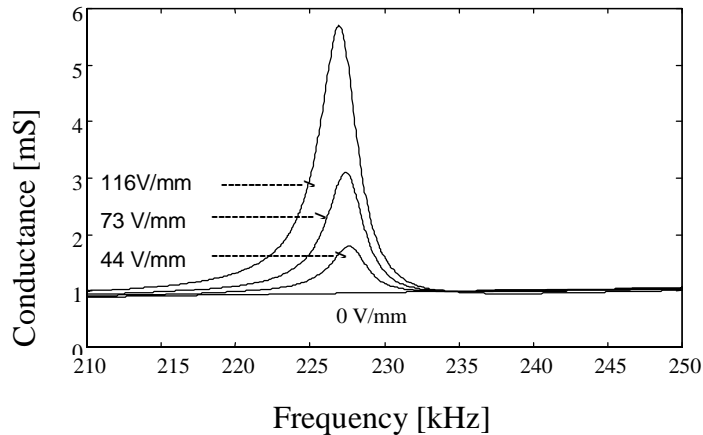


Figure 37. Resonance behavior of a PMN-PT-ST with dc-bias field. [Lockheed Martin Generation 2 from Leary 1998].

Transducer Performance

Early transducer performance is reported in Pilgrim 1993 wherein a Lockheed Martin Class IV single shell flextensional bested an equivalent Navy III transducer by >5 dB SPL across the band 1 to 4 kHz. Additional details of these tests are available in NRL USRD 1991.

More recently another single shell Class IV transducer was built and modeled with FlexT5.6 using ceramic properties of Lockheed Martin Generation 2 PMN (properties as those in the LBVDS testbed array). The actual material was coated in an attempt to make it suitable for transducers—it came from a rejected lot originally. The modeled results predicted that the transducer should develop a transmit voltage response (TVR) of 127 dB re 1 μ Pa @ 1 m per V. The model and actual TVR's are shown in Fig. 38 (from Bridger 1998).

The test series consisted of a free field measurement to determine the driving properties of the material at low level compared with those predicted. The TVR was measured at a drive level of 200 V_{rms}, with 3800 VDC bias (0.7 MV/m), for a depth of 30 ft. The measured resonant frequency (5300 Hz) agrees with the predicted value, but the measured Q, taken from the 3 dB down points, (5.2) was lower than predicted (6.4) giving the curves a slightly different shape. Both measured and predicted Q values are higher than usual for PMN-based 4.5-kHz transducers. The enhanced Q is most probably due to the smaller radiating area of the single shell — giving rise to low radiation loading on the transducer compared to the normal double-shell transducer.

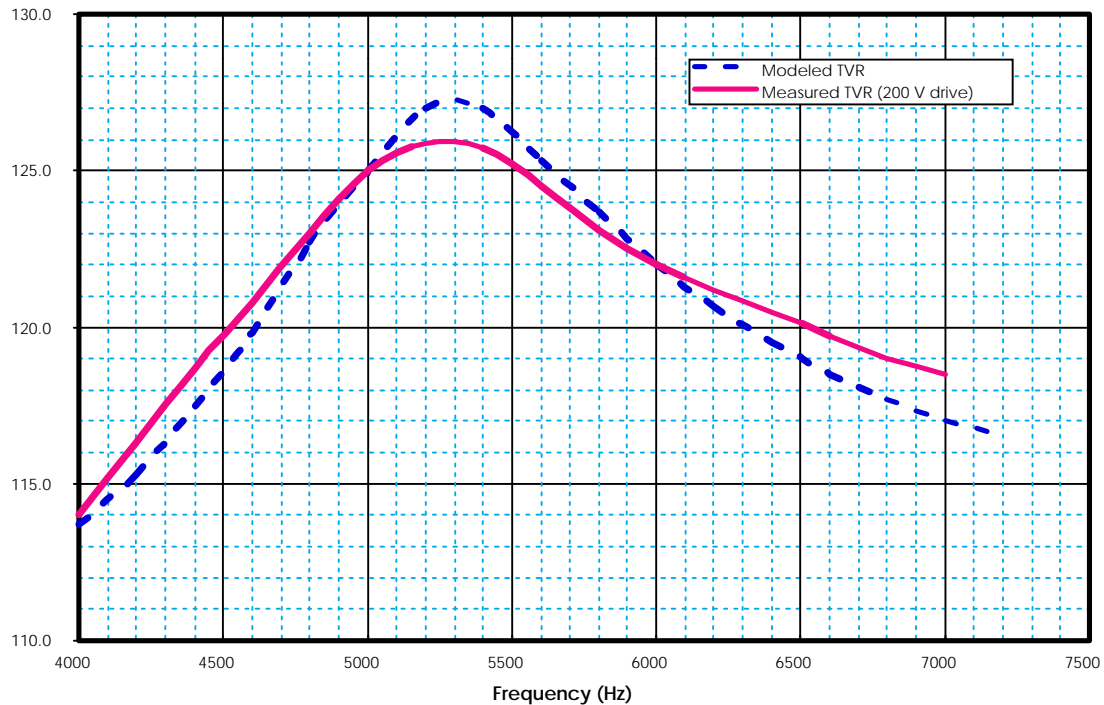


Figure 38. Measured and predicted TVR's of the transducer using surface modified PMN-PT-BT (from Bridger 1998).

The results and model predict that a full 4.5-kHz transducer would have a TVR of 138 dB re 1 μ Pa@ 1 m per V which is about 1 dB lower than the units currently in the LBVDS testbed array and about 2 dB lower than a Generation 3 PMN transducer. These results show not only the promise of PMN electrostrictors, but suggest that with better understanding further improvements in performance may be possible.

Summary

The PMN materials have demonstrated potential and promise as improved transducer materials. They broaden the range of design options by providing a mix of properties unavailable in traditional piezoelectrics. Although some outstanding transducers have been made, the present state of understanding and processing require improvement.

Typical properties are: 1000 microstrain on the interval 0-1 MV/m with a coupling of 0.5; high-field electrical impedance ~5 times that of traditional piezoelectrics, gracefully and repeatably changing with temperature, frequency, and prestress; recoverable change of properties with temperature

As caveats, the user **MUST** remember that PMN's are not direct replacements for traditional piezoelectrics. They are distinct materials with different electromechanical behaviors. This difference is most obvious in the electromechanical response behavior of the electrostrictive materials with changes in bias field, drive level, frequency, and prestress. In addition, the knowledge base for reproducible and reliable processing is still

emerging. The ‘rules-of-thumb’ for traditional piezoelectrics, both processing and use, do not wholly apply—the new rules are still under development. Despite this lack of maturity, the majority of PMN-based transducers have demonstrated improved performance when compared to traditional piezoelectrics.

References

This collection of references is not exhaustive. Much good work has been omitted. However, most have been cited in the chapter and all provide good sources for additional learning on piezoelectrics and electrostrictors.

- A.F. Devonshire, “Theory of Ferroelectrics,” *Philosophical Magazine* **3** (10), 85-130, (1954).
- V.A. Isupov, "On The Question Of Causes Of Formation Of A Curie Range Of Temperatures In Certain Ferroelectric Solid Solutions," *Sov. Phys. Tech. Phys.* **26**, pp. 1846-1849 (1956).
- G.A. Smolenskii and A.I. Agranovskaya, “Dielectric Polarization and Losses of Some Complex Compounds,” *Sov. Phys.—Tech. Phys. (Engl. Transl.)*, **3**, pp. 1380-82 (1958).
- D.A. Berlincourt, “Piezoelectric and ferroelectric energy conversion,” *IEEE Trans. Sonic. Ultrason.*, vol. SU-15, no.2, pp. 89-97, (April 1968).
- F. Jona and G. Shirane, Ferroelectric Crystals, Dover 1993, Pergamon (1962).
- G.M. Smolenskii, "Physical Phenomena in Ferroelectrics with Diffused Phase Transition," *Proc. Intl. Meeting on Ferroelectrics*, 2nd, 1969, 26-36 (1970).
- B. Jaffe, W.R. Cook, and H. Jaffe, Piezoelectric Ceramics, NY NY, Academic Press (1971).
- T.L. Reinecke and K.L. Ngai, "Disorder In Ferroelectrics: Relaxation Effects," *Ferroelectrics*, Vol. 16, pp. 85-87 (1977).
- M.E. Lines and A.M. Glass, Principles and Applications of Ferroelectrics and Related Materials, Oxford University Press Section 8.4.1, pp. 285-292 (1977).
- S.-J. Jang, "Electrostrictive Ceramics for Transducer Applications," Ph.D. Thesis, The Pennsylvania State University, University Park, PA (1979).
- J.F. Nye, Physical Properties of Crystals, Oxford University Press, pp. 68-77 (1979).
- J. Kuwata, K. Uchino, and S. Nomura, "Electrostrictive coefficients in $\text{Pb}(\text{Mg}_{1/3}\text{Nb}_{2/3})_3$ ceramics," *Japanese Journal of Applied Physics* **19** (11), 2099-2103, (1980).
- K. Uchino, Y. Tsuchiya, S. Nomura, T. Sato, H. Ishikawa, and O. Ikeda, "Deformable Mirror Using the PMN Electrostrictor," *Applied Optics*, Vol. 20, No. 17, pp. 3077-3080 (1981).
- Y. Tsuchiya, K. Uchino, and S. Nomura, “Approximate formulas for a low-Q electromechanical resonator and their applications to electrostrictive PMN-based ceramics,” *Jap. J. Appl. Phys.*, vol. 20, no.10, pp. 1841-47, (Oct. 1981).
- S. Nomura, "Complex Perovskite-type Oxides," Landolt-Bornstein Numerical Data and Functional Relationships in Science and Technology Ferroelectrics and Related Substances Subvolume a: Oxides, K.-H. Hellwege and A.M. Hellwege, ed., Springer-Verlag, Vol 16a, pp. 87-108 (1981).

- S.L. Swartz and T.R. Shrout, "Fabrication of Perovskite Lead Magnesium Niobate," *Mater. Res. Bull.*, **17**, 1245-1250 (1982).
- J.M. Herbert, *Ferroelectric Transducers and Sensors*, Gordon and Breach, NY (1982).
- J.M. Herbert, *Ceramic Dielectrics and Capacitors Vol. 6 of Electrocomponent Monographs*, Gordon and Breach (1985).
- O.B. Wilson, "*An Introduction to the Theory and Design of Sonar Transducers*," US Gov. (1985).
- K. Uchino, "Electrostrictive Actuators: Materials and Applications," *Ceramic Bulletin*, Vol. 65, No. 4, pp. 647-652 (1986).
- L.E. Cross, "Relaxor Ferroelectrics," *Ferroelectrics*, Vol. 76, pp. 241-267 (1987).
- R.J. Bobber, *Underwater Electroacoustic Measurements*, Peninsula, Los Altos, (1988).
- IEEE Standard on Piezoelectricity*, Institute of Electrical and Electronics Engineers Ultrasonics, Ferroelectrics, and Frequency Control Society, ANSI/IEEE Std 176-1987(January 1988)
- W.A. Schulze and K. Ogino, "Review of Literature on Aging of Dielectrics," *Ferroelectrics*, Vol. 87, pp. 361-377 (1988).
- W.Y. Pan, W.Y. Gu, J. Taylor, and L.E. Cross, "Large Piezoelectric Effect Induced by Direct Current Bias in PMN:PT Relaxor Ferroelectric Ceramics," *Japanese Journal of Applied Physics*, Vol. 28, No. 4, pp. 653-661 (1989).
- M.P. Harmer, J. Chen, P. Peng, H.M. Chan, and D.M. Smyth, "Control of Microchemical Ordering in Relaxor Ferroelectrics and Related Compounds," *Ferroelectrics*, **97** pp. 263-274 (1989).
- S.R. Winzer, N. Shankar, A.P. Ritter, "Designing Cofired Multilayer Electrostrictive Actuators for Reliability," *J. Am. Cer. Soc.*, **72** (12) 2246-2257 (1989).
- M.F. Yan, H.C. Ling, and W.W. Rhodes, "Preparation and Properties of PbO-MgO-Nb₂O₅ Ceramics Near the Pb(Mg_{1/3}Nb_{2/3})O₃ Composition," *J. Mater. Res.*, Vol 4 No 4 Jul/Aug pp. 930-944 (1989).
- M.F. Yan, H.C. Ling, and W.W. Rhodes, "Effects of Dopants on PbO-MgO-Nb₂O₅ Ceramics Near the Pb(Mg_{1/3}Nb_{2/3})O₃ Composition," *J. Mater. Res.*, Vol 4 No 4 Jul/Aug pp. 945-966 (1989).
- S.R. Winzer, A.E. Bailey, K. Bridger, G.L. Childs, R. Herring, M. Massuda, S. M. Pilgrim, F.C. Poppe, A.P. Ritter, L.L. Rouch, N. Shankar, and A.E. Sutherland, "Deformable Mirror Actuators for Rapid Retargeting- WL-TR-89-20 DTIC," Defense Technical Information Center, Alexandria, VA, 1989.
- J. Chen, H. Chan, and M.P. Harmer, "Ordering Structure and Dielectric Properties of Undoped and La/Na-Doped Pb(Mg_{1/3}Nb_{2/3})O₃," *J. Am. Ceram. Soc.*, **72** [4], pp. 593-98 (1989).
- Q. Zhang, W. Pan, A. Bhalla, and L.E. Cross, "Electrostrictive and Dielectric Response in Lead Magnesium Niobate-Lead Titanate (0.9PMN-0.1PT) and Lead Lanthanum Zirconate Titanate (PLZT 9.5/65/35) under Variation of Temperature and Electric Field," *J. Am. Ceram. Soc.*, **72** [4], pp. 599-604 (1989).
- S.R. Winzer, N. Shankar, A.P. Ritter, "Designing Cofired Multilayer Electrostrictive Actuators for Reliability," *J. Am. Ceram. Soc.*, **72** [12], pp. 2246-57 (1989).
- S.R. Winzer, Bailey, A.E., Bridger, K., Childs, G.L., Herring, R., Massuda, M., Pilgrim, S. M., Poppe, F.C., Ritter, A.P., Rouch, L.L., Shankar, N., and Sutherland, A.E., "Deformable Mirror Actuators for Rapid Retargeting- WL-TR-89-20 DTIC," Defense Technical Information Center, Alexandria, VA (1989).

- C.A. Randall and A.S. Bhalla, "Nanostructural-Property Relations in Complex Lead Perovskites," *J. J. Appl. Phys.*, **29** 2, pp. 327-333 (1990).
- T. Furukawa and N. Seo, "Electrostriction as the Origin of Piezoelectricity in Ferroelectric Polymers," *Japanese Journal of Applied Physics*, Vol. 29, No. 4., pp. 675-680 (1990).
- F.S. Galasso, F.S., *Perovskites and High Tc Superconductors*, Gordon and Breach, pp. 95-129 (1990).
- S. M. Pilgrim, A. E. Sutherland, and S. R. Winzer, "Diffuseness as a Useful Parameter for Relaxor Ceramics," *J. Amer. Ceram. Soc.*, Vol. 73 No. 10, pp. 3122-3125 (1990).
- A.E. Sutherland, S.M. Pilgrim, A.E. Bailey, and S.R. Winzer, "Dielectric Aging of Doped PMN-PT Ceramics," *Ceramic Transactions-Materials and Processes for Microelectronic Systems Vol. 15*, eds. K.M. Nair, R.Pohanka, and R.C. Buchanan, Am. Ceram. Soc., pp. 105-127 (1990).
- T. Ikeda, 1990, "Complex Perovskite-type Oxides," *Landolt-Bornstein Numerical Data and Functional Relationships in Science and Technology Ferroelectrics and Related Substances Subvolume a: Oxides*, E. Nakamura and T. Mitsui ed., Springer-Verlag, Vol 28, pp. 81-96 (1990)
- H. Takeuchi, H. Masuzawa, and C. Nakaya, "Relaxor ferroelectric transducers," *Proc. IEEE Ultrason. Symp.*, pp. 697-704 (1990).
- A.P. Ritter, P. Kuhn, S.M. Pilgrim, J.M. Sewell, and S.R. Winzer, "Applications of Very High Energy Density Electrostrictive Ceramics for Underwater Projectors," 121st Annual Meeting of the Acoustic Society of America, Baltimore MD, April 1991.
- M. Massuda and S.M. Pilgrim, "Temperature Dependence of Strain and Polarization for Electrostrictive Materials," presented at the Joint Electronics & Glass and Optical Materials Fall Meeting of the American Ceramic Society, Arlington VA, October 1991.
- D. Viehland, S.-J. Jang, and L.E. Cross, 1991, "Local Polar Configurations In Lead Magnesium Niobate Relaxors," *J. Appl. Phys.* 69 (1), pp. 414-419.
- C.E. Wheeler and B.G. Pazol, "Multilayer Electrodisplacive Actuators," *Ceramic Bulletin*, Vol. 70, No. 1, pp. 117-119 (1991).
- A.E. Bailey, S.R. Winzer, A.E. Sutherland, and A.P. Ritter, "Electrostrictive ceramic materials including a process for the preparation thereof and application thereof," US Patent 5,032,558, 16 July 1991.
- A.E. Bailey, S.R. Winzer, A.E. Sutherland, and A.P. Ritter, "Electrostrictive ceramic materials including a process for the preparation thereof and application therefor," US Patent 5,023,032, 11 June 1991.
- NRL/USRD "Transducer Test Report S400-9384 March 1991"
- S.M. Pilgrim, M. Massuda, and A.E. Sutherland, "Electromechanical Determination of the High-Field Phase Transition of $\text{Pb}(\text{Mg}_{1/3}\text{Nb}_{2/3})\text{O}_3\text{-PbTiO}_3\text{-(Ba,Sr)TiO}_3$ Relaxor Ferroelectrics," *J. Am. Ceram. Soc.* 75 [7], pp. 1970-74 (1992).
- R.L. Snyder,, "X-Ray Diffraction," *Materials Science and Technology--a Comprehensive Treatment*, R.W. Cahn et. al, ed., VCH, Vol. 2, Chapter 4, pp. 320-334 (1992).
- V. Sundar, and R.E. Newnham, R.E., "Electrostriction and Polarization," *Ferroelectrics* Vol. 135, pp. 431-446 (1992).

- S.M. Pilgrim, A.E. Bailey, M. Massuda, J.D. Prodey, and A.E. Sutherland, "Effective Electromechanical Properties of Some $\text{Pb}(\text{Mg}_{1/3}\text{Nb}_{2/3})\text{O}_3\text{-PbTiO}_3\text{-(Ba,Sr)TiO}_3$ Ceramics, in Proceedings of the 1992 ISAF, Greenville SC, (August 1992).
- S.M. Pilgrim, M. Massuda, J.D. Prodey, and A.P. Ritter, "Electromechanical Properties of Some $\text{Pb}(\text{Mg}_{1/3}\text{Nb}_{2/3})\text{O}_3\text{-PbTiO}_3\text{-(Ba,Sr)TiO}_3$ Ceramics: Part One, "J. Am. Ceram. Soc., **75** [7], 1964-1969 (1992).
- S.M. Pilgrim, M. Massuda, and A.E. Sutherland, "Electromechanical Determination of the High-Field Phase Transition of $\text{Pb}(\text{Mg}_{1/3}\text{Nb}_{2/3})\text{O}_3\text{-PbTiO}_3\text{-(Ba,Sr)TiO}_3$ Relaxor Ferroelectrics," J. Am. Ceram. Soc., **75** [7] 1970-1974 (1992).
- D. J. Taylor, "Electric and elastic coefficients of lead magnesium niobate -based ceramics under dc bias for active smart sensor applications," Ph.D. dissertation, Penn State Univ., May 1992.
- S.M. Pilgrim, M. Massuda, J.D. Prodey, and A.P. Ritter, "Electrostrictive Sonar Drivers for Flexensional Transducers," Transducers for Sonics and Ultrasonics, Eds. M. McCollum, B.F. Hamonic, and O.B. Wilson, Technomic, Lancaster PA (1993).
- M. Massuda, K. Bridger, J.D. Prodey, and S.M. Pilgrim "High-field Electromechanical Properties of Some PMN-PT-based Relaxors," in proceedings of the 8th International Meeting on Ferroelectricity, Gaithersburg MD, August 1993.
- E.R. Seydel, I.K. Lloyd, S.M. Pilgrim, and K. Bridger," Correlations Between Phase Transition Characteristics in Doped $\text{Pb}(\text{Mg}_{1/3}\text{Nb}_{2/3})\text{O}_3\text{-PbTiO}_3$ Relaxor Ferroelectrics," in Proceedings of the Sixth US-Japan Seminar on Dielectric and Piezoelectric Ceramics, Lahaina, Hawaii, November, 1993.
- K.M. Rittenmyer, " Electrostrictive Ceramics for Underwater Transducer Applications," J. Acoust. Soc. Am, **94** [2] 849-856 (1994).
- S.R. Winzer, M. Massuda, C.L. Hom, S.A. Brown, and E. Passaro, "Results Review NCCOSC N66001-93-C-6017," (19 October 1994).
- M. Massuda, K. Bridger, J.D. Prodey, and S.M. Pilgrim "High-field Electromechanical Properties of Some PMN-PT-based Relaxors," *Ferroelectrics*, **158**, 337-342 (1994).
- C.L. Hom, S.M. Pilgrim, N. Shankar, K. Bridger, M. Massuda, and S.R. Winzer, "Calculation of Quasi-Static Electromechanical Coupling Coefficients for Electrostrictive Ceramic Materials," *IEEE Transactions on Ultrasonics, Ferroelectrics, and Frequency Control*, Vol. 41, No. 4, pp. 542-551 (1994).
- C.L. Hom and N. Shankar, "A Fully Coupled Constitutive Model for Electrostrictive Ceramic Materials," *J. Intel. Matl. Sys. and Structs.*, **5** pp. 795-801 (1994).
- L.E. Cross, "Relaxor Ferroelectrics: An Overview," *Ferroelectrics*, vol 151 pp. 305-320 (1994).
- S. M. Pilgrim, M. Massuda, and J. D. Prodey, "Electromechanical properties of some $\text{Pb}(\text{Mg}_{1/3}\text{Nb}_{2/3})\text{O}_3\text{-PbTiO}_3\text{-(Ba,Sr)TiO}_3$ Ceramics: Part Two," *J. Am. Ceram. Soc.*, vol. 78, no.6, pp.1501-1506, 1995.
- K.H. Yoon, Y.S. Cho, and D.H. Kang, "Dielectric and Electrostrictive Properties of $\text{Pb}(\text{Mg}_{1/3}\text{Nb}_{2/3})\text{O}_3$ -based Ceramics," Ceramics: Charting the Future, Techna Srl pp 2535-2542 (1995).
- S.E Prasad, S. Varma, T. Hoang, T.A. Wheat, and A. Ahmad, "The Role of Statistical Design in th Development of Electrostrictive Materials," in *Proc. Ninth ISAF*, IEEE CH3416-5 0-7803-1847-1/95, pp.762-765 (1995).

- J. Zhao, Q.M. Zhang, N. Kim, and T. Shrout, "Electromechanical properties of Relaxor Ferroelectric Lead Magnesium Niobate-Lead Titanate Ceramics," *Jpn. J. Appl. Phys.*, Vol 34 pp. 5658-5663 (1995).
- S. A. Brown, C. L. Hom, M. Massuda, J.D. Prodey, K. Bridger, N. Shankar, and S.R. Winzer, "Electromechanical testing and modeling of a $\text{Pb}(\text{Mg}_{1/3}\text{Nb}_{2/3})\text{O}_3$ - PbTiO_3 - BaTiO_3 relaxor ferroelectric," *J. Am. Ceram. Soc.*, vol. 79, no. 9, pp. 2271-82, (1996).
- C. L. Hom, S. A. Brown, and N. Shankar, "Constitutive and failure models for relaxor ferroelectric ceramics," *Proc. of SPIE - The International Society for Optical Engineering*, vol. 2715 pp. 316-328, (1996).
- Y. Yamashita and N. Ichinose, "Can Relaxor Piezoelectric Materials Outperform PZT? (Review), *Proc. Tenth IEEE Int. Symp. Appl. Ferroelec* 0-7803-3355-1/96, pp. 71-77, (1996).
- H.C. Robinson, *J. Acous. Soc. Amer.* **100** pp. 2729(A) (December 1996).
- J.-H. Park, B.-K. Kim, and S.J. Park, "Electrostrictive Coefficients of the $0.9\text{Pb}(\text{Mg}_{1/3}\text{Nb}_{2/3})\text{O}_3$ - 0.1PbTiO_3 Relaxor Ferroelectric Ceramics in the Ferroelectricity-Dominated Temperature Range," *J. Am. Ceram. Soc.* Vol 79 No. 2 pp 430-434 (1996).
- S.P. Leary and S.M. Pilgrim, "Method for Calculating Nonlinear Electromechanical Coupling," *1997 IEEE Ultrasonics Symposium Proc.* 97CH36118, pp. 541-544 (1997).
- J. Kelly, M. Leonard, C. Tantigate, and A. Safari, "Effect of Composition on the Electromechanical Properties of $(1-x)\text{Pb}(\text{Mg}_{1/3}\text{Nb}_{2/3})\text{O}_3$ - $x\text{PbTiO}_3$ Ceramics," *J. Am. Ceram. Soc.* Vol 80 No. 4 pp 957-964 (1997).
- R.S. Janus, M.B. Moffett, and J.M. Powers, "Large Signal Characterization of PMN-PT-Ba (90/10/3)," *NUWC-NPT Reprint Report 10,860*, (1997). [Lockheed Martin Generation 3]
- S. M. Pilgrim ed., *1997 PMN Measurements Workshop*, ONR Code 321 and ONR Code 322, Alfred University, 9 October 1997.
- M.C. Barber, "Thermal Properties of Electromechanical Materials for Transducers," B.S. Thesis, Alfred University (May 1997).
- J.C. Piquette and S.E. Forsythe, *J. Acous. Soc. Amer.* **101** pp. 289-296 (January 1997).
- S. P. Leary and S. M. Pilgrim, "Harmonic analysis of the polarization response in $\text{Pb}(\text{Mg}_{1/3}\text{Nb}_{2/3})\text{O}_3$ -based ceramics--A study in aging," *IEEE Trans. Ultrason. Ferroelec. Freq. Contrl.*, vol. 45, no. 1, pp. 163-170, January 1998.
- E.A. McLaughlin, J.M. Powers, M.B. Moffett, H.C. Robinson, and R.S. Janus, "Characterization of PMN-PT-La for use in high power electrostrictive projectors," submitted to *J. Acoust. Soc. of Amer.*, (1998).
- S.P. Leary and S.M. Pilgrim, "Measuring the Electric Field Dependence of the Elastic Moduli of $\text{Pb}(\text{Mg}_{1/3}\text{Nb}_{2/3})\text{O}_3$ -based Relaxor Ferroelectrics," accepted *Proceedings of ISAF XI, IEEE*, Montreux Switzerland (1998).
- L. Ewart, "Analysis of flexural strength and failure in PMN-PT," *Advances in Dielectric Ceramic Materials Vol. 88*, eds. K.M. Nair and A.S. Bhalla, pp. 337-342, Am. Ceram. Soc. Westerville OH (1998).
- K. Bridger, J.M. Sewell, P. Kuhn, E.J. Passaro, Y. S. Cho, H. Giesche, C.H. Yoon, and S. M. Pilgrim, "Phase I-Option Final Technical Report STTR Ph-I OPT 980910,"

- N00014 - 97 - C – 0298, MOD. No. P00001, “Frequency-Agile High-Power-Density Transducers” (September 1998).
- K.M. Rittenmyer, S.M. Pilgrim, and E.R. Seydel, “Analysis of Electrically Excited Strain in Relaxor Ferroelectric Ceramics,” Advances in Dielectric Ceramic Materials Vol. 88, eds. K.M. Nair and A.S. Bhalla, pp. 337-342, Am. Ceram. Soc. Westerville OH (1998).
- S.M. Gupta and D. Viehland, “Electromechanical and Piezoelectric Properties of La-Doped Lead Magnesium Niobate-Lead Titanate Compositions Near to the Morphotropic Phase Boundary,” Advances in Dielectric Ceramic Materials Vol. 88, eds. K.M. Nair and A.S. Bhalla, pp. 319-327, Am. Ceram. Soc. Westerville OH (1998).
- EDO Electroceramic Products, Salt Lake City Utah (1998).

Chapter 10

Rare Earth Magnetostrictive Materials

Dr. Arthur E. Clark
Art Clark Associates

Many magnetic materials containing the elements Ni, Co, and Fe are magnetostrictive. In addition, there are a large number of rare earth containing alloys that are also magnetostrictive. In these rare earths, the magnetic properties arise from a highly magnetic anisotropic electron configuration situated deeply within the atoms. The electron shells are strongly coupled to the crystalline lattice and in the presence of a magnetic field can give rise to very large saturation magnetostrictions and magnetomechanical coupling factors. Because of their unique properties, as well as their relatively recent introduction in production quantities, the rare earth materials warrant a separate chapter in this handbook.

There are three important classes of magnetostrictive materials containing rare earths. All three classes contain the elements Tb and Dy: (1) $Tb_{1-x}Dy_x$ alloys, (2) $Tb_{1-x}Dy_xZn$ alloys and (3) $Tb_{1-x}Dy_xFe_2$ alloys. The first two classes possess giant saturation magnetostrictions (> 2000 ppm) but are magnetic only at cryogenic temperatures.* The third class also possesses giant saturation magnetostrictions; however, this magnetostriction persists at room temperature and in some alloys at temperatures as high as $250^{\circ}C$.** Table 10-1 lists the magnetic ordering temperatures, magnetizations and intrinsic saturation magnetostriction constants for Tb and Dy materials in these three classes. In this handbook only the alloys of class (3) will be reported. In Table 10-2, the room temperature saturation magnetostrictions of some rare earth-iron polycrystal materials are listed and compared with the magnetostrictions of the elements Ni, Fe, and Co. Rare earth alloys with negative magnetostrictions, such as $SmFe_2$, will not be discussed in this handbook.

* Clark, A. E., M. Wun-Fogle, J. B. Restorff, and J. F. Lindberg, IEEE Trans. on Magnetics, **MAG-28**, 3156 (1992); Clark, A. E., J. P. Teter, M. Wun-Fogle, J. B. Restorff, and J. F. Lindberg, IEEE Trans. on Magnetics, **MAG-31**, 4032 (1995).

** Clark, A. E. and D. N. Crowder, IEEE Trans. on Magnetics, **MAG-21**, 1945, (1985).

The most highly investigated rare earth alloy to date is $Tb_{1-x}Dy_xFe_{2-y}$ with $0 \leq x \leq 1.0$ and $0 \leq y \leq 0.1$ (Terfenol-D). In this alloy, the large saturation magnetostrictions of Tb and Dy have been combined in order to minimize the magnetic anisotropy and hysteresis. Table 10-3 displays the signs of the magnetostriction and magnetic anisotropies of the magnetostrictive rare earth elements. $Tb_{1-x}Dy_xFe_{2-y}$, $Tb_{1-x}Ho_xFe_{2-y}$ and $Tb_uDy_vHo_wFe_{2-y}$ ($u+v+w=1$) have compensating anisotropy signs and are acceptable transducer materials. The major portion of this section focuses on Terfenol-D, $Tb_{1-x}Dy_xFe_{2-y}$ with $x \cong 0.7$, a highly magnetostrictive alloy optimized for room temperature transduction. Some details concerning the $Tb_{1-x}Ho_xFe_{2-y}$ and $Tb_uDy_vHo_wFe_{2-y}$ alloys will be given in section 10.7.

Table 10-1. Magnetic and Magnetostrictive Properties of Tb and Dy Materials.

	T _C (K)	$\mu_0 M_{s,T \rightarrow 0}$ (Tesla)	Magnetostriction $\lambda_{T \rightarrow 0}$ (10 ⁻³)	Tb atom density (atoms/nm)	Magnetic Easy Axis
Tb	230	3.3	$\lambda^{\gamma,2} = 9.6$	31.3	[10-0] (b-axis)
Dy	179	3.6	$\lambda^{\gamma,2} = 9.4$	--	[11-0] (a-axis)
TbZn	204	2.2	$3\lambda_{100}/2 = 6.0^*$	21.9	[100][110]
DyZn	140	2.3	$3\lambda_{100}/2 = 6.5$	--	[100]
TbFe ₂	710	1.4	$3\lambda_{111}/2 = 6.6$	20.2	[111]
DyFe ₂	635	1.6	$3\lambda_{111}/2 = 6.4^*$	--	[100]

*Extrapolated from measurements at higher temperatures

Table 10-2. Magnetostriction and Curie Temperatures of Ni, Fe, Co, and some Rare Earth-Iron Compounds.*

Material	$(3/2)\lambda_s \times 10^6$	T _C (°C)
Ni	-50	360
Fe	-14	770
Co	-93	1130
SmFe ₂	-2340	415
TbFe ₂	2360	431
DyFe ₂	650	362
HoFe ₂	120	332
ErFe ₂	-449	320
TmFe ₂	-195	287
SmFe ₃	-317	377
TbFe ₃	1040	379
DyFe ₃	528	333
HoFe ₃	86	300
ErFe ₃	-104	280
TmFe ₃	-65	264

*See A. E. Clark in *Ferromagnetic Materials*, Vol. I, chapter 7, and K H. J. Buschow, *Ferromagnetic Materials*, Vol. I, chapter 4, ed. E. P. Wohlfarth, North Holland Press, (1980). For the rare earth compounds $(3/2)\lambda_s$ denotes $\lambda_{||} - \lambda_{\perp}$ at 25 kOe.

Table 10-3. Polarity of the Magnetostriction Constants (λ), and the two Lowest Order Magnetic Anisotropy Constants (K_1 and K_2) of the Rare earth-Fe₂ Compounds.

	SmFe ₂	TbFe ₂	DyFe ₂	HoFe ₂	ErFe ₂	TmFe ₂	YbFe ₂
λ	-	+	+	+	-	-	-
K_1	-	-	+	+	-	-	+
K_2	0	+	-	+	-	+	-

10.1 Mechanical, Thermal, and Magnetic Properties of Terfenol-D.

Table 10.1-1 is a listing of some common mechanical, thermal, and magnetic properties of Terfenol-D at room temperature.

Table 10.1-1. Typical Room Temperature Terfenol-D Mechanical, Thermal, and Magnetic Properties.

Property	mks units	Ref.
Density	9250 kg/m ³	1
Bulk Modulus	370 GPa	1
Young's Modulus, ($1 / s_{33}^H$)	25 – 35 GPa	3
" " , ($1 / s_{33}^B$)	50 – 70 GPa	3
Sound Speed, v^H	~1700 m/s	3
" " , v^B	~2500 m/s	3
Tensile Strength	~28 MPa	3
Compressive Strength	~880 MPa	4
4-Point Bending Strength	~40 MPa	4
Thermal Expansion	12 x 10 ⁻⁶ /°C	2
Heat Capacity	320 – 370 J/kg°C	2
Thermal Conductivity	10.5 – 10.8 W/m°C	2
Electrical Resistivity	60 x 10 ⁻⁸ ohm/m	1
Curie Temperature	380°C	6
Magnetization	1.0 T	6
Permeability, relative	5 - 10	5
Saturation magnetostriction	1.5 – 2.0 x 10 ⁻³	6
Piezomagnetic constant, d_{33}	1.0 – 1.5 x 10 ⁻⁸ m/A	5
Coupling factor, k_{33}	0.65 – 0.75	1,5

1. A. E. Clark, *Ferromagnetic Materials*, ed. E. P. Wohlfarth, Vol. I, Chapter 7, p. 531, North Holland Publishing Co. 1980.
2. Fact Sheet, ETREMA, Inc. Ames IA, 1996.
3. J. L. Butler, Application Manual for the Design of ETREMA Terfenol-D Magnetostrictive Materials, ETREMA, Inc., Ames IA, 1988.
4. K. Kondo and K. Shinozaki, Proc. Int. Conf. on Giant Magnetostrictive Materials, Tokyo, Japan, Nov. 5-6, 1992.
5. M. B. Moffett, A. E. Clark, M. Wun-Fogle, J. Lindberg, J. P. Teter, and E. A. McLaughlin, J. Acoust. Soc. Amer. **89**, 1448 (1991).
6. A. E. Clark and D. N. Crowder, IEEE Trans. on Magnetics, **MAG-21**, 1945, (1985).

10.2 Temperature Dependence of the Magnetostriction of Terfenol-D

The saturation magnetostriction of Terfenol-D decreases slightly with temperature above room temperature due to a decrease in the magnetization as the Curie temperature (380°C) is approached. The magnetostriction also decreases as the temperature is reduced below room temperature due to a magnetic spin reorientation away from the highly magnetostrictive [111] axis. The temperature of the peak magnetostriction can be adjusted by altering the value of x in Terfenol-D ($\text{Tb}_{1-x}\text{Dy}_x\text{Fe}_{1-y}$). The temperature dependence of $\text{Tb}_{.3}\text{Dy}_{.7}\text{Fe}_{1.9}$ near room temperature is given in Fig. 10.2-1 for various fields and two compressive stresses. The high temperature dependencies of the magnetostrictions of TbFe_2 and $\text{Tb}_{.27}\text{Dy}_{.73}\text{Fe}_{1.95}$ are given in Fig. 10.2-2.*

* Clark, A. E. and D. N. Crowder, IEEE Trans. on Magnetics, **MAG-21**, 1945, (1985).

10.3 Magnetic Field and Compressive Stress Dependencies of the Magnetostriction of [112] Textured $\text{Tb}_{.3}\text{Dy}_{.7}\text{Fe}_2$ at Room Temperature

Because of a large magnetostriction anisotropy in the cubic crystal of Terfenol-D ($\lambda_{111} \gg \lambda_{100}$), the magnetostriction is strongly dependent upon the orientation of the crystallites in the sample. The preferred crystalline growth direction in Terfenol-D is [112] which yields a saturation magnetostriction approximately 80% as high as the largest magnetostriction, λ_{111} . Thus, because of the lower cost, samples are frequently prepared with the [112] texture. Moffet et al.* have documented many magnetostriction vs field and magnetostriction vs stress dependencies for large diameter (~1.5") $\text{Tb}_{.3}\text{Dy}_{.7}\text{Fe}_2$ prepared with this [112] texture. Fig. 10.3-1 gives the hysteresis loops of the magnetostriction curves vs applied magnetic field for fixed compressive stresses up to 65 MPa. See Table 10.3-1. Some minor loops are also shown, biased around typical values of magnetic field. Fig. 10.3-2 shows the stress dependence of the strain at fixed values of magnetic field for fields up to 2.2 kOe. Figs. 10.3-1 and 10.3-2 are representative of the magnetostriction of large diameter (1.5") rods prepared using the Bridgman growth technique. The magnetization, magnetostriction, and elastic modulus of even larger (2.5") rods have also been measured.**

* Moffet, M. B., A. E. Clark, M. Wun-Fogle, J. Lindberg, J. P. Teter, and E. A. McLaughlin, J. Acoust. Soc. Am. **89**, 1448 (1991).

** Restorff, J. B., and M. Wun-Fogle, NSWCCD-TR-97/004. [Limited Distribution]

A crucibleless (free-standing zone) method of preparation yields somewhat larger values of saturation strain, but is generally limited to small diameter (0.4") samples. The performance of these materials is strongly dependent upon sample preparation and is not reported here.*

* Savage, H. T., R. Abbundi, A. E. Clark, and O. D. McMasters, J. Mag. And Mag. Materials, **15-18**, 609 (1980).

Table 10.3-1. Compressive Prestress and Magnetic Bias Conditions for curves shown in Figs. 10.3-1 and 10.3-2.

Bias Condition	Compressive Stress		Magnetic Bias Field	
	(ksi)	(MPa)	(kOe)	(kA/m)
1	1.01	6.9	0.15	11.9
2	2.22	15.3	0.4	31.8
3	3.43	23.6	0.7	55.7
4	4.64	32.0	1.0	79.6
5	5.86	40.4	1.3	103.0
6	7.07	48.7	1.6	127.0
7	8.28	57.1	1.9	151.0
8	9.49	65.4	2.2	175.0

10.4 Magnetic Field Dependent Stress-Strain and Young's Modulus Curves for Terfenol-D at Room Temperature.

Because of the large magnetostriction, the stress-strain relation of Terfenol-D is strongly magnetic field dependent. Fig. 10.4-1 shows how the strain depends upon stress for various magnetic fields up to 1500 Oe. Fig. 10.4-2 shows the softening of the modulus due to the magnetostriction over the same field range.*

* Savage, H. T., A. E. Clark, and D. Pearson, 4th Joint MMM-Intermag Conf, Vancouver, Canada, July 1988, unpublished.

10.5 The Piezomagnetic Matrix and Low Magnetic Field Properties of Terfenol-D

The piezomagnetic matrix equation relating the Cartesian strain (S_i) and magnetic induction (B_i) components to stress (T_i) and magnetic field (H_i) components for a planar isotropic [112] textured Terfenol-D sample which is polarized and stressed along the 3 axis (i.e. $T_1, T_2, T_4, T_5, T_6, H_1$, and H_2 are small) can be written:*

$$\begin{pmatrix} S_1 \\ S_2 \\ S_3 \\ S_4 \\ S_5 \\ S_6 \\ B_1 \\ B_2 \\ B_3 \end{pmatrix} = \begin{pmatrix} s_{11}^H & s_{12}^H & s_{13}^H & 0 & 0 & 0 & 0 & 0 & d_{31} \\ s_{13}^H & s_{11}^H & s_{13}^H & 0 & 0 & 0 & 0 & 0 & d_{31} \\ s_{13}^H & s_{13}^H & s_{33}^H & 0 & 0 & 0 & 0 & 0 & d_{33} \\ 0 & 0 & 0 & s_{44}^H & 0 & 0 & d_{14} & d_{15} & 0 \\ 0 & 0 & 0 & 0 & s_{44}^H & 0 & d_{15} & -d_{14} & 0 \\ 0 & 0 & 0 & 0 & 0 & (s_{11}^H - s_{12}^H) & 0 & 0 & 0 \\ 0 & 0 & 0 & d_{14} & d_{15} & 0 & \mu_{11}^T & 0 & 0 \\ 0 & 0 & 0 & d_{15} & -d_{14} & 0 & 0 & \mu_{11}^T & 0 \\ d_{31} & d_{31} & d_{33} & 0 & 0 & 0 & 0 & 0 & \mu_{33}^T \end{pmatrix} \begin{pmatrix} T_1 \\ T_2 \\ T_3 \\ T_4 \\ T_5 \\ T_6 \\ H_1 \\ H_2 \\ H_3 \end{pmatrix}$$

Here S_i 's are the conventional Voigt elastic strain components and T_i 's are the conventional stress components under the condition of total zero torque.

*Du Tremolet de Lacheisserie, E., *Magnetostriction*, CRC Press, Boca Raton, FL (1993);
Claeyssen, F., *Design and Construction of Low-frequency Sonar Transducers Based on Rare earth-iron Alloys*, Ph.D. Thesis, Institut National des Sciences appliquees de Lyon, Lyon France (1989).

This matrix is often written in the following way with repeated indices (α, β, m, n):

$$S_\alpha = s_{\alpha\beta}^H T_\beta + d_{n\alpha} H_n$$

$$B_m = d_{m\beta} T_\beta + \mu_{mn}^T H_n$$

F. Claeyssen has reported all the coefficients of this matrix for $H = 60$ kA/m and $T = 20$ MPa:*

$$s_{11}^H = 2.7 \times 10^{-11} \text{ Pa}^{-1}$$

$$s_{12}^H = -0.43 \times 10^{-11} \text{ Pa}^{-1}$$

$$s_{13}^H = -1.9 \times 10^{-11} \text{ Pa}^{-1}$$

$$s_{33}^H = 4.2 \times 10^{-11} \text{ Pa}^{-1}$$

$$s_{44}^H = 16.7 \times 10^{-11} \text{ Pa}^{-1}$$

$$s_{66}^H = 6.26 \times 10^{-11} \text{ Pa}^{-1}$$

$$d_{31} = -0.52 \times 10^{-8} \text{ m/A}$$

$$d_{33} = 1.04 \times 10^{-8} \text{ m/A}$$

$$d_{15} = 2.8 \times 10^{-8} \text{ m/A}$$

$$\mu_{11}^T = 6.9 \mu_0$$

$$\mu_{33}^T = 4.4 \mu_0$$

$$k_{33} = 0.69$$

$$k_{31} = 0.43$$

$$k_{15} = 0.74$$

Note when the magnetic field is applied parallel to the stress axis (i.e. retaining only T_3 and H_3):

$$\begin{aligned} S_1 &= s_{13}^H T_3 + d_{13} H_3 & B_1 &= 0 \\ S_2 &= s_{13}^H T_3 + d_{13} H_3 & B_2 &= 0 \\ S_3 &= s_{33}^H T_3 + d_{33} H_3 & B_3 &= d_{33} T_3 + \mu_{33}^T H_3 \\ S_4 &= 0 \\ S_5 &= 0 \\ S_6 &= 0 \end{aligned}$$

For this case the important coefficients reduce to only five (Poisson's ratio $\equiv \nu$):

$$\begin{aligned} s_{33} &= 1 / E & d_{33} & & \mu_{33} \\ s_{13} &= -\nu / E & d_{31} & & \end{aligned}$$

For the matrix defined by the alternative relationships:

$$\begin{aligned} T_\alpha &= c_{\alpha\beta}^H S_\beta - e_{n\alpha} H_n \\ B_m &= e_{m\beta} S_\beta + \mu_{mn}^S H_n \end{aligned}$$

the coefficients become:*

$$\begin{aligned} c_{11}^H &= 10.7 \times 10^{10} \text{ Pa} & e_{31} &= -0.90 \times 10^2 \text{ T} \\ c_{12}^H &= 7.48 \times 10^{10} \text{ Pa} & e_{33} &= 1.66 \times 10^2 \text{ T} \\ c_{13}^H &= 8.21 \times 10^{10} \text{ Pa} & e_{15} &= 1.68 \times 10^2 \text{ T} \\ c_{33}^H &= 9.81 \times 10^{10} \text{ Pa} \\ c_{44}^H &= 0.60 \times 10^{10} \text{ Pa} & \mu_{11}^S &= 3.16 \mu_0 \\ c_{66}^H &= 1.61 \times 10^{10} \text{ Pa} & \mu_{33}^S &= 2.28 \mu_0 \end{aligned}$$

*Claeyssen, F., *Design and Construction of Low-frequency Sonar Transducers Based on Rare earth-iron Alloys*, Ph.D. Thesis, Insitutut National des Sciences Appliquees de Lyon, Lyon France (1989).

10.6 Magnetic Field and Compressive Stress Dependence of the Piezomagnetic Properties of Terfenol-D at Room Temperature

Table 10.6-1 lists some of the piezomagnetic coefficients of Terfenol-D at a fixed bias field of 90 kA/m for compressive stresses from 30 MPa to 50 MPa.

Table 10.6-1 Longitudinal Magnetomechanical Coefficients of Terfenol-D at 90 kA/m.*

T(MPa)	30	35	40	50
Y^H (GPa)	29	21	23	40
s_{33}^H (GPa ⁻¹)	0.034	0.048	0.043	0.025
Q^H	4.6	3.5	4.3	8.3
μ_{33}^T / μ_0	3.7	4.2	3.8	3.0
Q^T	2.0	1.9	2.2	2.8
d_{33} (nm/A)	8.0	11.0	9.7	5.0
k_{33}	.63	.69	.67	.52

* Claeyssen, F., J. Alloys and Compounds, **258**, 61 (1997).

Table 10.6-2 lists some piezomagnetic properties of Terfenol-D when the magnetic bias is optimized to a given compressive prestress. Note values of compliance and coupling factor are almost stress independent under this condition.*

Table 10.6-2. Piezomagnetic Properties of Terfenol-D under Certain Compressive Stress and Magnetic Bias Conditions.

T (MPa)	7	10	14	21
H_{bias} (kA/m)	12	18	30	48
s_{33}^H (GPa ⁻¹)	0.050	0.053	0.053	0.055
d_{33} (nm/A)	22.6	19.8	17.4	9.62
μ_{33}^T / μ_0	14.6	12.9	10.0	9.6
k_{33}	.75	.68	.67	.69

* Wakiwaka, H. et al., J. Alloys and Compounds **258**, 87 (1997)

In section 10.3 are reported minor loops of strain vs magnetic field for stresses up to 65 MPa and strain vs stress curves for magnetic fields up to 5 kOe. Each of the minor loops of Fig. 1.3-1 of that section represents a possible ac drive condition. The slope of a line drawn through the end-points of each minor loop can be taken as the d_{33} coefficient corresponding to that drive condition. In Fig. 10.6-1 are plotted the values of d_{33} as a function of magnetic drive amplitude for each of the prestresses and magnetic bias conditions of Table 10.3-1. Except for very low drive levels (<400 Oe), d_{33} decreases with drive amplitude and with prestress. At high drive levels (> 2 kOe) saturation occurs and d_{33} becomes independent of the bias condition.

The relative permeabilities μ_{33}^T / μ_0 (μ_0 = permeability of free space) of Terfenol-D are plotted in Fig. 10.6-2. These data are taken from magnetic induction (B) vs magnetic field (H) minor loops obtained in a similar fashion to those of Fig. 10.3-1. The permeability decreases with increasing prestress but becomes nearly amplitude independent for prestresses greater than ~15 MPa.

From the stress-strain hysteresis loops of Fig. 10.3-2, the open-circuit compliance coefficients, s_{33}^H , were obtained and plotted in Fig. 10.6-3 as a function of the stress amplitude. For most of the bias conditions, there exists a maximum compliance, and at large stress amplitudes, the compliance becomes nearly independent of the bias level.

The piezomagnetic properties of Terfenol-D become non-linear under high drive conditions. There is an amplitude dependence of s_{33}^H , d_{33} and μ_{33}^T . However, a very useful first approximation to the behavior of Terfenol-D in a transducer is still the linear model. In Figs. 10.6-4 – 10.6-6, the bias conditions of Table 10.3-1 are used to yield two values of each of the constants. One choice, represented by the square symbols of s_{33}^H , d_{33} and μ_{33}^T in Figs. 10.6-4 – 10.6-6 involve the maximum values from Figs. 10.6-1 to 10.6-3. This choice, appropriate for medium signal levels, represents an approximation to maximum coupling. The second choice, represented by the circle symbols in Figs. 10.6-4 - 10.6-6, is the high-signal case. In this case, the zero-to-peak amplitudes are taken to be the magnetic fields listed in Table 10.6-3. The values of s_{33}^H , d_{33} and μ_{33}^T were obtained from the hysteresis loops of Figs. 10.3-1 and 10.3-2 such that the distortion in the strains is 15% to 20%.

Table 10.6-3. Maximum allowed zero-to-peak magnetic field and stress amplitudes corresponding to one hysteresis-loop-width deviation from linearity.

Bias Condition	Compressive Stress		Magnetic Bias Field	
	(ksi)	(MPa)	(kOe)	(kA/m)
1	1.0	6.9	0.15	12
2	1.7	12	0.4	32
3	2.6	18	0.5	40
4	2.9	20	0.7	56
5	2.9	20	0.8	64
6	2.9	20	0.8	64
7	2.9	20	0.8	64
8	2.9	20	0.8	64

Coupling factors, k_{33} , calculated from Figs. 10.6-4 - 10.6-6 are plotted in Fig. 10.6-7. Note the almost independent stress dependence of the coupling factor. The difference between the medium level and high level values of k_{33} is also not large, i.e. the coupling factor is nearly constant, independent of drive amplitude and stress. The coupling factor ranges from .65 to .8, over the 7 to 65 MPa range. These values are a factor of 2 greater than those of older magnetostrictive materials, such as nickel.

Kendall, D. and A. R., Piercy* calculated dynamic values of d_{33} and k_{33} for temperatures between – 21°C to 70°C using a rms drive field of 450 A/m.

* Kendall, D. and A. R., Piercy, IEEE Trans. on Magnetics, **26** 1837 (1990)

10.7 $\text{Tb}_u\text{Dy}_v\text{Ho}_w\text{Fe}_2$ ($u+v+w=1$) alloys

As indicated in Table 10-3, alloys containing Tb, Dy and Ho are suitable rare earth transducer materials. In Figs. 10.7-1,-2,-3 are compared the field dependencies of the magnetostriction, the piezomagnetic d_{33} constant, and the coupling factor, respectively, of the ternary $\text{Tb}_{1-x}\text{Dy}_x\text{Fe}_2$ and $\text{Tb}_{1-y}\text{Ho}_y\text{Fe}_2$ compounds optimized for transduction at room temperature ($x = 0.7$, $y \cong 0.75$).

In the quaternary $\text{Tb}_x\text{Dy}_y\text{Ho}_z\text{Fe}_2$ ($x+y+z=0$) alloys, the two lowest anisotropy constants can be minimized and the optimum magnetostriction/anisotropy (λ/K) ratio can be obtained. This room temperature optimized alloy is $\text{Tb}_{0.2}\text{Dy}_{0.22}\text{Ho}_{0.58}\text{Fe}_2$.^{*} For this alloy, the magnetostriction $\lambda_{111} = 820$ ppm, which is close to that of the ternary $\text{Tb}_{0.23}\text{Ho}_{0.77}\text{Fe}_2$ where $\lambda_{111} = 710$ ppm. In order to attain a low anisotropy and hysteresis, while at the same time reducing the magnetostriction only slightly from that of Terfenol-D ($\lambda_{111} = 1620$ ppm), dysprosium rich quaternary alloys with compositions close to Terfenol-D have been synthesized.^{**} Fig. 10.7-4 is a plot of the magnetostriction vs magnetic field for $\text{Tb}_{0.28}\text{Dy}_{0.57}\text{Ho}_{0.15}\text{Fe}_2$ at compressive stresses up to 70 MPa. Fig. 10.7-5 is a plot of the reduction in hysteresis with various concentrations of Ho for an applied peak-to-peak magnetic field of 900 Oe centered about a bias magnetic field situated at the largest d_{33} value. Fig. 10.7-6 depicts the accompanying reduction in magnetostriction with the addition of similar concentrations of Ho. The decrease in hysteresis is significant whereas the accompanying decrease in magnetostriction is small. At very high stresses, where the magnetostriction is reduced because of the stress, there is no appreciable further reduction in magnetostriction with Ho addition.

^{*}Williams, C. M., and N. C. Koon, *Physica*, **86-88B**, 147 (1977); Koon, N. C., C. M. Williams, and B. N. Das, *J. Magn. and Magn. Materials*, **100**, 173 (1991).

^{**}Wun-Fogle, M., J. B. Restorff, A. E. Clark, and J. F. Lindberg, *Proc. Conf. on Magn. and Magn. Mat's*, San Francisco, CA, Jan. 6-8, 1998.

Table 10.7-1 is a summary of the magnetomechanical coupling factor (k_{33}) and saturation magnetostriction (λ_{111}) for various rare earth-Fe₂ materials at room temperature.

Table 10.7-1. Maximum Magnetomechanical Coupling and Magnetostriction of Various Rare Earth-Fe Compounds.

Material	k_{33}	$\lambda_{111} \times 10^6$
TbFe ₂	0.35	2450
Tb _{0.5} Dy _{0.5} Fe ₂	0.51	1840
Tb _{0.27} Dy _{0.73} Fe ₂	0.53-0.70	1620
Tb _{0.23} Dy _{0.35} Ho _{0.42} Fe ₂	0.62	1130
Tb _{0.20} Dy _{0.22} Ho _{0.58} Fe ₂	0.60-0.66	820
Tb _{0.19} Dy _{0.18} Ho _{0.63} Fe ₂	0.59	810
SmFe ₂	0.35	-2100
Sm _{0.88} Dy _{0.12} Fe ₂	0.55	-1620
Sm _{0.7} Ho _{0.3} Fe ₂	0.35	-1370
Tb _{0.23} Ho _{0.77} Fe ₂ (oriented)	0.76	710
Tb _{0.27} Dy _{0.73} Fe ₂ (oriented)	0.74	1620

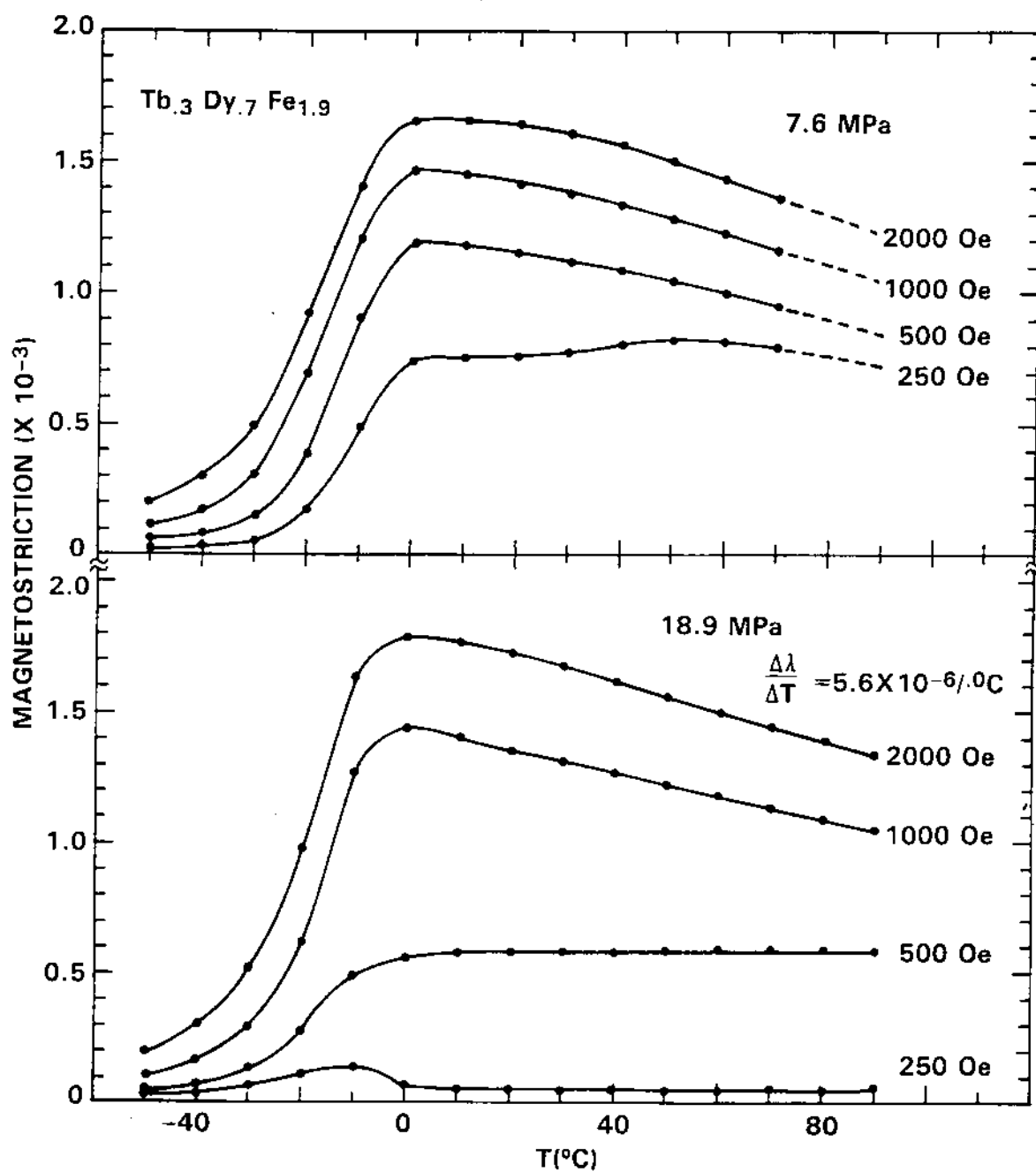


Figure 10.2-1 Temperature dependence of the magnetostriction of Terfenol-D at 7.6 MPa and 18.9 MPa.

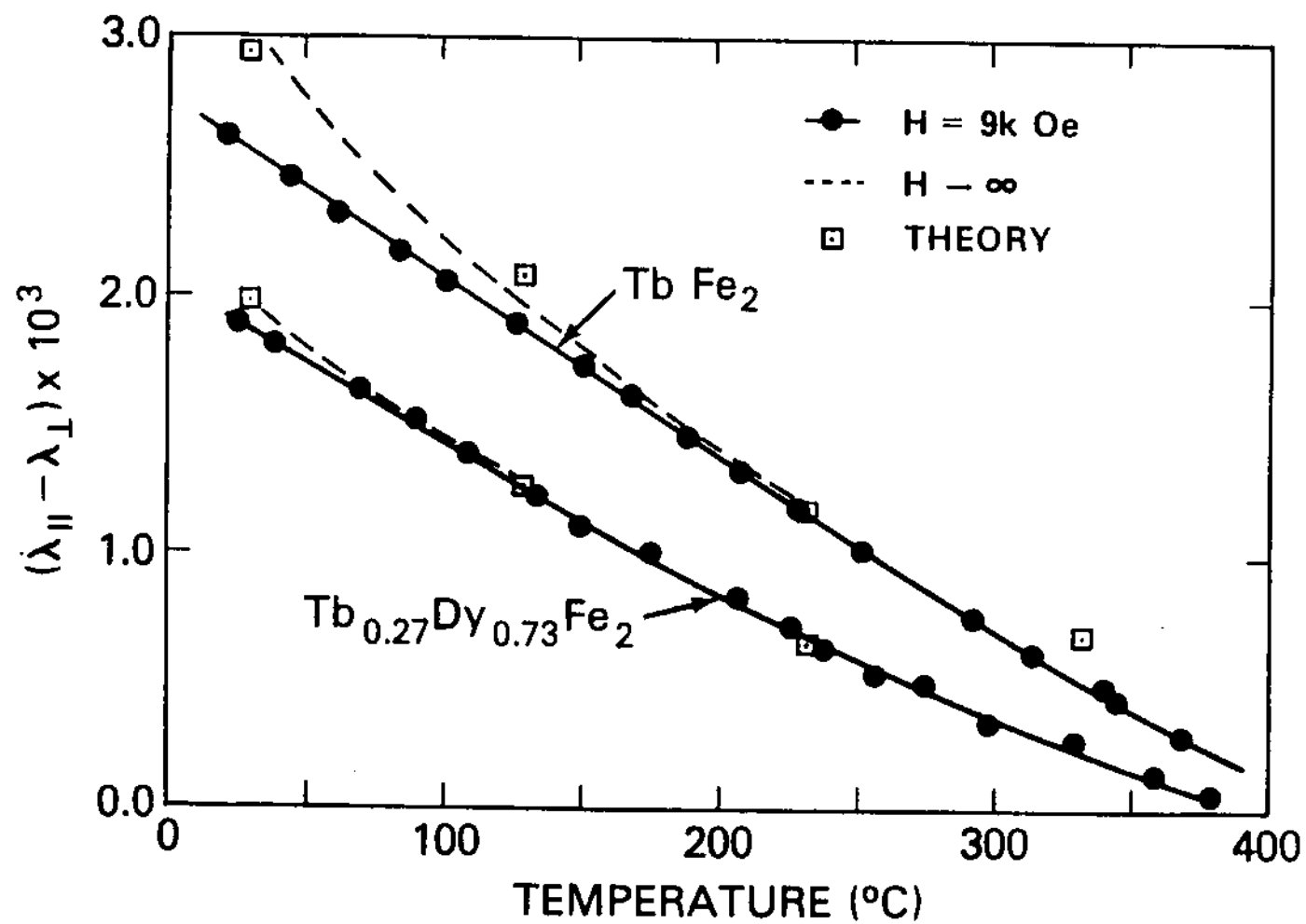


Figure 10.2-2 Temperature dependence of the magnetostriction of TbFe₂ and Tb_{0.27}Dy_{0.73}Fe₂ from 20°C to 375°C.

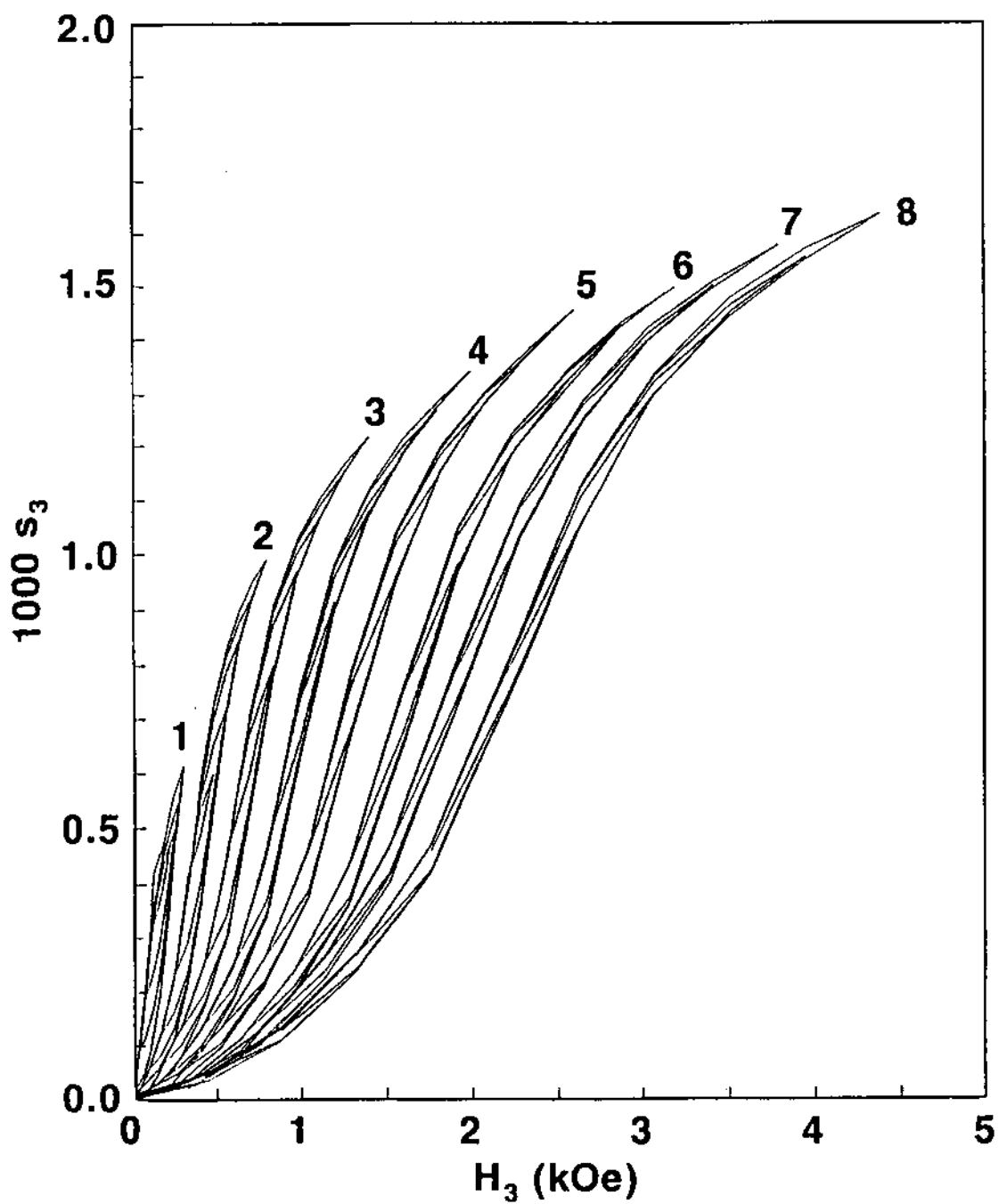


Figure 10.3-1 Hysteresis loops of extensional strain vs applied magnetic field for constant stress values of Table 10.3-1.

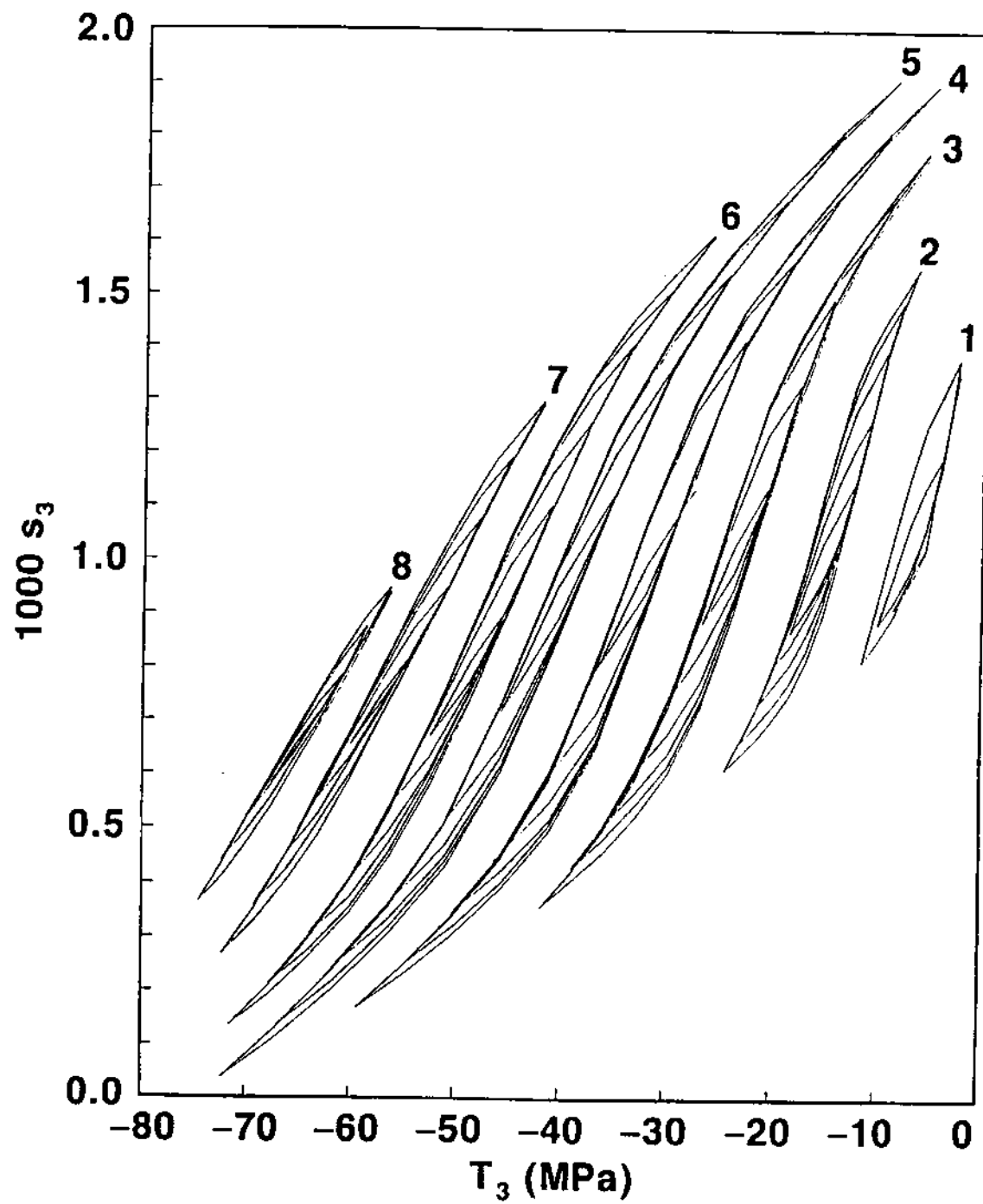


Figure 10.3-2 Hysteresis loops of extensional strain vs stress for the constant magnetic fields of Table 10.3-1.

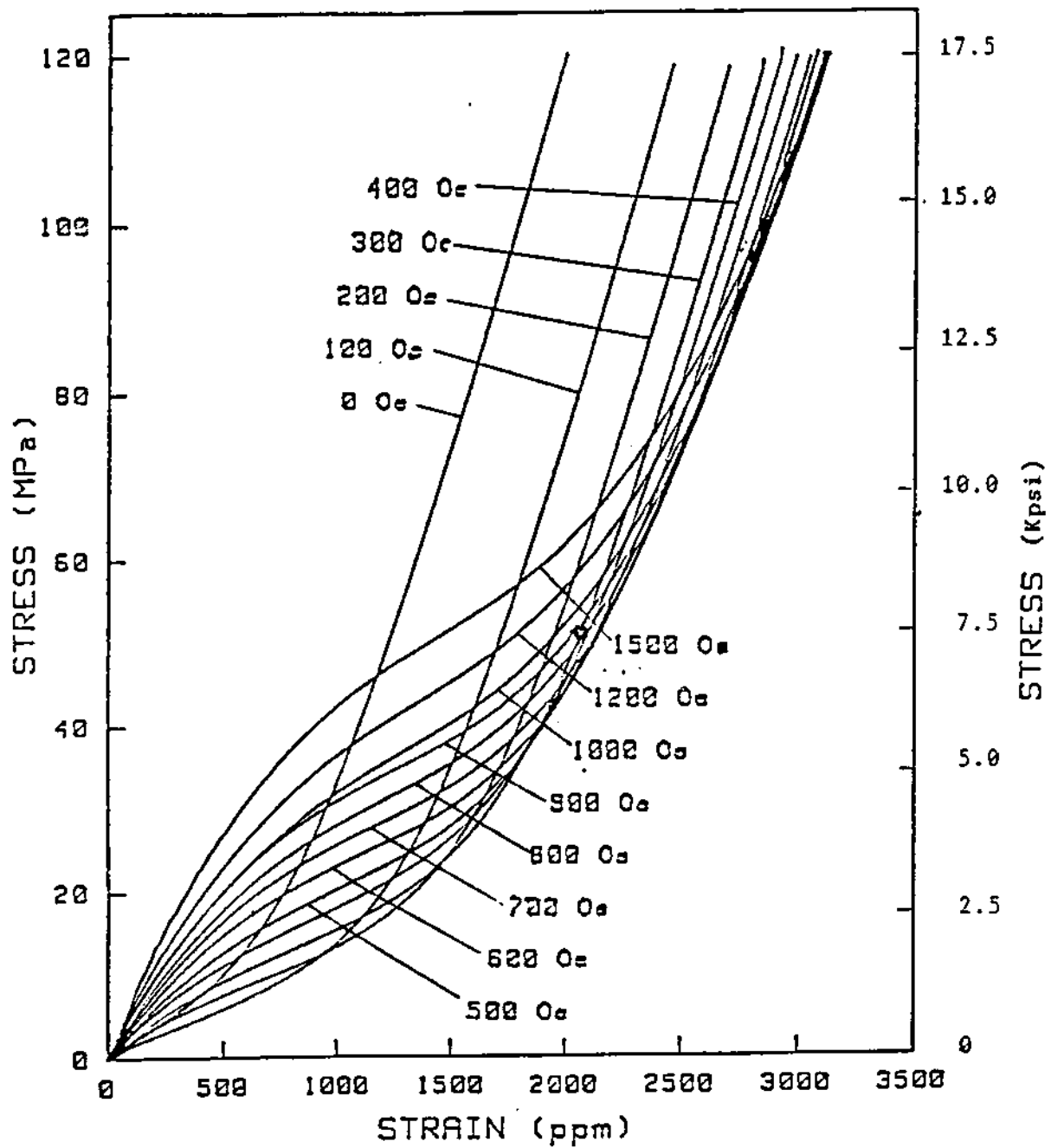


Figure 10.4-1 Stress-strain curves at various bias magnetic fields for Terfenol-D.

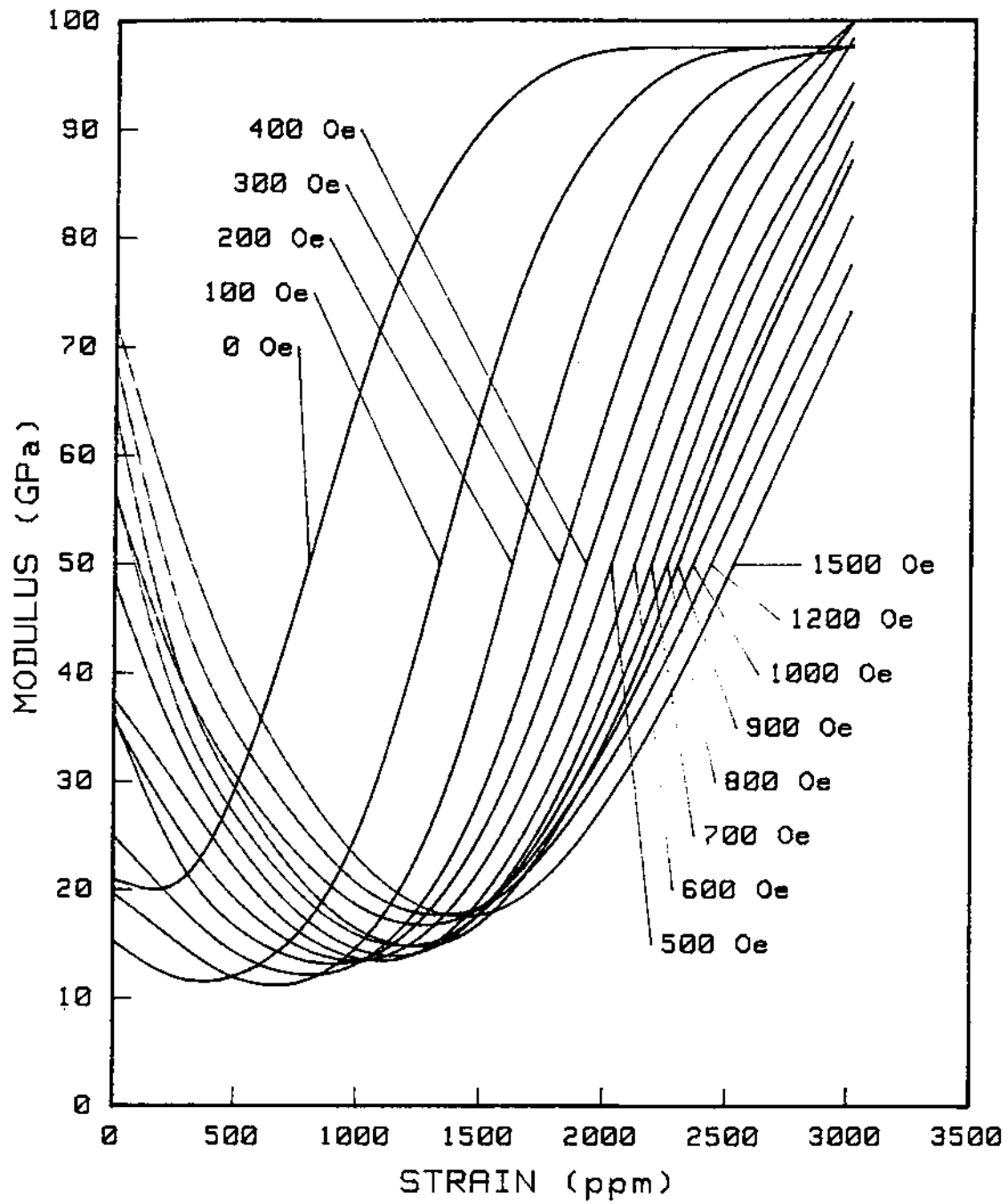


Figure 10.4-2 Young's modulus vs strain at bias fields from 0 to 1500 Oe for Terfenol-D.

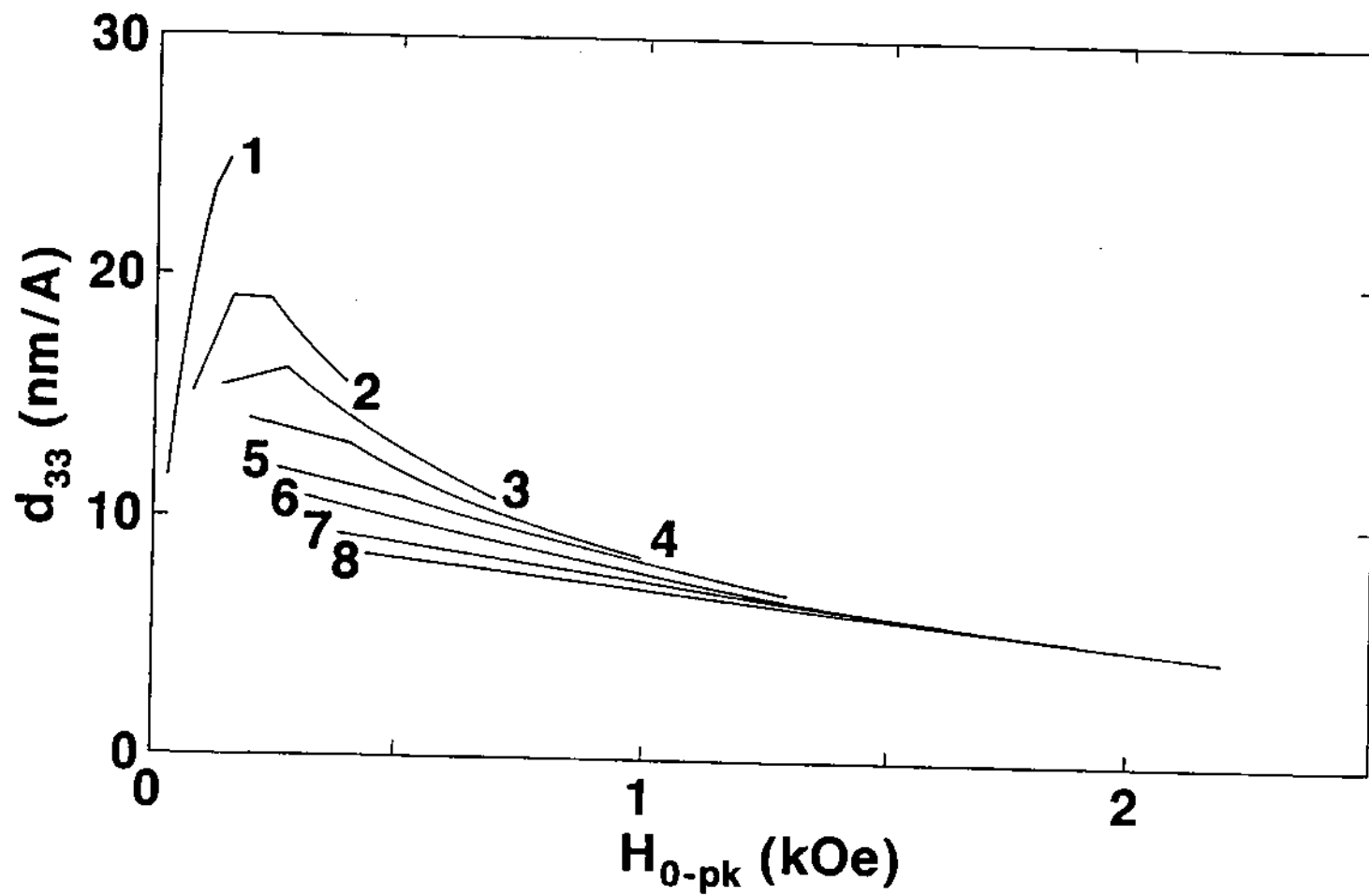


Figure 10.6-1 Dependencies of d_{33} on magnetic drive amplitudes for the prestress and magnetic bias combinations of Table 10.3-1.

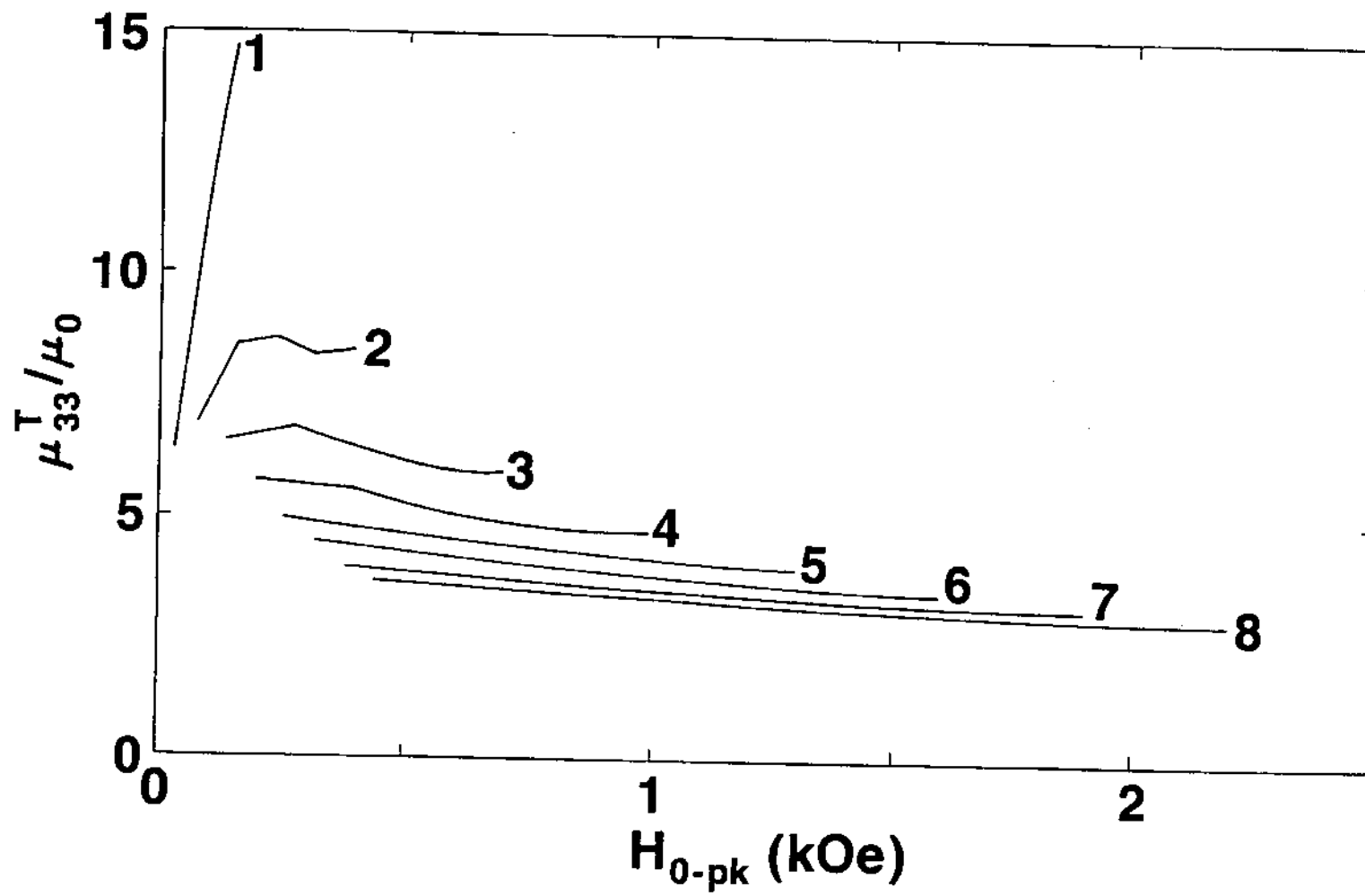


Figure 1.6-2 Dependencies of the relative permeability on magnetic drive amplitudes for the prestress and magnetic bias combinations of Table 10.3-1.

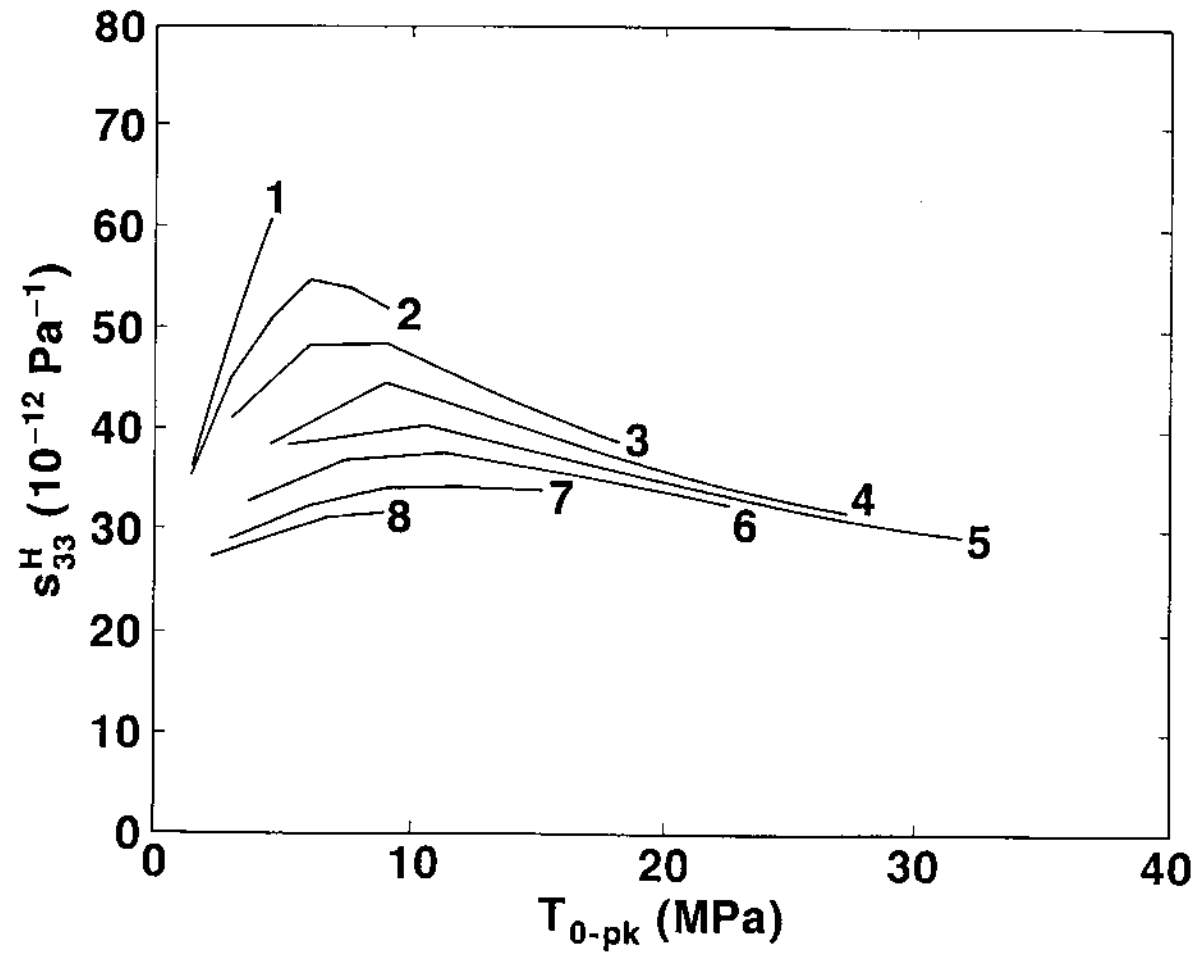


Figure 1.6-3 Dependence of the open-circuit compliance coefficient on stress amplitude for the prestress and magnetic bias combinations of Table 10.3-1.

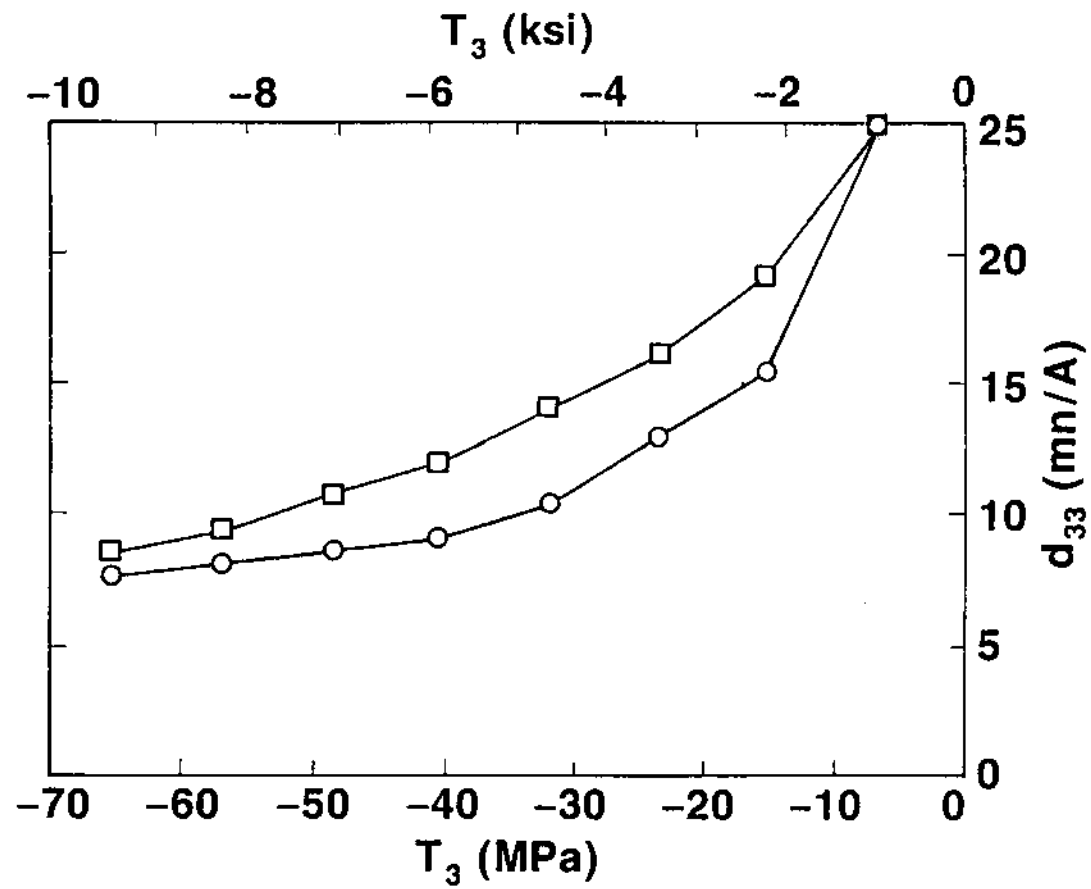


Figure 10.6-4 Piezomagnetic d_{33} constant for medium-level (squares) and high-level (circles) drive amplitudes as a function of prestress.

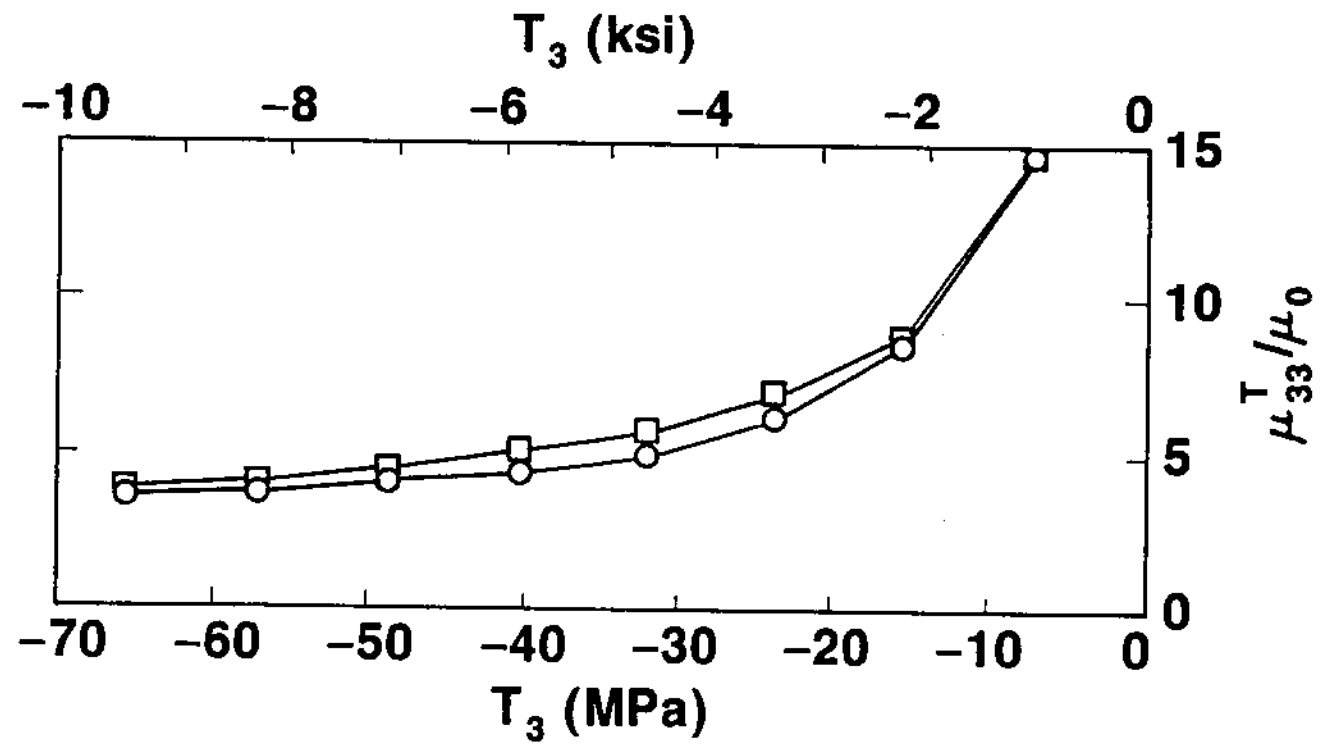


Figure 10.6-5 Relative permeability for medium-level (squares) and high-level (circles) drive amplitudes as a function of prestress.

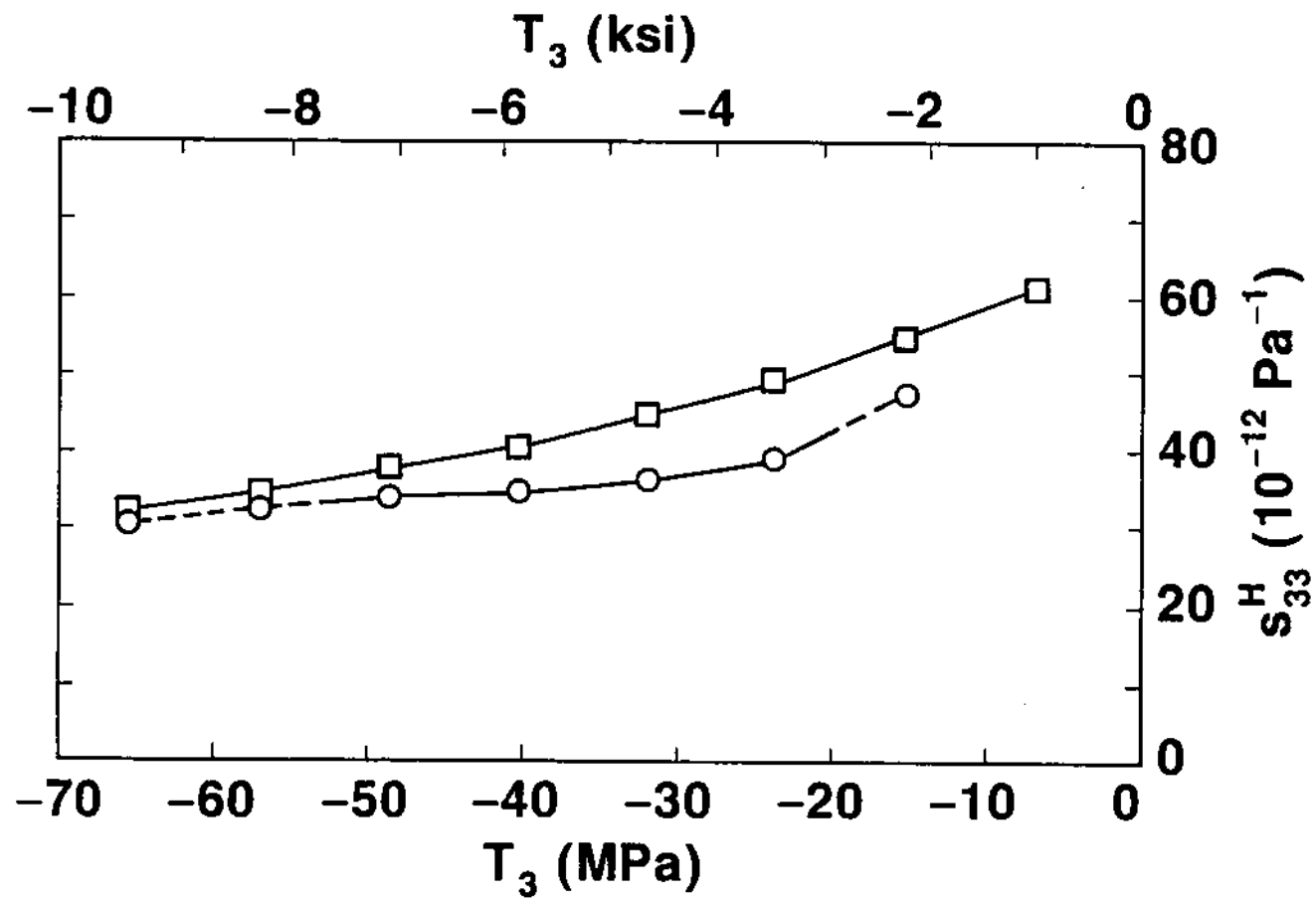


Figure 10.6-6 Open-circuit compliance for medium-level (squares) and high-level (circles) drive amplitudes as a function of prestress.

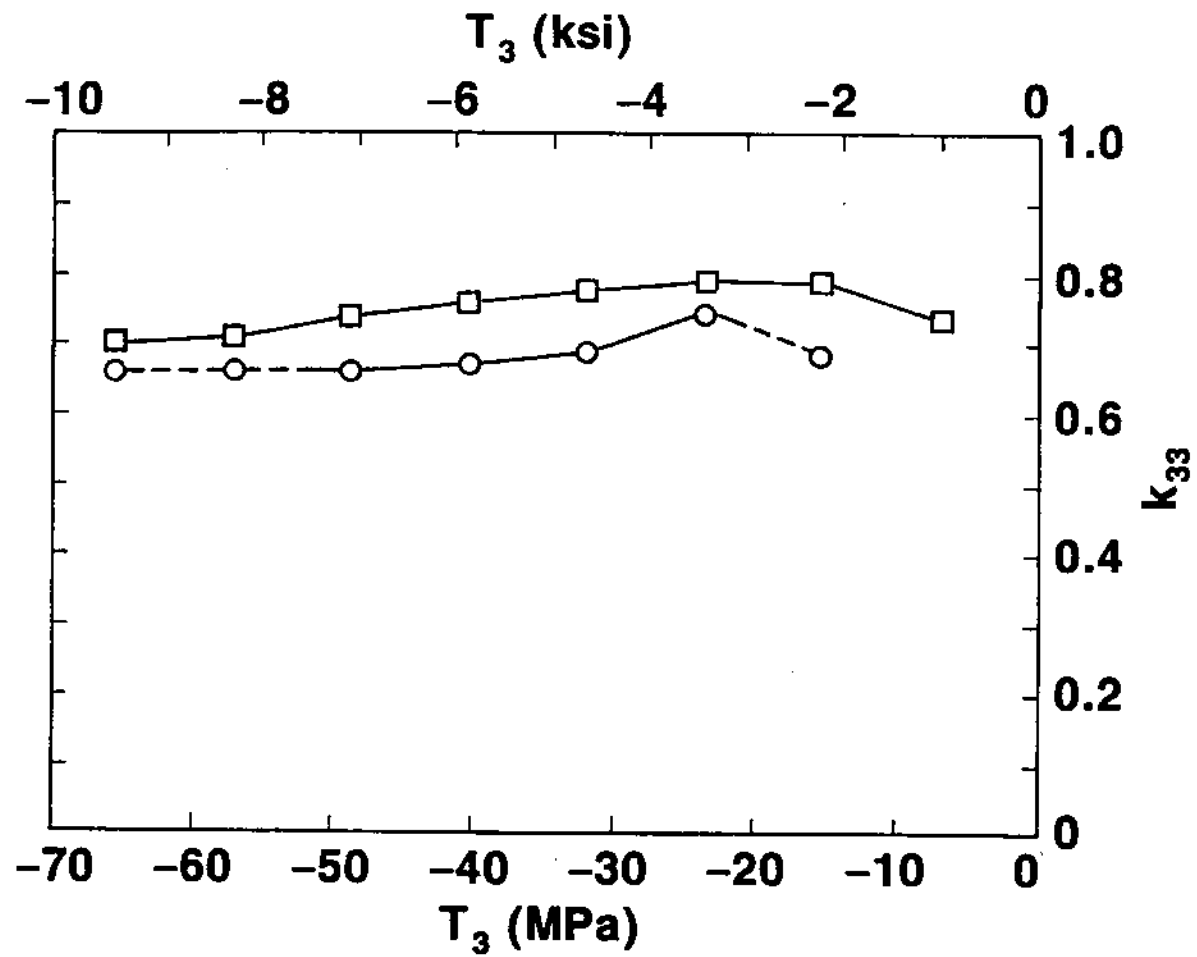


Figure 10.6-7 Magnetomechanical coupling factor for medium-level (squares) and high-level (circles) drive amplitudes as a function of prestress.

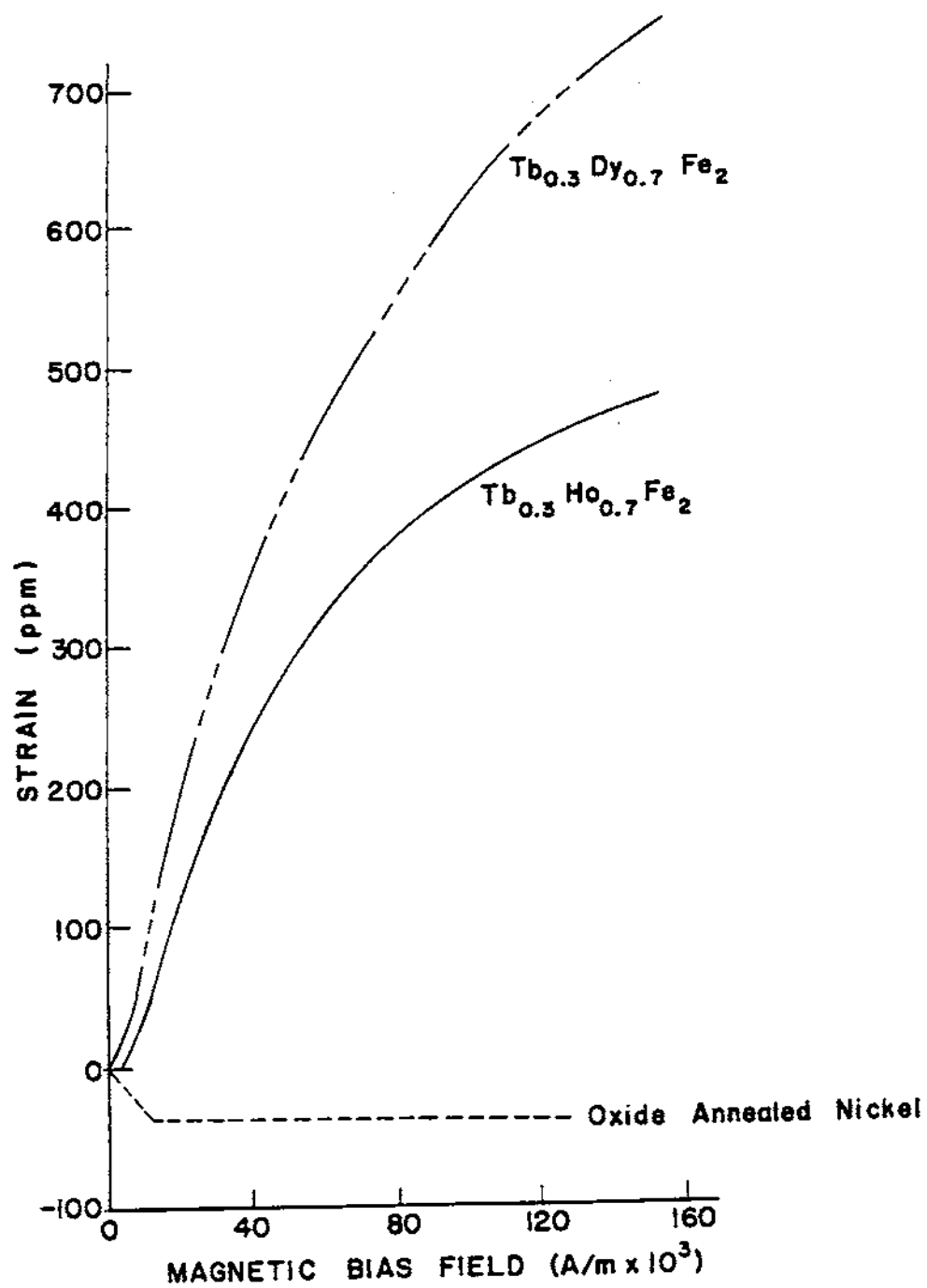


Figure 10.7-1 Magnetostriction of Tb_{0.3}Dy_{0.7}Fe₂, Tb_{0.3}Ho_{0.7}Fe₂, and oxide annealed nickel as a function of magnetic field.

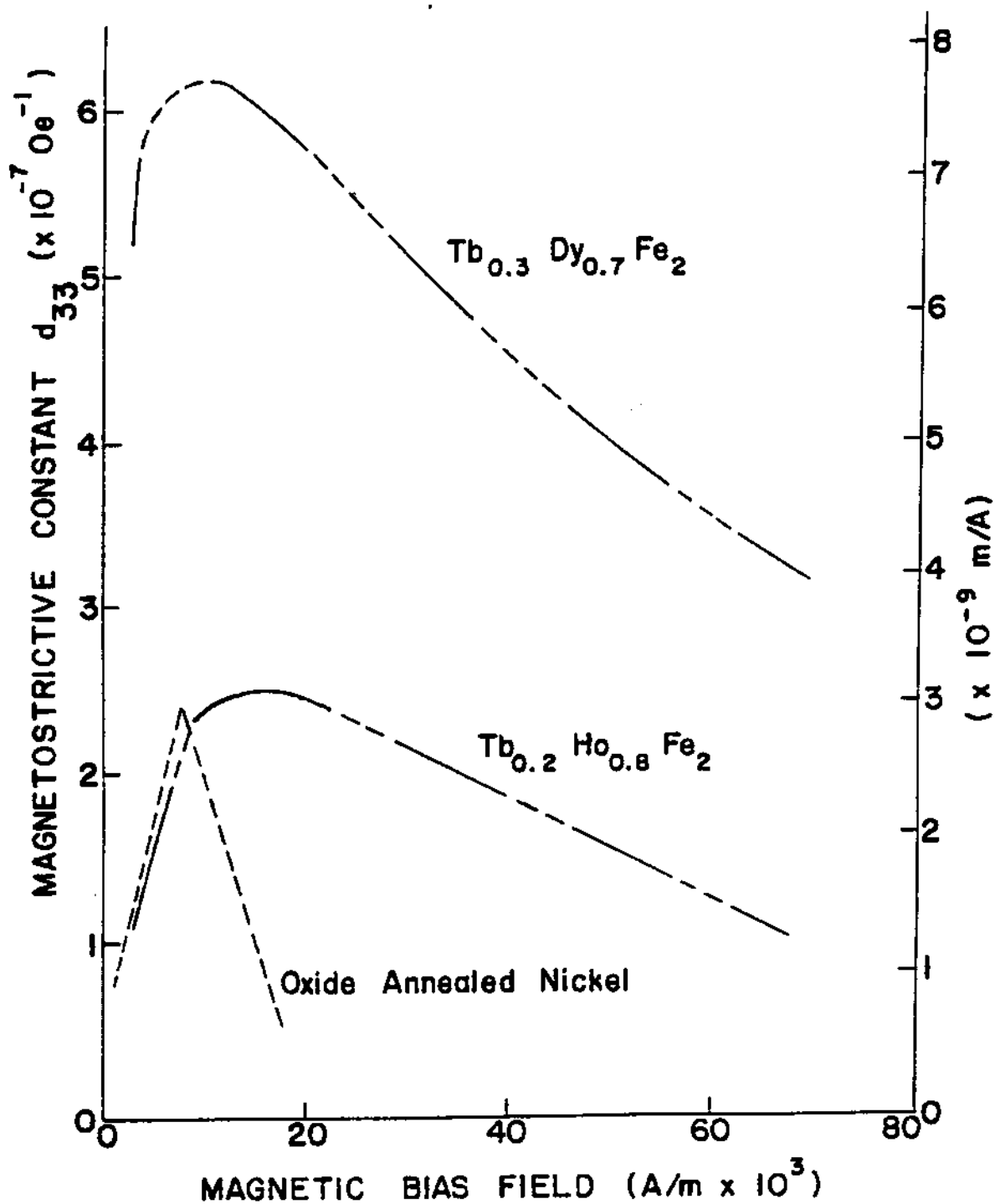


Figure 10.7-2 Piezomagnetic d_{33} constant of $\text{Tb}_{0.3}\text{Dy}_{0.7}\text{Fe}_2$, $\text{Tb}_{0.2}\text{Ho}_{0.8}\text{Fe}_2$, and oxide annealed nickel as a function of magnetic field.

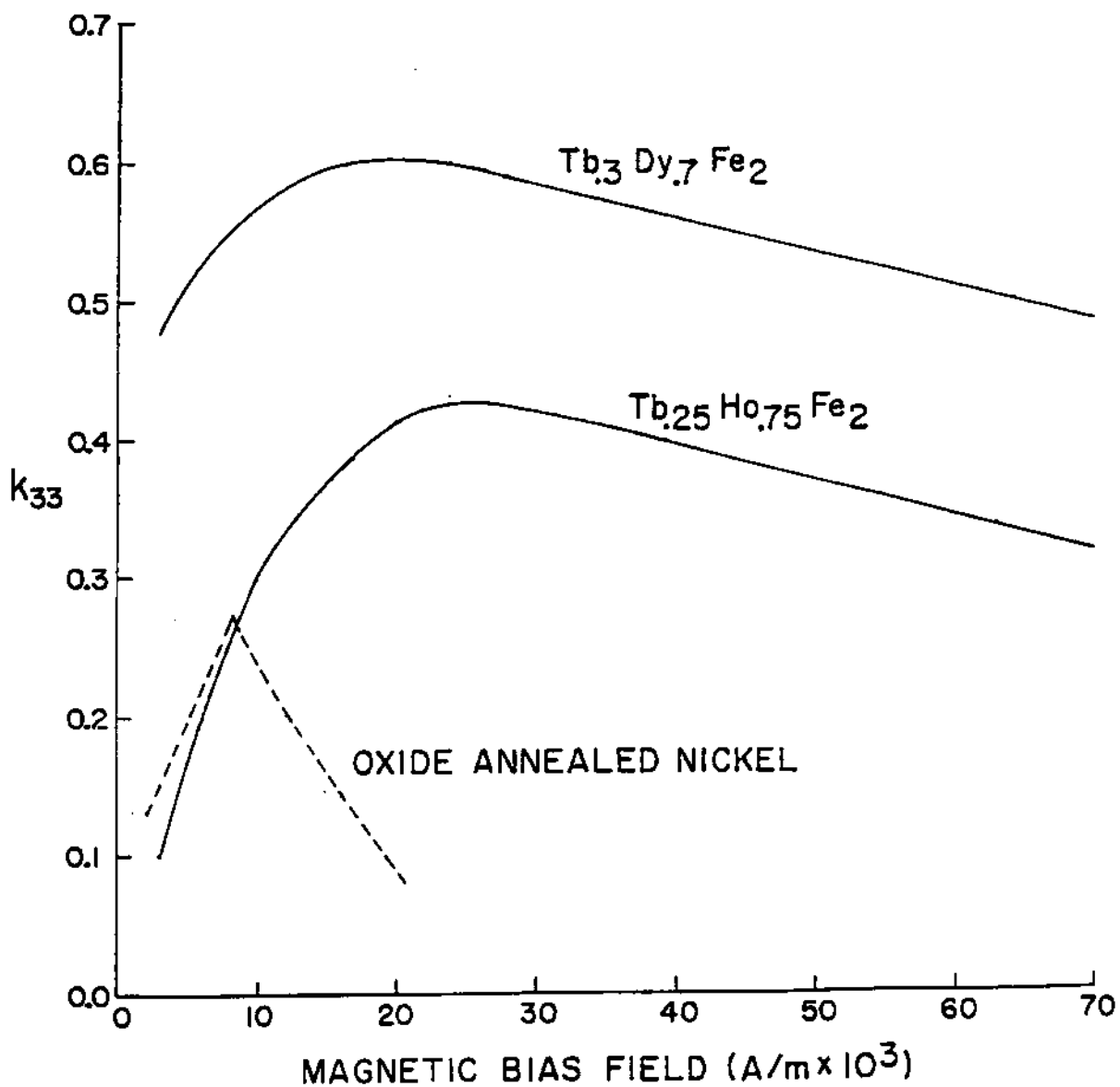


Figure 10.7-3 Magnetomechanical coupling factor of $\text{Tb}_{0.3}\text{Dy}_{0.7}\text{Fe}_2$, $\text{Tb}_{0.25}\text{Ho}_{0.75}\text{Fe}_2$, and oxide annealed nickel as a function of magnetic field.

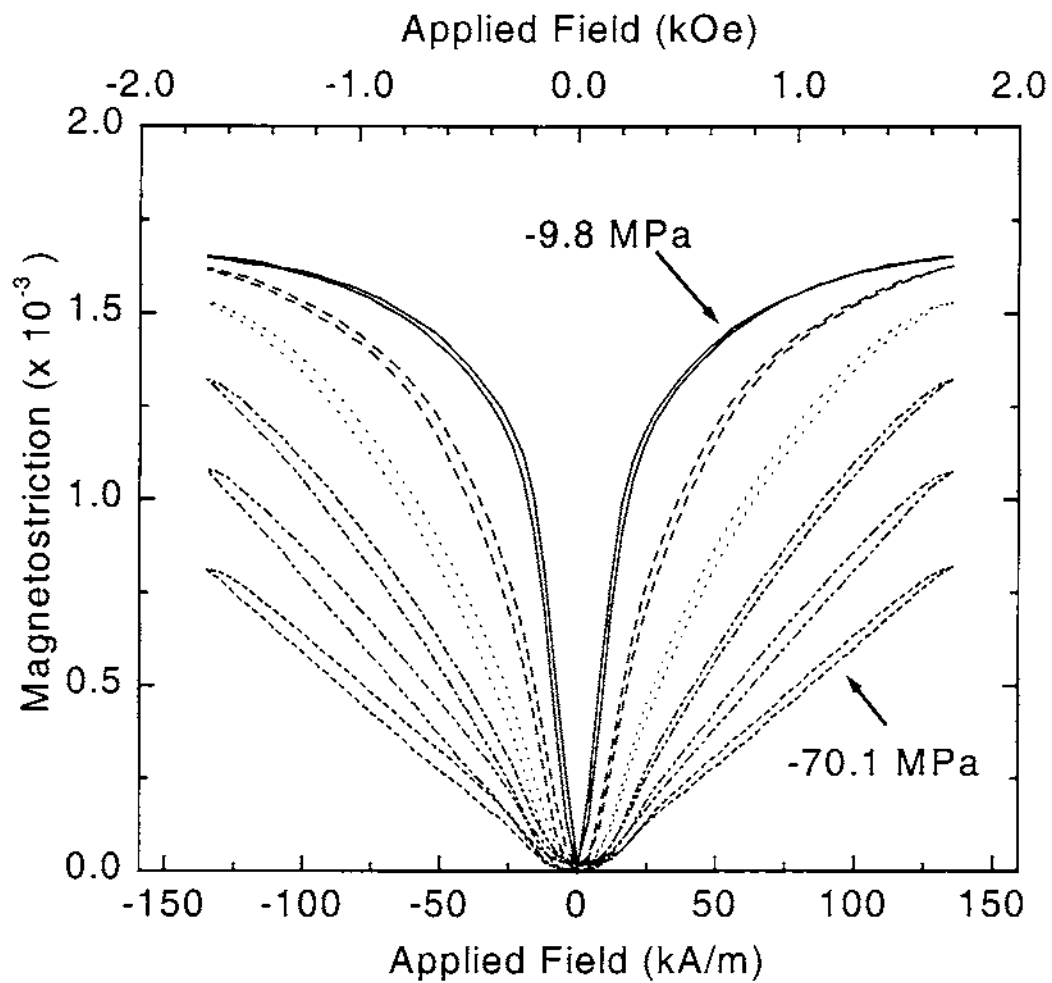


Figure 10.7-4 Magnetostriction vs applied magnetic field for $\text{Tb}_{0.28}\text{Dy}_{0.57}\text{Ho}_{0.15}\text{Fe}_2$ under compressive stresses of 9.8, 21.9, 33.9, 46.0, 58.1 and 70.1 MPa.

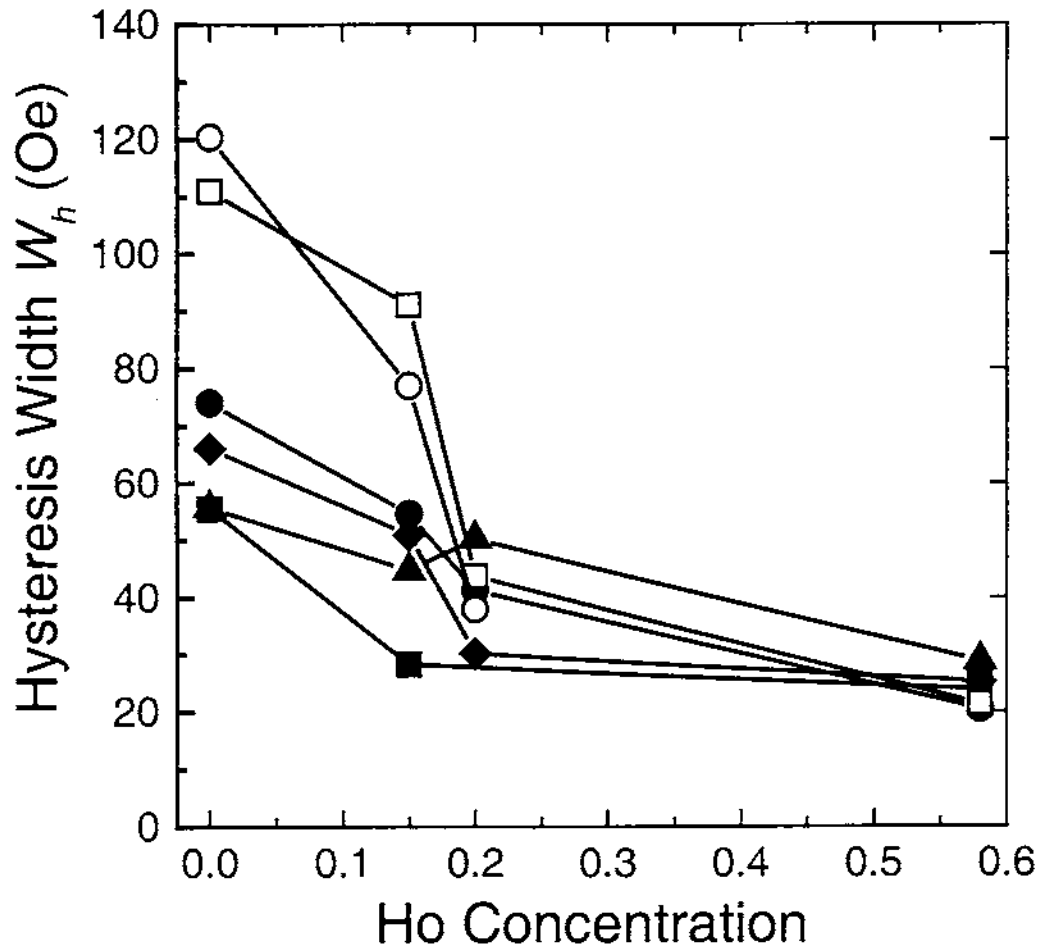


Figure 10.7-5 Hysteresis width W_h vs Ho concentration for $\text{Tb}_{0.3}\text{Dy}_{0.7}\text{Fe}_{1.95}$, $\text{Tb}_{0.28}\text{Dy}_{0.57}\text{Ho}_{0.15}\text{Fe}_{1.95}$, $\text{Tb}_{0.26}\text{Dy}_{0.54}\text{Ho}_{0.2}\text{Fe}_{1.95}$, and $\text{Tb}_{0.2}\text{Dy}_{0.22}\text{Ho}_{0.58}\text{Fe}_{1.95}$ for compressive stresses of 9.8 MPa (filled squares), 21.9 MPa (filled triangles), 33.9 MPa (filled diamonds), 46 MPa (filled circles), 58.1 MPa (open squares), and 70.1 MPa (open circles). The hysteresis width W_h is defined as the average width of the magnetic field-strain curve at the field where d_{33} is maximum.

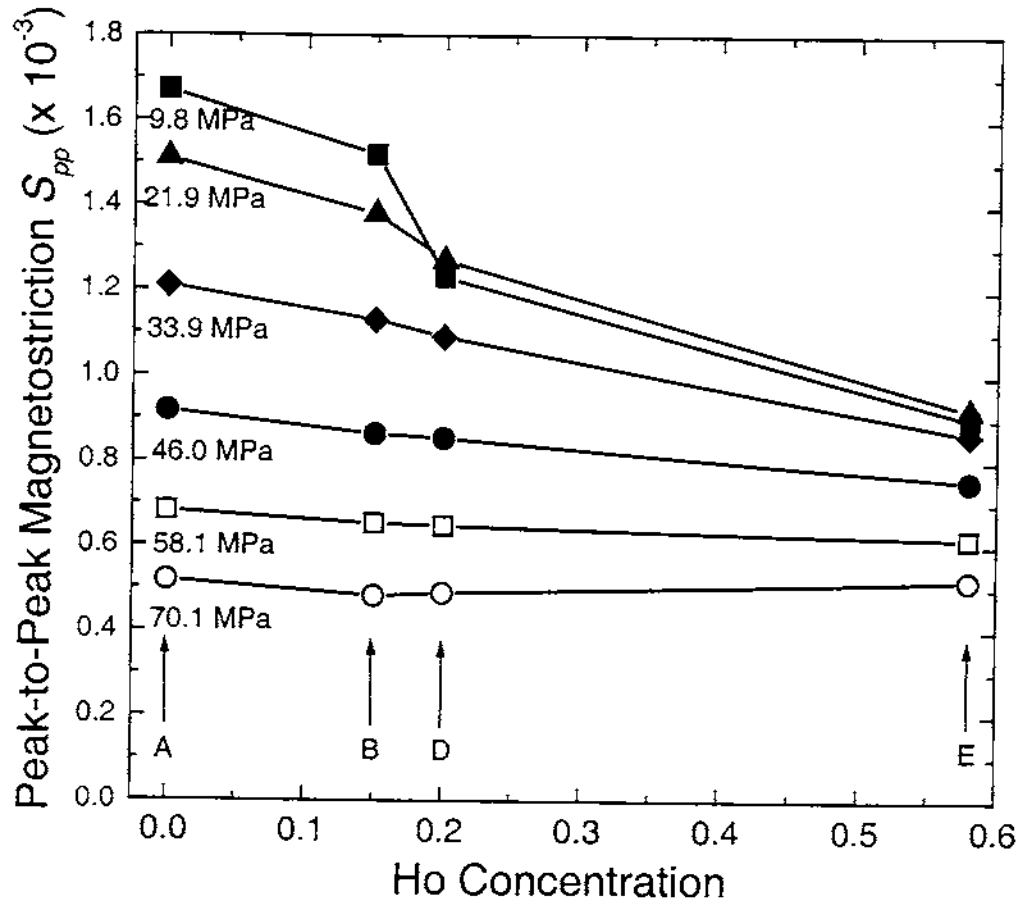


Figure 10.7-6 Peak-to-peak magnetostriction S_{pp} vs Ho concentration as a function of compressive stresses for $\text{Tb}_{0.3}\text{Dy}_{0.7}\text{Fe}_{1.95}$, $\text{Tb}_{0.28}\text{Dy}_{0.57}\text{Ho}_{0.15}\text{Fe}_{1.95}$, $\text{Tb}_{0.26}\text{Dy}_{0.54}\text{Ho}_{0.2}\text{Fe}_{1.95}$, and $\text{Tb}_{0.2}\text{Dy}_{0.22}\text{Ho}_{0.58}\text{Fe}_{1.95}$. The peak-to-peak magnetostriction S_{pp} is defined as the change in strain over a range of 71.6 kA/m (~ 900 Oe) centered around the field at which the piezomagnetic constant d_{33} is maximum, subject to the restriction that the field is always positive.

LIST OF DOCUMENTS ON CD

Acoustic Measurements for SONAR Transducer Test Personnel, Student Guide, Naval Underwater Systems Center, New London, CT, March 1990

Benthien, G. and Hobbs, S., *Solution of Kirchhoff's Time-Domain Integral Equation in Acoustics*, unpublished notes

Benthien, G. and Hobbs, S., *Calculation of Acoustic Loading on Transducers in the Time Domain*, OCEANS 2003 MTS/IEEE Conference Proceedings, September 2003, pp.2079–2084 [prepublication draft copy]

Benthien, G.W., *Symmetry Reductions*, unpublished notes

Benthien, G.W., *Far-Field Pressure Due to a Planar Piston of Arbitrary Shape*, unpublished notes

Benthien, G.W., *Mutual Interaction of Pistons of Arbitrary Shape on a Planar Rigid Baffle*, unpublished notes

Benthien, G.W., *Numerical Modeling of Array Interactions*, presented at the Second International Workshop on Power Transducers for Sonics and Ultrasonics, Toulon, France, June 1990, printed in *Power Transducers for Sonics and Ultrasonics*, Harmonic, B.F., Wilson, O.B., and Decarpigny, J.-N. (Eds), Springer-Verlag, 109–124 (1990) [prepublication draft copy]

Benthien, G.W. and Schenck, H.A., *Structure-Acoustic Coupling*, Boundary Element Methods in Acoustics, Ciskowski, R.D. and Brebbia, C.A. (Eds), Computational Mechanics Publications, Elsevier Applied Science, Chapter 6 (1991) [prepublication draft copy]

Benthien, G.W. and Barach, D., Time-Domain Model for a Hydroacoustic Transducer Array, NRaD Technical Report 1654, May 1994

Benthien, G.W. and Barach, D., Five Element Array Study, NRaD internal memorandum, October 1995

Benthien, G.W., Gillette, D., and Barach, D., *Control of Segment Interactions in Flexural Shell Transducers*, presented at the Third Joint Meeting of the Acoustical Society of America and the Acoustical Society of Japan, Honolulu, December 1996

Benthien, G.W. and Schenck, H.A., *Nonexistence and Nonuniqueness Problems Associated with Integral Equation Methods in Acoustics*, Computers & Structures, Vol. 65, No. 3, pp. 295–305 (1997)

Benthien, G.W., Barach, D., and Hobbs, S.L., CHIEF 2004 Users Manual, SSC San Diego Technical Document 3180, April 2004

Blottman III, J. and Kalinowski, A., *Coupled-field Finite Element/Spherical Harmonic Analysis for Close-Packed Arrays*, presented at the International Congress on Acoustics 2001

Capps, R.N. and Thompson, C.M., Handbook of Sonar Transducer Passive Materials, NRL Memorandum Report 4311, Naval Research Laboratory, October 1981

Ding, H.H., McCleary, L.E., and Ward, J.A., Computerized Sonar Transducer Analysis and Design Based on Multiport Network Interconnection Techniques, NUC Technical Paper 228, April 1973

Ginsberg, J.H., Pierce, A.D., and Wu, X.-F., A Variational Principle for Sound Radiation from Vibrating Bodies, Georgia Institute of Technology Acoustic and Dynamics Research Laboratory Technical Report GTADRL-86-101, November 1986

Scandrett, C. and Baker, S., T-matrix approach to array modeling, Naval Postgraduate School Technical Report NPS-UW-98-001, 1998

Scandrett, C. and Baker, S., Pritchards Approximation in Array Modeling, Naval Postgraduate School Technical Report NPS-UW-99-001, 1999

Sherman, C.H., Mutual Radiation Impedance Between Pistons on Spheres and Cylinders, USL Research Report No. 405, November 1958

Woollett, R.S., Sonar Transducer Fundamentals, Naval Underwater Systems Center

Woollett, R.S., The Flexural Bar Transducer, Naval Underwater Systems Center

Woollett, R.S., Theory of the Piezoelectric Flexural Disk Transducer with Applications to Underwater Sound, USL Research Report No. 490, December 1960